

**A Thesis Submitted for the Degree of PhD at the University of Warwick**

**Permanent WRAP URL:**

<http://wrap.warwick.ac.uk/143065>

**Copyright and reuse:**

This thesis is made available online and is protected by original copyright.

Please scroll down to view the document itself.

Please refer to the repository record for this item for information to help you to cite it.

Our policy information is available from the repository home page.

For more information, please contact the WRAP Team at: [wrap@warwick.ac.uk](mailto:wrap@warwick.ac.uk)

**EngD (International)**  
**INNOVATION REPORT**

**Vehicle Surface Contamination, Unsteady Flow  
and Aerodynamic Drag**

**by**

**Adrian Philip Gaylard**

A thesis submitted in partial fulfilment of the requirements for the degree of  
Doctor of Engineering

University of Warwick, WMG

October 2019

# TABLE OF CONTENTS

LIST OF FIGURES.....	ii
LIST OF TABLES.....	vi
ACKNOWLEDGEMENTS.....	vii
DECLARATION .....	viii
ABSTRACT.....	ix
DEFINITIONS/ABBREVIATIONS.....	x
CHAPTER 1 INTRODUCTION .....	1
1.1 Motivation.....	1
1.2 Research Strategy .....	3
1.3 Portfolio and Innovation Report Structure .....	6
CHAPTER 2 NUMERICAL SIMULATION.....	9
2.1 The Lattice Boltzmann Approach.....	9
2.2 SIMULIA PowerFLOW.....	12
2.3 Previous Validation Studies.....	19
2.4 Modelling Surface Contamination .....	23
CHAPTER 3 SIMPLE SYSTEMS .....	28
3.1 Motivation.....	28
3.2 Windsor Body.....	29
3.3 The Generic SUV .....	52
CHAPTER 4 SIMULATING REAR SURFACE CONTAMINATION FOR A PRODUCTION VEHICLE.....	66
4.1 Simulation Design .....	66
4.2 Predicted Aerodynamic Forces .....	71
4.3 Predicting Rear Surface Contamination.....	78
CHAPTER 5 FULL SCALE EXPERIMENTS .....	93
5.1 The FKFS Thermal Wind Tunnel .....	93
5.2 Tyre Spray Characterisation .....	94
5.3 Rear Surface Contamination Measurements.....	98
CHAPTER 6 CORRELATING AGAINST EXPERIMENT .....	108
6.1 Spray Model .....	108
6.2 Deposition Patterns .....	110
6.3 Relative Surface Contamination Factors.....	113
6.4 Simulation Accuracy for the Rear Surface Zones .....	117
6.5 Simulation Accuracy from an Engineering Development Perspective .....	119
CHAPTER 7 A PROCESS INNOVATION .....	121
7.1 Automotive Product Development.....	121
7.2 An Innovative Surface Contamination Process.....	123
7.3 Process Example: Rear Slotted Spoiler Validation .....	131
CHAPTER 8 CONCLUSIONS.....	134
CHAPTER 9 RECENT DEVELOPMENTS AND FUTURE WORK.....	136
9.1 Recent Developments in the Field .....	136
9.2 Future Work .....	138
REFERENCES.....	139
APPENDIX A: THE WINDSOR BODY .....	153
APPENDIX B: THE GENERIC SUV.....	154
APPENDIX C: THE 13MY RANGE ROVER.....	155

## LIST OF FIGURES

Figure 1. System of Axes and Basic Aerodynamic Quantities Used in this Work .....	x
Figure 2. A Heavily Soiled Range Rover (Hutchinson, 2016, 21 December) .....	1
Figure 3. Research Strategy: the Use of Progressively More Complex Geometries [Not to Scale] ...	4
Figure 4. Portfolio Structure .....	7
Figure 5 D3Q19 LB Model (Li <i>et al.</i> , 2004) .....	11
Figure 6 General Characteristics of the Boundary Layer .....	13
Figure 7 (a) Resolving Geometry and (b) Calculating Particle Fluxes, in a Cartesian Lattice (Li <i>et al.</i> , 2004) .....	15
Figure 8 (a) Particle “Bounce Back” and (b) Specular Reflection (Li <i>et al.</i> , 2004) .....	15
Figure 9 Variation of Lattice Spatial Resolution in PowerFLOW .....	17
Figure 10 Streamwise Wake Velocity Profiles in the Wake of the Ahmed Body with a 25° Rear Slant Angle Simulated With Three Levels of Spatial Resolution (Fares, 2006) .....	19
Figure 11 Variation of Drag Coefficient with Rear Slant Angle for the Ahmed Body (Keating <i>et al.</i> , 2008) .....	20
Figure 12 The Modular BMW Validation Model (Kandasamy <i>et al.</i> , 2012) .....	21
Figure 13 Effect of Selected Rear End Changes on Normalized Aerodynamic Drag for the BMW Validation Model (Kandasamy <i>et al.</i> , 2012) .....	22
Figure 14 Lagrangian Particle Model Schematic .....	24
Figure 15 Thin Film Model Schematic .....	26
Figure 16. Distribution of Spatial Resolution for the Windsor Body (a) In the $y=0$ Centre-Plane and (b) the Mid-Height $xy$ Plane .....	30
Figure 17. (a) Drag (b) Side and (c) Lift Force Coefficient Histories for the Baseline Windsor Body with the Mean Values Shown as Broken Lines. ....	31
Figure 18. Receding Average Functions for the Windsor Body Baseline Drag and Lift Force Coefficients .....	32
Figure 19. Force Coefficient Variation with Total Voxel Count Obtained for the Windsor Body: (a) Drag, (b) Lift, along with Difference from Experiment for (c) Drag and (d) Lift .....	34
Figure 20. Wake Flow Velocity and Streamlines for the Baseline Windsor Body from (a) Experiment (Perry, 2016:151) and Simulations using a Smallest Voxel Edge Length of (b) 0.75mm, (c) 1.0 mm, (d) 1.5 mm and (e) 2.0mm .....	35
Figure 21. Variation in Deposition History for the Complete Rear Surface of the Baseline Windsor Body with Smallest Voxel Edge Length .....	37
Figure 22. Cumulative Rear Surface Deposition Patterns for Lattices using a Smallest Voxel Edge Length of (a) 2.0 mm, (b) 1.5 mm, (c) 1.0 mm and (d) 0.75 mm .....	37
Figure 23. A Model for Wake Instability (Grandemange <i>et al.</i> , 2013) .....	38
Figure 24. Rear Surface Deposition for the Windsor Body (a) Predicted and (b) Measured (Kabanovs <i>et al.</i> , 2016) .....	38
Figure 25. Relative Predicted Film Thickness Profiles for the Baseline Windsor Body along (a) Vertical Centreline and (b) Horizontally Through the Deposition Peak .....	40
Figure 26. Airborne Spray Concentration and Flow streamlines through the Wake of the Baseline Windsor Body along (a) Vertical Centreline and (b) Horizontally at Mid-Body Height .....	41
Figure 27. The Wake Ring Vortex and Spray Core for the Baseline Windsor Body. The Spray is Visualised by an Isosurface of Fluid Volume Ratio Coloured by Mean Particle Diameter .....	42



Figure 28. Surface Static Pressure and Film Thickness on the Rear Surface of the Baseline Windsor Body (a) Along the Vertical Centreline and (b) Horizontally, Through the Deposition Peak .....	43
Figure 29. A Comparison between Measured and Simulated (a) Drag Coefficients and (b) Their Differences from Baseline for the Windsor Body as Ground Clearance and Underbody Roughness is varied .....	44
Figure 30. Flow Velocities and Streamlines on the Centre-Plane of the Windsor Body at 50 mm Ground Clearance as Underbody Roughness is Varied, Measured by Perry and Passmore (2013) [Left] and Predicted [Right].....	46
Figure 31. Flow Velocities and Streamlines on the Centre-Plane of the Windsor Body at 30 mm Ground Clearance as Underbody Roughness is Varied, Measured by Perry and Passmore (2013) [Left] and Predicted [Right].....	47
Figure 32. Variation in Deposition History for the Windsor Body as Ground Clearance and Underbody Roughness are Varied .....	49
Figure 33. Cumulative Rear Surface Deposition Patterns for the Windsor Body as Ground Clearance and Underbody Roughness are Varied .....	49
Figure 34. Wake Ring Vortex, Spray Core and Cumulative Surface Deposition Visualised for the Windsor Body as Ground Clearance and Underbody Roughness are Varied. Ring Vortex Isosurface is Coloured by Fluid Volume Ratio; Spray Isosurface by Mean Particle Diameter .....	50
Figure 35. Computational Lattice Used for the Generic SUV Shown (a) on the Vertical Centre-Plane and (b) at Mid-Body Height.....	53
Figure 36. Flow Topology for the Generic SUV, Shown by Isosurfaces of Q-Criterion Coloured by Vorticity Magnitude .....	53
Figure 37. Unsteady Force Coefficients and their Mean Values [broken line] for the Baseline Generic SUV (a) Drag and (b) Lift .....	54
Figure 38. Rear Surface Pressure Distributions for the Generic SUV (a) Measured by Forbes <i>et al.</i> (2014) and (b) Simulated by the Author .....	55
Figure 39. Velocity Distribution through the Wake of the Baseline Generic SUV from Experiment (Forbes <i>et al.</i> , 2014) and Simulation for (a-b) the $y=0$ , (c-d) $y=170$ mm and (e-f) $z=187$ mm Planes.....	57
Figure 40. Cumulative Rear Surface Deposition Pattern for the Generic SUV with (a) No Wheels and Central Sprayer Compared to a Laterally Offset Sprayer with (b) No Wheels and (c) Wheels Fitted.....	58
Figure 41. Cumulative Rear Surface Deposition Patterns for the Generic SUV (a) Measured (Kabanovs <i>et al.</i> , 2016b) and (b) Simulated.....	58
Figure 42. Drag and Lift Changes with Ground Clearance and Wheel Fitment for the Generic SUV: Absolute Changes in (a) Drag and, (b) Lift Coefficients; Changes from the Baseline for (c) Drag and (d) Lift Coefficients.....	60
Figure 43. Measured and Calculated Ring Vortex Core Locations on the Centre Plane for the Generic SUV as Ground Clearance and Wheel Fitment Varies .....	61
Figure 44. Cumulative Rear Surface deposition Pattern for the Generic SUV at (a) 50 mm, (b) 65 mm [Baseline] and (c) 80 mm Ground Clearance .....	61
Figure 45. Generic SUV (a-d) Ring Vortex Interaction with the Spray Plume and (e-h) Wheel Wake Changes with Ground Clearance and Wheel Fitment.....	63
Figure 46. Flow Streamlines Coloured by Fluid Volume Ratio Traced from the Deposition Maximum on the Generic SUV for Different Ground Clearance and Wheel Fitment Configurations .....	64
Figure 47. The Generic SUV and Windsor Body Compared against the Wake Stability Model of Grandemange <i>et al.</i> (2013) .....	65

Figure 48. The Lattice Design Used for the 13MY Range Rover, Shown on (a) $y=0$ and (b) $z=900$ mm .....	66
Figure 49. Tyre Spray Model .....	69
Figure 50. Drag Force Coefficient Histories for High, Baseline and Low Trim Heights [Mean Values Shown as Broken Lines] .....	72
Figure 51. Side Force Coefficient Histories for High, Baseline and Low Trim Heights [Mean Values Shown as Broken Lines] .....	73
Figure 52. Lift Force Coefficient Histories for High, Baseline and Low Trim Heights [Mean Values Shown as Broken Lines] .....	74
Figure 53. Correlation between Measured and Simulated (a) Drag and (b) Lift Coefficients at Low, Baseline and High Trim Heights .....	75
Figure 54. Drag Force Coefficient Histories for High, Baseline and Low Trim Heights [Mean Values Shown as Broken Lines] .....	77
Figure 55. Predicted Cumulative Rear Surface Contamination Distribution for the Baseline 13MY Range Rover .....	79
Figure 56. Simulated Deposition History for the Baseline 13MY Range Rover .....	79
Figure 57. Film Thickness on $y=0$ (a) Absolute, (b) Moving Average and Relative for the (d) Complete Run and (e) Last Two Seconds; Along with Film Thickness on a Horizontal Line (e) Absolute, (f) Moving Average and Relative for the (g) Complete Run and (h) Last Two Seconds....	81
Figure 58. Rear Surface Deposition Process: (a) Wheel Wake and Ring Vortex Interaction, (b) Spray Capture by the Ring Vortex and its Effect on the Spray in the (c) Lateral, (d) Vertical, and (e) Streamwise Directions .....	83
Figure 59. The Influence of Wheel Wakes as Shown by Flow Streamlines Tracked Upstream and Downstream from the Wheels Coloured by (a) the Release Location (b) Fluid Volume Ratio; Along with Streamlines Tracked Upstream and Downstream from the (c) Contamination Peak Coloured by Fluid Volume Ratio .....	84
Figure 60. Correlation Plots for Static Pressure and Film Thickness on the Rear Surfaces of a 13MY Range Rover: (a) Rear Screen, (b) Licence Plate, (c) Tailgate and (d) Rear Bumper .....	86
Figure 61. Predicted Cumulative Rear Surface Contamination Distribution for the 13MY Range Rover in (a) Baseline, (b) Low and (c) Height Trim Height Configurations .....	87
Figure 62. Differences in Simulated Deposition History for the 13MY Range Rover Changing from the Baseline Trim Height.....	89
Figure 63. The Effect of Trim Height on Wake Contamination Illustrated by Isosurfaces of Zero Total Pressure Coloured by Airborne Contaminant Concentration.....	90
Figure 64. Predicted Cumulative Rear Surface Contamination Distribution for the 13MY Range Rover in (a) Baseline and, (b) Improved Underfloor Configurations .....	91
Figure 65. Differences in Simulated Deposition History for Adding an Aerodynamically Improved Underfloor to the 13MY Range Rover .....	92
Figure 66 The FKFS Thermal Wind Tunnel (Kuthada <i>et al.</i> , 2002) .....	93
Figure 67. Laser Light Sheet Visualisation Experiment .....	95
Figure 68. Rear Tyre Spray Visualisation (a) 100 mm and (b) 200 mm behind a Range Rover .....	96
Figure 69. Rear Tyre Spray Core Boundary Ranges.....	97
Figure 70 Rear Surface Contamination Experiment.....	98
Figure 71 Rear Surface Contamination Intensity Distributions for the Range Rover in its Baseline Condition from 20s to 300s.....	99
Figure 72 Deposition Histories for the Rear Surface Zones on the Range Rover in its Baseline Condition.....	100

Figure 73. Rear Surface Deposition Distribution for the Range Rover at (a) High, (b) Baseline and (c) Low Trim Heights .....	103
Figure 74. Deposition History for the Complete Rear Surface of the Range Rover for Low, Baseline and High Trim Heights.....	105
Figure 75. Differences in Rear Surface Deposition Histories from the Baseline for the Range Rover at Low and High Trim Heights for (a) Rear Screen, (b) License Plate, (c) Tailgate and (d) Rear Bumper Surface Zones [* Statistically insignificant difference].....	105
Figure 76 Rear Surface Deposition Distribution for the Range Rover at its Baseline Trim Height for (a) Standard and (b) Improved Underfloor Condition .....	106
Figure 77. Deposition History for the Complete Rear Surface of the Range Rover for the Baseline and Improved Underfloor .....	107
Figure 78. Differences in Rear Surface Deposition Histories from the Baseline for the Range Rover with an Improved Underfloor, over the Rear Bumper, License Plate, Tailgate and Rear Screen....	107
Figure 79. Tyre Spray behind the 13MY Range Rover in Vertical Planes 100 mm and 200 mm Behind the Vehicle (a-b) Simulated (c-d) Measured.....	109
Figure 80. Rear Surface Contamination Distribution Pattern Simulations and Measurements for the 13MY Range Rover in High, Baseline and Low Trim Height Settings.....	111
Figure 81. Rear Surface Contamination Distribution Pattern Simulations and Measurements for the 13MY Range Rover with Baseline and an Aerodynamically Improved Underfloor.....	112
Figure 82. A Comparison of Measured and Simulated Relative Surface Contamination Factor Changes with Trim Height on the 13MY Range Rover.....	114
Figure 83. A Comparison of Measured and Simulated Relative Surface Contamination Factor Changes with Underfloor Improvement on the 13MY Range Rover.....	114
Figure 84. A Comparison of Simulated Lift Coefficient Histories for the Baseline and Improved Underfloor Configurations on the 13MY Range Rover .....	116
Figure 85. The Range Rover Compared against the Wake Stability Model of Grandemange <i>et al.</i> (2013).....	116
Figure 86. Relative Contamination Factors Compared for the Rear Surface of the 13MY Range Rover.....	118
Figure 87. A Generic Automotive Development Process (Schuetz <i>et al.</i> , 2016:381).....	122
Figure 88. The New Rear Surface Contamination Simulation Process as part of Aerodynamics Development at Jaguar Land Rover .....	124
Figure 89. Flow Chart Summarising the Aerodynamics Simulation Process with Activities Modified to Accommodate Rear Surface Contamination Simulation .....	125
Figure 90. Surface Contamination Distribution for the “On-Road” Configuration on (a) Body Side and (b) Rear Surfaces.....	128
Figure 91. Drag Coefficient Histories for the “On-Road” Configuration (a) Instantaneous, (b) Receding Average and (c) Forward Average.....	129
Figure 92. Rear Surface Contamination Patterns for the 18MY Range Rover Sport with the “Slotted” Spoiler Closed and Open from (a-b) Simulation and (c-d) Experiment.....	132
Figure 93. “Slotted” Spoiler Effect on Rear Wake Structure Shown as an Isosurface of Total Pressure Loss [ $C_{PTi}$ ] Cut on the $y=0$ Centre Plane: (a) Spoiler Slot Closed; (b) Spoiler Slot Open .	132
Figure 94. The Windsor Body with (a) Principal Dimensions Shown and (b) a Scheme for Representing Underbody Roughness (Perry and Passmore, 2013).....	153
Figure 95. The Generic SUV Shown with its (a) Principal Dimensions and (b) Mounting Details and an Optional Scheme for Underbody Roughness (Wood <i>et al.</i> , 2015).....	154
Figure 96. The 13MY Range Rover Principal Dimensions (a) in Side Elevation (b) from the Underside and (c) with an Aerodynamically Improved Underfloor.....	155

## LIST OF TABLES

Table 1 A Comparison of Calculated and Measured Drag and Lift Force Coefficients for the Baseline Windsor Body .....	33
Table 2 Calculated Force Coefficients Compared to the Measurements of Wood <i>et al.</i> (2015).....	55
Table 3 A Comparison of Relative Spatial Resolution in the Near-Wake for the Windsor Body, Generic SUV and Range Rover .....	68
Table 4 Vehicle Trim Height Settings .....	71
Table 5 A Comparison of Measured and Simulated Drag and Lift Force Coefficients .....	72
Table 6 Simulated Mean Force Coefficients for Baseline and Improved Underfloor cases. ....	76
Table 7 Differences between Simulated and Measured Relative Contamination Factors by Rear Surface Zone .....	117
Table 8 Selected FMEA Detection Event Ratings .....	120
Table 9 The Aerodynamic Impact of the 18MY Range Rover Sport Spoiler Slot .....	133

## ACKNOWLEDGEMENTS

I gratefully acknowledge Jaguar Land Rover and The Engineering and Physical Sciences Research Council for funding this Engineering Doctorate programme.

I would also like to acknowledge the advice and support of my supervisors, Professors Kerry Kirwan and Duncan Lockerby along with my industrial mentor, Nigel Taylor [J/LR].

I would also like to thank the many colleagues at Jaguar Land Rover who have helped and encouraged me. I have no doubt overlooked some, but special mention is due to: Alberto Vilariño Tarrío, Dr.-Ing. Sébastien Chaligné, Matthew Osborne, Richard Latimer, Chris Carey, John Pitman, Dr. Lara Schembri Puglisevich, Dr. Martin Davis and Will Suart.

I am also very grateful for the many useful discussions I have had over the years with friends and colleagues in academia, in particular: Professor Martin Passmore, Dr. Andrew Garmory, Dr. Anton Kabanovs, Graham Hodgson [All Loughborough University] and Dr. Anna-Kristina Perry.

This work would not have been possible without Exa Corporation developing their software to meet my needs. Special thanks are due to Dr. Jonathan Jilesen for his guidance and training along with Dr. Brad Duncan for organising my international placement.

On a personal note, completing this journey would not have been possible without the love of my life, Louise. She has put up with my writing on evenings, weekends and during holidays; supporting me every step of the way. I owe my father, Maxwell a particular debt: his unconditional love and encouragement have been a constant throughout my life and over my five year obsession with simulating the aerodynamics of cars getting dirty.

## DECLARATION

This thesis is submitted to the University of Warwick in support of my application for the degree of Doctor of Engineering. It has been composed by myself and has not been submitted in any previous application for any degree.

The work presented [including data generated and data analysis] was carried out by the author except in the cases outlined below:

Mr Alberto Vilariño Tarrío: Computational Fluid Dynamics models for the Range Rover.

Dr.–Ing. Sébastien Chaligné: Simulation data for the Range Rover Sport and the surface contamination post processing script.

Mr Matthew Osborne: Assistance with the experiments reported for the Range Rover and providing test data for the Range Rover Sport.

Mr John Pitman: aerodynamic force coefficient measurements for the Range Rover.

Parts of this thesis have been published by the author:

Gaylard, A. P., Kirwan, K. and Lockerby, D. A. (2017). Surface contamination of cars: a review. *Proceedings of the Institution of Mechanical Engineers, Part D: Journal of Automobile Engineering*, **231**(9): 1160-1176.

Gaylard, A. P., Kabanovs, A., Jilesen, J., Kirwan, K. *et al.* (2017). Simulation of rear surface contamination for a simple bluff body. *Journal of Wind Engineering and Industrial Aerodynamics*, **165**: 13-22.

## ABSTRACT

The rear surfaces of blunt-ended vehicles, such as SUVs, are vulnerable to the build-up of contaminants thrown up from wet road surfaces by their tyres. This can compromise drivers' vision, vehicle visibility, sensor performance and aesthetics. Vision will be reduced if the rear screen and lenses of camera systems become obscured. Similarly, sensing methods such as Light Detection and Ranging [LIDAR], introduced to support higher-level Advanced Driver Assistance Systems [ADAS] and autonomous driving are also vulnerable to contaminant accumulation. In addition, vehicle users may find that dirt is transferred to their hands and clothes as they access the rear load space. Finally, rapid soiling of external surfaces can be perceived as degrading the aesthetics of premium vehicles.

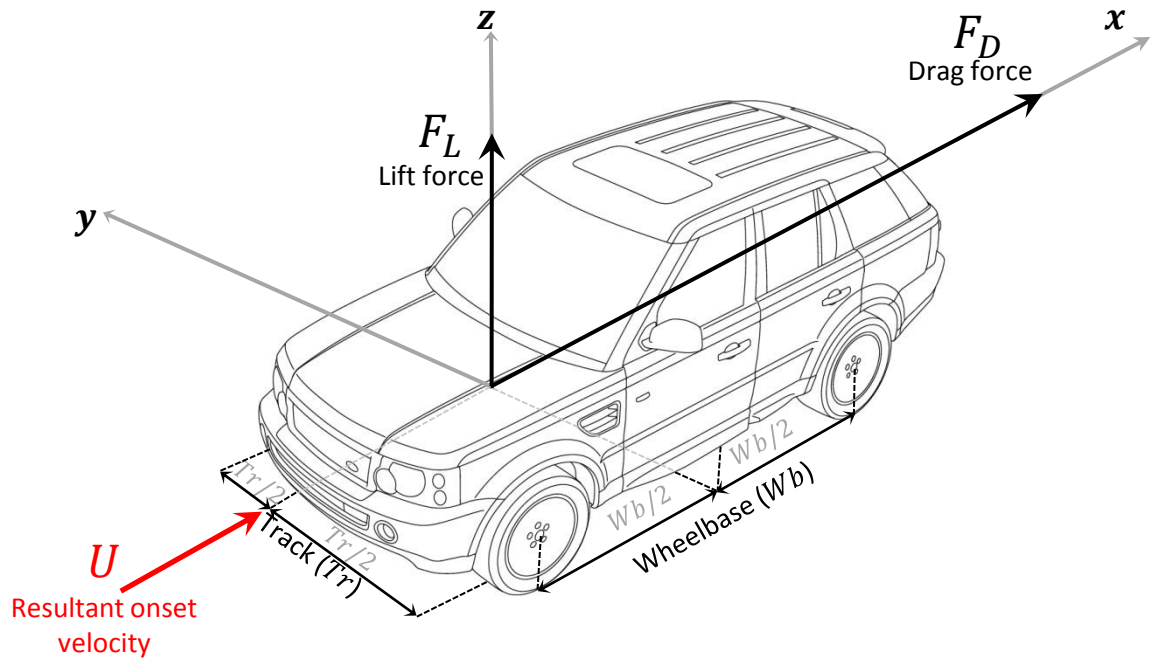
Such deposition is a manifestation of unsteady aerodynamics – particularly the interaction between tyre spray, wheel wakes and the vehicle rear wake. These wake structures also strongly influence aerodynamic drag which, in turn affects CO<sub>2</sub> emissions for Internal Combustion Engine [ICE] powered cars and the range of Battery Electric Vehicles [BEV]. Hence, automotive manufacturers need a simulation approach that can be used to minimise these characteristics concurrently during vehicle development.

This work met that need by developing and deploying an innovative simulation process which predicts both contaminant accumulation and drag at the same time, by numerically representing unsteady aerodynamics, tyre spray and surface water behaviour. It is now integrated into the vehicle development process at Jaguar Land Rover [J/LR] where it is being used to develop new cars. This has been achieved by using a series of novel simplified vehicle geometry and spray systems to incrementally develop and validate the simulation strategy. The work culminated with its application to a production vehicle and subsequent validation against full scale experiments, providing the first quantification of accuracy for simulations of rear surface contamination.

This novel simulation approach is combined with original experiments to show that reduced vehicle ride heights can lead to increased rear surface contamination, by reducing underbody flow and moving the vehicle wake closer to the highly contaminated wheel wakes. This provides a challenge for vehicle developers as lower ride heights are used to reduce aerodynamic drag; an increasingly important objective for both ICE and BEV product development, to support lower CO<sub>2</sub> emissions and enhanced range, respectively. Finally, the first evidence is presented to suggest that aerodynamically improved underfloors can increase rear surface contamination, or at least redistribute it towards the lower regions of the vehicle rear, such as the bumper. This raises a risk for future BEVs which combine aerodynamically advantageous smooth underfloors with vulnerable ADAS features, such as rear bumper mounted LIDAR.

## DEFINITIONS/ABBREVIATIONS

### BASIC AERODYNAMIC QUANTITIES



[Onset flow definitions based on the classical wind tunnel perspective of the moving observer]

**Figure 1. System of Axes and Basic Aerodynamic Quantities Used in this Work**

Quantities shown in Figure 1:

$F_D$	Drag force; the aerodynamic force opposing vehicle motion
$F_L$	Lift force; the aerodynamic force in the vertical [ $z$ ] direction
$Tr$	Vehicle track; the distance [in $y$ ] between wheel centres
$U$	Resultant velocity
$Wb$	Vehicle wheel base; the distance [in $x$ ] between wheel centres

### Additional English Symbols

$\vec{a}_p$	Particle acceleration vector
$A$	Vehicle projected frontal area
$c$	Speed of sound in air
$c$	Speed of air particles
$C$	Lattice Boltzmann collision operator



$C^*$	Relative ground clearance, $h_g/W$
$C_P$	Pressure coefficient = $(P - P_\infty)/\frac{1}{2}\rho U_\infty^2$
$C_{P_i}$	Total pressure loss coefficient
$C_D$	Drag force coefficient = $F_D/\frac{1}{2}\rho U_\infty^2 A$
$C_{D_{rec.}}$	Receding average of the drag force coefficient
$C_L$	Lift force coefficient = $F_L/\frac{1}{2}\rho U_\infty^2 A$
$C_{L_{rec.}}$	Receding average of the lift force coefficient
$d_p$	Particle or droplet diameter
$\bar{d}_p$	Average particle diameter
$\vec{D}$	Particle aerodynamic drag force vector
$f$	A continuous function
$f_i$	A discrete function
$f_{PD}$	Domain flow passes
$f_{PV}$	Vehicle flow passes
$h_g$	Height above ground
$h_f$	Surface film thickness
$\bar{h}_f$	Mean surface film thickness
$h_{rel.}$	Relative Surface film thickness
$h_r$	Height of underbody roughness elements
$h_t$	Vehicle trim height
$H$	Vehicle, or bluff body height
$H^*$	Relative body height, $H/W$
$i$	A numerical index

$I$	Re-emitted radiation intensity
$I_{rel}$	Relative re-emitted radiation intensity
$I_S$	Scattered radiation intensity
$I_{S_{Rel.}}$	Relative scattered radiation intensity
$k$	Turbulent kinetic energy
$l$	Integral length scale for turbulent flows
$L$	Characteristic (reference) length, usually vehicle or model length
$L_D$	Computational domain length
$m$	Number of discrete particle velocities
$m_p$	Particle [point] mass
$M$	Surface film mass
$\dot{M}$	Surface film [mass] deposition rate
$n$	Number of particles or droplets
$\mathbf{n}$	Surface normal vector
$N$	Total number of particles, droplets or data points
$N_v$	Total number of voxels
$p$	Static pressure
$P$	Pressure
$P_0$	Stagnation point
$P_T$	Total pressure
$q$	Dynamic pressure
$r$	Droplet radius
$r_P$	Pearson product-moment correlation coefficient
$R$	Gas constant

$R^2$	Coefficient of determination, in a linear regression analysis
$Re$	Reynolds number
$Re_H$	Height based Reynolds number
$t$	Time
$T$	Temperature
$u$	$x$ -velocity component
$\mathbf{u}$	Velocity vector
$u_\tau$	Shear velocity
$U_p$	Particle velocity
$U_\infty$	Undisturbed (freestream) velocity magnitude
$v$	$y$ -velocity component
$V_U$	$x$ -location of the centre of the wake ring vortex upper lateral arm
$V_L$	$x$ -location of the centre of the wake ring vortex lower lateral arm
$w$	$z$ -velocity component
$w_i$	Weighting parameter
$W$	Vehicle width

### **Additional Greek Symbols**

$\alpha$	Significance level [statistical]
$\alpha_T$	Ring vortex tilt angle, from the vertical
$\beta$	Rear body slant angle
$\dot{\gamma}$	Rate of shear
$\delta$	Boundary layer disturbance thickness
$\delta x$	[Streamwise] $x$ -position of the wake vortex lower lateral arm, relative to the base

$\delta\bar{x}_{RMS}$	RMS of the mean positional error in the [streamwise] $x$ -position of the wake vortex lower lateral arm, relative to the base
$\delta z$	[Vertical] $z$ -position of the wake vortex lower lateral arm, relative to the bottom of the base
$\delta z_{RMS}$	RMS of the mean positional error in the [vertical] $z$ -position of the wake vortex lower lateral arm, relative to the base
$\Delta P_T$	Total pressure loss
$\Delta t$	Simulation time step length
$\Delta x$	Length of a computational cell in $x$
$\varepsilon$	Eddy dissipation
$\theta$	Radiation scattering angle
$\kappa$	The von Kármán constant
$\mu$	Dynamic viscosity
$\mu_t$	Eddy viscosity
$\nu$	Kinematic viscosity
$\rho$	Fluid density
$\sigma_\tau$	Shear stress
$\tau$	Particle relaxation time
$\tau$	Shear
$\tau_w$	Wall shear stress
$\varphi$	Vehicle pitch angle
$\omega$	Angular [rotational] velocity
$\omega_c$	Particle collision frequency

## ABBREVIATIONS

ADAS	Advanced Driver Assistance Systems
BEV	Battery Electric Vehicle
CFD	Computational Fluid Dynamics
CPU	Central Processor Unit
DES	Detached Eddy Simulation
EC	European Commission
FKFS	Research Institute of Automotive Engineering and Vehicle Engines Stuttgart <i>[Forschungsinstitut für Kraftfahrwesen und Fahrzeugmotoren Stuttgart]</i>
FMEA	Failure Mode Effects Analysis
FVR	Fluid Volume Ratio
HPC	High Performance Computing
ICE	Internal Combustion Engine
J/LR	Jaguar Land Rover
LBM	Lattice Boltzmann Method
LIDAR	Light Detection and Ranging
SAE	Society of Automotive Engineers
SUV	Sport Utility Vehicle
UNECE	United Nations Economic Commission for Europe
VLES	Very Large Eddy Simulation
WLTC	Worldwide harmonized Light vehicles Test Cycle
WLTP	Worldwide Harmonised Light Vehicle Test Procedure

## CHAPTER 1 INTRODUCTION

### 1.1 MOTIVATION

The gradual build-up of contaminants on the rear surfaces of blunt-ended vehicles, such as Sports Utility Vehicles [SUV], estate and hatchback cars is a manifestation of unsteady multi-phase aerodynamics and at the same time presents a range of practical issues for vehicle manufacturers and their customers (Gaylard *et al.*, 2017a). From the drivers' perspective, rear vision can become compromised as unwiped regions of the rear screen and any camera lenses become obscured; further, the rear wash-wipe system may require activating more frequently than desired resulting in its reservoir being more quickly depleted. There is also a risk that the vehicle becomes less visible to other road users as rear lamp clusters become soiled. In the same vein, an obscured rear license plate can be viewed as an offence by law-enforcement in many jurisdictions. If the tailgate and any associated release mechanism become heavily contaminated then dirt may be transferred to the hands and clothes of vehicle users as they access the rear load space. Finally, rapid soiling of the rear surfaces may be perceived as degrading the vehicles' aesthetics, which can be a significant concern for owners of premium cars. All these issues are evident in the image of a heavily soiled Range Rover shown in Figure 2.



**Figure 2. A Heavily Soiled Range Rover (Hutchinson, 2016, 21 December)**

Recently, a new aspect of this issue has emerged. Advanced Driver Assistance Systems [ADAS] have become relatively common features on cars. These rely on a range of sensors to detect traffic signs, obstacles, pedestrians and other vehicles (Paul *et al.*, 2016). As a result, rear cameras are transitioning from an occasional parking aid to a full-time sensor for safety systems such as moving-object detection. In addition, as automotive manufacturers move towards more extensive ADAS capability and eventually full autonomy, rear-mounted Light Detection and Ranging [LIDAR] sensors are expected to feature on future vehicles. The performance of these systems is sensitive to the presence of environmental water and dirt. In addition, providing extra wash systems to cover ADAS sensors adds cost and complexity.

Therefore, it is important for manufacturers to be able to anticipate the degree and distribution of contamination deposited on the rear surfaces of this broad class of vehicles. Beyond this, they also need to reduce deposition in total, or at least in particularly sensitive locations. However, this must be seen in the context of vehicle aerodynamic performance, to which it is inextricably linked.

The linkage between rear surface contamination and aerodynamic resistance to forward motion [drag] results from the influence of the vehicle rear [base] wake on both issues. Contamination deposited on the rear of a blunt-ended vehicle overwhelmingly originates from the spray generated as its rear tyres interact with wet road surface. This so-called “self-soiling” (Kuthada & Cyr, 2006) starts with the rear tyres lifting water from the road containing a complex mix of suspended and solute contaminants. Some of the resulting spray is captured by the rear wheel wakes. These aerodynamic structures interact with the base wake, transferring a fraction of the airborne spray to it. Finally, the base wake then throws spray back towards the rear surfaces, where it is deposited. The base wake also contributes to the vehicle’s drag. For instance, the wake flow generated by blunt-ended cars typically causes more than one-third of their aerodynamic drag, by reducing the static pressure over the rear surfaces (Irving Brown *et al.*, 2010).

Aerodynamic drag is an increasingly important aspect of vehicle performance in its own right. At highway speeds around 70% of a car’s total resistance to forward motion is attributable to aerodynamic drag (Dávila *et al.*, 2013). This impacts fuel consumption for Internal Combustion Engine [ICE] powered vehicles and range for Battery Electric Vehicles [BEV]. Further, the introduction of new regulatory regimes, such as the Worldwide Harmonised Light Vehicle Test Procedure [WLTP] along with its Test Cycle [WLTC] has increased the sensitivity of homologated tail-pipe emissions to drag (UNECE, 2017; Tutuianu *et al.*, 2013). From 2020 onwards, every gram of CO<sub>2</sub> emissions will carry significant costs for manufacturers. These will vary across different markets in both size and timing (ADL, 2014), but as an example the EU have set targets for the

“fleets” of vehicles manufacturers sell in their territory from 2020 onwards. For *every gram* manufacturers exceed their fleet-averaged target a fine of 95€ will be levied *per vehicle sold* (EC, 2017). Given that large manufacturers sell cars by the million into this market, these fines pose a significant economic risk. For example, PA Consulting (2017) has estimated that, “on current performance the fines can reach or rise above the €1bn mark for some carmakers.” This provides a substantial economic imperative for drag reduction. It also means that solutions which improve rear surface contamination at the expense of aerodynamic drag are likely to be unpalatable. Therefore, vehicle aerodynamic drag and rear surface contamination performance must be developed concurrently to find balanced solutions.

This work addressed these needs by developing and deploying an innovative numerical simulation process that predicts the distribution of contaminants over the rear surfaces of SUVs concurrently with their aerodynamic drag. This has changed the way in which cars are developed aerodynamically at Jaguar Land Rover, with rear surface contamination and aerodynamic drag assessed in a digital process which complements a later phase of physical testing. The following section justifies the focus on SUVs and outlines the research strategy which culminated in the deployment of this innovative simulation process.

## 1.2 RESEARCH STRATEGY

The focus on SUVs is appropriate as they represent the most popular body style for new car buyers in both the European (JATO, 2016) and US markets (IHS Automotive, 2014). In addition to their blunt-ended rear shape rendering them susceptible to surface contamination (Maycock, 1966), it also tends to result in relatively high drag coefficients [ $C_D$ ]. When combined with their comparatively large frontal areas [ $A$ ] this typically leads to higher drag forces [ $\propto C_D A$ ] than would be experienced by saloon cars (Howell *et al.*, 2002). Finally, their large wakes are characterised by high degrees of flow unsteadiness (Sims-Williams *et al.*, 2001; Sterken *et al.*, 2016). Hence they exemplify the connection between rear surface contamination, unsteady flow and aerodynamic drag.

Given that these physical characteristics are closely connected, they need to be developed concurrently as vehicles move through the product design process. This raises the question, “how can it be done?” Broadly, there are two options: physical testing and numerical simulation. In the field of aerodynamics both approaches have been gradually integrated within the same development process (Gaylard, 2009). The most conservative approach is to add numerical simulation as an early “virtual” development phase; a precursor to reduced and full-scale wind tunnel testing (Froling & Juechter, 2005; Hahn *et al.*, 2007; Mayer & Wickern, 2011; Machida *et al.*, 2015). In contrast, a more radical approach has been to replace reduced-scale wind tunnel



testing with numerical simulation (Amodeo, 2004; Gaylard, 2008; Samples *et al.*, 2010; Palin *et al.*, 2012; Chen, *et al.*, 2013; Kremheller, 2014; Chaligné *et al.*, 2018). This latter scheme integrates numerical simulation and full-scale wind tunnel testing in a single development process. Therefore, if surface contamination is to be addressed in this context both numerical simulation and physical test are required. However, as shown in the comprehensive review of this field by the author (Gaylard *et al.*, 2017a) numerical simulation is currently less developed than its experimental counterpart. Hence, this work focussed on developing a numerical simulation approach to the point where current vehicle development practise could be changed substantially by using simulation as a lead design tool and complement to later physical testing.

The strategy used to achieve this goal is illustrated in Figure 3. It shows a programme of research that started with highly simplified geometries, which were combined with spray models to form digital representations of the rear surface contamination problem. These “simple systems” were used as tools to develop and refine a novel simulation approach before it was applied to a production vehicle and integrated into an innovative vehicle development process. The concept of using simplified geometries, which represent a few salient features, is widely used in automotive aerodynamics (Le Good & Garry, 2004). It enables key aerodynamic processes to be investigated without the myriad interactions seen in real production vehicles, or having to cope

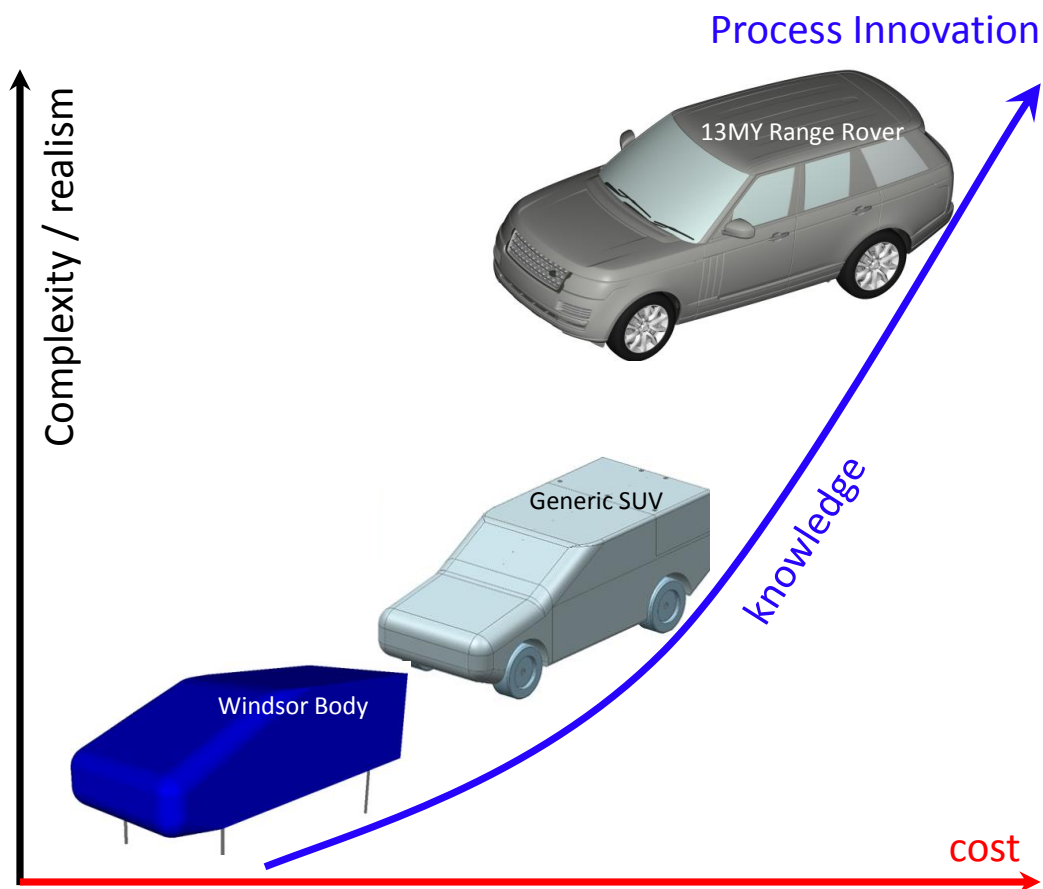


**Figure 3. Research Strategy: the Use of Progressively More Complex Geometries [Not to Scale]**

with their geometric complexity. Essentially, they provide an improved signal-to-noise ratio, by omitting geometry responsible for generating flow features not relevant to the problem under investigation.

Following this strategy, two novel simple systems have been developed for the investigation of rear surface contamination. These were based on simplified geometries drawn from the field of automotive aerodynamics. In each case, previously published physical test data was drawn on to validate key aspects of their performance. The first simple system used the Windsor Body<sup>1</sup> (Windsor, 1991) to determine the requirements for accurate simulation of the rear wake generated by a “square-backed” vehicle, its interaction with an airborne spray and role in depositing contamination on a rear surface. This was extended to investigate the effect of underbody flow, its influence on wake structure and subsequent surface deposition. The next stage in advancing towards a simulation of a production vehicle was to add the influence of static [i.e. non-rotating] wheels and their wake structures. This was addressed by the second simple system which used the Generic SUV<sup>2</sup> (Wood *et al.*, 2015) as its vehicle representation. This basic car shape has overall proportions matching those of a Range Rover at one-fifth scale; it has three selectable ride heights and can be used with or without wheels. Combined with a single spray located behind a rear wheel, it formed a simple system that allowed the emerging simulation approach to be tested on a geometry with more car-like features and a different wake structure. This enabled the role of the wheel wakes to be elucidated as the ride height was changed. Next, the progressive process development focussed on applying the novel simulation approach to a fully-detailed production vehicle, the 13MY Range Rover<sup>3</sup>. To correlate the simulation approach against physical test data, two full-scale test campaigns were conducted in the FKFS Thermal Wind Tunnel [TWT]. These provided the first characterisation of the spray generated by the rear tyres of a production SUV, the source of rear surface contamination. For the first time, the effects of ride height and aerodynamically improving the vehicle underfloor on rear surface contamination were determined. Finally, the research programme culminated with the correlated simulation methodology being integrated into an innovative vehicle development process. This innovative process has changed the way cars are developed at Jaguar Land Rover, by enabling improvement of rear surface contamination concurrently with aerodynamic drag through simulation. Evidence of this is provided by describing the development of a “slotted” spoiler for the 18MY Range Rover Sport that dramatically reduces rear screen soiling, whilst reducing drag.

The following sections describe the complete portfolio of work that this summary report draws on, before outlining its overall structure.

---

<sup>1</sup> See APPENDIX A.

<sup>2</sup> See APPENDIX B.

<sup>3</sup> See APPENDIX C.

## 1.3 PORTFOLIO AND INNOVATION REPORT STRUCTURE

### 1.3.1 Portfolio

The portfolio of work that this report draws on is illustrated by Figure 4. It comprises three distinct phases: [1] a survey of the field providing the background for this work and defining the research questions; [2] the incremental development of a novel simulation approach for rear surface contamination through the use of two simple systems – the Windsor Body and Generic SUV; [3] the development and deployment of an innovative vehicle development process. It contains four main reports [A – D], supported by two peer-reviewed journal papers [A.1 & B.1]. These are described below.

- A. *Unsteady flow, Vehicle Surface Contamination and Aerodynamic Drag: Background Report (Portfolio Report A)* introduces key concepts in automotive aerodynamics and then surveys the overall topic of vehicle surface contamination, justifying the focus on the rear surfaces and defining the research questions for this work. This is supported by a comprehensive review paper which embodies a new taxonomy for the field and covers all aspects of external, upper body surface contamination:

Gaylard, A. P., Kirwan, K. and Lockerby, D. A. (2017). Surface contamination of cars: a review. *Proceedings of the Institution of Mechanical Engineers, Part D: Journal of Automobile Engineering*, **231**(9): 1160-1176.

- B. *The Use of Simple Bluff Bodies to Investigate Rear Surface Contamination (Portfolio Report B)* justifies the use of the Windsor Body and Generic SUV model. Numerical simulation options are compared and the selection of the approach used in the work is outlined. It then reports the research undertaken on these two simple systems. Foundational work using the Windsor Body has also been published as a journal article:

Gaylard, A. P., Kabanovs, A., Jilesen, J., Kirwan, K. *et al.* (2017). Simulation of rear surface contamination for a simple bluff body. *Journal of Wind Engineering and Industrial Aerodynamics*, **165**: 13-22.

- C. *The Simulation of Rear Surface Contamination for a Fully Engineered SUV and its Application to Automotive Aerodynamics Development (Portfolio Report C)* takes the simulation approach developed in Portfolio Report B and applies it to the 13MY Range Rover. The simulations are correlated against the experiments detailed in *Portfolio Report D* for changes in the ride height and underbody condition. A numerical assessment was also made of an “on-road” configuration with a moving ground plane and spray emitted from all four tyres. This culminated with the definition of an innovative vehicle development process for rear surface contamination. Finally, an example is

provided of the new process being used to complete the development of the rear screen soiling reducing “slotted” spoiler fitted to the 18MY Range Rover Sport.

- D. *Full Scale Experimental Investigation of Rear Surface Contamination for an SUV (Portfolio Report D)* describes physical tests using the 13MY Range Rover in the FKFS Thermal Wind Tunnel [TWT]. This starts with the first characterisation of rear tyre spray generated by an SUV using Laser Light Sheet Illumination. It then moves on to document the first assessment of rear surface contamination for a range of systematic vehicle modifications. These include two aspects of particular importance to future vehicles: ride height reduction and aerodynamic underfloor improvement. They are particularly relevant to Battery Electric Vehicles in this segment, as these will be operated at lower ride heights and have aerodynamically smooth underfloors.

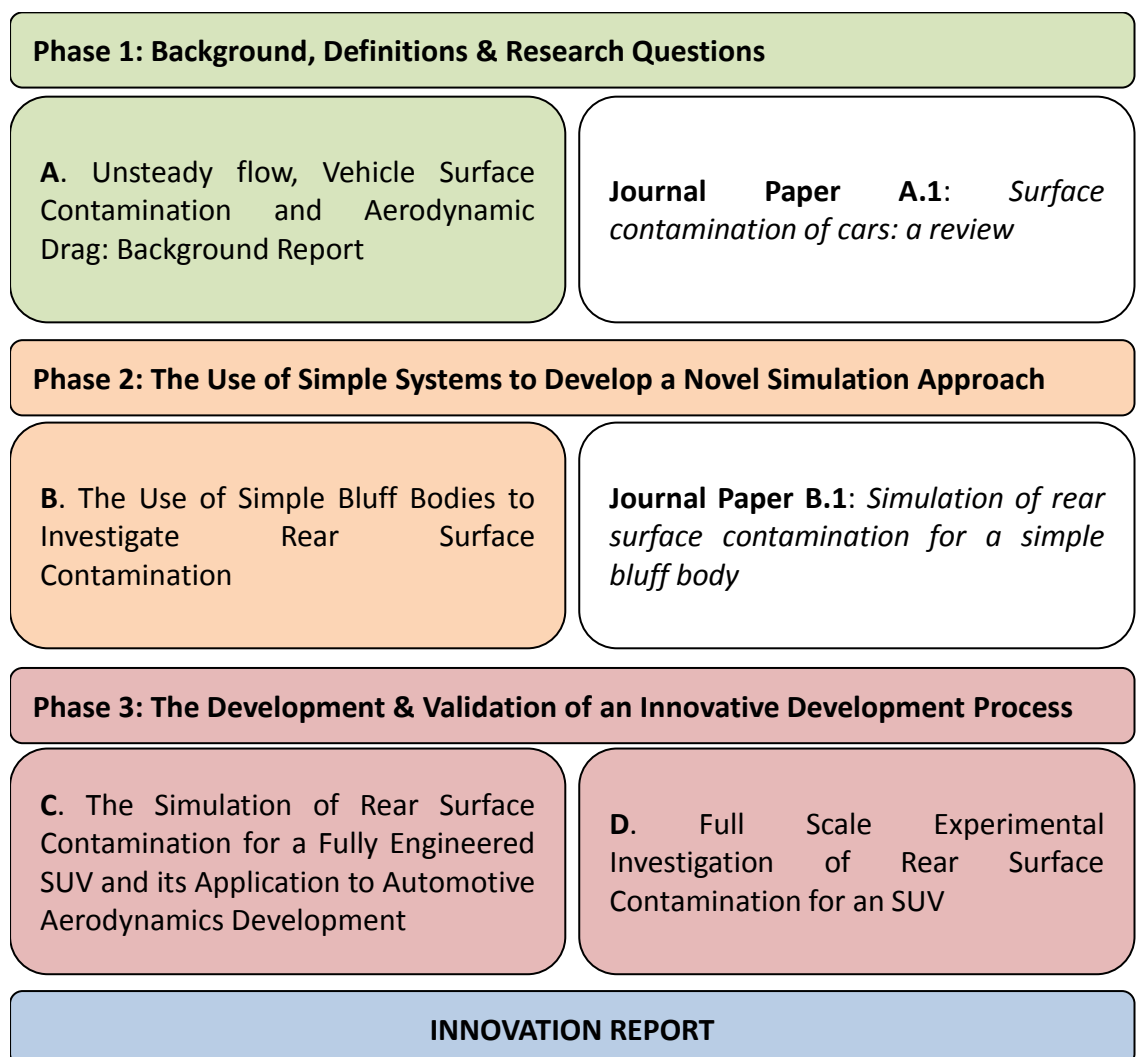


Figure 4. Portfolio Structure

### **1.3.2 Innovation Report**

This “Innovation Report” provides a retrospective summary of the portfolio of research work outlined in the previous section. CHAPTER 2 describes the numerical simulation approach used in this work; this is followed by CHAPTER 3 which summarises the development of the rear surface contamination simulation process through the use of two simplified geometries, with a particular focus on the requirements for an accurate representation of the vehicle wake and deposition processes. These simple systems are also used to explore the implications of ride height changes and underbody flow.

CHAPTER 4 builds towards the deployment of an innovative vehicle development process through documenting the first simulations of rear surface contamination deposition on a production vehicle for a range of ride heights and with a modification of its underfloor. These results also provide a series of important insights that underpin the use of numerical simulation; for example, they demonstrate that the simulated deposition process is linear and the consequent relative distribution of material over the rear surface is stable, with respect to time. This also provides the first comprehensive description of the rear surface deposition process, including the interaction between wheel wakes, underbody flow and the base wake as ride height is varied. In addition, a new perspective is provided on the correlation between surface pressure and contaminant deposition.

CHAPTER 5 describes the author’s full scale experiments, performed on a production vehicle. These enable the detailed simulations to be validated. This also includes the first characterisation of the spray generated by the rear tyres of an SUV and measurements of rear surface deposition as the vehicle was modified. Looking to the future, where this class of vehicle becomes increasingly produced with electric powertrains, the main focus is on underbody modification and vehicle ride height. This captures two key design trends: the move towards smooth underfloors and reduced ride heights. These data are used to validate the production vehicle simulations in CHAPTER 6, providing the first systematic assessment of the accuracy of rear surface contamination simulation. This demonstrates that the numerical approach developed in this work is suitable for inclusion in a vehicle development process.

The work culminates in CHAPTER 7 with the deployment at Jaguar Land Rover of an innovative process for the concurrent simulation of rear surface contamination and aerodynamic drag. Its successful operation is illustrated through the development of a new “slotted” spoiler for the 18MY Range Rover Sport, which reduces both rear screen soiling and drag. Finally, the main conclusions are outlined in CHAPTER 8 with recent development in the field and options for future work summarised in CHAPTER 9.

## CHAPTER 2 NUMERICAL SIMULATION

### 2.1 THE LATTICE BOLTZMANN APPROACH

The type of numerical simulation approach used for an investigation should be driven by the physics of the problem. As Blumrich *et al.* (2016:1068) noted, “... the real flow around vehicles is time-dependent. Separation and recirculation are subject to stochastic—and sometimes periodic—oscillations ...” This is particularly true of the rear wake behind SUVs, hence it is clear that any simulation approach must take this into account.

This work addresses the time-dependant nature of the aerodynamic flow field generated by these bodies through the use of an inherently unsteady Lattice Boltzmann [LB] based solver to provide what can be thought of as a Very Large Eddy Simulation [VLES] turbulence model (Chen *et al.*, 1992; Chen *et al.*, 1997; Chen *et al.*, 2003). Large scale turbulent motions are captured directly on a computational lattice of cubic elements that represent the air volume around a vehicle, with the effect of unresolved turbulence accounted for through modifying the behaviour of the LB simulation through an effective turbulent relaxation time, calculated via the RNG  $\kappa - \varepsilon$  transport equations (Chen *et al.*, 2003).

The technique derives from kinetic theory, where the dynamics of the constituent molecules of a gas are considered<sup>4</sup>. In principle, this could provide a description of the flow around a car — which is a macroscopic manifestation of the motion and collision of individual molecules that form the atmosphere. However, it is not feasible to consider the interactions between individual molecules in an analysis of air flow around an object of that scale. Therefore, a statistical approach is taken, which starts by using a velocity distribution function  $f(\mathbf{x}, \mathbf{c}, t)$  to define the number of particles<sup>5</sup> per unit volume [i.e. number density], moving with speed  $\mathbf{c}$  at a position  $\mathbf{x}$  and time  $t$ . The macroscopic properties of the fluid can then be obtained by integrating over the range of possible particle speeds  $\mathbf{c}$  [the phase space]:

$$\rho(\mathbf{x}, t) = \int f(\mathbf{x}, \mathbf{c}, t) d\mathbf{c}$$

Eqn. 1

$$\rho(\mathbf{x}, t) \cdot \mathbf{u}(\mathbf{x}, t) = \int f(\mathbf{x}, \mathbf{c}, t) \cdot \mathbf{c} d\mathbf{c}$$

Eqn. 2

$$E(\mathbf{x}, t) = \int f(\mathbf{x}, \mathbf{c}, t) \cdot (\mathbf{c} - \mathbf{v})^2 d\mathbf{c}$$

Eqn. 3

---

<sup>4</sup> This discussion follows the descriptions provided by Blumrich *et al.* (2016:1070-1077).

<sup>5</sup> In contrast to much of this work, “particle” in this discussion refers to a discrete constituent element of the air, rather than a material phase dispersed in the air.

These equations represent density [Eqn. 1], momentum [Eqn. 2] and energy [Eqn. 3] respectively. Pressure arises from two sources, first the equation of state which describes the relationship between pressure  $p$ , density  $\rho$  and temperature  $T$ ; where  $R$  is the gas constant:

$$p = \rho RT$$

**Eqn. 4**

Second, pressure arises from the momentum exchange when particles collide elastically with the domain walls.

Then, neglecting any external forces the Boltzmann equation can be written:

$$\frac{d}{dt}f(\mathbf{x}, \mathbf{c}, t) = \frac{\partial}{\partial t}f(\mathbf{x}, \mathbf{c}, t) + \mathbf{c} \cdot \nabla f(\mathbf{x}, \mathbf{c}, t) = C(\mathbf{x}, \mathbf{c}, t)$$

**Eqn. 5**

The left hand side of the equation is a [total] derivative that represents particle convection; whilst the right-hand side captures the effect of collisions between particles, hence is termed the *collision operator*.

As previously noted, it is not computationally viable to solve the Boltzmann equation directly. Hence, it is reformulated to capture the “dynamics of fictitious computational quasiparticles” (Chen *et al.*, 2003) as they move on a regular, discrete *lattice* with their interactions constrained to obey the physical laws that ensure the conservation of mass, momentum and energy. This *Lattice Boltzmann* [LB] method describes the fluid in terms of discrete particle number density functions. Instead of a continuous distribution of particle velocities, a finite number  $m$  of *discrete* particle velocities  $\mathbf{c}_i$  are permitted. Hence the continuous velocity distribution function  $f$  is replaced by  $m$  discrete functions  $f_i$ :

$$f(\mathbf{x}, \mathbf{c}, t) \rightarrow f_i(\mathbf{x}, t); 1 \leq i \leq m$$

**Eqn. 6**

This set of functions describes the particle number density at a lattice site  $\mathbf{x}$  and time  $t$  for each particle velocity  $\mathbf{c}_i$ . By applying the method of finite differences in time, the *change* of these discrete states is now expressed by the Lattice Boltzmann equation:

$$f_i(\mathbf{x} + \mathbf{c}_i \Delta t, t + \Delta t) - f_i(\mathbf{x}, t) = C_i(\mathbf{x}, t)$$

**Eqn. 7**

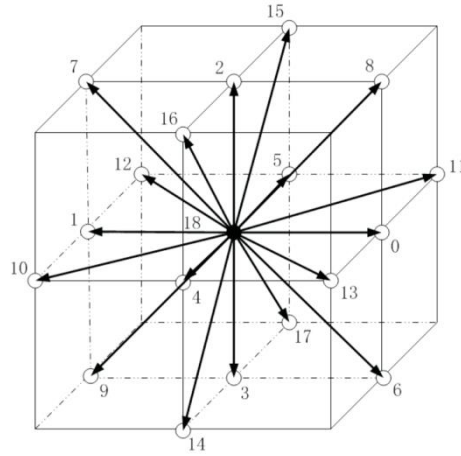


**Figure 5 D3Q19 LB Model (Li *et al.*, 2004)**

This now provides a discretised equation which also includes a time-step and hence naturally produces a time dependent flow field. Generally, these schemes are classified according to the number of lattice dimensions and discrete particle velocities. Hence, a three dimensional scheme permitting nineteen particle velocities is designated D3Q19; a schematic for this scheme is presented in Figure 5.

The main tool used in this work is a commercially-available LB based code, SIMULIA PowerFLOW. Hence, the following discussion summarises its specific characteristics, including the: collision operator formulation, turbulence and boundary layer models, surface boundary condition treatment, lattice structure and time step<sup>6</sup>.

---

<sup>6</sup> For an extended description, please see Blumrich *et al.*, 2016:1070-1077.



## 2.2 SIMULIA POWERFLOW

### 2.2.1 Collision Operator

PowerFLOW provides the first example of a LB code to be applied to automotive aerodynamics. The formulation of an appropriate collision operator was a key enabler for this development (Chen *et al.*, 2003). The Boltzmann equation defines the rate of change of the velocity distribution function  $f$  as it approaches thermodynamic equilibrium due to the action of the collision operator  $C$ . Hence, the main function of  $C$  is to drive the velocity distribution towards equilibrium (Bhatnagar *et al.*, 1954<sup>7</sup>). The collision operator used in PowerFLOW is defined as:

$$C_i(\mathbf{x}, t) = -\frac{1}{\tau} [f_i(\mathbf{x}, t) - f_i^{eq}(\mathbf{x}, t)]$$

Eqn. 8

In the above  $f_i^{eq}(\mathbf{x}, \mathbf{c}, t)$  is the equilibrium velocity distribution and  $\tau$  the relaxation time of the fluid, i.e. the time taken for the velocity distribution to reach equilibrium (Kotapati *et al.*, 2009). The LB equation can now be written as<sup>8</sup>:

$$f_i(\mathbf{x} + \mathbf{c}_i \Delta t, t + \Delta t) = \frac{1}{\tau} f_i^{eq}(\mathbf{x}, t) + \left(1 - \frac{1}{\tau}\right) f_i(\mathbf{x}, t)$$

Eqn. 9

PowerFLOW is based on a D3Q19 model [Figure 5] hence it uses nineteen discrete particle velocities, which is sufficient to guarantee the recovery of the Navier-Stokes equations (Frisch *et al.*, 1986), so long as the equilibrium distribution function satisfies the conservation laws for mass, momentum, etc. (Chen *et al.*, 1992).

The local equilibrium distribution function has the form (Li *et al.*, 2009),

$$f_i^{eq} = \rho w_i \left[ 1 + \frac{\mathbf{c}_i \cdot \mathbf{u}}{T} + \frac{(\mathbf{c}_i \cdot \mathbf{u})^2}{2T^2} - \frac{\mathbf{u}^2}{2T} + \frac{(\mathbf{c}_i \cdot \mathbf{u})^3}{6T^3} - \frac{\mathbf{c}_i \cdot \mathbf{u}}{2T^2} \mathbf{u}^2 \right]$$

Eqn. 10

where  $w_i$  are weighting parameters:

$$w_i = \begin{cases} 1/18, & \text{in 6 coordinate directions;} \\ 1/36, & \text{in 12 bi-diagonal directions;} \\ 1/3, & \text{rest particles} \end{cases}$$

and  $T$  is the lattice temperature, which is set to 1/3 for isothermal simulations.

<sup>7</sup> This is the BGK collision operator, named for the authors: Bhatnagar, Gross and Krook.

<sup>8</sup> Alternatively this can be written in terms of the collision frequency  $\omega_c = 1/\tau$ .

The viscosity can then be set by using its relationship to the relaxation parameter (Bhatnagar *et al.*, 1954; Chen *et al.*, 1991; Chen *et al.*, 1992):

$$\nu = \left( \tau - \frac{1}{2} \right) T$$

Eqn. 11

### 2.2.2 Turbulence Model

For practical engineering simulations it is not possible resolve all the spatial and temporal scales of unsteadiness present (Spalart, 2000; Hoffman & Johnson, 2006), therefore models must be used to account for the effect of unresolved motions. In PowerFLOW this is done by an implementation of a two-equation  $k - \varepsilon$  model; in this case a modification of the Yakhot and Orszag (1986) RNG<sup>9</sup>  $k - \varepsilon$  model. This is incorporated directly into the BGK collision operator via a modification to the relaxation time (Chen *et al.*, 2003; Kotapati *et al.*, 2009),

$$\tau_{turb} = \tau_0 + C_\mu \frac{k^2/\varepsilon}{T(1 + \eta^2)^{1/2}}$$

Eqn. 12

where  $\tau_0 (= \tau)$  is the unmodified relaxation time,  $C_\mu = 0.085$ ,  $\eta = Sk/\varepsilon$  and  $T$  is absolute temperature;  $k$  and  $\varepsilon$  are determined directly from the RNG  $k - \varepsilon$  transport equations (Kotapati *et al.*, 2009).

This combination of LB for resolving the larger scales of unsteadiness and a turbulence model to capture the effect of the unresolved motions provides what can be thought of as a Very Large Scale Eddy Simulation [VLES].

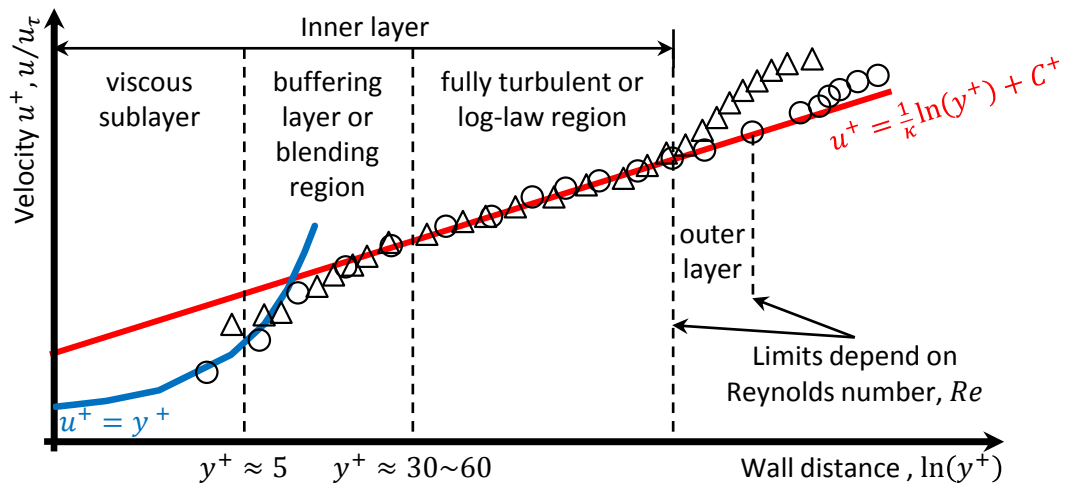


Figure 6 General Characteristics of the Boundary Layer

<sup>9</sup> Renormalization Group

### 2.2.3 Boundary Layer Model

Another important constraint typically seen in the analysis of engineering flows, such as those under study in this work, is that it is too computationally expensive to simulate the flow down to the surface, thorough the boundary layer. However, as shown in Figure 6, the measured characteristics of the boundary layer can be modelled by relatively straightforward equations. In this case, velocity parallel to a surface  $u$  is non-dimensionalised by the shear [or friction] velocity  $u_\tau$ :

$$u^+ = \frac{u}{u_\tau}$$

Eqn. 13

In the above:

$$u_\tau = \sqrt{\frac{\tau_w}{\rho}}$$

Eqn. 14

is defined by the wall shear stress  $\tau_w$  and fluid density  $\rho$ . Now, the [wall normal] distance of a point in the flow field to the wall  $y$  can be non-dimensionalised by a function that includes the relationship between wall sheat stress, fluid density and viscosity,

$$y^+ = \frac{yu_\tau}{\nu}$$

Eqn. 15

Consequently, the relationship between distance from the surface and flow velocity can be modelled for  $y^+ \leq 5$  by  $u^+ = y^+$  and in the fully turbulent region by,

$$u^+ = \frac{1}{\kappa} \ln(y^+) + C^+$$

Eqn. 16

where  $\kappa$  is the von Kármán constant [generally 0.41] and  $C^+$  the  $y$ -axis intercept for the regression.

In PowerFLOW this modelled is using a hybrid [wall] function<sup>10</sup> (Kotapati *et al.*, 2009),

$$u^+ = \begin{cases} y^+ & \text{for } y^+ < 5 \\ g(y^+) & \text{for } 5 < y^+ < 35 \\ \frac{1}{\kappa} \ln(y^+) + C^+ & \text{for } y^+ > 35 \end{cases}$$

Eqn. 17

---

<sup>10</sup>  $g(y^+)$  is a proprietary blending function.

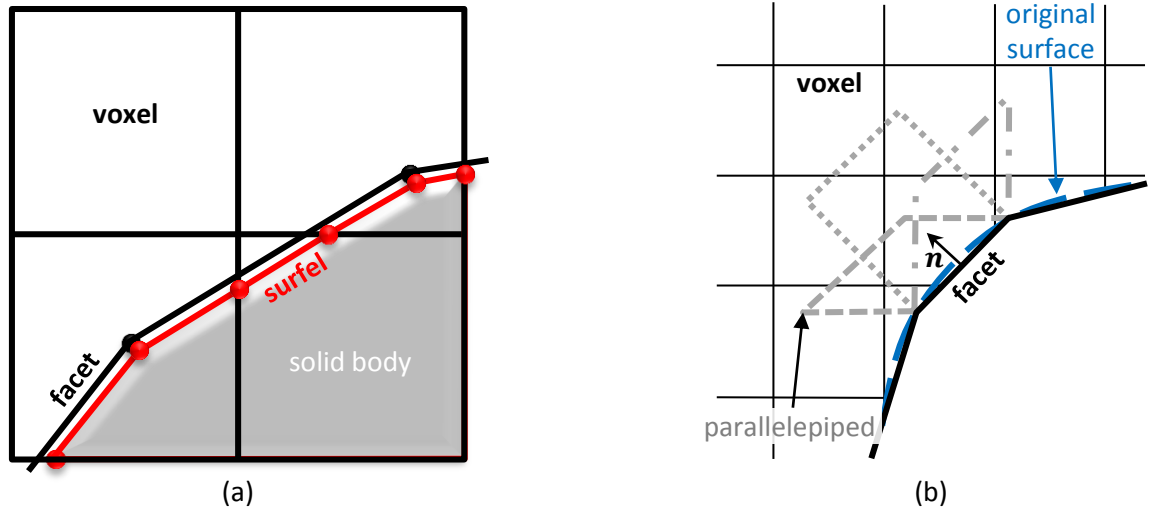


**Figure 7 (a) Resolving Geometry and (b) Calculating Particle Fluxes, in a Cartesian Lattice (Li et al., 2004)**

The boundary layer model also includes the effects of the local pressure gradient on the velocity profile. This is particularly important for capturing separations driven by adverse pressure gradients, such those at the rear of a car.

#### 2.2.4 Surface Boundary Condition

As noted previously, the LB/VLES simulation is carried out on a Cartesian, axially aligned cubic lattice. However, complex geometries of engineering interest are rarely composed of surfaces aligned to the Cartesian coordinate directions. This gives rise to significant difficulty for lattice based methods. First, the shape of the surface must be accurately captured and second, the particle fluxes at the wall must be accurately calculated if physical fluid behaviour is to be recovered.

Figure 7(a) shows how the shape of bodies are resolved on the lattice: their geometry is defined by a faceted mesh, similar to those produced by CAD systems for rapid prototyping. Where these are cut by the volumetric elements in the lattice [voxels] a new planar surface element [surfel] is created; if a facet falls completely within a voxel, a surfel is also formed. This combination of voxels bounded by surfels accurately resolves complex faceted geometry. In the trimmed voxels, only a fraction of particles are advected than would be the case if they remained pure cubes, effectively allowing irregular near-surface voxels. This process handles complex geometries

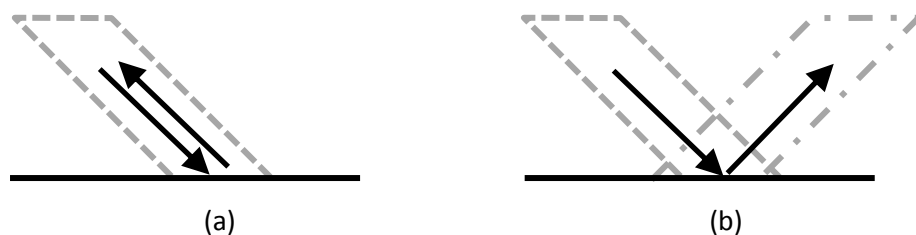


**Figure 8 (a) Particle "Bounce Back" and (b) Specular Reflection (Li et al., 2004)**

robustly and allows what is usually a complex process to be automated. A key requirement is therefore, that the faceted mesh closely conforms to the original surfaces of the body around which flow is to be simulated.

As detailed in Li *et al.* (2004) the approach taken in PowerFLOW is to construct a volumetric wall boundary condition. This is based on parallelepipeds extruded back into the fluid domain from the bounding facets which define the wall [Figure 7(b)]. For each discrete particle velocity  $c_i$  it is possible to construct a parallelepiped which captures all particles which will be advected to a facet. By the same token, parallelepipeds can be constructed to capture the particles scattered back into the fluid domain. This procedure allows for the accurate control of momentum and other hydrodynamic fluxes. The scheme is also extended to second order accuracy using a correction based on the local velocity gradient (Li *et al.*, 2004). This approach allows for the exploitation of a useful characteristic of LB methods: a simple particle “bounce back” [Figure 8(a)] imposes a “no-slip” boundary condition, whereas a specular reflection [Figure 8(b)] sets “free slip” boundary. In addition, these two classes of particle-wall interaction are used in the turbulent wall boundary layer model to control skin friction (Kotapati *et al.*, 2009).

### 2.2.5 Lattice Structure

In a flow field strong gradients of aerodynamic quantities are generally found relatively close to the vehicle. Moving away from it, the influence of the vehicle geometry on the flow lessens. Hence, it is desirable to have a spatial discretisation scheme which reflects this, allowing for high resolution in regions of strong gradients and then reducing this in regions where pressure and velocities etc. are varying little with distance. This type of approach, common in CFD simulations, provides resolution where it is needed and takes advantage of where it is not to provide extra computational economy.

In this context, this means allowing for voxels of different sizes in locations which can be set based on a general knowledge of the flow structure. As shown in Figure 9 this is achieved in PowerFLOW by successively doubling the characteristic voxel edge length  $[L_{Vx}]$  at specified spatial locations. Regions of a set voxel dimension are denoted by their Variable Resolution [VR] level; for example, in a simulation with ten voxel sizes across the fluid domain  $[i = 10]$ , the regions comprising the smallest voxels are labelled as  $VR(10 - 1) = VR9$  and those containing the largest voxels are identified by the label  $VR0$ .

Voxels in adjacent VR regions will differ in edge length by a factor of two. On a VR boundary particle states are evenly “exploded” [from fine to coarse] or coalesced [from coarse to fine] conserving mass and momentum, whilst maintaining continuous fluid velocity and density across the interface (Li *et al.*, 2004).

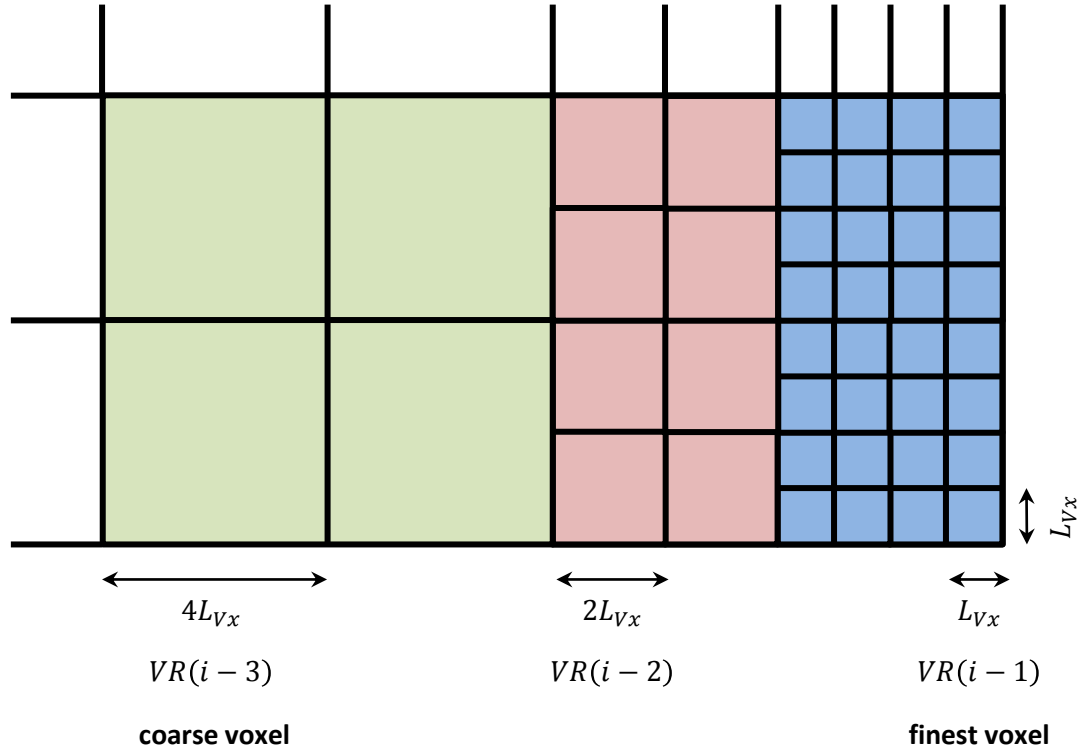


**Figure 9 Variation of Lattice Spatial Resolution in PowerFLOW**

This approach allows for the economic resolution of regions where the flow is little affected by the presence of a vehicle and consequently the provision of very low blockage<sup>11</sup> computational domains. This latter point is particularly helpful in vehicle aerodynamics where the presence of flow boundaries alters the flow field local to the vehicle and hence the forces and pressures. In the context of wind tunnel testing, correction methods are required to adjust the quantities to “open air” values. The economic representation of distant parts of the flow domain using “low numbered” VR regions allows PowerFLOW simulations to be undertaken with boundaries placed at distances from the vehicle sufficient to ensure that the simulation results do not require this type of correction.

### 2.2.6 Time step

As previously noted the Lattice Boltzmann equation naturally provides a time-dependent description of the flow field as it contains a time step  $\Delta t$ . In PowerFLOW this is a function of the finest lattice spacing  $L_{vx}$ , Mach number  $Ma$ , and onset flow velocity  $U_\infty$ ,

$$\Delta t = c_{Lattice} Ma \frac{L_{vx}}{U_\infty}$$

**Eqn. 18**

<sup>11</sup> Solid [domain] blockage is simply the ratio of vehicle frontal area  $A$  to domain cross sectional area, or wind tunnel test section cross section for a closed test section design,  $A_T$  i.e  $A/A_T$ . Typically this is 0.001 (0.1%) for a PowerFLOW simulation.

Hence  $\Delta t \propto Ma$ , so to improve computational economy it is general practise to solve at a higher Mach number. This introduces an error due to differences in the effect of compressibility between the two Mach numbers; however, this is small in the range generally used (Blumrich *et al.*, 2016: 1077).

The LB/VLES method, as embodied in PowerFLOW has characteristics which are very useful in the context of automotive aerodynamics simulations, these include: high space-time resolution, good scalability on parallel computing systems; efficient and robust handling of complex geometries; automatic generation of the spatially discretised domain and a higher-level implementation of turbulence models (Chen *et al.*, 2003). As a consequence, it has been used extensively in the field of automotive aerodynamics. This has resulted in the publication of a number of studies that demonstrate validation against measured aerodynamics quantities; a selection of these are summarised in the following section.

### 2.3 PREVIOUS VALIDATION STUDIES

Before applying PowerFLOW to the problem at hand, it is important to note that it has been previously validated for predicting the aerodynamics performance of bodies spanning the range of complexity explored in this work, from research-focussed bluff bodies to full production vehicles. For example, Fares (2006) investigated the wake structures generated by the simple Ahmed body with 25° and 35° rear body slant angles [ $\beta$ ] using three different levels of spatial resolution. This is illustrated in Figure 10, which provides a schematic of the (a) geometry and (b) two views of the streamwise [ $x -$ ] velocity field on the  $y = 0$  centre plane for the more challenging  $\beta = 25^\circ$  case. This shows excellent agreement between test and simulation for the finest lattice [ $18.4 \times 10^6$  voxels].

In contrast, Keating *et al.* (2008) focussed on predicting the trend for drag change with slant angle measured by Ahmed *et al.* (1984) on this simple body. As shown in Figure 11, not only was the trend for total drag well captured by the numerical simulation, with a mean difference to experiment of 4%, but breaking it down by geometric zone shows that the simulation provides an excellent representation of the drag change over the rear surfaces. The dramatic reduction in total drag seen the experiment once  $\beta$  exceeds  $30^\circ$  is also evident in the simulation results.

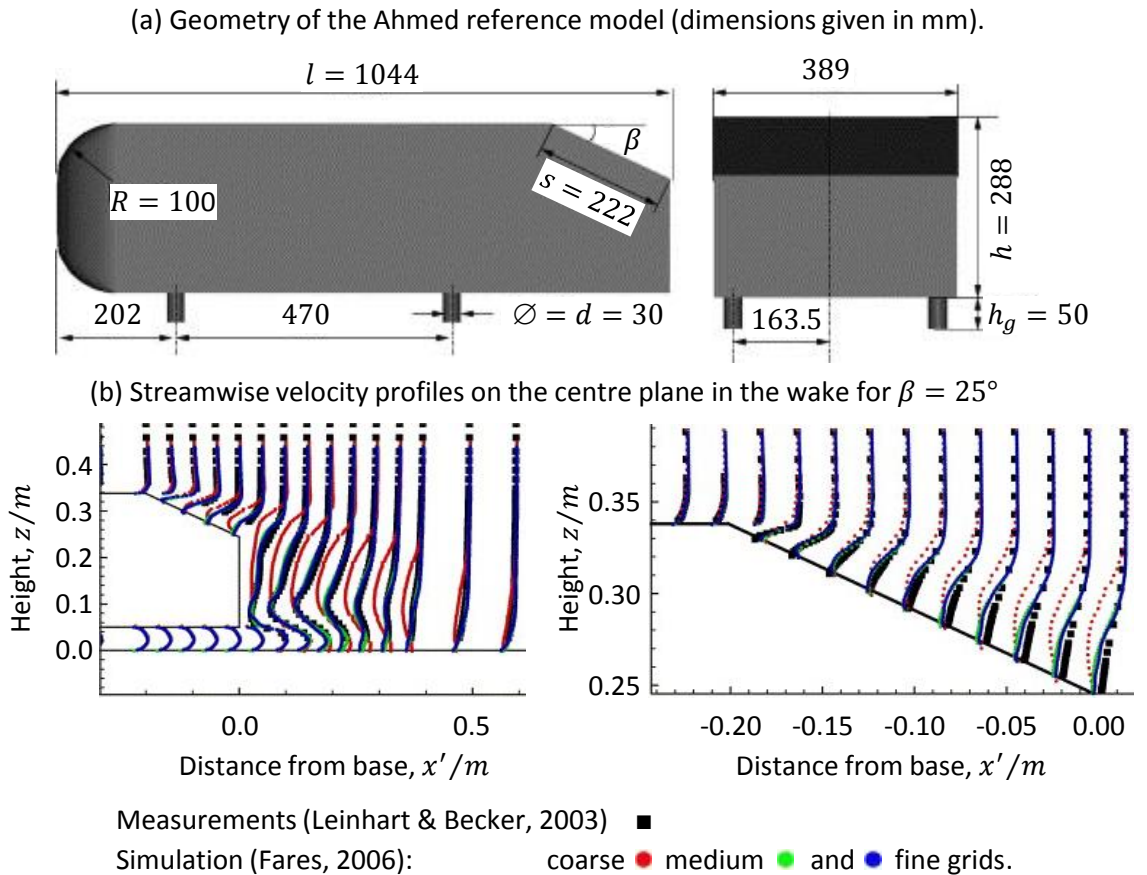


**Figure 10 Streamwise Wake Velocity Profiles in the Wake of the Ahmed Body with a 25° Rear Slant Angle Simulated With Three Levels of Spatial Resolution (Fares, 2006)**



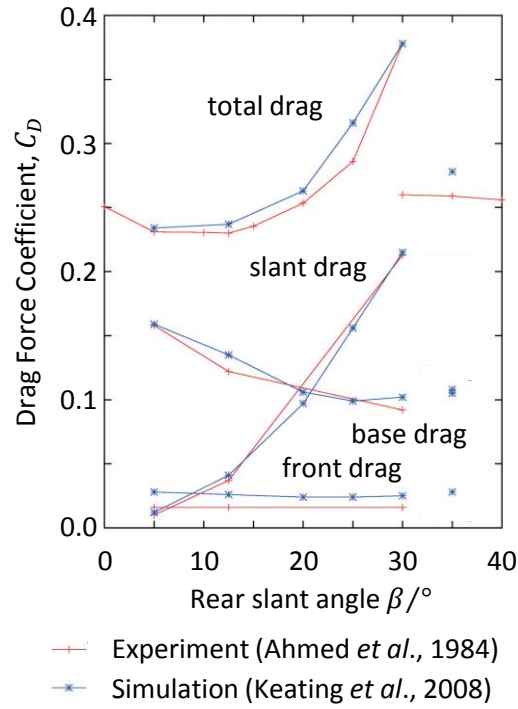


**Figure 11 Variation of Drag Coefficient with Rear Slant Angle for the Ahmed Body (Keating *et al.*, 2008)**

At the next level of geometric complexity, validation studies have been performed using basic car shapes. These provide more car-like characteristics, representing the overall form of a vehicle by including features such as the bonnet, wind screen, roof, rear screen and boot deck. Lietz *et al.* (2000) provide an example of this approach, using a set of standard calibration models with an upper body representing a contemporary saloon but without the added complexity of wheels, underbody details, engine bay or cooling flows. They demonstrated good agreement with wind tunnel measurements for surface static pressure distributions, along with time-averaged wake flow structures. A follow-on study extended the investigation to include assessment of the drag coefficient (Lietz *et al.*, 2002), demonstrating a mean difference between measurement and calculation of 5% over six different rear-end configurations.

Moving towards production car levels of complexity, validation studies have been undertaken using detailed reduced-scale models that also incorporate the effects of wind tunnel boundaries on the flow field. For instance, Fischer *et al.* (2008) investigated a 1/5<sup>th</sup> scale model of a notchback car and obtained a drag coefficient within 1.4% of the experimentally measured value. Similarly, Cyr *et al.* (2011) were able to predict the drag of a 1/4<sup>th</sup> scale model of the Hyundai Genesis saloon car to an *absolute* accuracy better than 0.006  $C_D$  [average 0.004  $C_D$ ] as five under body modifications were made, with the wind tunnel operating in both fixed and moving ground modes. Moreover, they demonstrated that the predictive accuracy of the CFD code could be improved to below 0.002  $C_D$  if the pressure gradients imposed by the proximity of the wind tunnel boundaries were accurately accounted for.

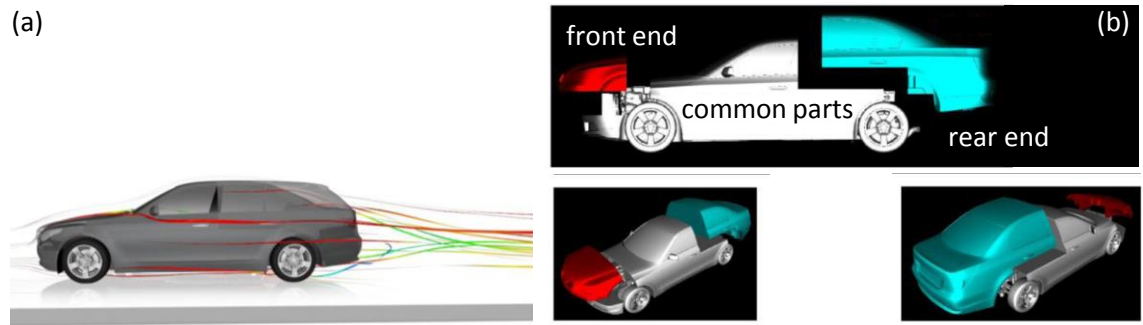


**Figure 12 The Modular BMW Validation Model (Kandasamy *et al.*, 2012)**

Moving to full scale, an extensive validation study was reported by Kandasamy *et al.* (2012) based on a modular test property representing a BMW car; a schematic showing the general configuration of the test property is shown in Figure 12, illustrating its capability to represent changes to both its front and rear end geometry. They investigated sixteen mainly rear-end geometry changes and obtained drag coefficients from simulation within  $\pm 2\%$  of the experimental value. A selection of these results are shown in Figure 13, along with images illustrating the baseline geometry for each of the rear end configuration “families”. In the context of this work with its focus on blunt-ended SUVs, it is notable that the squarebacked variants [configurations denoted by “B –”] provide both the largest drag values and a deviation from experiment of no more than 1.9%.

Commercial considerations permitting, workers have also reported short validation studies conducted during vehicle development programmes. Kremheller (2014) stated that during the development of the Nissan Qashqai SUV numerical simulations produced drag coefficients within 6% of full-scale wind tunnel measurements. In addition, he provides a comparison of the static pressure distribution along the vehicle centreline and on its rear surfaces. Generally, the correlation was good along the centreline, though significant differences were found over the rear surfaces. In contrast, Wang *et al.* (2017) measured and simulated eleven design changes made to the Buick Excelle GT saloon car. With the CFD model including a representation of the wind tunnel moving ground system, they reported an average difference between drag coefficients obtained from test and CFD of 0.7%. The largest single difference was 1.4%, with the majority of simulation results falling within  $\pm 1\%$  of their measured counterpart. Finally, Chaligné *et al.* (2018) described the aerodynamic development of the 2017MY Land Rover Discovery. They reported configuration changes that matched experiment to  $\pm 0.001 C_D$ , aside from those associated with closing the central front end air intakes, which were poorly predicted.

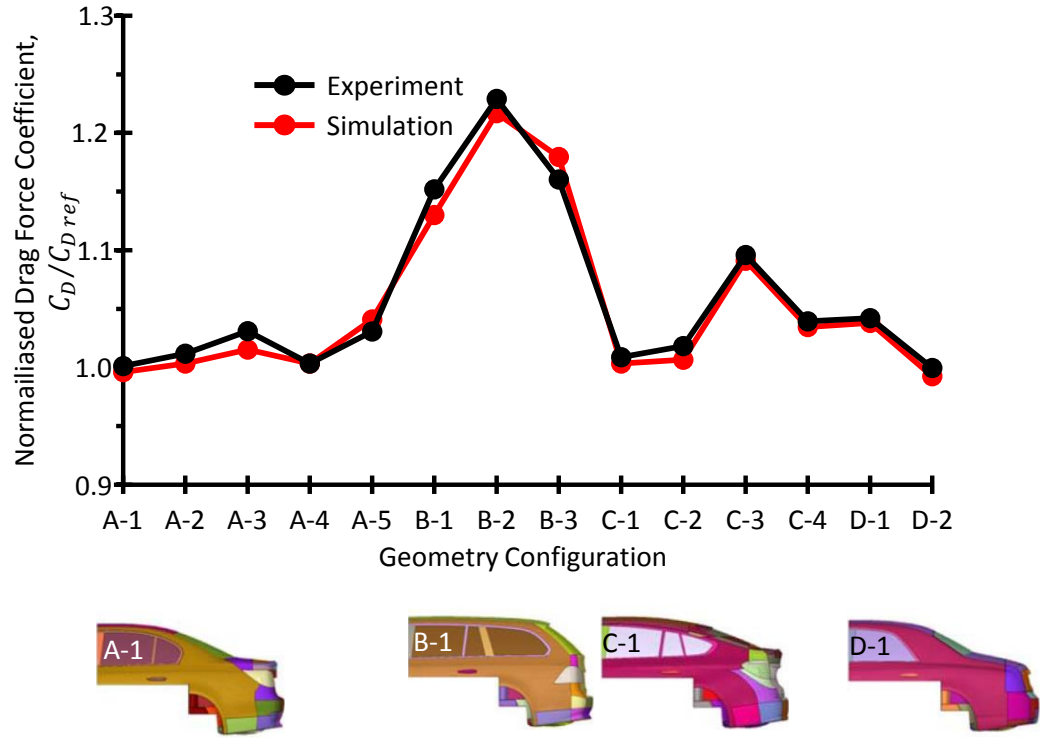


**Figure 13 Effect of Selected Rear End Changes on Normalized Aerodynamic Drag for the BMW Validation Model (Kandasamy *et al.*, 2012)**

The foregoing demonstrate that the simulation approach selected for this work is capable of providing a good numerical representation of the aerodynamic drag of a range of vehicle geometries relevant to the research strategy outlined for this work in CHAPTER 1. Further, investigations reported for the simple Ahmed body demonstrate that the velocity field associated with the time-averaged wake can be well predicted.

The best levels of agreement were seen for simulations that explicitly model the wind tunnel test section (Fischer *et al.*, 2008) or ground simulation system (Wang *et al.*, 2017). However, this requires a level of insight into the test facility that is not always available, particularly if it is run by a third party; so it is reassuring that Kandasamy *et al.* (2012) have demonstrated that without including these elements of the wind tunnel airline, but using high geometric fidelity models, drag coefficient predictions can fall within 2% of the experimental value for a squarebacked car.

It is challenging to correlate simulation methods on production vehicle geometry. There is a high level of additional geometric complexity typically associated with the engine bay and cooling flows. This goes hand in hand with reduced certainty in the relationship between components due to tolerance stack-up and part deformation under aerodynamic load. In this context it is unsurprising to see a larger difference between experiment and CFD reported by Kremheller (2014) during the Nissan Qashqai development. However, Chaligné *et al.* (2018) show that even when dealing with production geometry *differences* between configurations can be well predicted.

## 2.4 MODELLING SURFACE CONTAMINATION

### 2.4.1 Overview

Having described the LB/VLES solver used to simulate the unsteady aerodynamic flow field and illustrated the level of agreement that can be expected with experiment, the following sections explore the capabilities added to the LB-VLES flow solver at the author's request to enable the modelling of airborne spray and surface films. In brief, the droplets which form the spray are represented by a Lagrangian particle model (Bai & Gosman, 1995) run concurrently with the flow solver, coupling particle and flow time. As a consequence, airborne particles are able to respond to unsteadiness in the surrounding flow field. This approach also supports two-way momentum transfer between the particles and the flow, allowing their motion to affect the surrounding air volume (Dukowicz, 1980; Subramaniam, 2013). The particle model includes the effects of breakup due to aerodynamic shear whilst airborne (O'Rourke & Amsden, 1987) and splash at surfaces (Mundo *et al.*, 1995; O'Rourke & Amsden, 2000). Particles may also transfer mass into a thin surface film at the surfaces they interact with (O'Rourke & Amsden, 1996). Finally, the local aerodynamic shear may strip surface film mass back into the flow field as particles, via a re-entrainment model (Jilesen *et al.*, 2015). These extensions provide a model for droplet advection which can accurately capture particle-flow interactions and is valid over a wide range of particle Reynolds numbers (Subramaniam, 2013), along with a representation of the surface water dynamics sufficient for this work. However, it is important to note that both the particles and film are *virtual* in the sense that they do not occupy any physical volume within the computational lattice. These models are explored in more detail in the following sections.

### 2.4.2 Particle Modelling

Lagrangian particle models have been used to represent airborne droplets by other workers in the field of automotive engineering [see Hagemeier *et al.*, 2011 for a review]. Initially, this technique was used to simulate in-cylinder fuel spray (Borman & Johnson, 1962), for which extensions were added to represent wall impingement, splash and droplet break-up (Bai & Gosman, 1995; Mundo *et al.*, 1995; O'Rourke P & Amsden, 1987, 2000).

A basic Lagrangian particle scheme is illustrated in Figure 14. In this relatively simple approach particles occupy no physical volume, i.e. they are "point particles" (Elghobashi, 1994). In essence it is a tracking technique in which the fluid flow affects the particles, but the particles have no effect on the flow field [i.e. one-way coupled]. Particle advection is calculated by considering the balance between the inertial force acting on the particle [ $F_{inertia}$ ], as well as the forces resulting from aerodynamic drag [ $F_{Drag}$ ] and the effect of gravity [ $F_{Gravity}$ ].

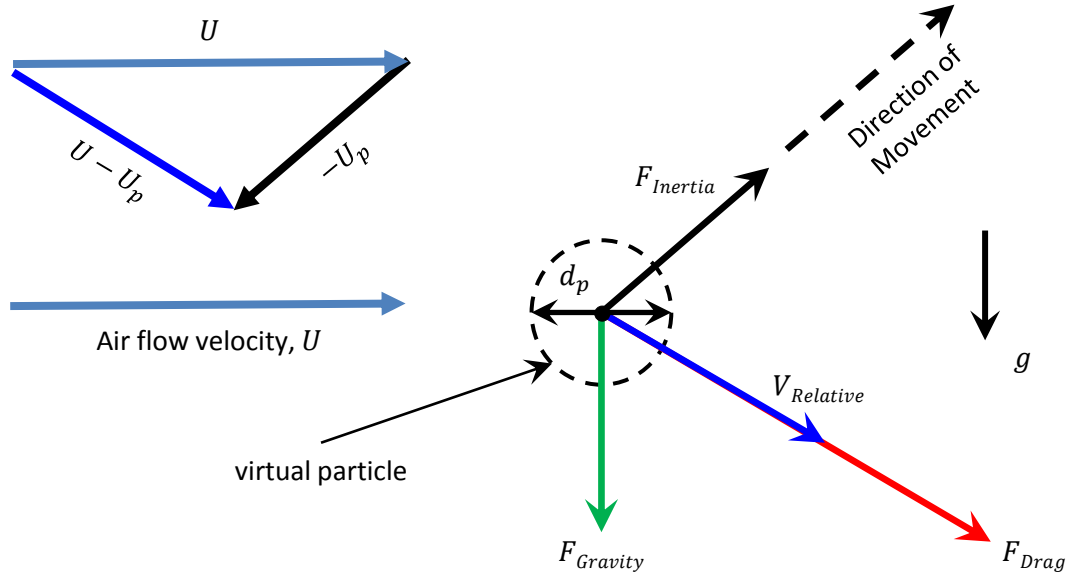


**Figure 14 Lagrangian Particle Model Schematic**

In this case, the equation of motion for each particle can be written,

$$m\vec{a}_p = \sum \vec{F} = \vec{D} + m\vec{g}$$

**Eqn. 19**

where  $\vec{F}$  represents the total force on the particle,  $\vec{D}$  is the aerodynamic drag force,  $\vec{a}_p$  is the resulting particle acceleration,  $m_p$  is the particle [point] mass and  $\vec{g}$  acceleration due to gravity. In more detail,

$$m_p\vec{a}_p = m_p \frac{d\vec{U}_p}{dt} = C_D \frac{1}{2} \rho |\vec{U} - \vec{U}_p|^2 \frac{1}{4} \pi d_p^2 \frac{(\vec{U} - \vec{U}_p)}{|\vec{U} - \vec{U}_p|} + m_p \vec{g}$$

**Eqn. 20**

with  $\vec{U}$  standing for the airflow velocity;  $\vec{U}_p$  particle velocity;  $\rho$  air density and  $\frac{1}{4} \pi d_p^2$  the particle frontal area, based on its diameter  $d_p$ . This approach also requires the definition of a particle drag coefficient  $C_D$ , which is typically treated as a function of the particle Reynolds number  $Re_p$ ,

$$C_D = \frac{24}{Re_p} (1 + 0.15 Re_p^{0.687}) + \frac{0.42}{(1 + 42500 Re_p^{-1.16})}$$

**Eqn. 21**

with,

$$Re_p = \frac{\rho |\vec{U} - \vec{U}_p| d_p}{\mu}$$

**Eqn. 22**

This empirical particle drag equation, proposed by Clift and Gauvin (1970) has been frequently used for automotive surface contamination simulation (Kuthada & Cyr, 2006).

Overall, the Lagrangian particle tracking scheme treats particles as spherical, with their properties located at a point in space. Their advection is calculated via time-integration of the equation of particle motion to obtain the instantaneous velocity vector for each particle (Elghobashi, 1991).

This basic approach has been enhanced to model more of the characteristics of droplets via three main extensions:

1. two-way momentum coupling, which allows particle motion to affect the motion of the surrounding air volume (Dukowicz, 1980; Subramaniam, 2013);
2. empirical splash correlations to provide for a more realistic interaction with surfaces, by allowing both the retention of a fraction of particle mass at the surface along with reflection of the remaining mass into a pre-determined number of “child” particles, following experimentally derived correlations (Mundo *et al.*, 1995; O'Rourke and Amsden, 2000);
3. Taylor Analogy Break-up [TAB] model of O'Rourke and Amsden (1987) which uses an analogy to a mass-spring-damper system to approximate droplet vibration, which is a precursor to break-up, predicting when a deformation sufficient to result in a break-up event would occur.

These extensions provide a model for droplet advection which can capture particle-flow interactions and is valid over a wide range of particle Reynolds numbers. (Subramaniam, 2013).

### **2.4.3 Surface Film Modelling**

When droplets hit a surface, some part of their original mass is transferred to it and hence the surface is wetted. This generally results in a combination of droplets, rivulets and film accumulating on a surface. The dynamics of this process are complex: droplets can build into rivulets which subsequently form films; films can breakdown into rivulets which then generate droplets; finally, droplets can be stripped directly out of films in a re-entrainment process.

To make the problem tractable a “thin film” model is used in this work. This simplifies the physics by making a range of assumptions (O'Rourke & Amsden, 1996; Meredith *et al.*, 2011), including:

- advection normal to the surface is negligible;
- diffusion tangential to the surface is negligible;
- surface film thicknesses are small compared to the radii of surface curvature;
- film flow is laminar, tangent to the surface and varies linearly in the normal direction;

- air flow velocities over the film are large enough, compared to the surface film velocities, for the surface to still be treated as solid for the purposes of the airflow calculation.

These assumptions allow for the film to be represented by a simplified set of equations. As illustrated by the schematic shown in Figure 15, film thickness  $h_f$  [with density  $\rho_{film}$ ] and velocity  $\mathbf{u}_{film}$  arises from a balance of the shear force between the liquid and surface  $\tau_{friction}$ , aerodynamic shear between the liquid and air  $\tau_{air}$ , a reaction force  $\mathbf{F}_{Reaction}$  and the effect of gravity [ $\mathbf{F}_{gravity}$ ]. The balance of forces per unit area can be expressed, in a simplified summary form as,

$$\rho_{film} h_f \frac{d\mathbf{u}_{film}}{dt} = \tau_{air} + \tau_{friction} + \mathbf{F}_{Gravity} + \mathbf{F}_{Reaction}$$

Eqn. 23

keeping the terms in the same order, this equates to,

$$\rho_{film} h_f \frac{d\mathbf{u}_{film}}{dt} = \tau_{air}(u^+, \hat{\mathbf{n}}) - 2\mu \frac{\mathbf{u}_{film}}{h_f} + \rho_{film} h_f \mathbf{g} - \rho_{film} h_f (\mathbf{g} \cdot \hat{\mathbf{n}}) \hat{\mathbf{n}}$$

Eqn. 24

The surface shear exerted by the air is computed by the aerodynamics LB/VLES solver.

For surface contamination simulation, the effect of droplets impacting an existing surface film needs to be modelled. This is handled by [a] adding the tangential momentum lost by the Lagrangian particles as a tangential momentum source for the film and [b] converting the normal component of particle momentum into an interfacial pressure on the film at the particle impact point. The physical significance of [b] is that without it particles impacting normal to the surface would not affect film inertia, regardless of their velocity (O'Rourke & Amsden, 1996).

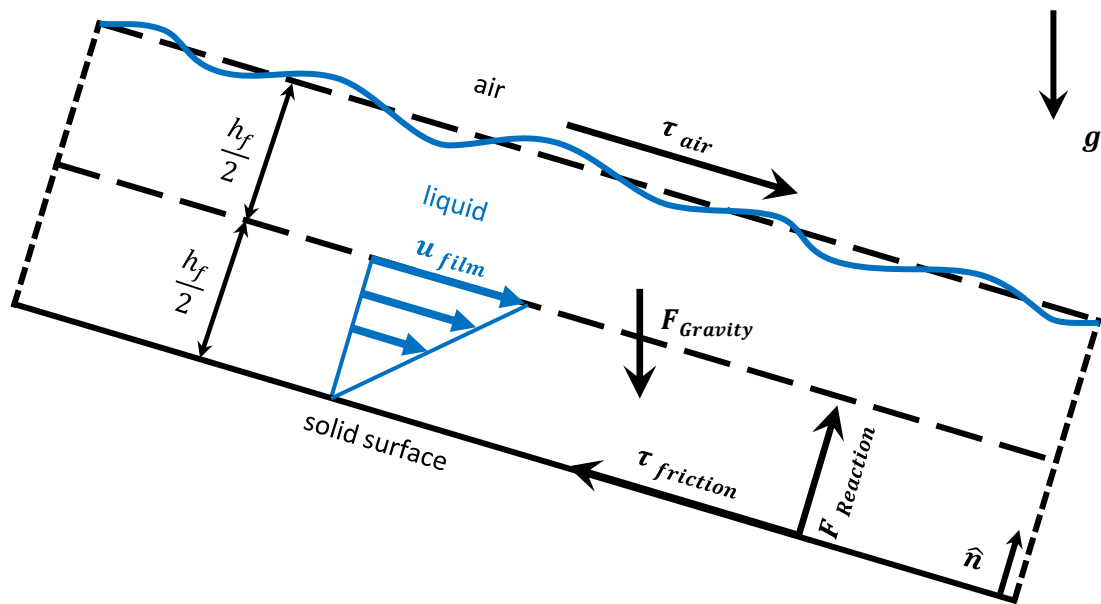


Figure 15 Thin Film Model Schematic

Although providing a practical approach, thin film modelling has a number of limitations relevant to its application for vehicle surface contamination generally. For example, film thickness on vehicle surfaces can become significant relative to local surface curvature, violating a key assumption of the “thin film approximation”. This is particularly evident at the vertical edges of the a-pillar, where the vehicle geometry steps up from the wind screen, and at the transition from door frame to side glass. Local boundary layer flow separation can also occur at these sharp edges, which should result in droplet stripping from the film [re-entrainment]. The break-down of the thin film approximation at these locations requires the use of additional sub-models. In addition, water film depth in heavily contaminated areas may become sufficient to contravene other assumptions [e.g. advection normal to the surface] compromising the validity of this simplified approach. Finally, partial wetting is common in automotive surface water flows; for example, both rivulet and droplet advection is a common feature of water flow over the front side glass.

However, in this work the film model is just used to “record” the pattern and quantity of deposition on the rear surfaces, not model surface water motion as would be the case in applications concerned with water flow onto the front side glass. Hence, it is reasonable to take this approach, rather than resorting to more demanding methods which explicitly resolve the film on the computational lattice.

The foregoing has described the general properties of the LB/VLES solver, particle and thin film models that have been brought together to provide a computational approach with the capability to concurrently simulate rear surface contamination and aerodynamic drag. This work aims to develop a novel engineering simulation process based on this toolset for application to the aerodynamics development of SUVs. The first step in that journey is to establish the requirements for accurate representation of the aerodynamic flow field and credible prediction of rear surface contamination using two simplified systems.



## CHAPTER 3 SIMPLE SYSTEMS

### 3.1 MOTIVATION

This chapter draws on *Portfolio Report B* and starts the progress towards a novel simulation process by developing two simple systems exemplifying rear surface contamination for blunt-ended vehicles. This enabled simulation requirements to be identified without going to the expense of working with complex production vehicle geometry. These novel simulation systems also provided original insights into the flow mechanisms responsible for rear surface deposition.

At their core are two standard geometrically simplified bluff body models. The use of such geometries is a well-established practise in automotive aerodynamics (Le Good & Gary, 2004) and aeroacoustics. In the former field they tend to represent complete vehicles, whilst in the latter they are usually local models of the a-pillar (Uchida & Okumura, 1999; Cho *et al.*, 2014) and door mirrors (Höld *et al.*, 1999; Ask & Davidson, 2006). The aim is to improve the effective “signal to noise ratio” by reducing the complexity of the flow field, enabling mechanisms to be elucidated more readily. These simplified bodies can be experimentally investigated at reduced scale and computationally analysed at reduced cost. Also, as they are standardised, workers without access to experimental facilities can correlate their numerical simulations against published data. To date, this approach has been little exploited for surface contamination studies; where used, workers have typically borrowed geometries from these related fields. For example, surface contamination by water deposition and movement has been studied using a simple a-pillar model (Harada *et al.*, 2015) along with simplified door mirror models (Borg & Vevang, 2006; Tivert & Davidson, 2010) originally developed for aeroacoustics investigations. More relevantly, Paschkewitz (2006) simulated wake interaction with airborne spray using the idealised heavy truck model devised by Storms *et al.* (2004) for drag reduction studies.

There have been few studies using this approach to systematically explore rear surface contamination. Kabanovs *et al.* (2016a) investigated rear face soiling for a single configuration of the Windsor body<sup>12</sup> but did not use an unsteady eddy-resolving flow solver or surface film model. The same workers followed this by using the more complex Generic SUV model<sup>13</sup> (Kabanovs *et al.*, 2016b) but at a fixed ride height. The physical data provided by these and other published studies enabled the author to validate two original computational systems, distinguished by their use of unsteady eddy-resolving flow simulation and systematic geometry change to capture the effects of underbody flow and vehicle ride height on rear surface soiling. The following section describes the development of the simpler of the two systems, based on the Windsor body.

---

<sup>12</sup> See APPENDIX A, Figure 94(a)

<sup>13</sup> See APPENDIX B, Figure 95

## 3.2 WINDSOR BODY

### 3.2.1 Baseline Model Development

The Windsor body provided the starting point for the numerical investigation. Although lacking wheels, this simple body generates a base wake of a similar structure to that commonly seen for blunt-ended vehicles, such as SUVs. Hence, when combined with a model to represent road spray it provided a simplified representation of the rear soiling problem. The main focus of this part of the work was to develop a computational strategy for accurately capturing the wake and main rear surface deposition process. This had two elements [1] numerically reproducing the physical aerodynamic performance and rear face soiling pattern of the Windsor body in its baseline configuration; [2] capturing the effects on rear surface deposition caused by underfloor flow-driven changes to the rear wake structure.

This original baseline simulation has been published by the author (Gaylard, *et al.* 2017b) and is summarised here. It started by developing a numerical representation of the wind tunnel from which the published experimental data were taken (Johl *et al.*, 2004). Next, an initial spatial resolution strategy [i.e. lattice design] was tested, illustrated in Figure 16. This shows the lattice structure immediately around the Windsor body on (a) the  $y = 0$  centre-plane and (b) a  $xy$  plane at the body mid-height. This starting point was based on previously published studies using the same LB-VLES CFD solver (Lietz *et al.*, 2002; Fischer *et al.*, 2008; Fischer *et al.*, 2010; Samples *et al.*, 2010). These address the distribution of spatial resolution required to capture the flow structures generated by automotive bodies. The lattice uses cubic elements [voxels] with the smallest set to a 1 mm edge length, to provide the highest resolution at: the radiused leading edges where strong velocity and pressure gradients are expected; the rear edges where the attached boundary layers will separate and form the shear layers that bound the wake, along with the rear face [base]. As described in CHAPTER 2, the solver allows resolution to be varied through the lattice by employing embedded hierarchical regions where the local voxel edge length can be double that of the next finest resolution region. As seen in Figure 16, this enables the progressive relaxation of resolution for regions of the lattice further away from the Windsor body. The resulting lattice comprised  $21.9 \times 10^6$  voxels and  $1.18 \times 10^6$  surface elements [surfels], a level of resolution similar to that used in previously published investigations of a similar simple body. Specifically, Sims-Williams and Duncan (2003) used a smallest voxel edge length of 1.3 mm and obtained good results for the trailing vortex structures generated by a  $25^\circ$  rear slant angle variant, for both time-averaged and unsteady quantities. In addition, Fares (2006) used a similar resolution strategy to that proposed here with a smaller total number of voxels [ $18.4 \times 10^6$ ] but nevertheless obtained excellent results for the wake of the same simple body variant.

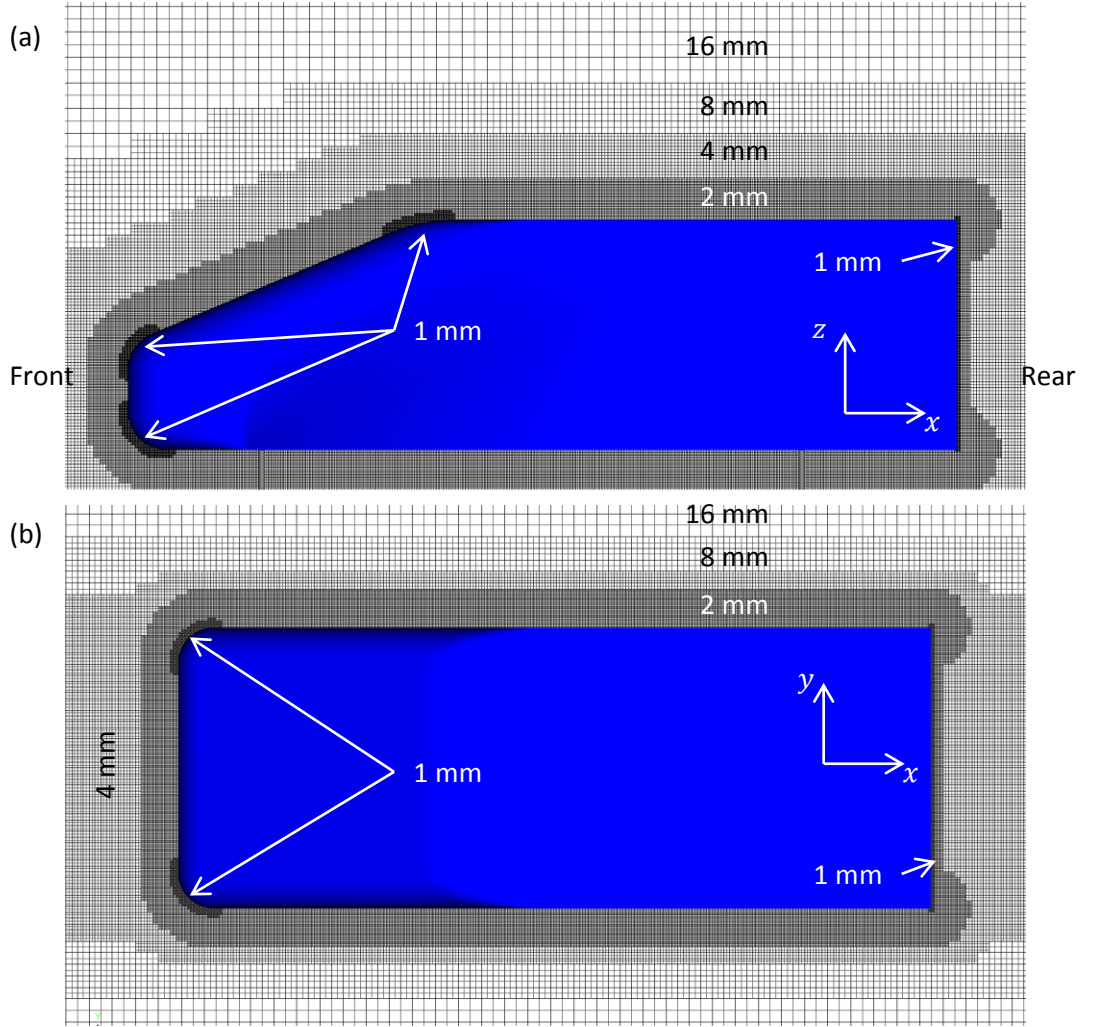


**Figure 16. Distribution of Spatial Resolution for the Windsor Body (a) In the  $y=0$  Centre-Plane and (b) the Mid-Height  $xy$  Plane**

With the inlet velocity set to 30.5 m/s to match the wind tunnel experiments of Kabanovs *et al.* (2016a) surface  $y^+$  values were generally below 120 for regions of attached flow; appropriate for the wall model used to represent the boundary layer (Krastev & Bella, 2011). This also resulted in a Reynolds number ( $Re_H$ ) of  $6.65 \times 10^5$  and a time-step length  $[\Delta t]$  for the simulations of  $5.06 \times 10^{-6}$  s.

The simple system was completed by the inclusion of an idealised spray source (Kabanovs *et al.* 2016a). The emitter was placed on the vertical centreline ( $y = 0$ ) plane on the simulation domain floor, immediately beneath the trailing Windsor body's trailing edge, with its main axis at  $45^\circ$  above the horizontal. The experimental droplet size distribution was matched by a Gamma distribution with a mean particle diameter of  $25.6 \times 10^{-6}$  m. As in the experiments, water was used as the contaminant.

The first stage in ensuring that the aerodynamics of the body was correctly represented by the simulation was to examine the lift and drag force coefficients it provided, comparing them with those measured experimentally and published in the literature; principally Perry *et al.* (2015).

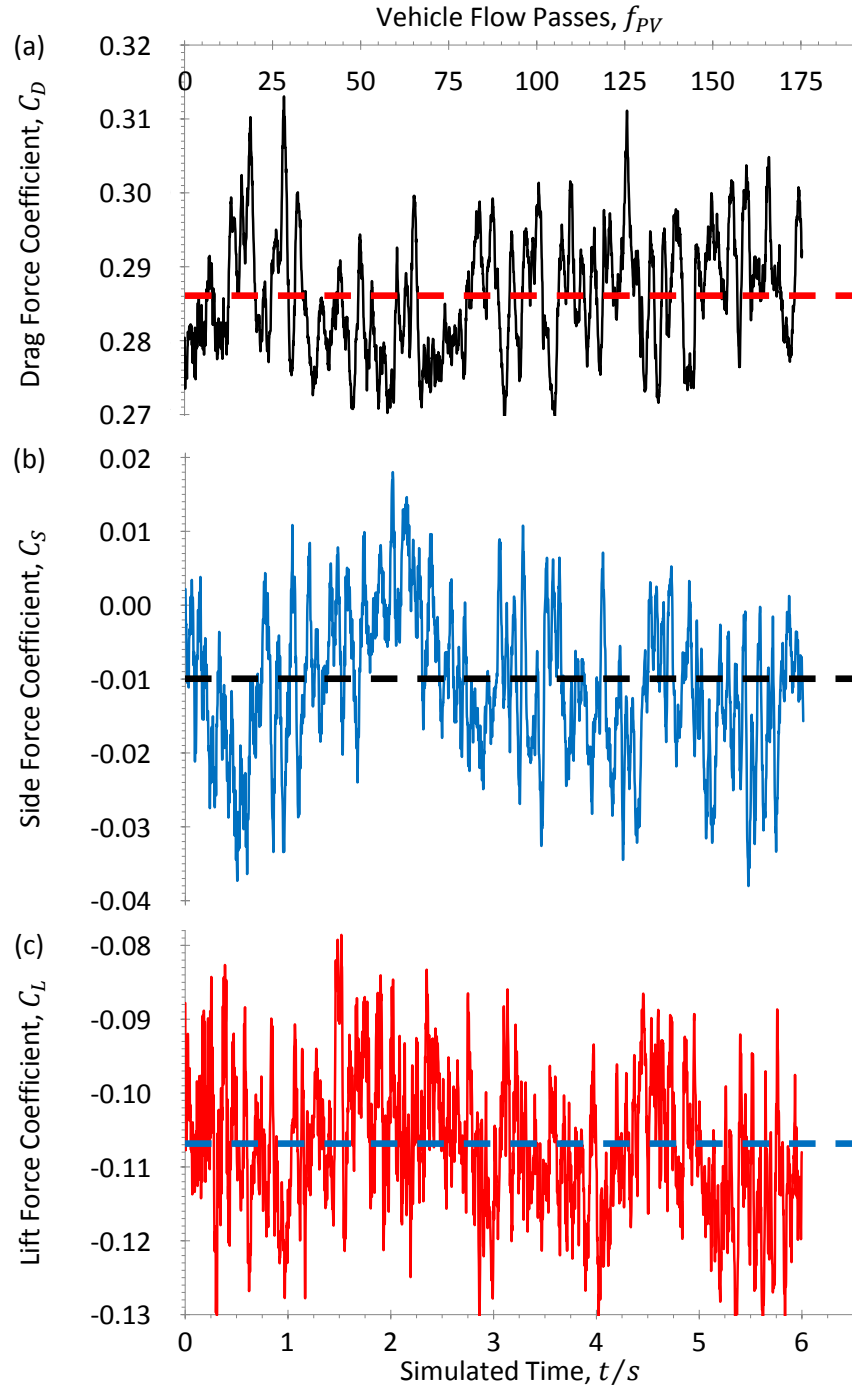


**Figure 17. (a) Drag (b) Side and (c) Lift Force Coefficient Histories for the Baseline Windsor Body with the Mean Values Shown as Broken Lines.**

The drag, side and lift force coefficients obtained for the initial baseline numerical model are plotted in Figure 17. The forces are clearly unsteady: given that flow over the surfaces of the Windsor body is attached until the geometrically fixed separation lines along its rear edges, this unsteadiness is almost exclusively associated with the dynamics of the rear wake. The force coefficients are plotted against both dimensioned and non-dimensional simulated time. The latter is obtained by scaling against the time taken for the bulk flow to pass one vehicle length, i.e.  $L/U_\infty$ , characterising time as a number of “vehicle flow passes”  $f_{PV}$ . The force coefficients have been corrected for domain [i.e. wind tunnel test section] blockage using the one-

dimensional continuity correction of Carr and Stapleford (1983), the same approach used for correcting the test data (Perry *et al.*, 2015).

The calculations were run for a sufficient time to allow a stable [i.e. stationary] mean to be reliably determined for both drag and lift. This was assessed using the simple pragmatic approach developed by the author and published in Gaylard *et al.* (2017b). This original approach systematically excludes any early-time data affected by transient start-up effects and then highlights when stable mean values have been obtained. This is achieved by applying receding average functions to the time histories, such as shown in Figure 17. These generate series comprising averages [means] obtained for successively smaller samples by sequentially removing early-time data:

Eqn. 25

$$\sum_{t_1}^{t_N} C_D / N, \sum_{t_1+\Delta T}^{t_N} C_D / (N-1), \sum_{t_1+2\Delta T}^{t_N} C_D / (N-2) \dots$$

where  $t_1$  and  $t_N$  are the first and last times, respectively, for which drag coefficient  $C_D$  data was recorded and  $N$  is the total number of data points in the time series. Finally,  $\Delta T$  is the interval for recording data [not the simulation time step].

Equivalent functions can also be constructed for the side and lift force coefficient histories; for brevity only the drag and lift functions are plotted in Figure 18. Initially, the functions are the average of the complete time-series, but as they develop early-time data is progressively excluded. If any start-up effects are present the receding averages exhibit large initial changes. Here, the use of a “seeding” flow field has eliminated this [1]. If the data are physically consistent and a sufficiently long sample has been acquired to average out low-frequency content the

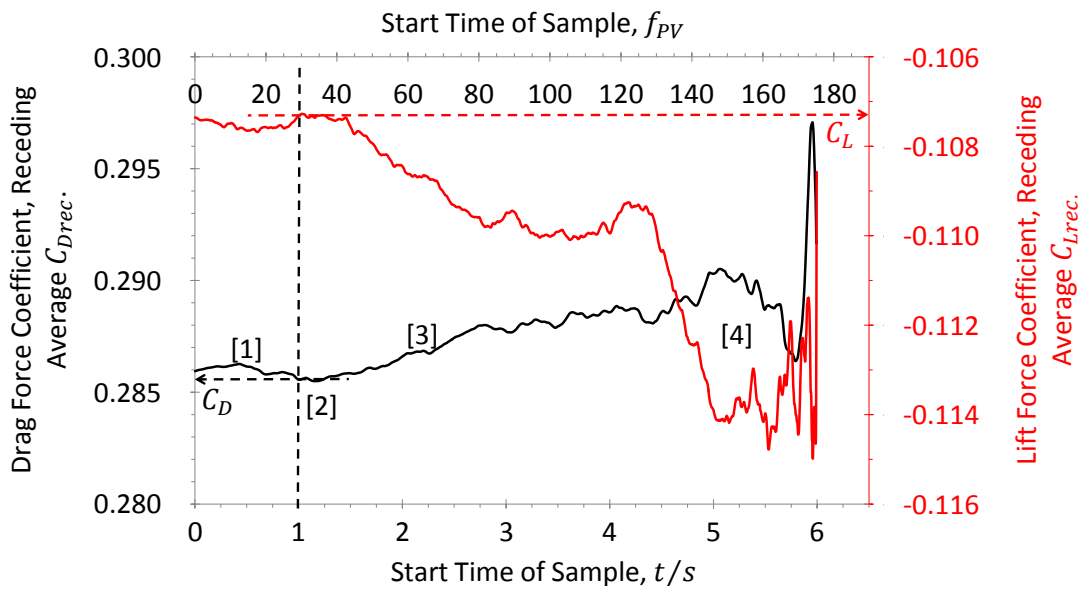


Figure 18. Receding Average Functions for the Windsor Body Baseline Drag and Lift Force Coefficients

functions plateau at what are effectively stationary mean values [2]. As more data is removed and the averaging period becomes short relative to the timescales present in the flow then the receding average functions drift away from the settled mean values [3] and then finally destabilise [4]. This procedure produced the mean force coefficients shown in Table 1, which also compares them with the experimental measurements of Perry *et al.* (2015). The confidence intervals for the simulated force coefficients are estimates which account for time-based dependence between data points in the force histories [i.e. autocorrelation].

**Table 1 A Comparison of Calculated and Measured Drag and Lift Force Coefficients for the Baseline Windsor Body**

Drag Force Coefficient, $C_D$				Lift Force Coefficient, $C_L$			
CFD	$\pm 95\%$ C.I.	Experiment	$\Delta(\%)$	CFD	$\pm 95\%$ C.I.	Experiment	$\Delta(\%)$
0.286	0.003	0.282	+1.3	-0.107	0.003	-0.103	-4.2

Agreement between experiment and simulation agreement is excellent for this initial baseline. However, to draw robust lessons which will inform the development of an innovative simulation process for production vehicles, it is important to test the *sensitivity* of the approach to varying levels of spatial resolution and also test its capability using local quantities in the wake, rather than just integral force coefficients. Therefore, a refinement study was undertaken which preserved the lattice structure but varied the edge length of the smallest voxels and consequently voxels through the complete lattice. It is important to note that this also changes the temporal resolution, as the simulation time step is a function of the smallest voxel edge length (Blumrich *et al.*, 2016: 1076). In turn, this changes the ability of the simulation to resolve the spectral content of the flow field. However, even the lowest resolution lattice investigated here is capable of resolving the frequency content of the wake up to 1.2 kHz (*Portfolio Report B*: 178-179). This is more than three times the frequency associated with significant wake unsteadiness measured for a similar bluff body by Duell and George (1999). Hence, it is appropriate to treat the following as a *de facto* spatial assessment of *sensitivity* to spatial resolution.

Additional lattices were constructed with smallest voxel edge lengths,  $L_{V_x}$  of: 0.50 mm, 0.75 mm, 1.25 mm, 1.50 mm and 2.00 mm; this varied the total number of voxels between  $3.5 \leq N_v/10^6 \leq 160$ . The resulting changes to the drag and lift coefficients are shown in Figure 19. The relationship between resolution and force coefficient is non-linear: increased resolution not necessarily leading to a result that is closer to experiment. However, the drag coefficient values for all but the coarsest lattice are within their margins of uncertainty. The lack of a clear trend can be linked to two factors. First, the initial lattice choice [ $L_{V_x} = 1$  mm] already provides excellent resolution through the near-wake, resolving more than 80% of the turbulent kinetic energy [See *Journal Paper B.1*]; hence, approaching or surpassing this level of refinement may not

confer significant incremental benefit in the calculation of the integral force coefficients. Second, with scale-resolving methods, increased spatial refinement leads to more turbulence scales being resolved; therefore, this *sensitivity* assessment cannot be interpreted as a conventional grid *convergence* study (Weinman *et al.*, 2006) where predictions are expected to approach a target solution in a monotonic or oscillatory manner (Stern *et al.*, 2001; Lockard, 2010).

In addition, the lattice with  $L_{V_x} = 1$  mm provides the best estimate for the lift coefficient; on this measure, using a smallest voxel of 1 mm provides the best balance between accuracy and economy — a balance that is central to the practise of engineering .

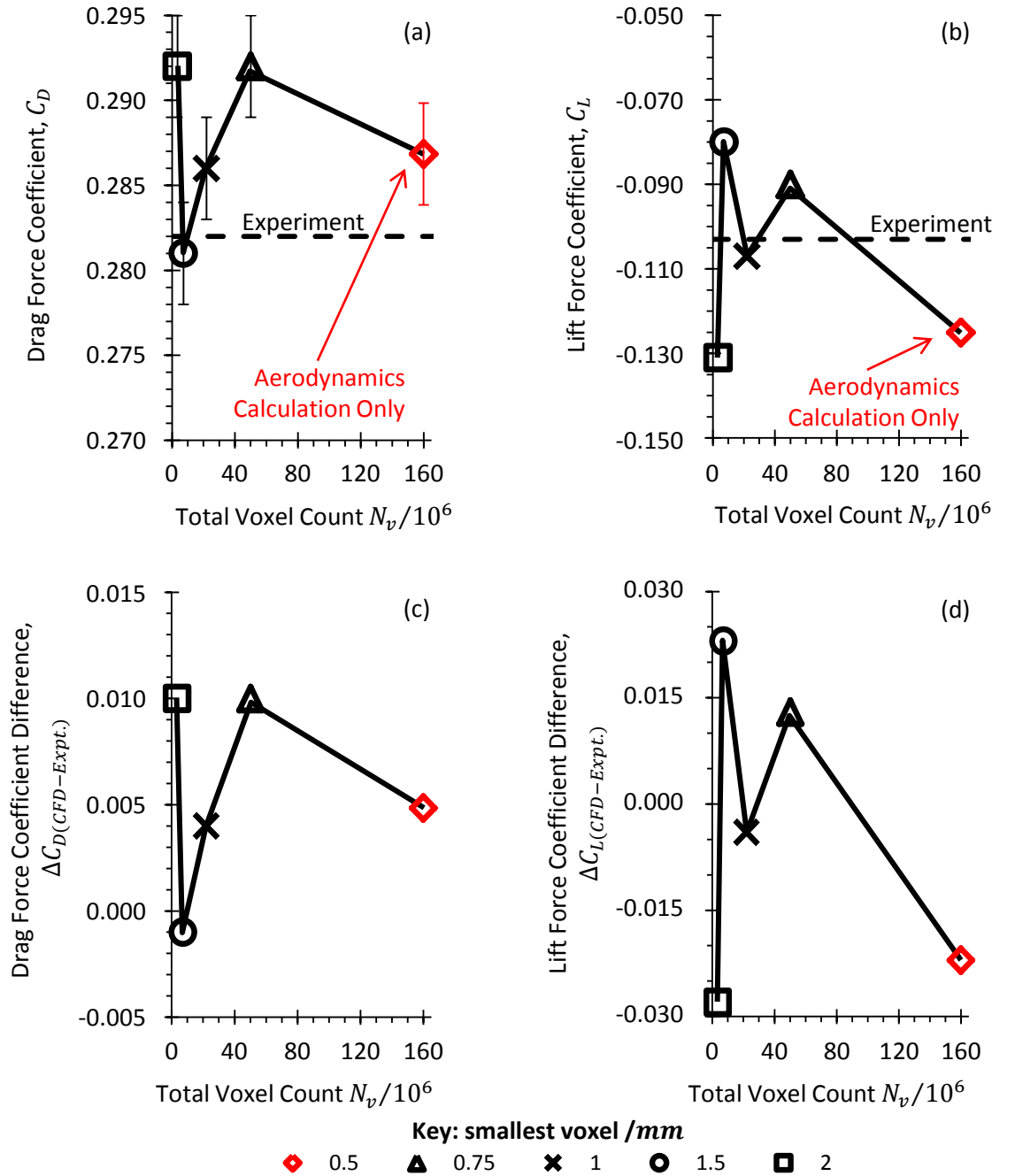
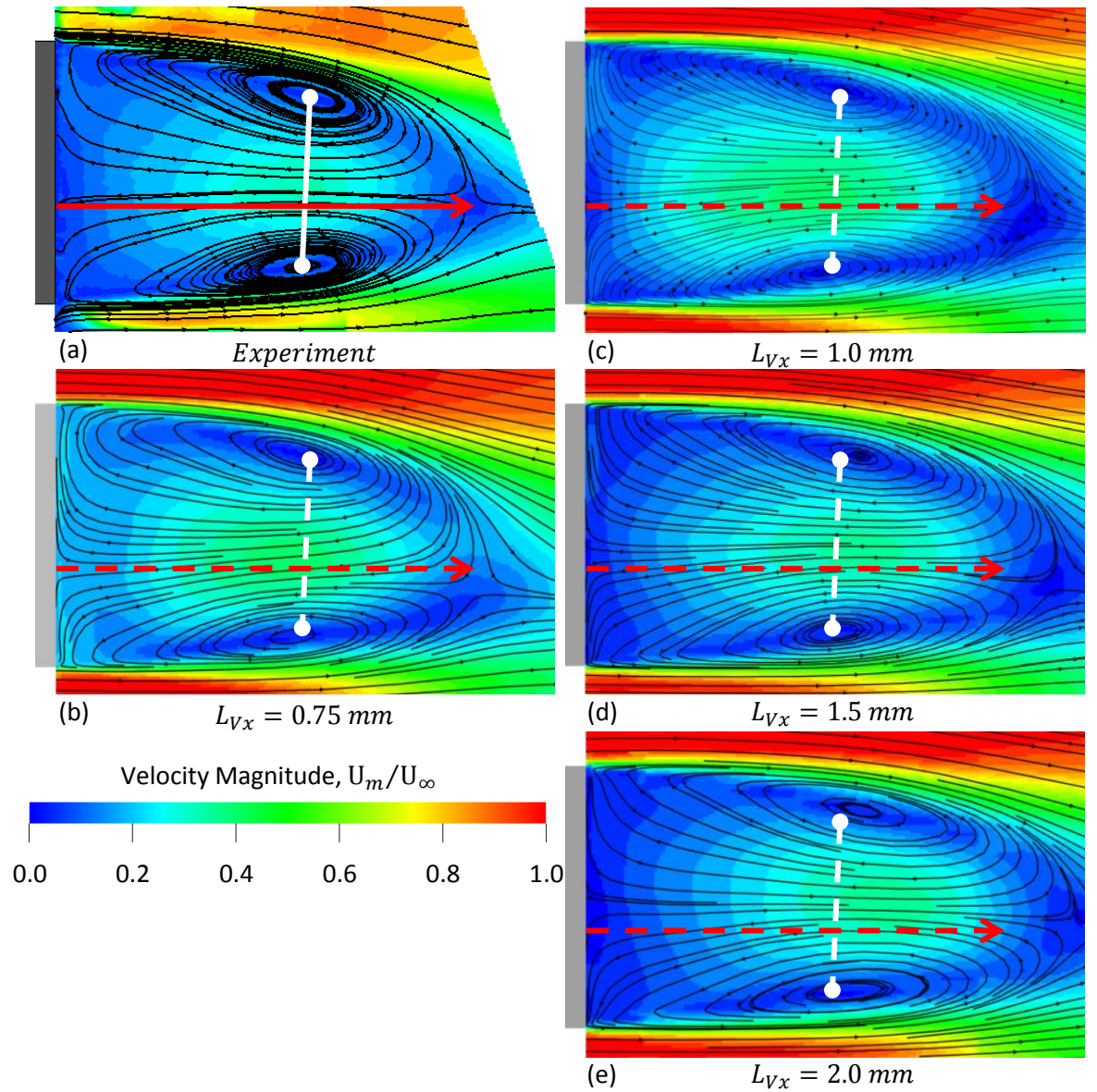


Figure 19. Force Coefficient Variation with Total Voxel Count Obtained for the Windsor Body: (a) Drag, (b) Lift, along with Difference from Experiment for (c) Drag and (d) Lift



As this work depends on being able to accurately capture the wake of vehicles to simulate their interaction with airborne spray, it is also important to assess lattice design in terms of how well the simulation recovers wake characteristics. Figure 20 compares flow velocity and streamlines measured on the  $y = 0$  plane<sup>14</sup> with the comparable results from four of the lattices [the finest lattice was removed from further consideration on the grounds of its large computational cost]. This vertical cut through the flow reveals a toroidal, wake ring vortex similar to that described by Krajnović & Davidson (2003) for a bus-shaped body and later by Rouméas *et al.* (2009) for simplified square-back geometry. The experimentally determined relationship between the upper and lower arms of this vortex is indicated [white line] along with the wake length [red arrow]. Generally the simulations capture the wake structure well, with increasing resolution shortening the simulated wakes, tilting the ring vortex back towards the upper trailing edge of the Windsor



**Figure 20. Wake Flow Velocity and Streamlines for the Baseline Windsor Body from (a) Experiment (Perry, 2016:151) and Simulations using a Smallest Voxel Edge Length of (b) 0.75mm, (c) 1.0 mm, (d) 1.5 mm and (e) 2.0mm**

<sup>14</sup> For brevity, comparisons for horizontal planes are not included, but can be found in *Portfolio Report B*.



body and reducing the over-estimation of flow velocity in the return flow between the vortex foci. In these respects, the lattice with  $L_{V_x} = 0.75$  mm performed best; however, for a complete assessment of simulation sensitivity to lattice design the metric which is at the heart of the work – surface deposition – needed to be taken into account.

The influence of lattice resolution on the deposition of spray over the rear surface is explored in Figures 21 and 22. The accumulation of film mass over the rear face is plotted against time in Figure 21. This indicates that for all lattices accumulation tends to be linear with time. The least refined lattice is a clear outlier, with the lowest total deposition. Of the remaining lattices, the  $L_{V_x} = 1$  mm design delivers the largest deposited mass, followed by the  $L_{V_x} = 1.5$  mm and  $L_{V_x} = 0.75$  mm designs. It is surprising that, of this group, the finest lattice produces the lowest deposition. The reason for this can be inferred from Figure 22, which provides cumulative deposition patterns for each of the lattices. Increasing resolution leads to the emergence of a radial distribution, biased towards the lower edge of the body. This is at its most centred and even with  $L_{V_x} = 1$  mm (d). Increasing resolution further (c) results in a highly asymmetric distribution, which has significant film depth to the right-hand edge of the base. Hence, it can be inferred that some spray mass that would have been captured, had the pattern been centred, “misses” the surface and is advected away in the bulk flow. This implies either lateral instability in, or displacement of the wake; which is a plausible hypothesis as Al-Garni *et al.* (2004) noted lateral “wake flapping” instabilities for a bluff bodied vehicle model. In addition, bi-stable, intermittent wake instability for this type of simple body has been parameterised by Grandemange *et al.*, (2013) who were able to classify predispositions to lateral or vertical wake instability based on the ratio of body height to width [ $H^*$ ] and ground clearance to body width [ $C^*$ ]; this model is shown in Figure 23 with the position of the Windsor body in its baseline condition [ $h_g = 50$  mm] indicated. The Windsor body is placed in the lateral  $y$  –instability zone. This is characterised by the, “coexistence of two states of the wake which switches randomly between the right-hand side and the left-hand side of the body” (Grandemange *et al.*, 2013). This type of wake instability has been directly observed for the Windsor body (Pavia *et al.*, 2016; Perry *et al.*, 2016). Therefore, the reduced deposited mass and displaced deposition pattern [Figure 22(c)] may be due to having sufficient resolution to capture a laterally displaced wake-state.

Setting aside the result for the  $L_{V_x} = 0.75$  mm design, relative to the  $L_{V_x} = 1.0$  mm lattice the  $L_{V_x} = 2.0$  mm option returned 20% less deposition; moving to the  $L_{V_x} = 1.5$  mm lattice, this deficit reduced to only 3%. This suggests that mesh dependency with respect to total deposition for the  $L_{V_x} = 1.0$  mm lattice is likely to be low. As previously noted, it also provides excellent results for integral force coefficients and the wake velocity field. Finally, it requires 50% of the computational effort of the  $L_{V_x} = 0.75$  mm lattice.

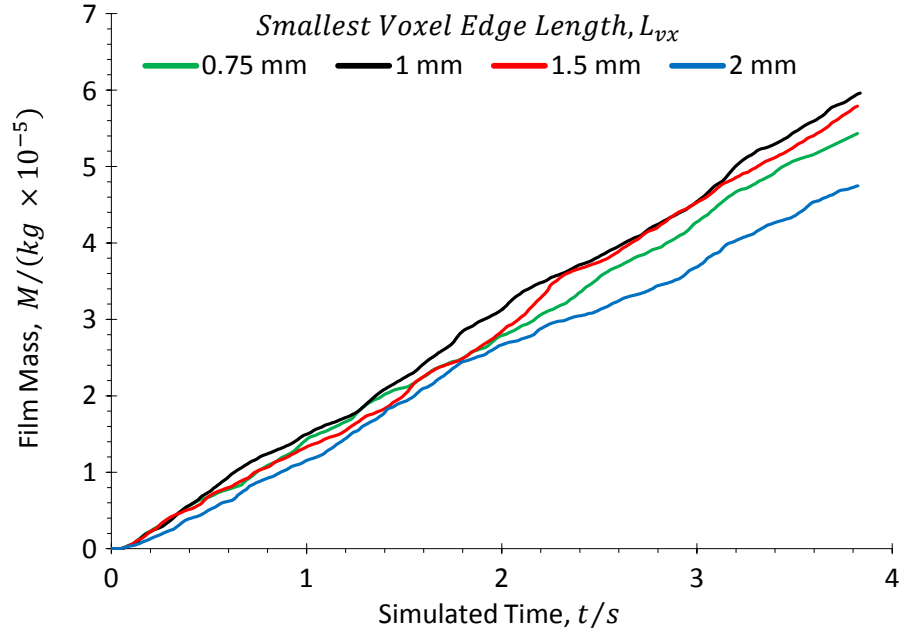


Figure 21. Variation in Deposition History for the Complete Rear Surface of the Baseline Windsor Body with Smallest Voxel Edge Length

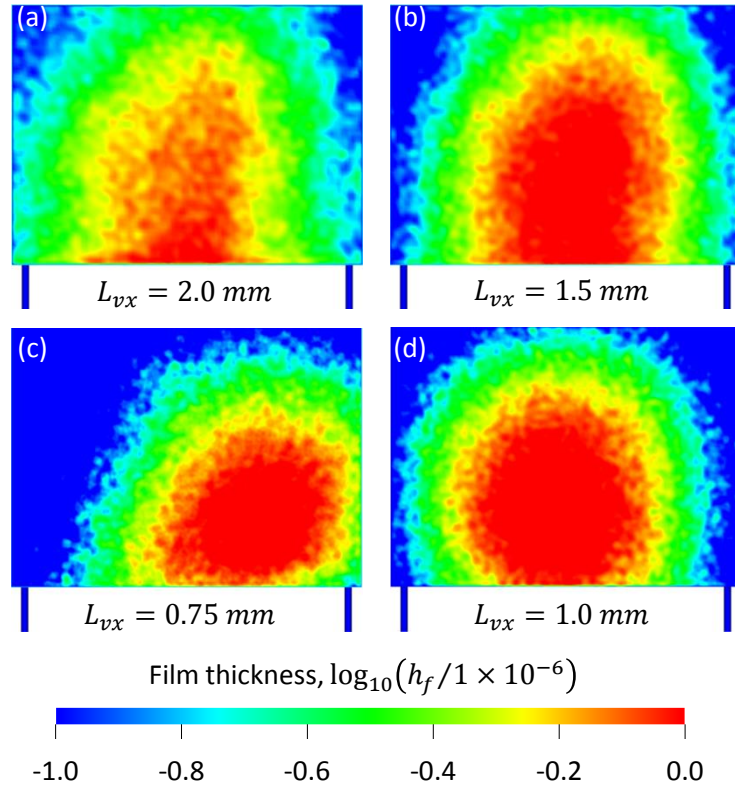


Figure 22. Cumulative Rear Surface Deposition Patterns for Lattices using a Smallest Voxel Edge Length of (a) 2.0 mm, (b) 1.5 mm, (c) 1.0 mm and (d) 0.75 mm

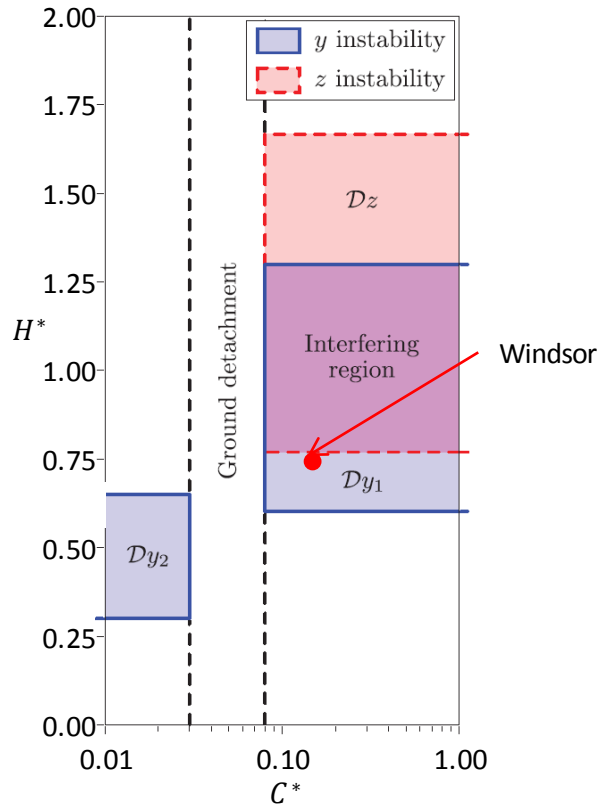


Figure 23. A Model for Wake Instability (Grandemange *et al.*, 2013)

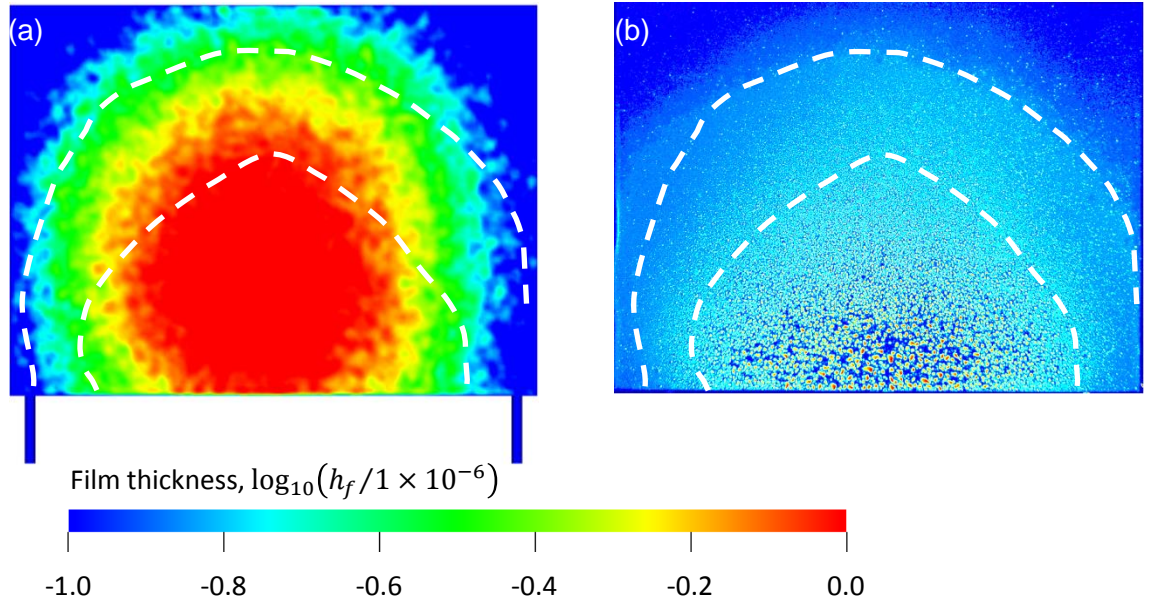


Figure 24. Rear Surface Deposition for the Windsor Body (a) Predicted and (b) Measured (Kabanovs *et al.*, 2016)

Therefore, taking into account the balance between accuracy in predicting the aerodynamics of the bluff body, sensitivity of rear surface deposition to lattice design and the computational resources required, the  $L_{V_x} = 1.0$  mm lattice was selected as the baseline design for this work. This is a key lesson for the development of the simulation approach for production vehicles: the quality of the computational outcomes needs to be balanced against the available resources.

Further justification for this choice is presented in Figure 24. This compares the surface deposition pattern obtained from (a) the  $L_{V_x} = 1$  mm lattice with (b) physical measurements by Kabanovs *et al.* (2016a). The broken lines delineate zones of high, medium and low contamination inferred from the experiment. The simulation appears to provide a credible match to the overall pattern, though it exhibits less lateral and more vertical dispersion.

Having confirmed by reference to published experimental data that this novel simulation model using a lattice with  $L_{V_x} = 1$  mm provided a good representation of aerodynamic forces, wake structure and deposition patterns it was important to ensure that the four seconds of time being simulated was adequate. In essence, could it be considered to provide a distribution indicative of that obtained in longer experiments, or even customer experience of production vehicles?

In an original analysis, surface film thickness profiles were extracted at approximately 0.25 s intervals through the calculation, along the  $y = 0$  centreline and a horizontal line through the deposition peak. Figure 25 presents this data, with the film thicknesses divided through by the peak film thickness for each particular profile, i.e.  $h_f/h_{f(max)}$ . It is evident that these relative thickness profiles collapse, within a reasonable tolerance, onto common curves. This collapse also improves as the simulation progresses. These observations indicate that the relative film depth distribution converges quickly, with the overall pattern of the distribution relatively time-invariant. Hence, over time, the form of the distribution changes little aside from a proportionate increase in depth. This original observation provided a crucial part of the justification for comparing the results of relatively short simulations with longer experiments, that the *relative* distribution provided by numerical simulations of just a few seconds of time will hold true over the hundreds of seconds typical of physical experiments. Taken along with the approximate linearity of deposition with time, short simulations can then be understood to produce results for rear surface deposition which can be considered equivalent to their physical counterparts.

With the reliability of this novel simulation approach established and a clear indication obtained for the spatial resolution strategy required to correctly represent a wake similar to that of a typical SUV, the simulation was interrogated to provide original insights into the flow mechanisms responsible for rear surface deposition. The following section focusses on the role of the rear wake in capturing spray and surface pressure distribution on its subsequent deposition.

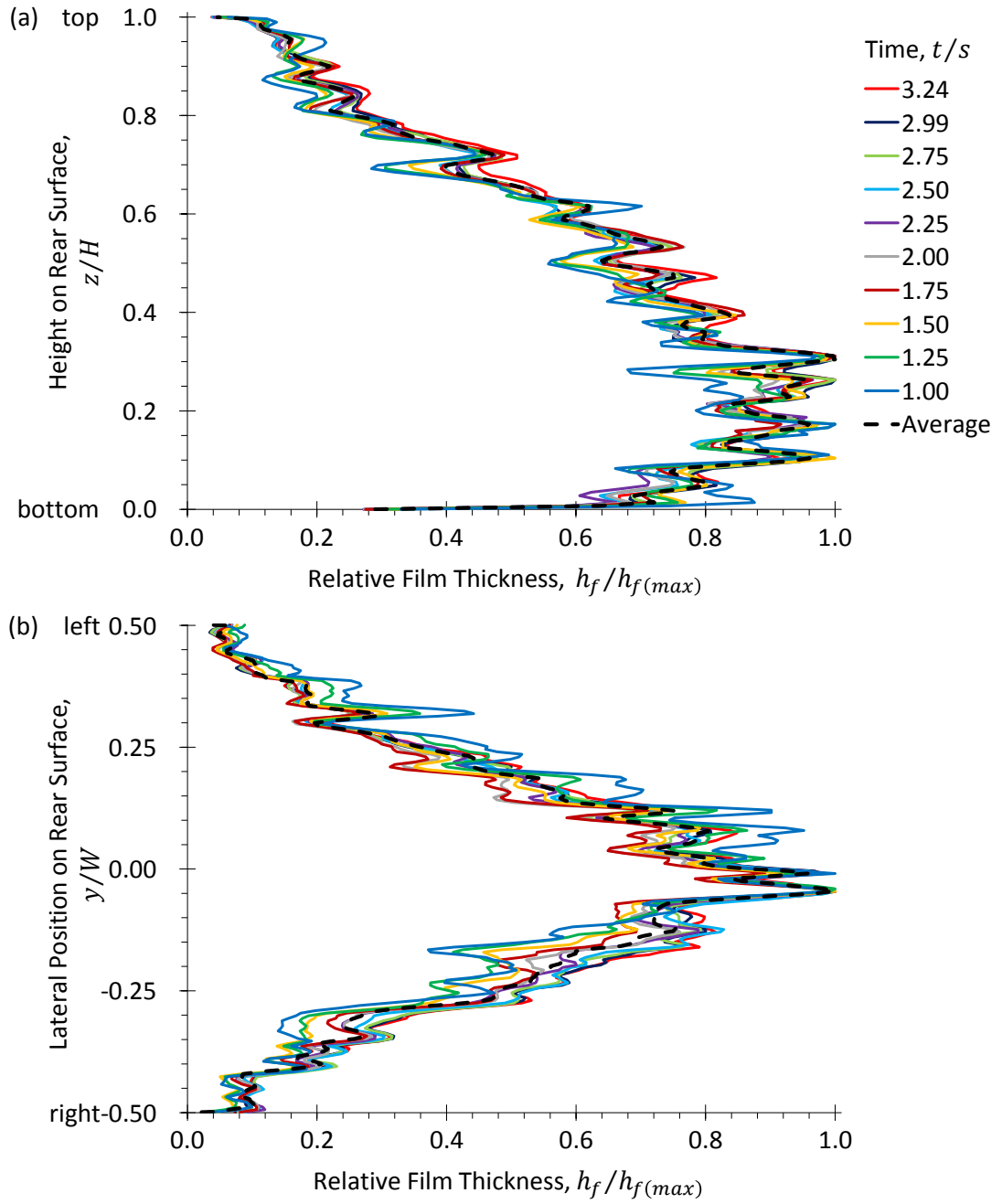


**Figure 25. Relative Predicted Film Thickness Profiles for the Baseline Windsor Body along (a) Vertical Centreline and (b) Horizontally Through the Deposition Peak**

### 3.2.2 Deposition Mechanisms

One of the key advantages of using Computational Fluid Dynamics is the depth of insight that can be provided for flow fields, as long as the simulation is credible (Gaylard, 2009). Given the successful correlation of the simulation approach against experimental data, any insights into the flow field can be reasonably expected to represent the flow physics. Therefore, the following section uses the baseline simulation to highlight key aspects of the interaction between the wake and contaminant spray. Figure 26 provides a view of the flow field and spray using two planes. The vertical  $y = 0$  plane (a) shows the spray being captured by the lower lateral arm of the ring vortex which turns it back towards the rear face of the body. Further, downwards curvature of the streamlines close to the rear face is seen to force the contamination peak to sit relatively low on the base, at around 20% of the body height; below the rear face flow impingement point. The horizontal  $z -$  plane (b) shows the vertical arms of the ring vortex focussing deposition towards the centre of the rear surface. Therefore, the distribution patterns [Figure 24] and film thickness profiles [Figure 25] can be thought of as bearing the imprint of the wake ring vortex structure.

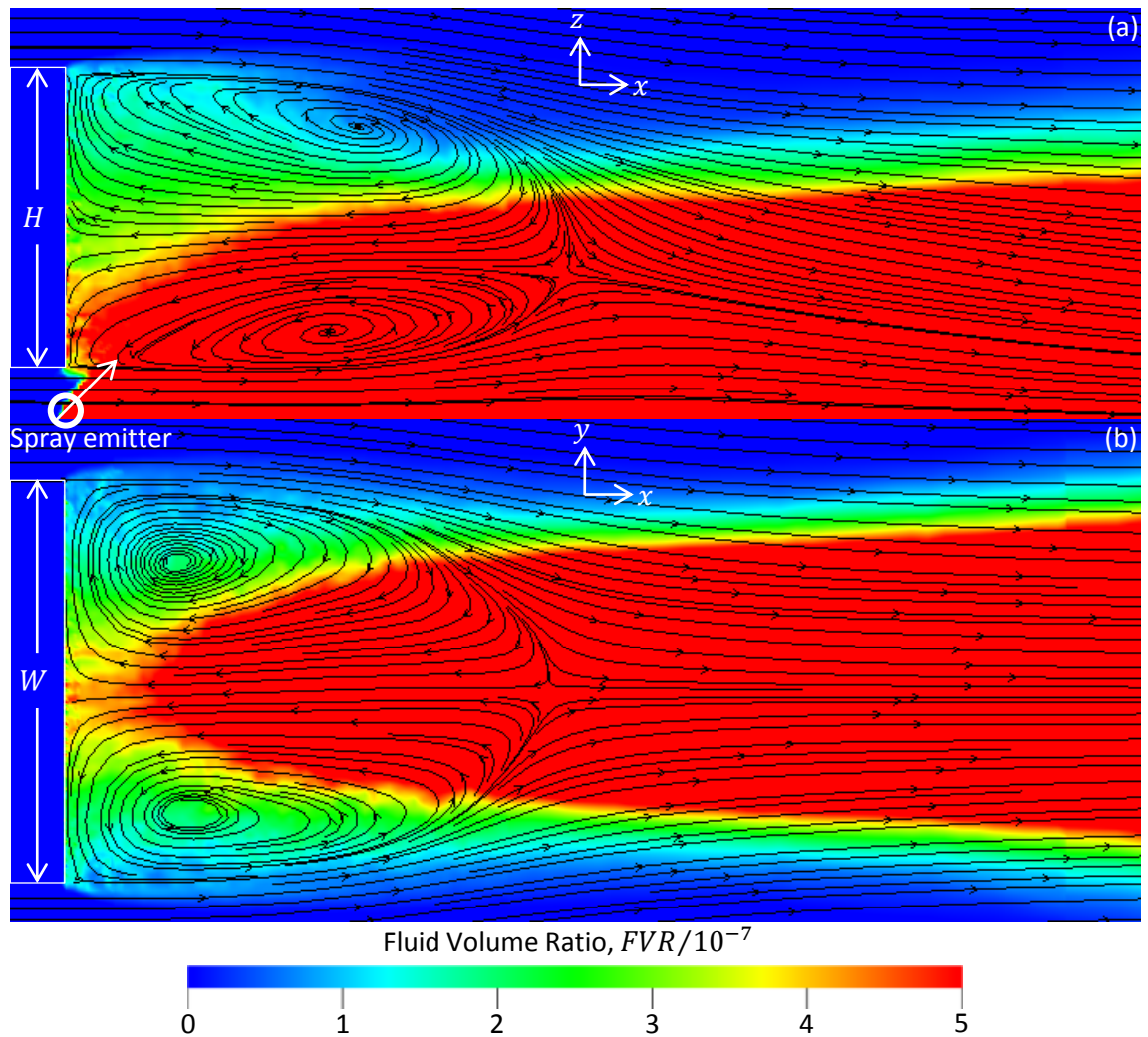
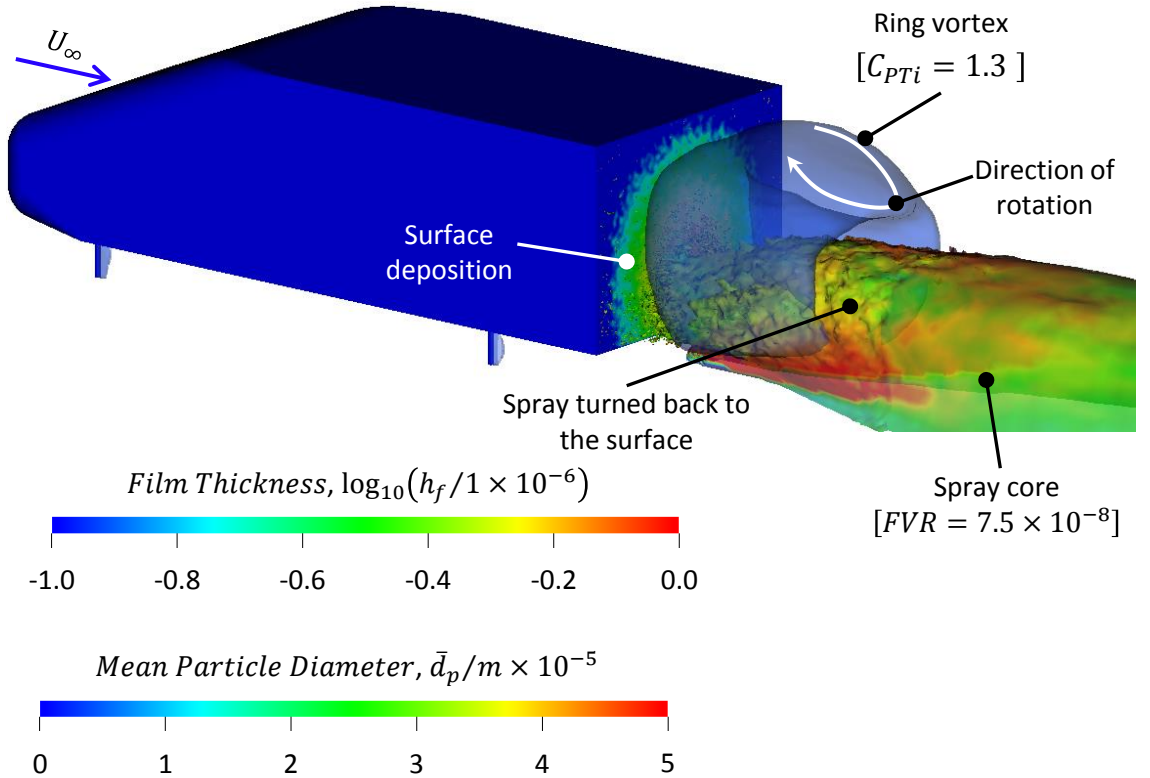
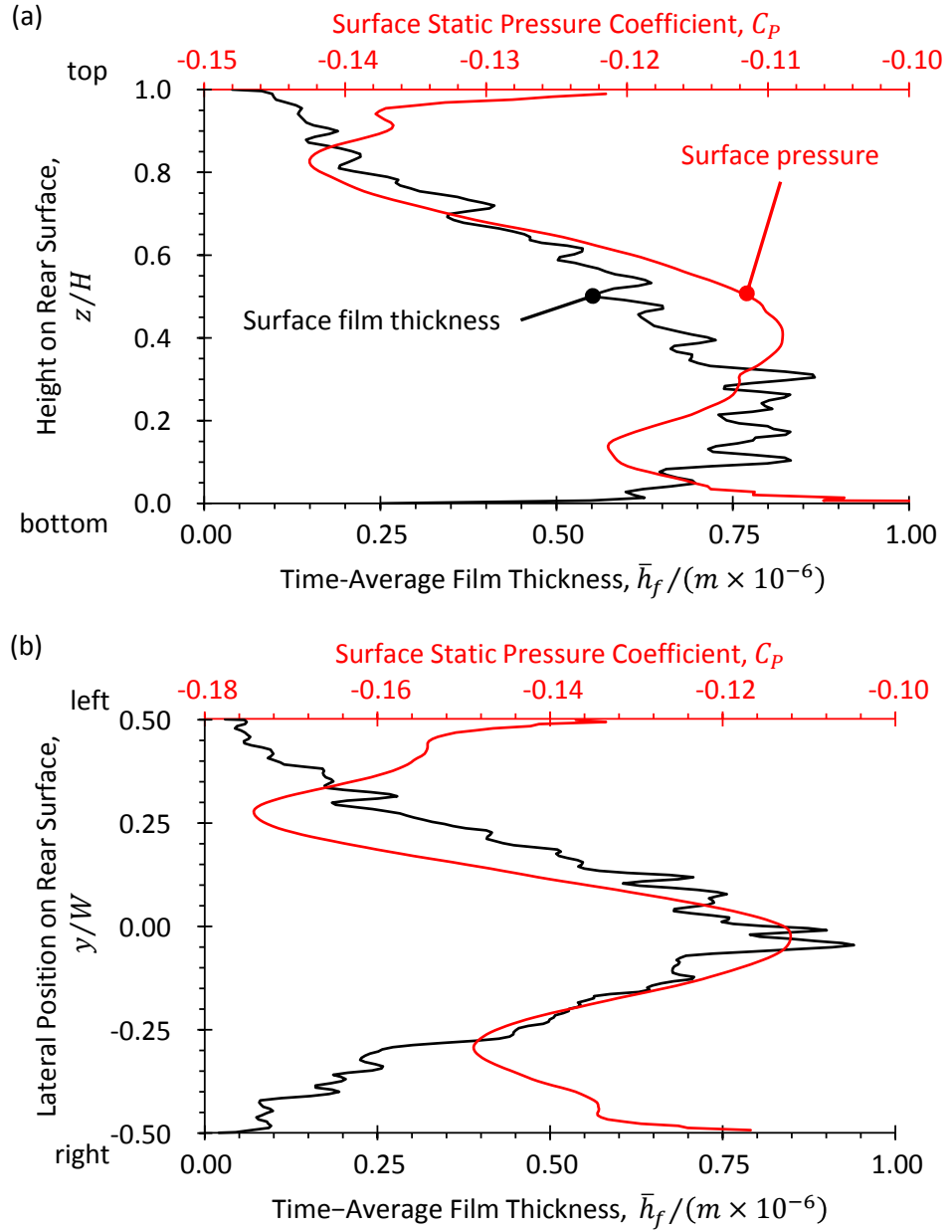


Figure 26. Airborne Spray Concentration and Flow streamlines through the Wake of the Baseline Windsor Body along (a) Vertical Centreline and (b) Horizontally at Mid-Body Height

A three-dimensional view of the ring vortex and spray core is provided in Figure 27, using isosurfaces of total pressure deficit [ $C_{PTi}$ ] and fluid volume ratio [ $FVR$ ], respectively. It shows that a fraction of the spray is captured by the ring vortex and pulled back towards the body by its rotation. The return flow through the centre of the vortex ring directs the captured spray and controls where it impinges on the rear face. Colouring the boundary of the spray core by mean particle diameter [ $\bar{d}_p$ ] shows that the bulk of the larger particles pass under the ring and are carried downstream by the main flow. Their declining prevalence with distance downstream is likely due to them dropping out of the flow. The association between the return flow which impinges on the rear surface and the captured spray fraction leads to the correlation between surface pressure and deposited film thickness shown in Figure 28. Generally, higher surface pressures are associated with high levels of deposition and *vice versa*. This breaks down at the edges of the rear face where relatively high surface pressures are predicted by the simulation and deposition is low. Hence, relatively high levels of pressure on the rear surface are a *necessary* but *insufficient* condition for deposition: local availability of airborne spray is also required. The structure of the ring vortex focusses the spray towards the centre of the rear face, away from the edge. Therefore, although the local pressure field would tend to favour deposition the concentration of airborne spray available for deposition is low. This observation provides a significant extension to the association between pressure and deposition inferred from experiment by Costelli (1984).



**Figure 27. The Wake Ring Vortex and Spray Core for the Baseline Windsor Body. The Spray is Visualised by an Isosurface of Fluid Volume Ratio Coloured by Mean Particle Diameter**



**Figure 28. Surface Static Pressure and Film Thickness on the Rear Surface of the Baseline Windsor Body (a) Along the Vertical Centreline and (b) Horizontally, Through the Deposition Peak**



### 3.2.3 Underfloor Effects

The previous section established a novel approach for simulating the deposition of spray onto the rear surface of a simple representation of a vehicle. As we step towards an approach suitable for developing production vehicles it is imperative that it can robustly predict different wake structures and their effect on rear surface contamination, as these will differ between vehicles. The following section describes an extension to the simple system based on the Windsor body, by changing its underfloor geometry to drive changes in the rear wake structure as described in the aerodynamics experiments of Perry and Passmore (2013). This provides the first numerical exploration of the aerodynamics of these underfloor modifications and a novel approach to investigating the effect of wake structure changes on rear surface deposition.

The experimenters modified the roughness of the underfloor by adding five lateral roughness strips to the otherwise smooth model; these came in two heights [ $h_r$ ]: 6 mm and 10 mm [See APPENDIX A, Figure 94(b)]. They also used two ground clearance settings [ $h_g$ ]: 50 mm and 30 mm (Perry & Passmore, 2013). Their purely aerodynamic experiments provided drag force coefficients, along with flow streamline and velocity data on the  $y = 0$  centre-plane through the wake.

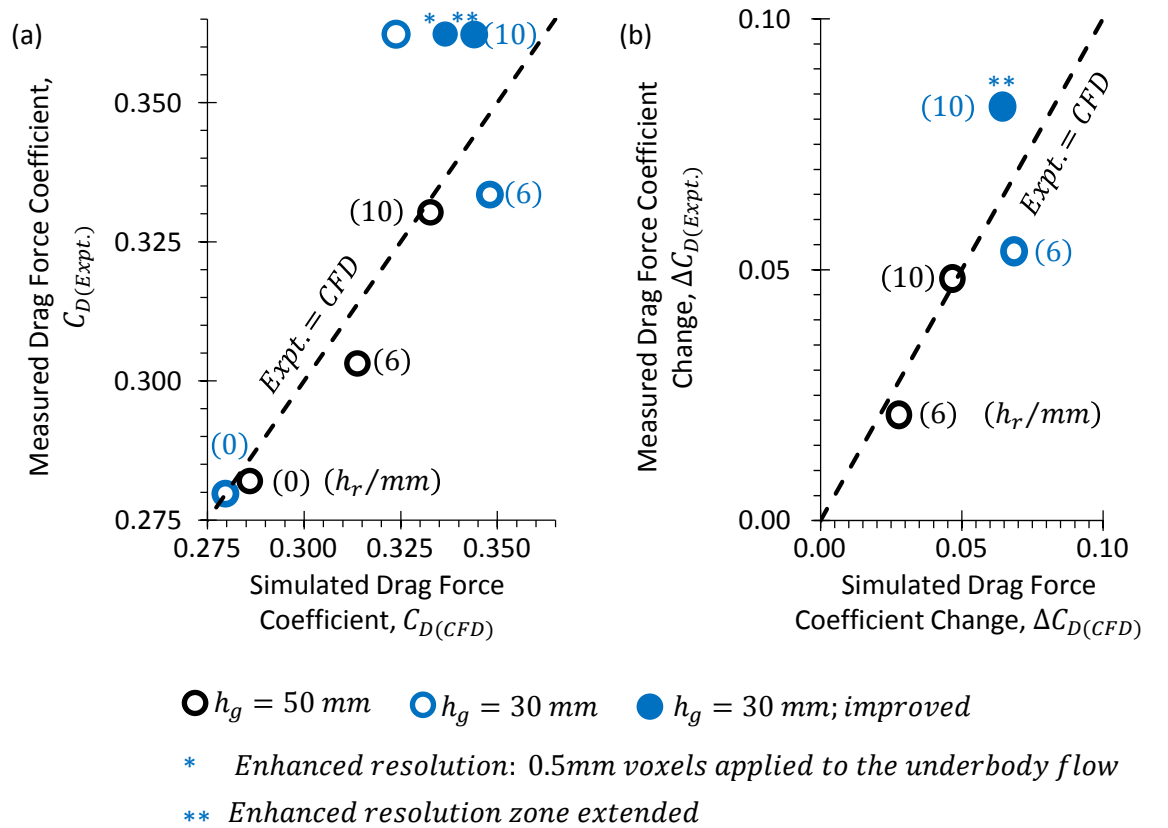


**Figure 29. A Comparison between Measured and Simulated (a) Drag Coefficients and (b) Their Differences from Baseline for the Windsor Body as Ground Clearance and Underbody Roughness is varied**

The drag measurements derived from Perry and Passmore (2013) are compared with the results of their equivalent numerical simulations in Figure 29(a). This is accompanied by a comparison of the differences from the smooth-underfloor baseline cases (b). The two different ground clearances are distinguished by colour. Generally the comparison between measurement and simulation is good, with absolute differences within  $\pm 5\%$ . Compared to experiment, the numerical simulations have a tendency to over-state the aerodynamic drag force; for example simulation shows a significant reduction in  $C_D$  when ground clearance is reduced [ $\Delta C_D = -0.006$ ], whereas the experiment indicates a smaller reduction [ $\Delta C_D = -0.002$ ]. The combination of lowest ground clearance and largest roughness strip breaks this trend, with the CFD simulation initially under-estimating  $C_D$  substantially, by 11% compared to experiment. Partially resolving the underbody flow with 0.5 mm voxels [\*] reduced this difference to 7% and extending the additional resolution through the complete underbody volume [\*\*] provided additional improvement, reducing the difference to 5%. The need for additional spatial resolution is not surprising, as the roughness strips block 1/3 of the clearance between the body underside and wind tunnel floor, substantially changing the flow underneath the body. However, the numerical simulations clearly provide good estimates for the aerodynamic drag forces for these configurations.

The plots of flow streamlines and velocities provided by Parry and Passmore (2013) on the vertical centre-plane provided an opportunity to test the ability of the simulation to correctly capture changes in rear wake structure; Figures 30 and 31 compare this data [left] with the results of the CFD simulations [right]. These structural comparisons between simulation and experiment are excellent, with the wake vortex core positions relative to the rear surface predicted to within  $9 \leq \delta \bar{x}_{RMS}(\%) \leq 20$  and  $10 \leq \delta \bar{z}_{RMS}(\%) \leq 15$  for longitudinal and vertical locations, respectively. For the velocity field, the general impression is that this is over-predicted by the CFD models; however, the converse is actually the case. Perry (2016: 151) repeated three of these measurements and found generally higher flow velocities and slightly changed ring vortex orientation. Using the data for the three re-measured cases the error in locating the ring vortex centre reduces substantially to  $2 \leq \delta \bar{x}_{RMS}(\%) \leq 5$  and  $2 \leq \delta \bar{z}_{RMS}(\%) \leq 4$ . This highlights the value in combining experiment with simulation, enabling both to be cross-checked and anomalies more easily detected.

In terms of underbody flow, the more reliable CFD flow fields show a decrease in the velocity of air exiting the underbody as roughness is increased and ground clearance decreased. This results in the ring vortex developing an increasing tilt, with its lower lateral arm moving closer to the rear surface of the body. In turn, the return flow through the centre of the vortex becomes angled more strongly upwards, with the height of the rear impingement increasing.

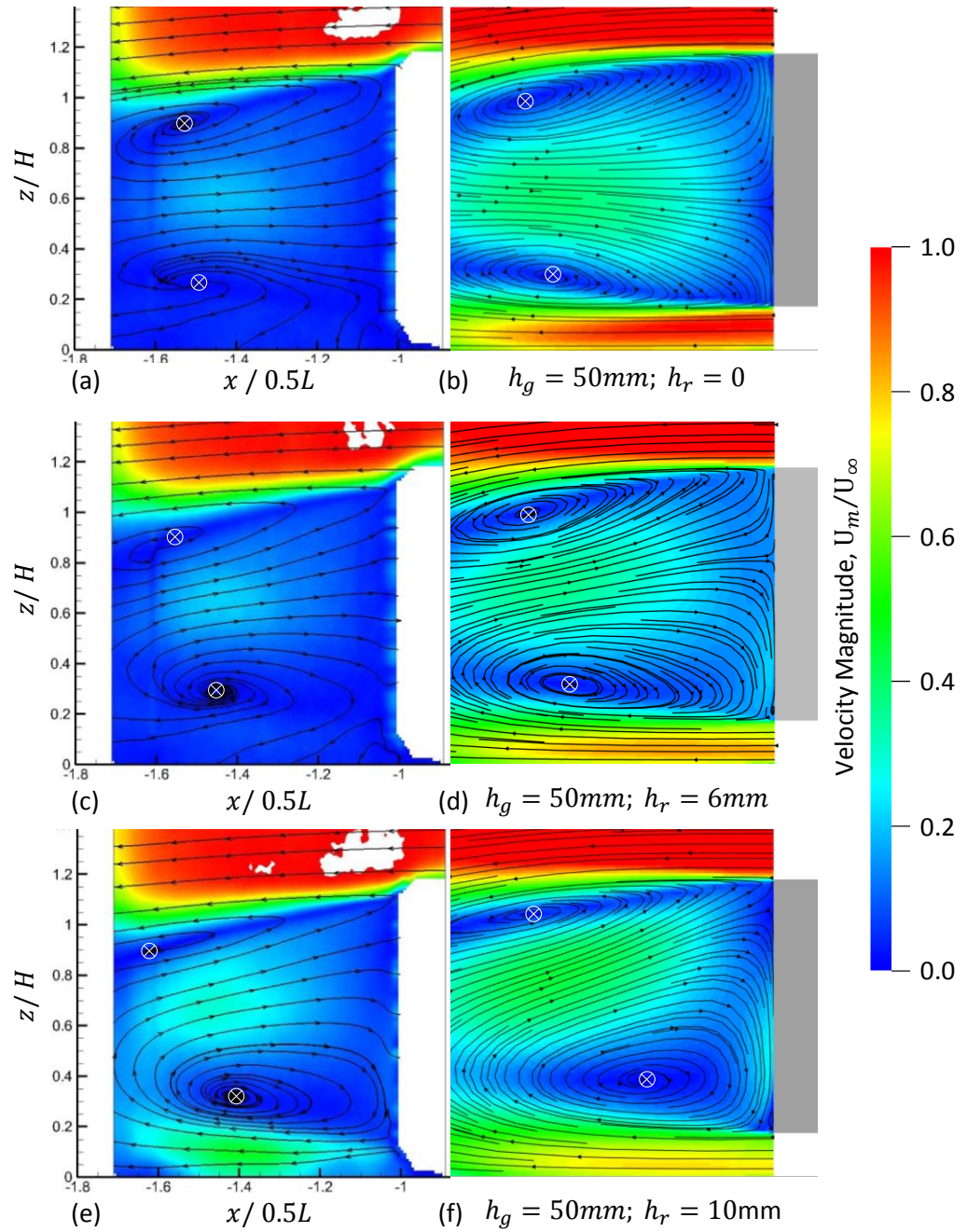


**Figure 30. Flow Velocities and Streamlines on the Centre-Plane of the Windsor Body at 50 mm Ground Clearance as Underbody Roughness is Varied, Measured by Perry and Passmore (2013) [Left] and Predicted [Right]**

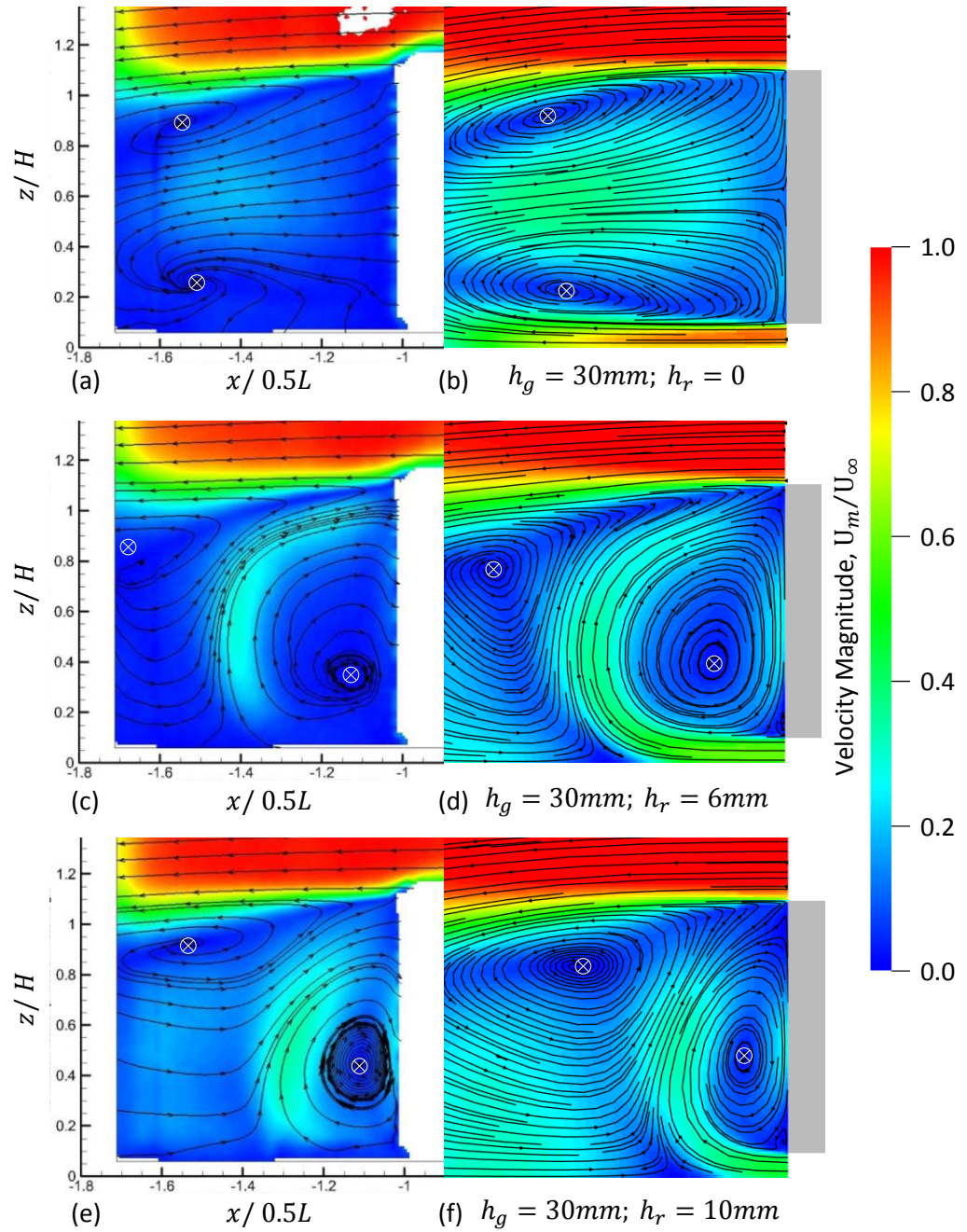


**Figure 31. Flow Velocities and Streamlines on the Centre-Plane of the Windsor Body at 30 mm Ground Clearance as Underbody Roughness is Varied, Measured by Perry and Passmore (2013) [Left] and Predicted [Right]**

Finally, as shown in Figure 31(c) to (f), the underbody flow velocity reduces to a point where the lower vortex arm rolls up over the complete rear surface, its rotation both directing the return flow to the top of the rear face and drawing flow downwards over it. This dramatic tilt of the wake vortex, which is in the range  $64 \leq \alpha(^{\circ}) \leq 69$ , is also associated with the highest drag values.

The changes in wake structure are mirrored in the deposition histories provided in Figure 32. These can be differentiated by ground clearance: the highest ground clearance cases have the lowest total deposition and the lowest rate of deposition; with the baseline smooth under-bodied 50 mm ground clearance case having the lowest rear face deposition. Reducing the ground clearance to 30 mm increases deposition dramatically; by a factor of eight. As noted previously, roughening the underfloor at this lower ground clearance results in a profound change to the rear wake structure, this increases deposition by factors of 11 and 20 compared to the baseline.

It is important to note that although the wake structure undergoes profound changes, contaminant deposition remains linear with respect to time; a regression analysis returned coefficients of determination [ $R^2$ ] no lower than 0.997, i.e. a linear relationship explains at least 99.7% of the variation in the data. This important result indicates that relative linearity of contaminant deposition is likely to be found for a wide range of vehicle designs. This provides yet more evidence that simulation capturing relatively short periods of physical time can provide information relevant to the longer time periods seen in both experiments and vehicle operation.

As shown in Figure 33, the shift in wake structure is also associated with a change in the distribution of contaminant over the rear surface. The initial baseline (a) shows a radial distribution, biased towards the lower edge of the rear face, with its peak at around 20% of the rear surface height. Adding roughness and slowing the underbody flow displaces this vertically (b) until it is biased to the top edge of the rear face (c). Reducing the ground clearance to 30 mm for the smooth-floor Windsor Body maintains the same overall wake structure and actually reduces the vertical tilt of the ring vortex from  $10^{\circ}$  to  $7^{\circ}$ . However, the increased proximity of the lower arm of the ring vortex to the spray increases its entrainment into the wake and deposition increases in intensity, whilst exhibiting the same basic radial distribution. Restricting the flow under the body by adding roughness strips at this lower ground clearance leads to a change in the form of the distribution (e, f). Its main gradients are now vertical as the lower arm of the ring vortex wraps up onto the rear face and draws airborne spray towards its top and then drags it downwards over initially most (e) and then all (f) of the rear face.

This set of original simulations provides the first indication that reduced ground clearance increases rear surface contamination; an important result as reducing ground clearance is an effective drag reduction technique for cars.



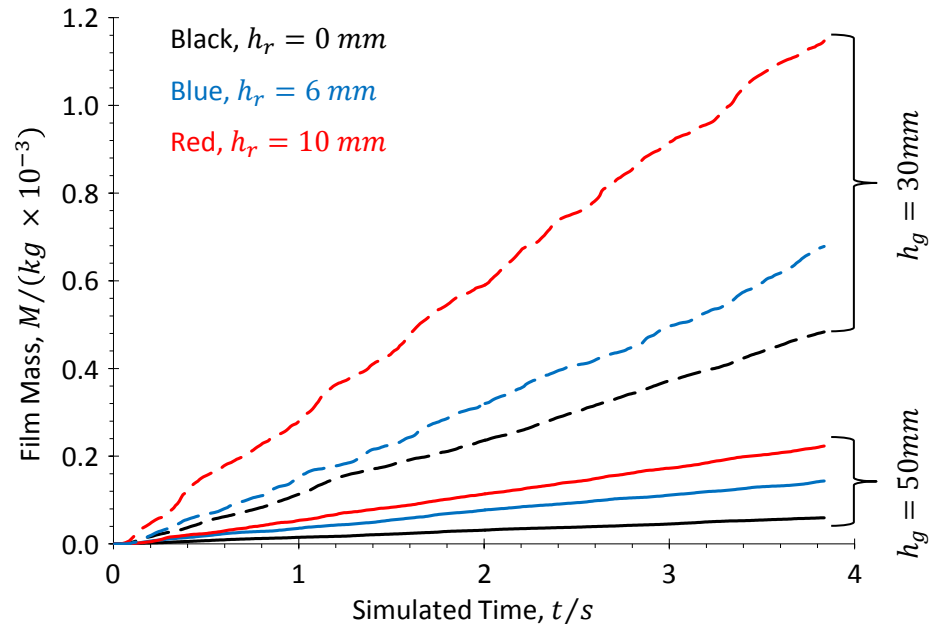


**Figure 32. Variation in Deposition History for the Windsor Body as Ground Clearance and Underbody Roughness are Varied**

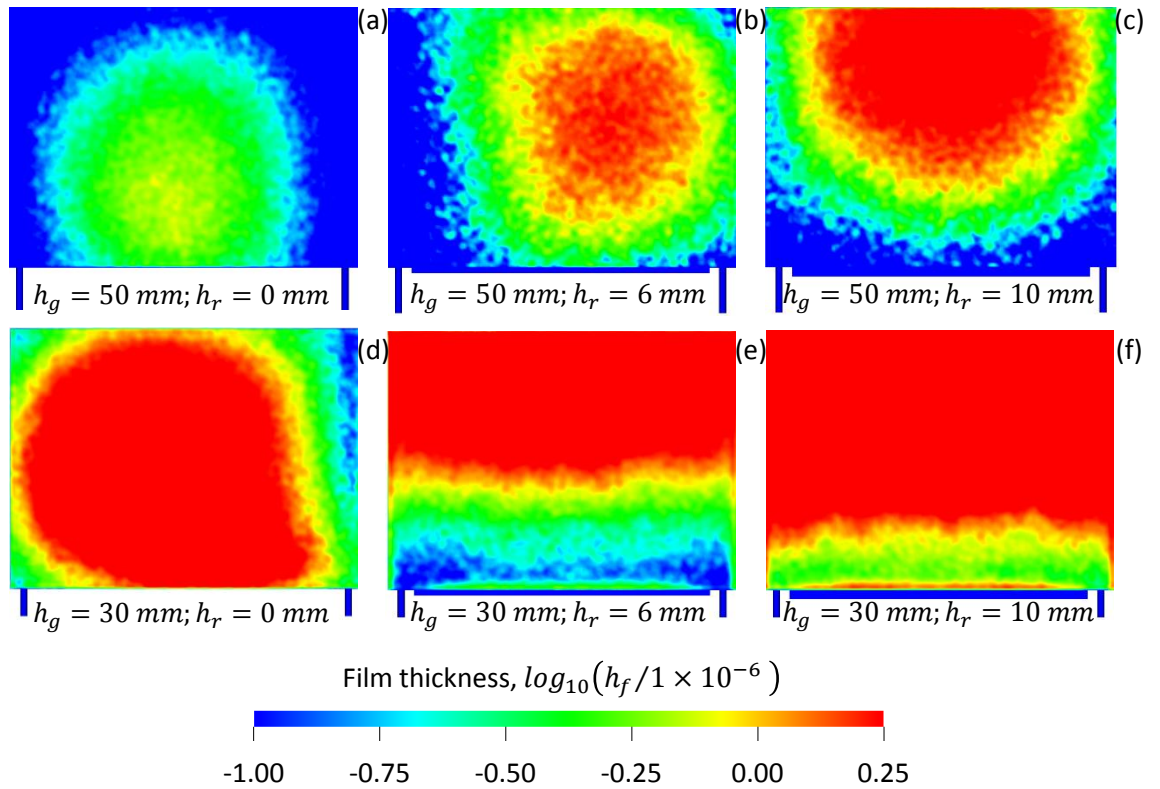


**Figure 33. Cumulative Rear Surface Deposition Patterns for the Windsor Body as Ground Clearance and Underbody Roughness are Varied**

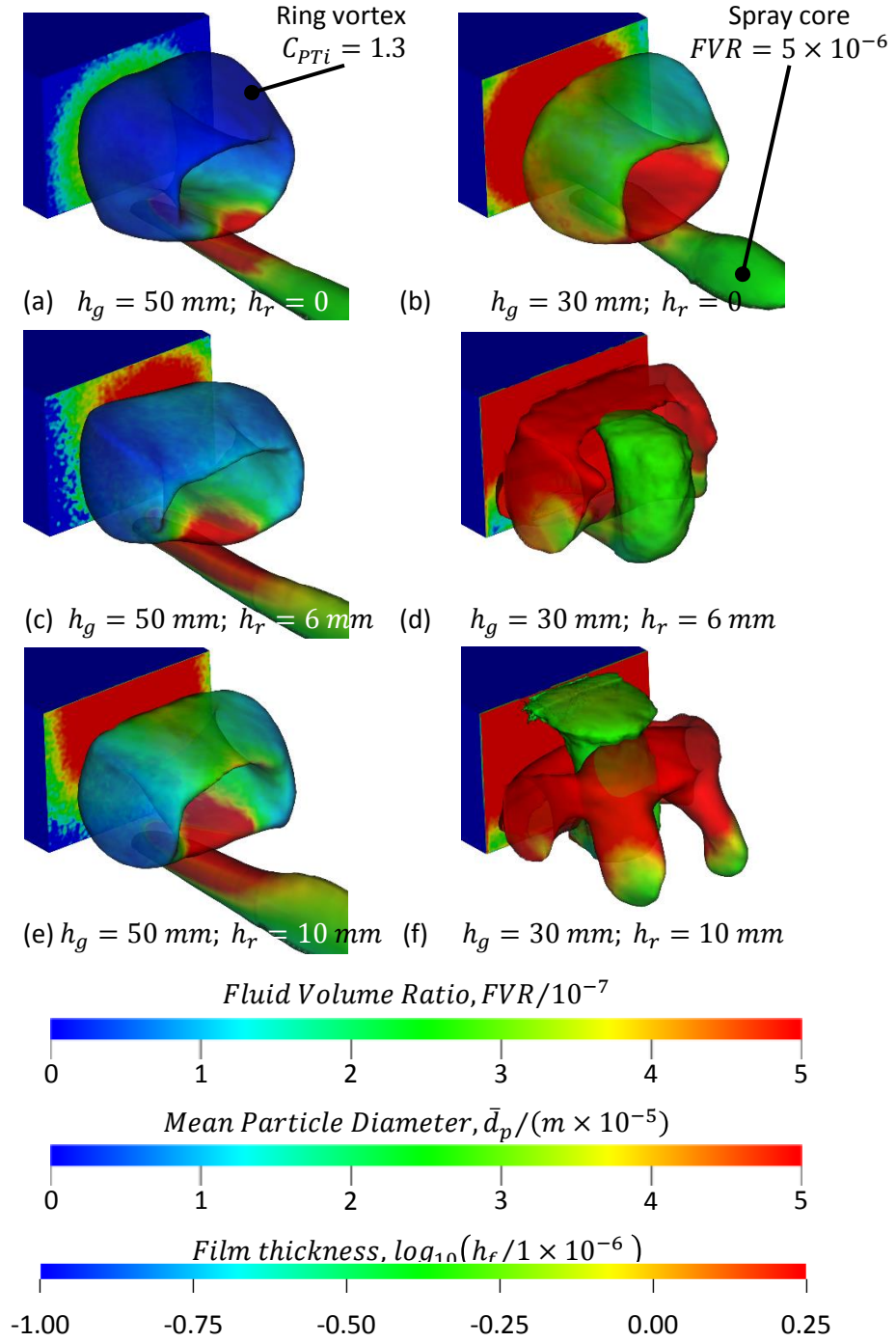


**Figure 34. Wake Ring Vortex, Spray Core and Cumulative Surface Deposition Visualised for the Windsor Body as Ground Clearance and Underbody Roughness are Varied. Ring Vortex Isosurface is Coloured by Fluid Volume Ratio; Spray Isosurface by Mean Particle Diameter**

The mechanism responsible for the changes in surface deposition is shown in Figure 34 which visualises the ring vortex and spray core using isosurfaces, displaying them along with the cumulative deposition distribution over the rear face. This highlights the interaction between the advected spray and the wake vortex, with its attendant effect on rear surface deposition. Initially (a) the bulk of the spray core is advected downstream, away from the body, and the lower part of the ring vortex only captures a small fraction of it. Reducing the underbody flow velocity by adding roughness leads to (c) more spray being captured by the wake and (e) it being directed higher on the rear face. Reducing ground clearance (a – b) changes the rear wake little, but dramatically increases the transfer of spray into it and hence deposition. The shift in deposition mechanism shows the ring vortex capturing the spray core, directing it to the top of the rear surface (d). This is drawn down the rear surface by rotation in the lower arm of the ring vortex, which wraps up over the rear face (f).

Overall, this novel simulation approach has been shown to provide an excellent representation of aerodynamic forces and wake flow topology over a wide range of wake structures. This provides a robust foundation for developing an innovative process that can simulate rear surface contamination and aerodynamic drag concurrently, for production vehicles. In addition, the linearity of the deposition process seen for the baseline case holds with very different wake structures. This continues to provide confidence that short-time simulations can be a useful tool in a product engineering context.

Finally, a number of inferences can be drawn from these results:

- the lower lateral arm of the wake ring vortex provides a key deposition mechanism;
- reduced ground clearance can lead to increased deposition;
- the lowest deposition was seen for the next-to-lowest drag configuration, indicating that a wake with low tilt [ $\alpha_T < 10^\circ$ ] can potentially be a low-drag and low-contamination arrangement;
- higher vortex tilts are associated with higher levels of total deposition with a distribution displaced higher on the rear surface, and similarly
- reduced underbody flow velocity appears to lead to more rear surface soiling.

From a vehicle development perspective, this suggests that reduced levels of rear surface contamination could be achieved by reducing the interaction between the wake ring vortex and any airborne spray. However, on actual vehicles the spray is generated at the rear wheels and carried rearwards in the wheel wakes. Exploring this further required the introduction of the wheels and a more representative spray model. This was provided by the Generic SUV. In the next section the computational approach is developed further, modifying it to cope with more realistic vehicle geometry, including wheels and their attendant wake structures.



### 3.3 THE GENERIC SUV

#### 3.3.1 Baseline Model Correlation

In the final step before moving to actual vehicle geometry, a novel simple system was constructed based on the Generic SUV [See APPENDIX B]. This basic car shape was designed to reflect the proportions of a contemporary SUV and was explicitly conceived for the study of wake dynamics (Wood *et al.*, 2015). Unlike the Windsor body it features: a bonnet, windscreen, wheel arches and, vitally, wheels. This enabled the simulation approach successfully demonstrated on the Windsor body to be evaluated on a flow field containing additional aerodynamic structures, particularly wheel wakes. It also afforded the opportunity to explore the role of wheel wakes, underbody flow and ground clearance on rear surface contamination.

The computational lattice developed for this stage of the work is shown in Figure 35. It derives from the approach used for the Windsor body with the highest levels of resolution [ $L_{vx} = 1 \text{ mm}$ ] applied to radiused leading edges, as well as over the complete rear surface. However, changes have been made to account for the more complex flow; such as the extensive use of voxels with a 2 mm edge length to capture the flow approaching the vehicle as well as the wake structures. This approach is consistent with the exclusively aerodynamic simulations reported by Forbes *et al.* (2014) using the same CFD solver. The resulting lattice comprised 42 million voxels and 18 million surfels. In order to match the published experimental data the onset flow velocity was increased to 40 m/s (Forbes *et al.*, 2014; Wood *et al.*, 2015). This resulted in compromising on the  $y^+$  criterion proposed by Krastev and Bella (2011); however, Forbes *et al.* (2014) demonstrated that the simulation code used here performs well at this level of resolution, compared to other simulation methods.

The additional flow complexity provided by this geometry is highlighted in Figure 36 by using isosurfaces of the Q-criterion (Hunt *et al.*, 1988). Both front and rear wheel wakes can be seen along with the rear wake structure. The latter is characterised by a ring vortex, along with a pair of longitudinal trailing vortices. These features are typical for this class of bluff body in ground proximity. However, compared to the Windsor body the vortex ring is deformed, vertically “pinched” particularly in the centre, with the distance between top and bottom shear layers reduced [X-X’]. This is a result of the strong up-wash generated by the angled underbody surface behind the rear wheels, which effectively acts as a diffuser (Perry *et al.*, 2016). Hence, this case tested the numerical simulation technique against a significantly different wake structure, along with a flow field containing wheel wakes.

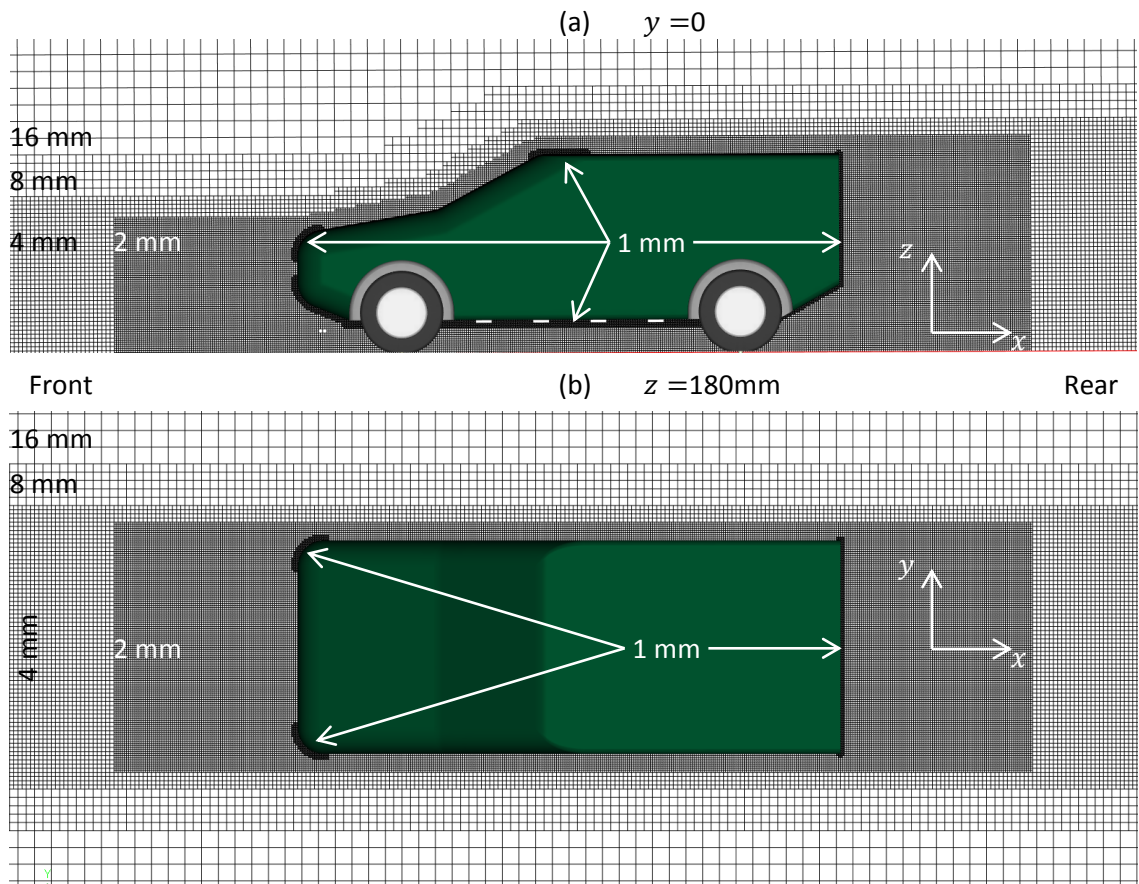


Figure 35. Computational Lattice Used for the Generic SUV Shown (a) on the Vertical Centre-Plane and (b) at Mid-Body Height

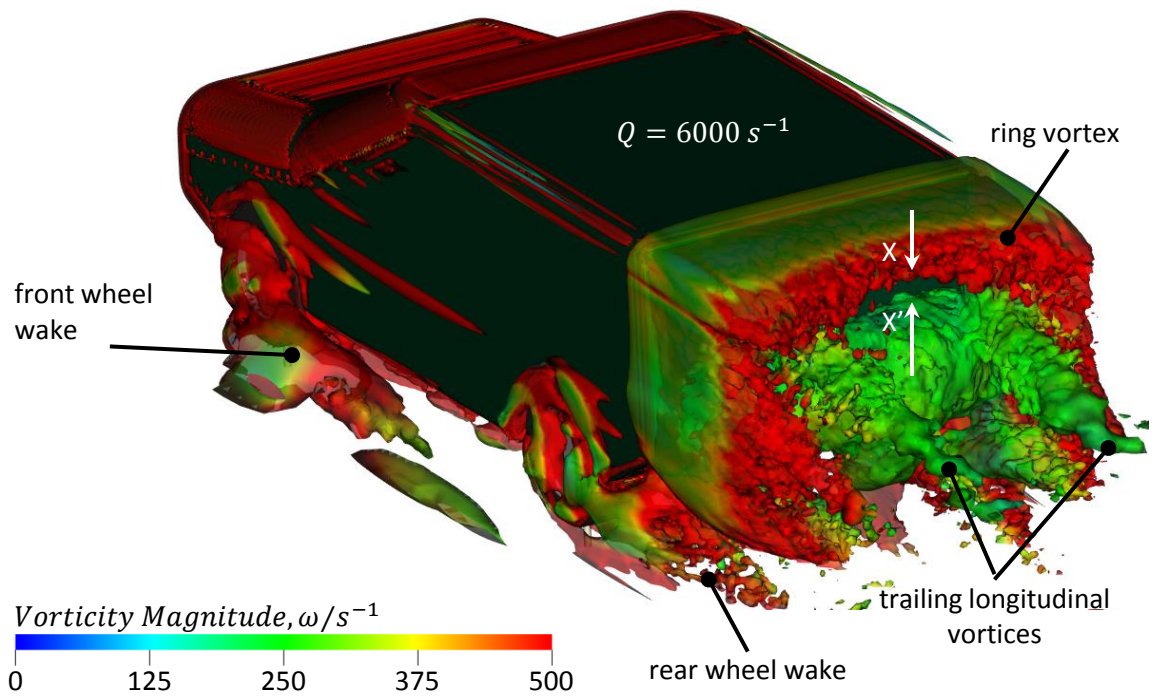
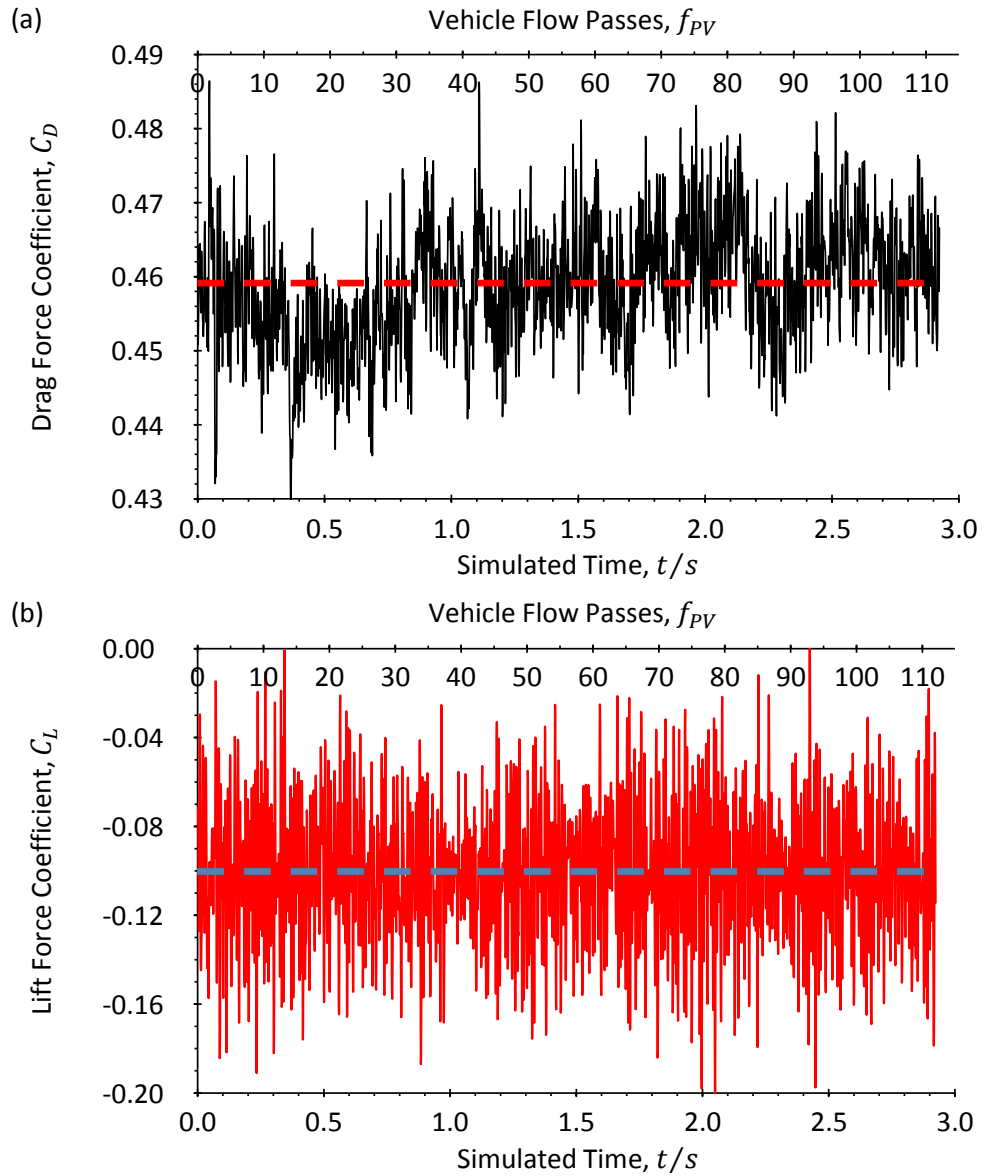


Figure 36. Flow Topology for the Generic SUV, Shown by Isosurfaces of Q-Criterion Coloured by Vorticity Magnitude

As with the simple system based on the Windsor body, the first step was to verify that the simulation technique could capture the aerodynamic characteristics of the geometry provided by physical experiments. To this end, an initial calculation was run for 3 s of simulated time; requiring 4872 CPU hours of computational effort. The drag and lift force coefficient histories obtained are shown in Figure 37. Both force components exhibit high-frequency fluctuations modulated by lower-frequency variation, with a higher level of unsteadiness apparent in the lift signal. Nevertheless, using the author's receding average technique (Gaylard *et al.*, 2017b), this initial baseline calculation provided stable time-mean force coefficients. These are compared to the experimental values published by Wood *et al.* (2015) in Table 2. The drag coefficient obtained compares well with experiment, differing by only 1.1%. In contrast, the lift coefficient appears poorly predicted, differing from experiment by -0.104.



**Figure 37. Unsteady Force Coefficients and their Mean Values [broken line] for the Baseline Generic SUV (a) Drag and (b) Lift**

**Table 2 Calculated Force Coefficients Compared to the Measurements of Wood *et al.* (2015)**

Drag Force Coefficient, $C_D$				Lift Force Coefficient, $C_L$			
CFD	$\pm 95\%$ C.I.	Experiment	$\Delta(\%)$	CFD	$\pm 95\%$ C.I.	Experiment	$\Delta$
0.459	0.003	0.464	-1.1	-0.101	0.004	0.003	-0.104

This lift prediction discrepancy is also seen in the aerodynamics simulations performed on the same geometry by Forbes *et al.* (2014). They reported calculations undertaken with the same LB-VLES solver and two Detached Eddy Simulation [DES] methods; the latter gave lift coefficients of -0.166 and -0.132. One potential source of this discrepancy is that the wind-tunnel model mounting method is not fully represented by the CFD models. In the physical experiment the wheels have a flat lower edge and are supported on rods that pass through holes in the wind tunnel floor, which in turn connect to an underfloor force balance. To ensure that the balance reacts the full aerodynamic load by avoiding any dynamic contact between rods and the wind tunnel floor, the diameter of the holes exceeds that of the rods and there is a gap between the wheel flat and floor. This leaves an annular gap which allows some flow from the balance room into the wind tunnel test section, as the latter will be at a lower static pressure when the wind tunnel is running. This also prevents flow between the wheel flats and floor generating a strong negative pressure and hence a spurious negative lift component. In contrast, the CFD models have a simplified representation of the mounting arrangement, terminating the supporting rods at a solid floor. As a consequence, airflow in the gap between the wheel flat and floor generated a reduced pressure causing an additional negative lift contribution not present in the experiment. Calculations suggest that this accounted for up to 50% of the lift discrepancy. However, given the focus of this study is on aerodynamic drag, errors in lift force prediction are not a significant issue as long as base pressure distribution and rear wake structure are well represented by the numerical models.

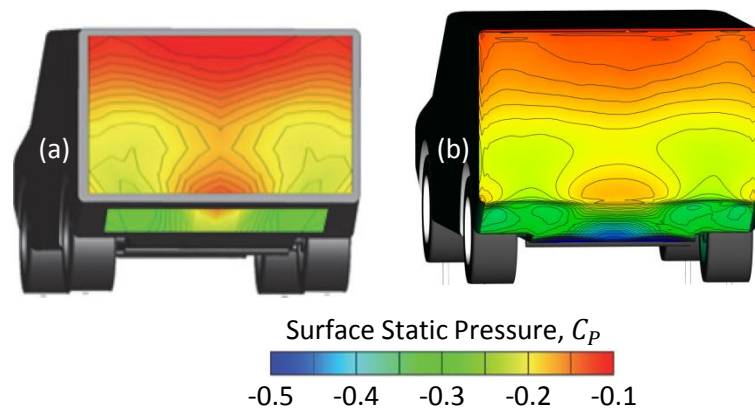


**Figure 38. Rear Surface Pressure Distributions for the Generic SUV (a) Measured by Forbes *et al.* (2014) and (b) Simulated by the Author**

The measured (a) and simulated (b) base pressures are provided in Figure 38, which shows excellent agreement. The pressure distributions have their highest levels in the upper third of the base and the centre of the lower part of the base. Two regions of lower pressure are seen in the outboard regions of the lower base – likely influenced by the trailing vortices shown in Figure 36. Given the correlation between high pressure and deposition demonstrated for the Windsor body, this raises the expectation that contamination will tend to accumulate higher on the base in this case.

The published data also enabled the credibility of the simulation method for recovering the time-averaged wake structure to be assessed. Figure 39 compares measurements of the streamwise [ $x$ ] velocity distribution made by Forbes *et al.* (2014) with the initial baseline numerical simulation. Overall, the simulations compare well with the experimental data; examining the velocity field and the  $y = 0$  centre-plane (a — b) reveals a strong up-wash due to the presence of the underbody diffusing surface, which is well captured by the numerical simulation. The  $y = 170$  mm plane is important in the context of this work, as it sits directly behind the rear wheel – the location of the spray. In this region, the initial simulation (d) provides a velocity distribution that closely corresponds to the experimental measurement (c). Finally the flow field in the horizontal  $z = 187$  mm plane (e — f) contains two clear lobes of low-to-negative  $x$ -velocity indicating the expected presence of a wake ring-vortex. Whilst the simulation appears to predict velocities which are lower than the measured values, the flow topology is well represented.

It is clear that the simulation approach used in this work provided an excellent numerical representation of the physical flow field at the rear of the Generic SUV, both in terms of the surface pressures and flow velocity distribution through the wake. The next step was to complete this novel simple rear surface contamination system by including a spray model that would reflect the generation of spray at the rear wheels.

In order to maintain comparability with the work conducted for the Windsor Body the same standard spray was used. Figure 40(a) provides a rear surface deposition pattern for the Generic SUV in a configuration which reflected the work done on the Windsor Body: no wheels and a central spray injection under the trailing edge of the geometry. This generates a deposition pattern that reflects the base pressure distribution, with the highest deposition in the region of highest pressure [Figure 38]. Offsetting the spray injector laterally to sit directly behind the outboard rear wheel position resulted in very low surface contamination [Figure 40(b)], and then adding the wheels generated an offset deposition pattern [Figure 40(c)]. This last configuration was used throughout this phase of the research as by only introducing spray from one wheel position the transport of material across the  $y = 0$  centreline was highlighted. It also aligned with the available experimental data (Kabanovs *et al.*, 2016b).

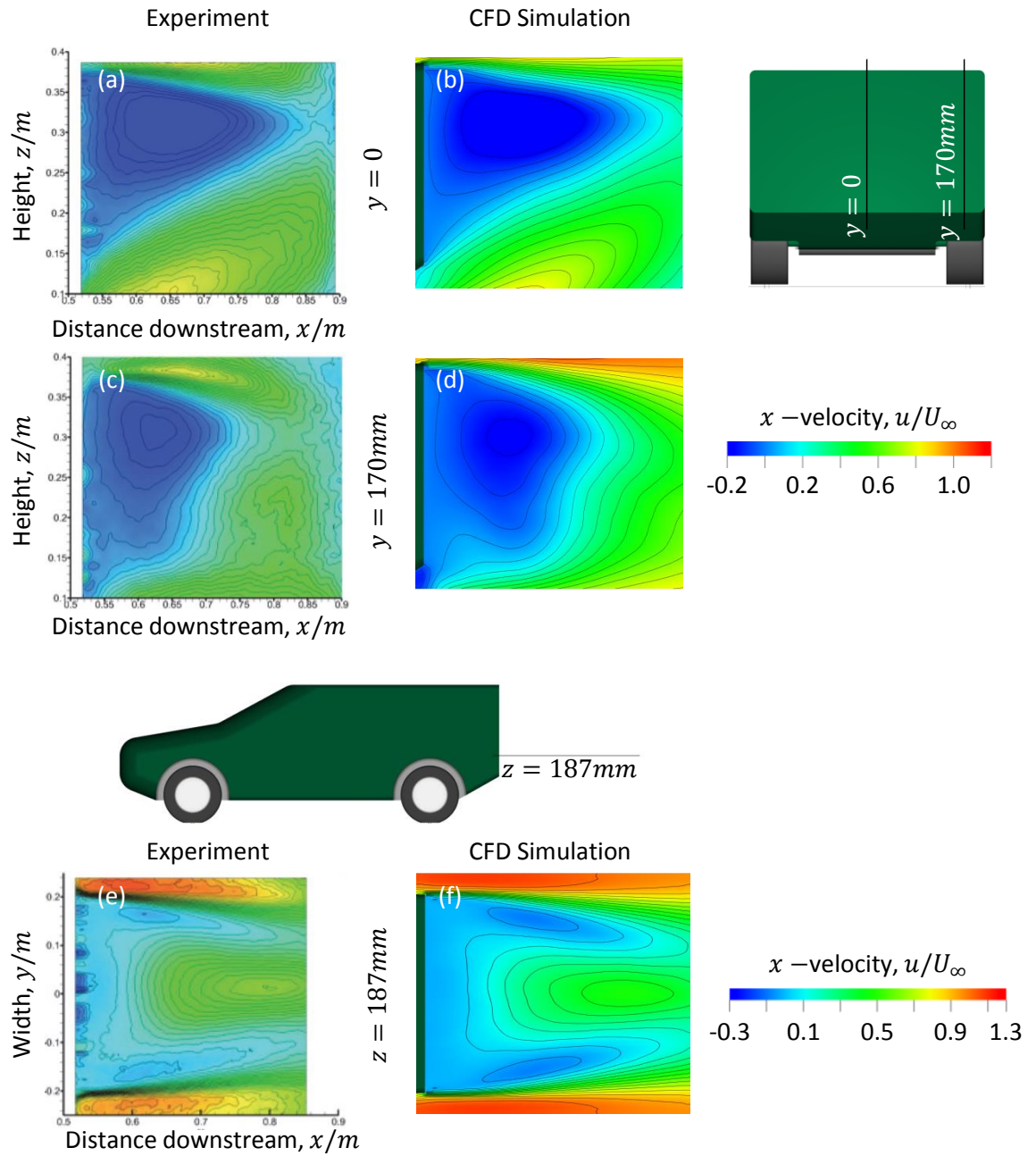


**Figure 39. Velocity Distribution through the Wake of the Baseline Generic SUV from Experiment (Forbes *et al.*, 2014) and Simulation for (a-b) the  $y=0$ , (c-d)  $y= 170$  mm and (e-f)  $z=187$  mm Planes**



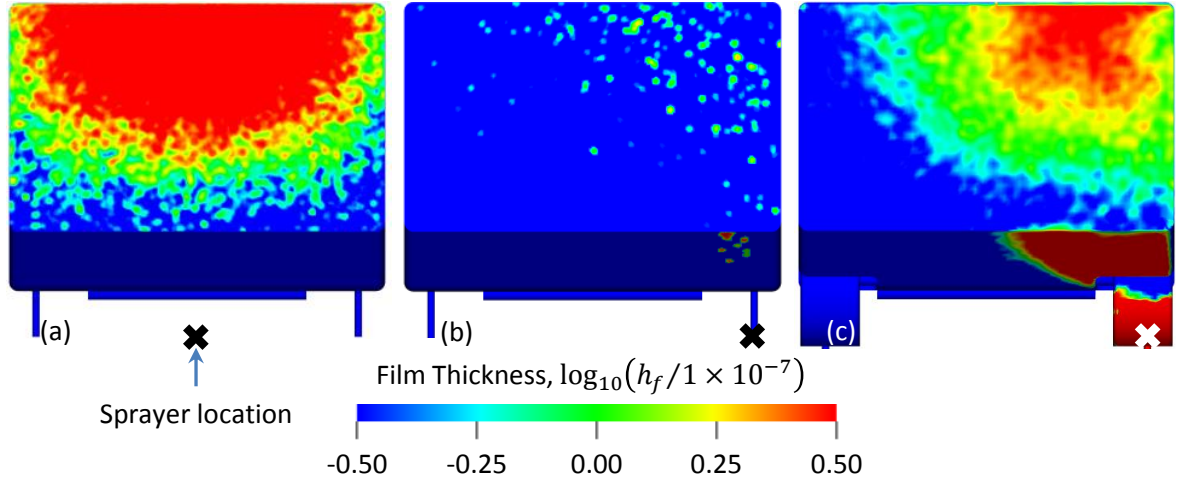


**Figure 40. Cumulative Rear Surface Deposition Pattern for the Generic SUV with (a) No Wheels and Central Sprayer Compared to a Laterally Offset Sprayer with (b) No Wheels and (c) Wheels Fitted**

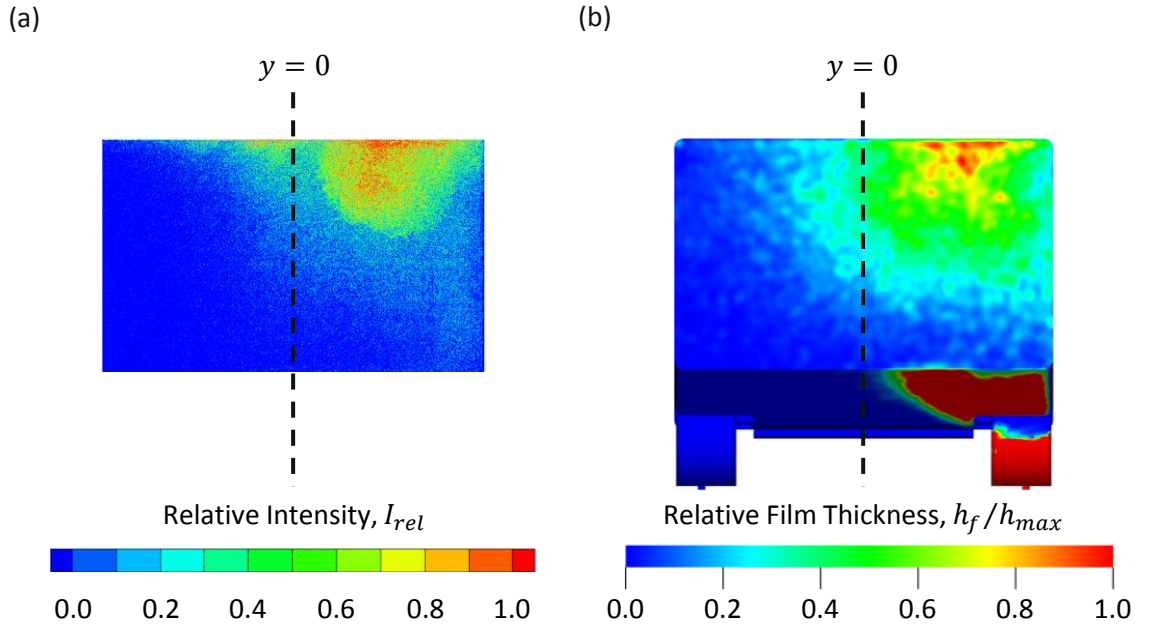


**Figure 41. Cumulative Rear Surface Deposition Patterns for the Generic SUV (a) Measured (Kabanovs *et al.*, 2016b) and (b) Simulated**

The final stage in confirming that the simulation approach could cope with the more realistic Generic SUV was to correlate the rear surface deposition patterns against experiment. This is illustrated in Figure 41 which contrasts the *relative* surface intensity distribution measured by Kabanovs *et al.* (2016b) with *relative* cumulative film thickness plot taken from the baseline simulation. The need for making a relative comparison emphasises a degree of incommensurability: no common units of measure are as yet available in the physical and numerical domains for this problem. However, scaling both intensity and film thickness by their maximum values reveals a good *relative* match for the deposition peak and overall distribution; though the simulation over-predicts the mid-range deposition region. This may be due to evaporation in the reduced-scale experiment, which is not a physical process that is included within the numerical model. However, the simulated surface deposition pattern is credible.

### 3.3.2 The Effect of Ground Clearance

Having developed a novel digital representation of the deposition of spray onto the rear surfaces of the Generic SUV, the next stage in building towards simulations for production vehicles was to undertake a series of original simulations to explore the effect of changing the ground clearance [ $h_g$ ]. This basic car shape has three standard settings: 50 mm, 65 mm [baseline] and 80 mm. Wood *et al.* (2015) published force measurements and wake flow streamlines for this complete set of ground clearances, providing an opportunity to ensure that the numerical simulation can predict drag force and surface contamination concurrently.

The force coefficients obtained using the numerical simulations are compared with the physical measurements by Wood *et al.* (2015) in Figure 42. The simulations show the expected trends of reducing drag with reducing ground clearance; along with the body without wheels fitted having the lowest overall drag were obtained (a). These match the physical experiments: the absolute values for the configurations with wheels differing from experiment by between -0.4% and -1.1%. The case with wheels removed is predicted less well, the numerical simulation differing from experiment by -6.2%. This is a larger discrepancy than that seen for the baseline Windsor body case; however, the Generic SUV effectively includes a diffuser which on which the boundary layer partially separates when wheels are not installed. The larger error likely results from the additional challenge of predicting flow separation due to the adverse pressure gradient on this surface. Given that this phase of the work is focussed on the cases for which wheels are fitted, this extra uncertainty is not relevant.

The degree to which the rear wake structure was captured by the simulation is summarised in Figure 43. This plots the centres of the ring vortex for each of the ground clearance and wheel fitment configurations investigated by Wood *et al.* (2015) extracted from either experiment or simulation. The comparison is generally good, with the differences ranging from  $5 \leq \delta \bar{x}_{RMS}(\%) \leq 10$  and  $5 \leq \delta \bar{z}_{RMS}(\%) \leq 7$  for the longitudinal and vertical directions, respectively. This typifies the degree to which simulation is capable of an accurate representation of rear wake structure for this geometry.

In terms of observations on the structure of the wake, the strong up-wash caused by flow attachment to the diffusing surface reduces the tendency of the ring vortex to tilt. Removing the wheels (b) causes the boundary layer on the diffusing surface to separate; these simple, solid wheels effectively act as “end-plates” constraining the flow laterally. In their absence the underbody exit flow velocity reduces, leading to the lower lateral arm of the ring vortex moving closer to the rear surface. Hence this configuration has the highest degree of ring vortex tilt on the  $y = 0$  centre-plane.



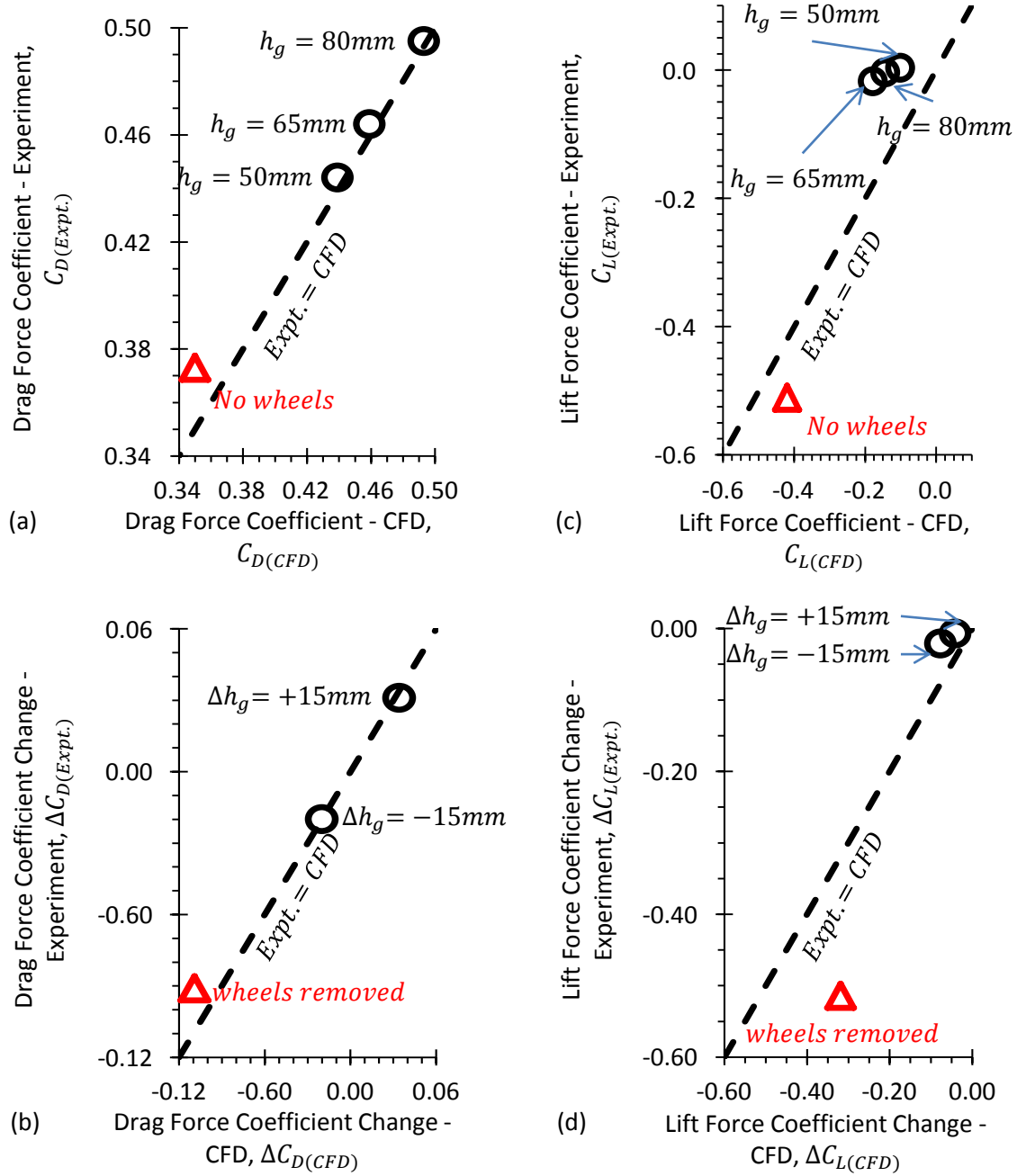
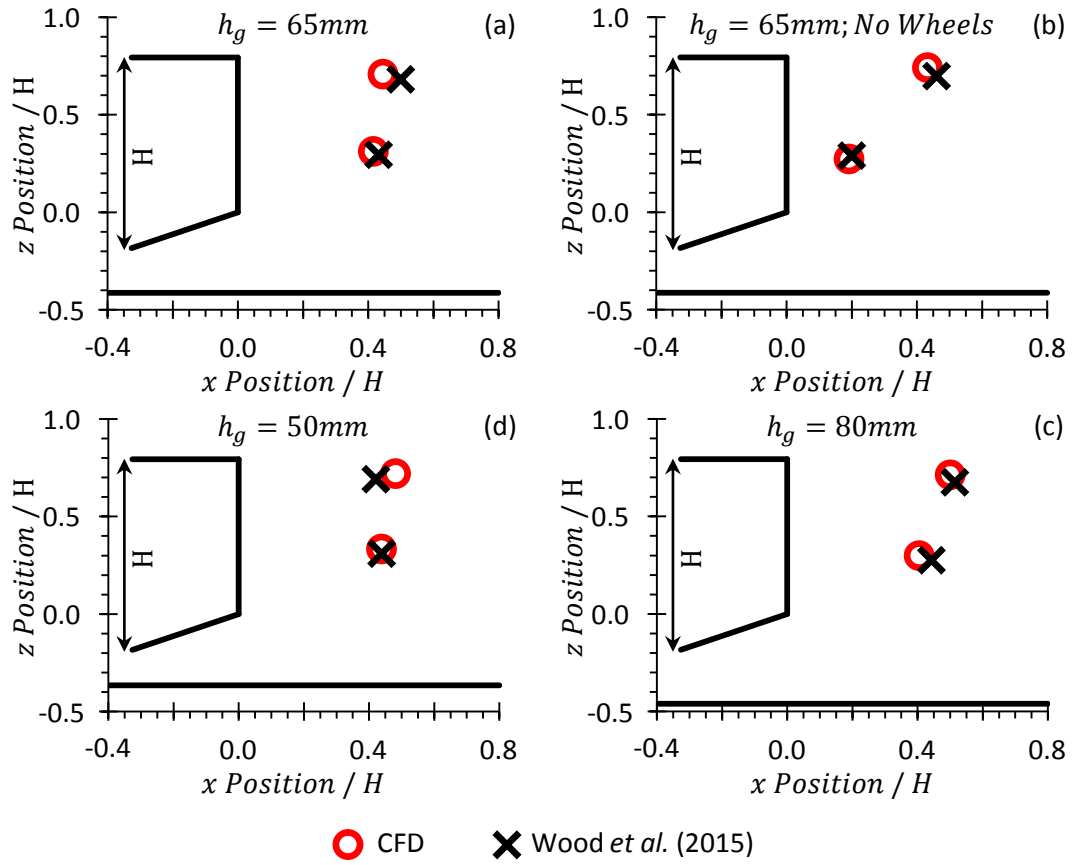
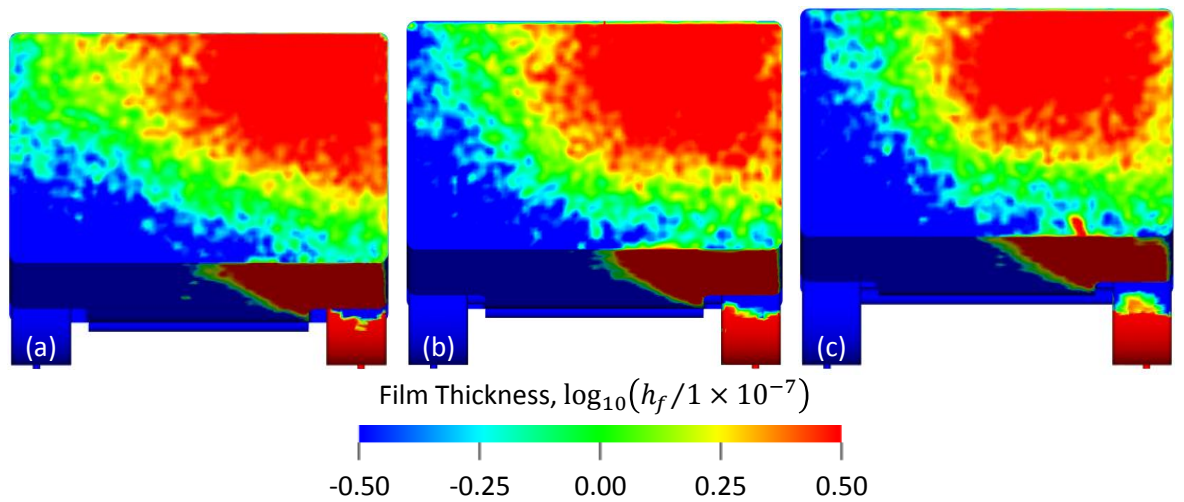


Figure 42. Drag and Lift Changes with Ground Clearance and Wheel Fitment for the Generic SUV: Absolute Changes in (a) Drag and, (b) Lift Coefficients; Changes from the Baseline for (c) Drag and (d) Lift Coefficients



**Figure 43. Measured and Calculated Ring Vortex Core Locations on the Centre Plane for the Generic SUV as Ground Clearance and Wheel Fitment Varies**



**Figure 44. Cumulative Rear Surface deposition Pattern for the Generic SUV at (a) 50 mm, (b) 65 mm [Baseline] and (c) 80 mm Ground Clearance**

To this point the author's work had produced a novel simple system that provided an excellent numerical representation of the aerodynamic forces, wake structure and rear surface deposition pattern associated with this basic car shape. This enabled a series of original simulations to be performed to examine the effect of vehicle ground clearance on the distribution of contaminant over the rear surface. The results are provided in Figure 44; this shows a clear trend for increased lateral and vertical spread of deposited material as ground clearance is reduced. It broadly aligns with the numerical findings for the Windsor body. In the case of the Windsor body, the increasing proximity of the lower lateral vortex arm to the spray source was suggested as the mechanism which lead to higher levels of deposition for lower ground clearances – with little change seen in ring vortex orientation. The same explanation holds here. Significant shifts in the pattern of deposition, with little change to wake orientation, point to the increased proximity of the rear surface to the spray emitter as a likely cause. In addition, in contrast to the Windsor body, the spray-laden wheel wakes present in this simple system provide an additional source of spray. Their role is reviewed in the following section.

### 3.3.3 The Role of Wheel Wakes

The deposition of spray on the rear surface and the changes seen with ground clearance depends on the influence of the wheel wakes, which is visualised in Figure 45. Initially, the spray injected from the wheel position interacts little with the wake ring vortex (a) and there is little deposition. Adding the geometry for the wheels draws spray inboard (b) to a position where the lower part of the ring vortex can turn it back towards the rear surface. Reducing ground clearance (c) results in the spray being drawn further inboard. This is being controlled by the length of the wheel wakes, shown from below and visualised by isosurfaces of zero total pressure coloured by Fluid Volume Ratio [*FVR*] in Figure 45(e – h). Moving from the baseline ground clearance  $h_g = 65$  mm (f) to  $h_g = 50$  mm (g) the wheel wakes lengthen and penetrate further inboard, advecting spray with them across the  $y = 0$  centre-plane. Conversely, increasing ground clearance to the maximum value  $h_g = 80$  mm (h) reduces their inboard extent. As a consequence, the degree to which the two rear wheel wakes interact and carry spray across the centre-plane increases as ground clearance decreases, and *vice versa*. These changes to the wheel wakes also influence the velocity of the flow emerging from the underbody, reducing it as ground clearance reduces.

The consequence of reduced underbody flow velocity, inboard penetration of the wheel wakes and the base wake being brought into closer proximity to the spray can be seen by comparing Figure 45(c) and (d), the lowest and highest ground clearances respectively. At reduced ground clearance, the spray plume has a generally larger volume and the fraction captured by the wake ring vortex is increased, leading to higher levels of deposition over the rear surface.

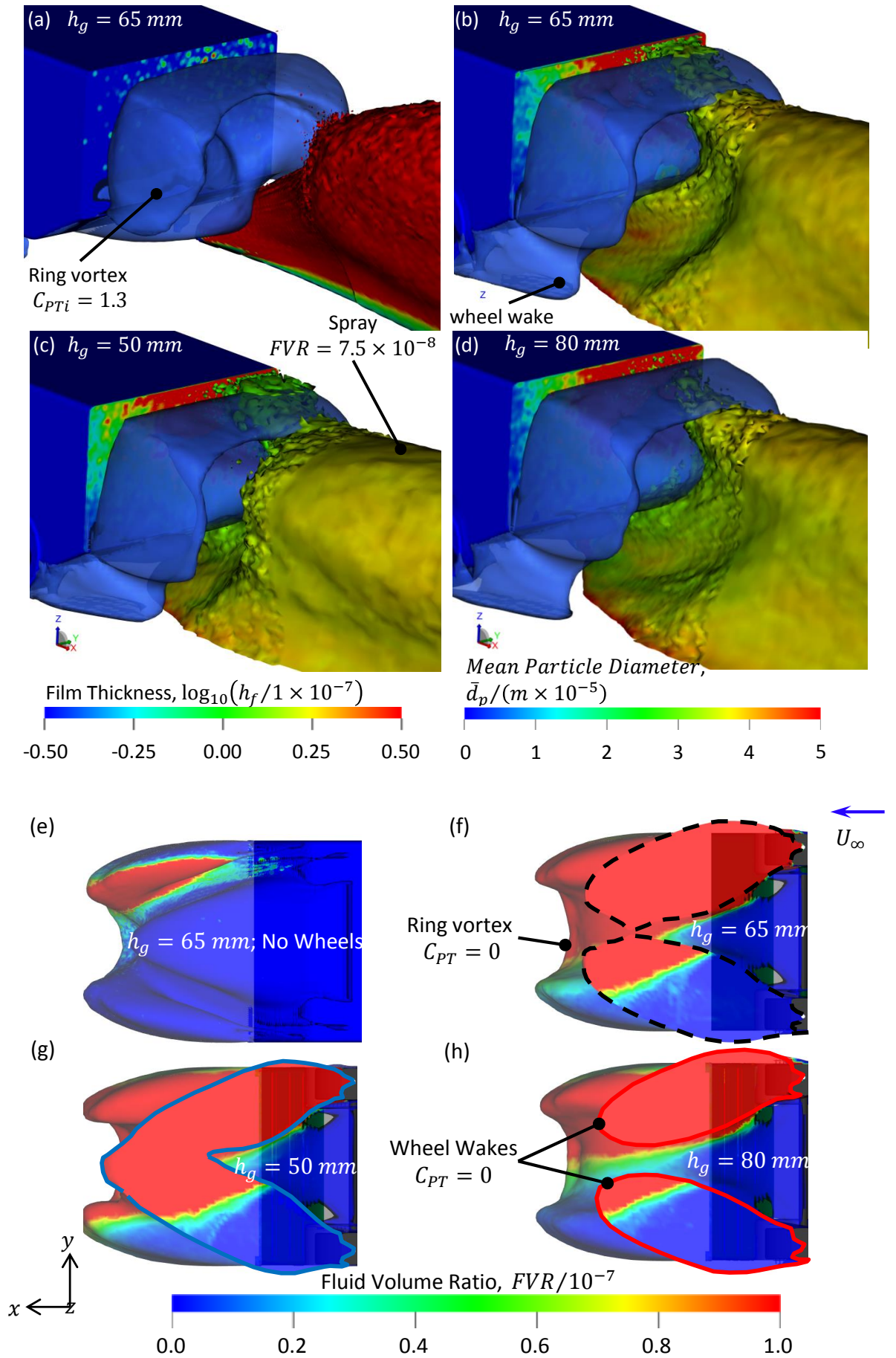
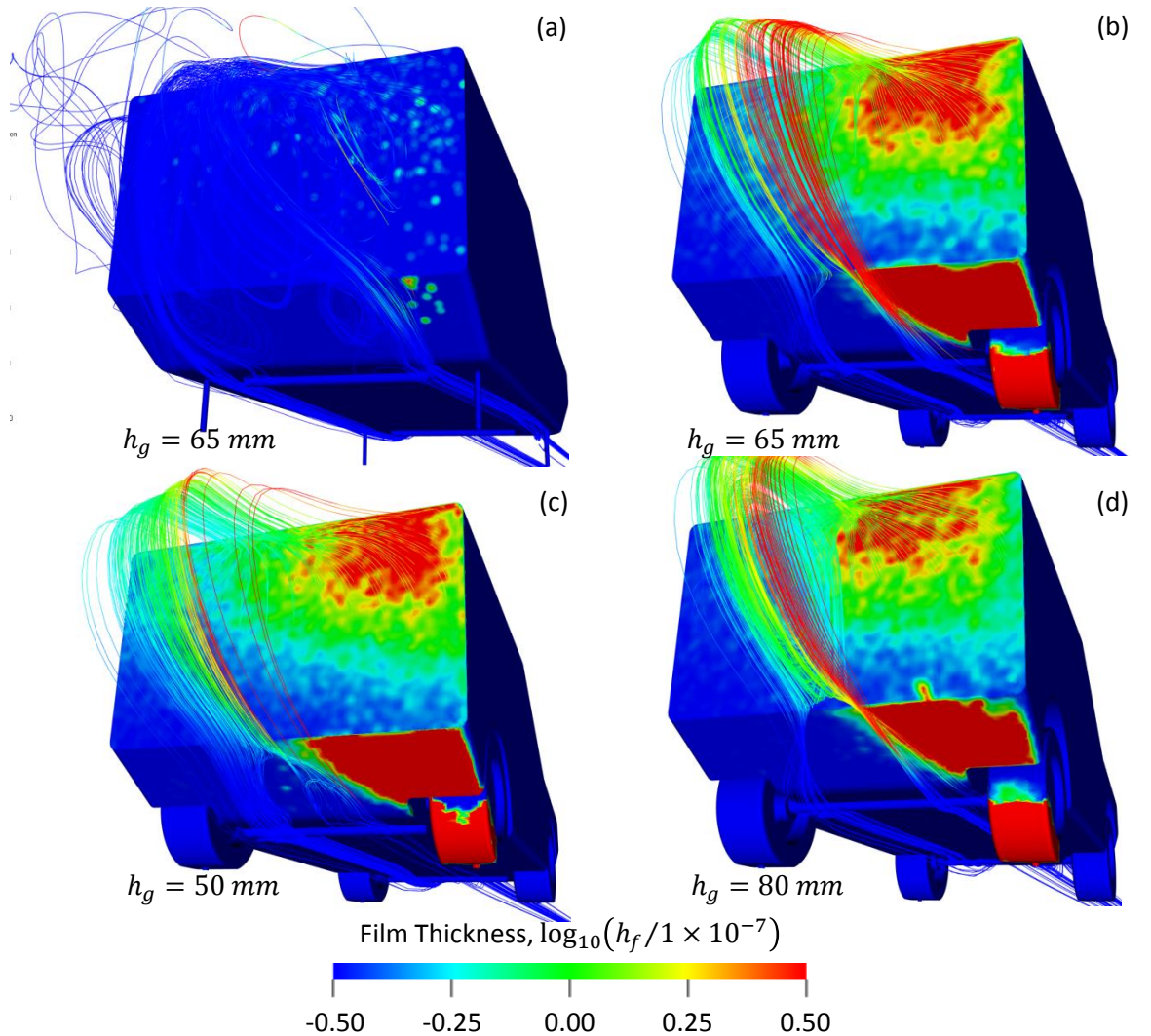


Figure 45. Generic SUV (a-d) Ring Vortex Interaction with the Spray Plume and (e-h) Wheel Wake Changes with Ground Clearance and Wheel Fitment

### 3.3.4 Underbody Flow

The literature makes the general suggestion that material deposited at the contamination peak on the rear surface of an SUV is associated with flow past the inside of the rear wheels (Jilesen *et al.*, 2013). Examining the flow field for the Generic SUV provides the first explicit numerical confirmation of this view. Figure 46 traces flow streamlines from this point *upstream* to examine their origin. For the cases with wheels (b – d), at each ground clearance setting, the flow providing the advection path [in the time-average] for airborne spray to the surface contamination peak passes by the inside of the rear wheels. Further, the imprint of the contaminated wheel wakes is seen on the angled diffusing surface downstream of the rear axle. The flow streamlines pass the inboard edge of this deposition zone, which is where they particularly start to advect spray, as shown by their colour change. This, once more, highlights the important role of the wheel wakes as an effective source of contamination and indicates that the simulation approach pioneered in this work can form the basis of a development process for production vehicles.



**Figure 46. Flow Streamlines Coloured by Fluid Volume Ratio Traced from the Deposition Maximum on the Generic SUV for Different Ground Clearance and Wheel Fitment Configurations**



### 3.3.5 Wake Unsteadiness

The Generic SUV showed no trace of the large-scale lateral wake unsteadiness seen for the baseline Windsor body. Given their similar proportions this might appear to be inconsistent. Figure 47 highlights this apparent discrepancy by plotting the position of both geometries, across the range of ground clearances used in this work, on the wake stability model of Grandemange *et al.* (2013). Both fall at the upper edge of the lateral  $y$  instability region, where intermittent switching between bi-stable modes may be expected. However, Perry *et al.* (2016) demonstrated that increasing up-wash in the wake of the Windsor body reduced bi-stability and shifted the location of maximum pressure fluctuation towards the top of the rear surface. The presence of the diffusing surface in the Generic SUV model provides a wake which has a high degree of up-wash; therefore, it should not be expected to behave in the manner indicated by the “Grandemange” model. Nevertheless, the presence of deposition on the opposite side of the rear surface to the spray indicates the potential for some lateral instability, likely akin to the more general tendency of SUV geometries to exhibit “wake flapping” (Al-Garni *et al.*, 2004).

An original approach has been developed using a series of correlated novel simplified systems for the concurrent numerical simulation of rear surface contamination and aerodynamic drag. The following chapter extends this work further, by developing the approach to simulate surface contamination on a production vehicle.

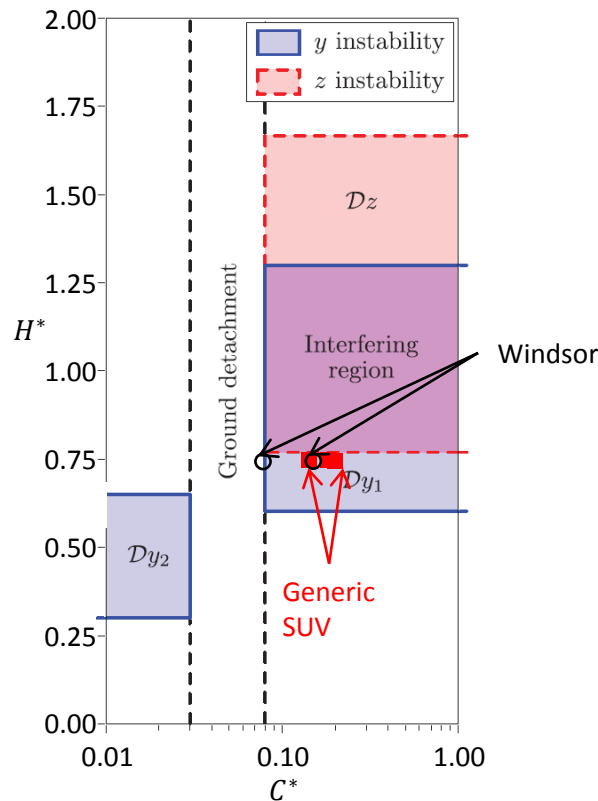


Figure 47. The Generic SUV and Windsor Body Compared against the Wake Stability Model of Grandemange *et al.* (2013)

## CHAPTER 4 SIMULATING REAR SURFACE CONTAMINATION FOR A PRODUCTION VEHICLE

### 4.1 SIMULATION DESIGN

#### 4.1.1 Lattice and Domain Design

This work charts the development and deployment of an innovative process for the engineering development of SUVs that enables rear surface contamination and aerodynamic drag to be addressed concurrently, by using unsteady numerical simulation. This has involved developing two simplified systems, based on two levels of simplified geometry: a simple body with no wheels and a basic car shape with wheels. In both cases the author's original numerical simulations have been validated using published experimental data for aerodynamic forces, wake topology and flow velocities, in addition to rear surface deposition. The final development of the simulation approach is described in this chapter, summarising the work detailed in *Portfolio Report C*: its application to a production vehicle, the 13MY Range Rover [See APPENDIX C].

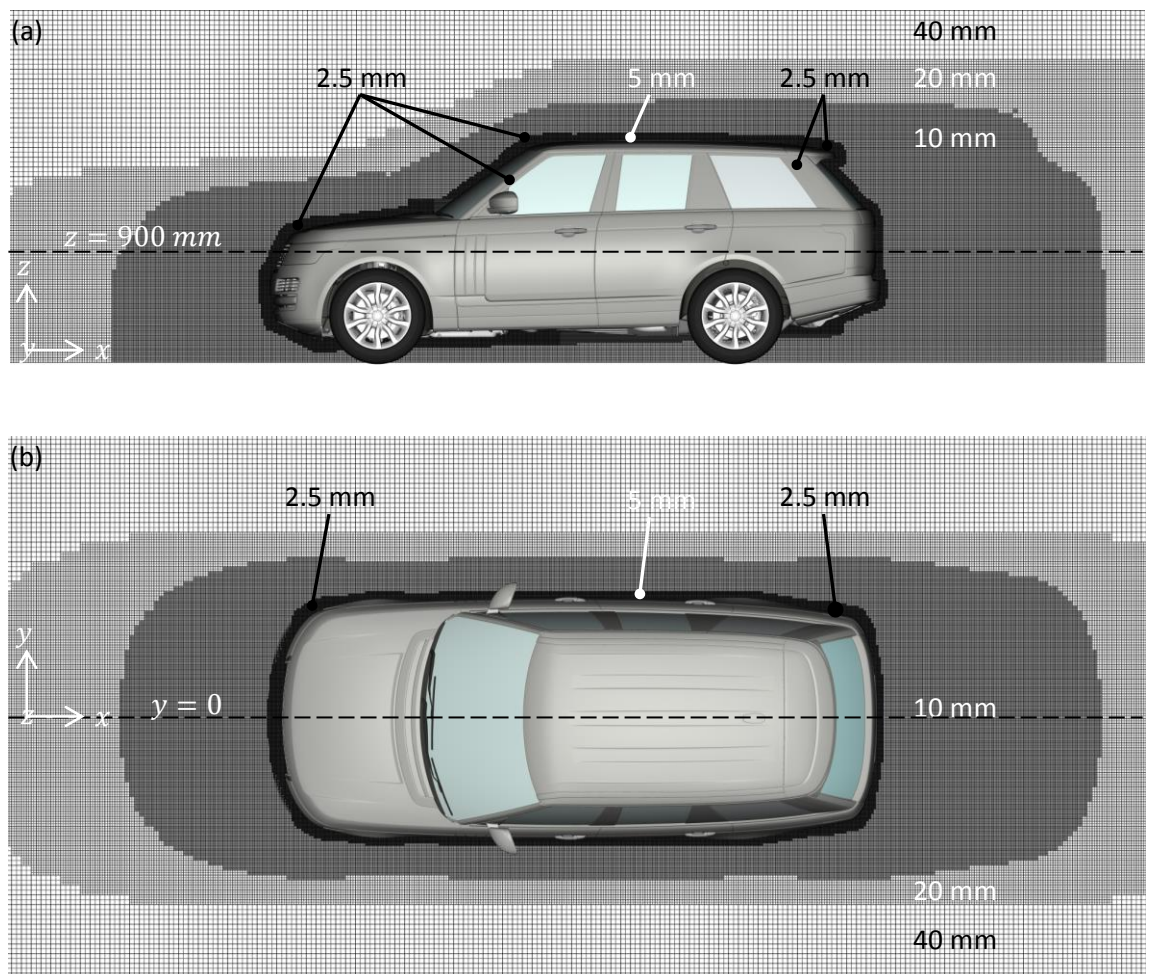


Figure 48. The Lattice Design Used for the 13MY Range Rover, Shown on (a)  $y = 0$  and (b)  $z = 900 \text{ mm}$

In contrast to the simplified geometries used so far, this complex digital model has a fully-detailed exterior surface and includes: a detailed underbody, engine bay with cooling flow paths, styled wheels, and tyres. Hence, the lattice designs used for the simple models discussed in CHAPTER 3 were taken as a starting point and modified to account for the additional geometric complexity. In this regard, the published literature on aerodynamic simulation for production vehicles was used as an additional guide to the resolution of the additional features.

The resulting lattice design is shown, for the region immediately surrounding the vehicle, in Figure 48. It shows that the bulk of the near wake zone at the rear of the vehicle is resolved by voxels with an edge length of 10 mm; with 5 mm voxels generally used to resolve the flow immediately adjacent to the vehicle surfaces. Exceptions to this are at the front corners, roof header, a-pillar, spoiler, rear-pillar and base surfaces where the smallest voxels [ $L_{Vx} = 2.5$  mm] are used. Away from the region immediately surrounding the vehicle, further nested resolution zones with reducing resolution were used to fill the complete domain. In total, the domain had overall dimensions of 122.9 m x 61.0 m x 51.0 m [length x width x height] resulting in a solid blockage [ $A/A_T$ ] of 0.1%, removing the need to correct forces and pressures for blockage effects. Within this, the vehicle was placed with its front  $28.4H$  downstream of the flow inlet, and its rear  $37.9H$  upstream of the outlet, minimising any interference between the vehicle body and flow boundaries. The use of ten nested variable resolution regions, the five finest of which are illustrated in Figure 48, enabled 53% of the voxels to be allocated to the finest scale with the five coarsest levels accounting for just 2% of the total. Hence, little computational effort is spent on calculating the flow furthest from the vehicle, with the simulation focussed on resolving the flow around the vehicle.

In order to match the boundary conditions of the test facility used for validating this work [FKFS TWT] the ground plane is fixed; however, upstream of the vehicle it is a slip-boundary, i.e. it does not allow the formation of a boundary layer. From 6.3 m upstream of the front of the vehicle this switches to a no-slip boundary condition, allowing the growth of a floor boundary layer matching the conditions in the test facility. Finally, in this work the inlet flow velocity  $U_\infty$  is set to 22.22 m/s [80 km/h] to match the test conditions. This is lower than typically used for aerodynamics simulations, though it reduces the near-wall resolution required by the boundary layer model.

In terms of building on the lessons from the simple systems discussed in CHAPTER 3, the wake resolution is comparable with that used for the two simple geometries featured in this work. Table 3 demonstrates this by comparing the number of the *largest* voxels spanning three key reference lengths through the near-wake, i.e. the fluid volume extending from the rear surfaces of the vehicle through to the wake closure point [see Figure 20(a) for a definition]. In each coordinate direction the lattice for the Range Rover provides higher levels of spatial resolution



than used for the Windsor body. Compared to the Generic SUV, resource constraints have led to a lower level of spatial resolution laterally [ $y$ ] and vertically [ $z$ ]; nevertheless, the Range Rover lattice provides more streamwise [ $x$ ] resolution. Overall, the lattice used for the production vehicle provides wake resolution within the range used for the simple systems, generally trending towards the higher end of this range.

**Table 3 A Comparison of Relative Spatial Resolution in the Near-Wake for the Windsor Body, Generic SUV and Range Rover**

Direction	Reference Length	Number of Voxels along Reference Length		
		Windsor	Generic SUV	Range Rover
$x$	Wake closure length	122	138	143
$y$	Width, $W$	97	170	144
$z$	Body height, $H$	72	157	129

Due to the additional complexity provided by this production vehicle geometry, the overall distribution of resolution and minimum voxel size were also guided by previously published studies which used the same solver for aerodynamics (Samples *et al.*, 2010) and rear surface contamination simulation (Gaylard & Duncan, 2011; Jilesen *et al.*, 2013; Gaylard *et al.*, 2014) for fully-engineered SUVs. As a consequence, this work used the same minimum voxel edge length as these previous engineering analyses.

In total, this baseline computational lattice comprised 153 million voxels and 41 million surfels. This *exceeds* the baseline mesh size used by Sterken *et al.* (2016) to investigate the aerodynamics of an SUV using the unsteady DES technique [140 million cells]. In addition, Sterken and colleagues conducted their work at a higher Reynolds number [ $Re_H = 3.67 \times 10^6$  compared to  $2.72 \times 10^6$  in this work] leading to the need for higher spatial resolution in the boundary layer. Nevertheless, they were able to predict the drag coefficient to within 2.1% — 3.2% of experiment, depending on the details of their mesh design. Given the additional physics embodied in the simulations undertaken for this work, the lattice design presented here provides credible levels of spatial resolution when compared to previously published work in the field of automotive aerodynamics.

The following section describes the contamination source used for these production vehicle simulations.

#### 4.1.2 Tyre Spray Model

The main difference between this full simulation and the simple systems described in CHAPTER 3 is the application of a more realistic representation of the rear tyre spray. This, as illustrated in Figure 49, includes detailed representation of the wheel and tyre. Overall, the model contains three main elements:

1. A representative wheel hub contained in a cylindrical “sliding mesh zone” [its outboard interface is shown by a broken line] which is subject to a geometric rotation about the axle at an angular velocity  $\omega_{wheel}$  matched to the translational speed of the vehicle.
2. An axisymmetric tyre with an angular velocity  $\omega_{tyre}$  appropriate to the translational speed of the vehicle applied as a boundary condition to its surface.
3. Thirty-five particle emitter boxes matched to the tyre width distributed uniformly around the circumference of the tyre.

The first two elements combine to provide a model of a rotating wheel and tyre system. However, only the central hub undergoes geometric rotation, whilst the tyre remains fixed but with a velocity applied to its surface, *modelling* rotation. This simplification is currently necessary

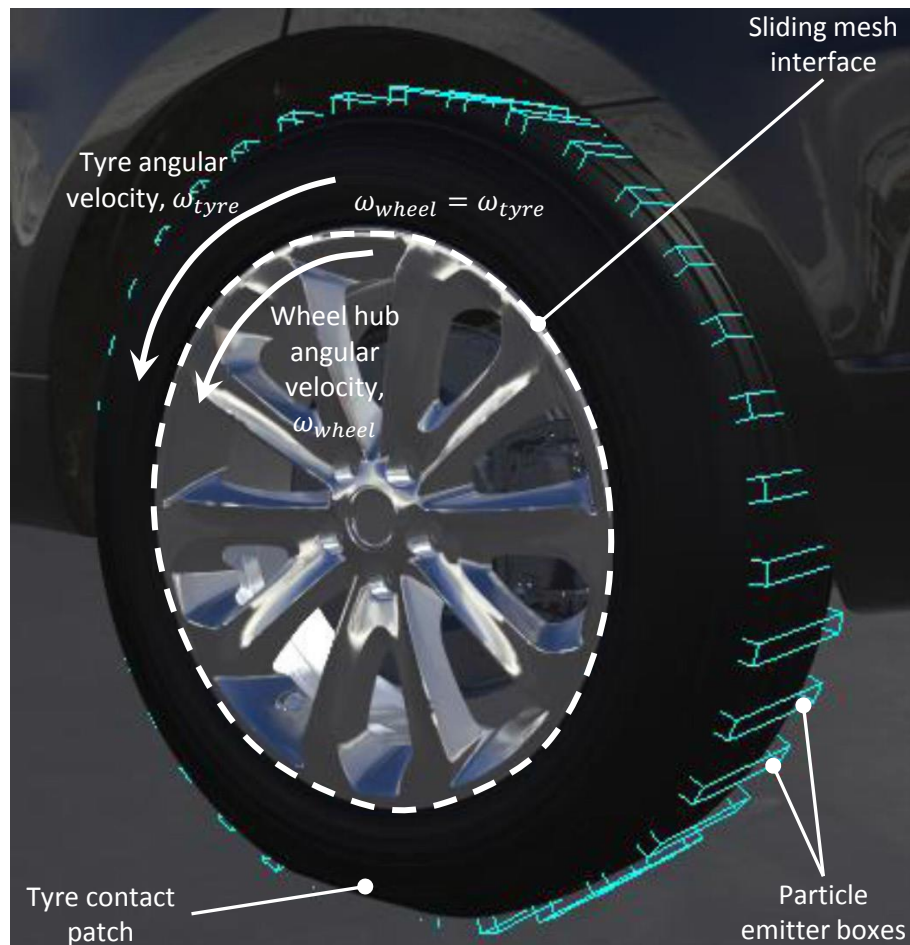


Figure 49. Tyre Spray Model

to resolve a conflict at the interface between the tyre and ground: capturing all the tyre within the cylindrical sliding mesh zone would also capture part of the ground and rotate that with the tyre (Schnepf *et al.*, 2015).

The third element – circumferentially distributed emitter boxes – models the release of spray from the tyres in the form of Lagrangian “virtual” particles with a diameter of 0.165 mm following the particle size calibration of Spruss *et al.* (2011). Their physical properties were set to those of plain water and they were released tangential to the tyre surface with a velocity distribution having a mean matching the rotational velocity of the tyre, and a standard deviation  $\sigma$  of 5 m/s. In addition, their direction is allowed to vary within a solid angle of  $10^\circ$ . Finally, the rate of particle release is set to match the standard flow rate used in the FKFS Thermal Wind Tunnel.

These elements combine to provide a model which represents wheel hub and tyre rotation, along with the release of droplets from the tyre surface. Although this is the current state-of-the-art, it has a number of limitations whose implications are currently unknown. These have been discussed by the author in a recent review (Gaylard *et al.*, 2017a) and include: the use of a monodisperse distribution, not accounting for side splash or bow wave effects or distinguishing between tread throw and capillary adhesion droplet release mechanisms (Weir, 1980). This highlights the need for further research to provide more complete tyre spray simulation.

The following sections describe the aerodynamic and rear surface contamination data extracted from original simulations with the vehicle set to a range of ride [trim] heights and the addition of an aerodynamically improved underfloor. This demonstrates the capability of the novel simulation approach developed in this work to concurrently calculate both surface contamination and aerodynamic drag for a production SUV over a range of vehicle configurations; an essential capability if this approach is to be used as a general vehicle development tool.

## 4.2 PREDICTED AERODYNAMIC FORCES

### 4.2.1 Variation with Trim Height

Reducing the clearance between the underside of the vehicle and road surface typically reduces aerodynamic drag, as the bodywork covers more of the face of the front tyre and also reduces the exposure of suspension arms to high-speed flow. Hence, manufacturers commonly provide dynamic ride height reduction for SUVs with four-corner air suspension; generally triggered once a steady cruising speed has been achieved. This drag-saving approach can also be exploited by building vehicles with permanently reduced ground clearance. The pressures on manufacturers to reduce drag for both ICE and BEV vehicles, discussed in CHAPTER 1, means that both of these approaches will be used more frequently on future vehicles. This will be more evident with BEV vehicles, where the adoption of this new propulsion technology requires customers concerns over range to be alleviated. Yet, its effect on rear surface contamination had never been determined. Therefore, ride height variation was selected as a key parameter to be investigated in this work. This was defined via the three trim height<sup>15</sup> variants defined in Table 4, denoted: “Low”, “Baseline” and “High”.

**Table 4 Vehicle Trim Height Settings**

Parameter	Description		
	Low	Baseline	High
Trim Height — Front, $h_{t,f} / mm$	$793 \pm 3$	$826 \pm 4$	$890 \pm 1$
Trim Height — Rear, $h_{t,r} / mm$	$789 \pm 4$	$843 \pm 5$	$895 \pm 1$
Vehicle Pitch (nom.), $\varphi / ^\circ$	+0.1	-0.3	-0.1

These were selected to match the trim heights obtained during the full scale experiments described in CHAPTER 5. As noted in *Portfolio Report D* the method of restraint available in the test facility offered limited precision for setting trim heights, which introduced commensurate variation in vehicle pitch angle  $[\varphi]$ , calculated as:

$$\tan(\varphi) = \frac{h_{t,f} - h_{t,r}}{Wb}$$

**Eqn. 26**

where  $h_{t,f}$  and  $h_{t,r}$  are the front trim and rear heights respectively, and  $Wb$  is the vehicle wheelbase.

Hence, as the simulation models were set to the nominal trim heights used in the experiments, their pitch angles differ as a consequence, falling in the range  $-0.3 \leq \varphi(^{\circ}) \leq +0.1$ .

<sup>15</sup> the usual measure of ground clearance; see APPENDIX C, Figure 96(a)

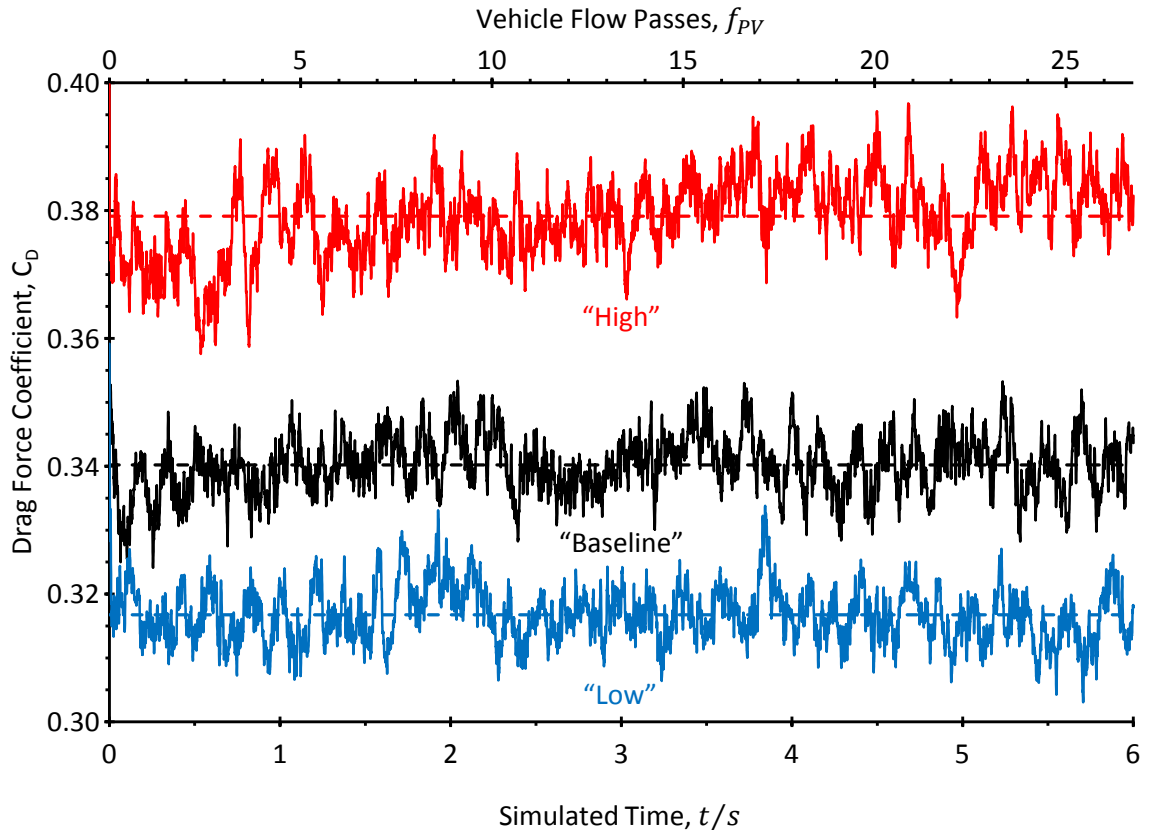


**Figure 50. Drag Force Coefficient Histories for High, Baseline and Low Trim Heights [Mean Values Shown as Broken Lines]**

The predicted drag coefficient histories for each of the three trim heights are presented in Figure 50; the corresponding histories for side and lift force coefficients are provided in Figures 51 and 52. The mean values have been determined using the author’s original “receding average” technique (Gaylard *et al.*, 2017b) and are shown as broken lines.

As expected, reduced trim height is strongly associated with reduced drag. The comparison between the mean force coefficients extracted from the time-histories and their measured counterparts is provided in Table 5 and illustrated in Figure 53. At the Baseline trim height drag is predicted to within 3.1% of experiment, which matches the accuracy achieved by Sterken *et al.* (2016); the High configuration is predicted to within 0.5%.

**Table 5 A Comparison of Measured and Simulated Drag and Lift Force Coefficients**

Configuration	Drag Force Coefficients				Lift Force Coefficients			
	$C_{D(CFD)}$	$\pm 95\%$	$C_{D(WT)}$	$\Delta(\%)$	Lift, $C_L$	$\pm 95\%$	$C_{L(WT)}$	$\Delta$
High	0.379	0.005	0.377	0.5%	0.155	0.013	0.143	0.012
Baseline	0.340	0.002	0.351	-3.1%	0.119	0.014	0.129	-0.010
Low	0.317	0.002	0.337	-5.9%	0.130	0.006	0.168	-0.038

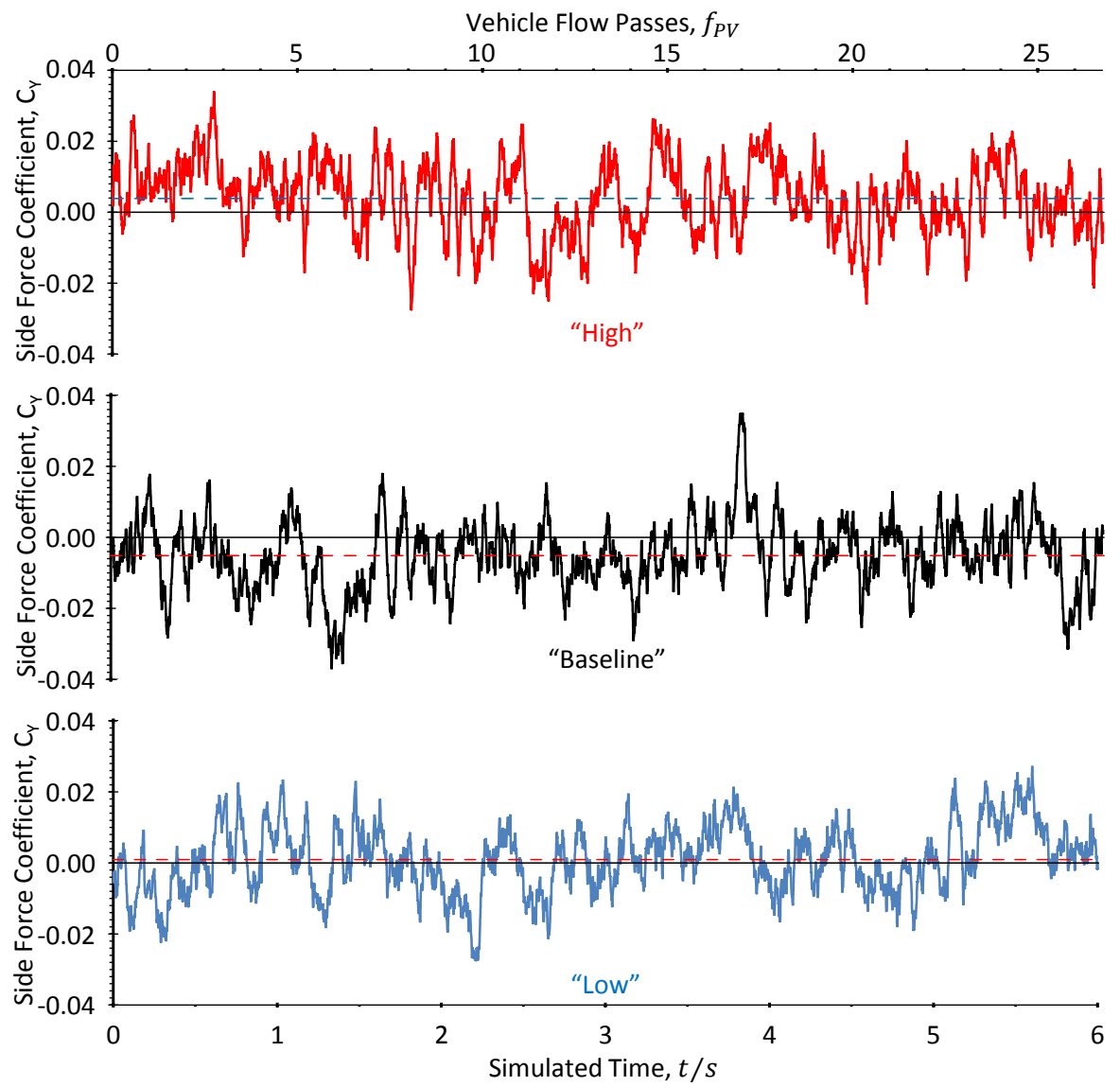


**Figure 51. Side Force Coefficient Histories for High, Baseline and Low Trim Heights [Mean Values Shown as Broken Lines]**

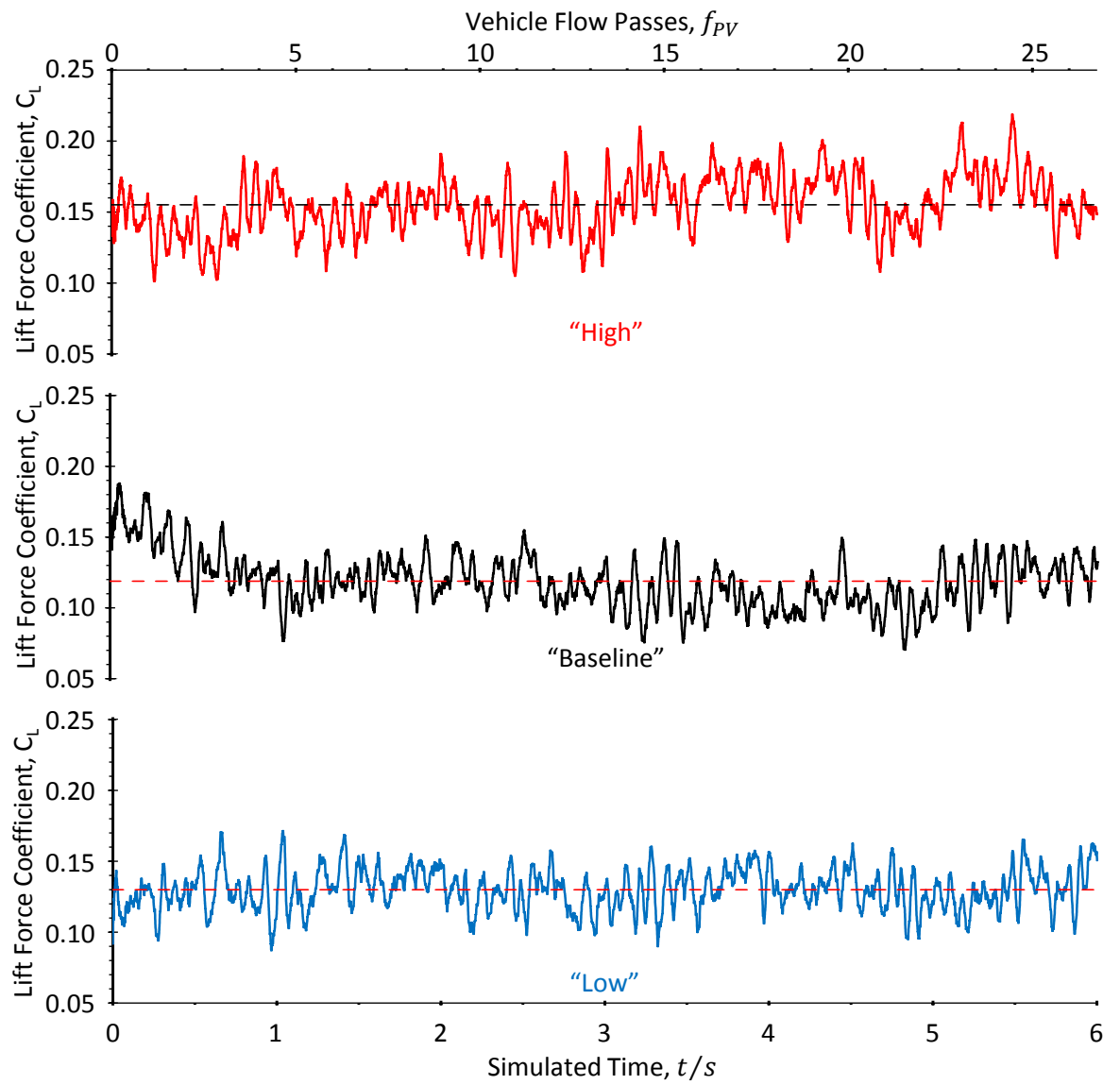


**Figure 52. Lift Force Coefficient Histories for High, Baseline and Low Trim Heights [Mean Values Shown as Broken Lines]**

As is typical for CFD simulations, lift coefficients are more poorly predicted than drag (Duncan *et al.*, 2010) with differences between simulation and experiment from +8.4% to -22.6%. However, the *absolute* differences are comparable to the range of 0.022 to 0.035 [ $\Delta C_L$ ] reported by Sterken *et al.* (2016), confirming that the lift predictions are within a typical tolerance.

The results show a trend towards higher lift values with increasing vehicle pitch angle. This is particularly marked for the experimental results, where the highest pitch angle [Low trim height] corresponds to the highest lift value, and the lowest pitch angle [Baseline trim height] aligns with the lowest lift measurement. This is consistent with full scale wind tunnel measurements reported by Bonnavion *et al.* (2019) who associated this trend with a vertical wake [ $z$ —] instability: a change in wake-state characterised by a shift in the base pressure gradient from positive [rising pressure with increasing  $z$ ] to negative [falling pressure with increasing  $z$ ]. This trend is also seen in the simulation results, with one exception: the Low trim height case, the only “nose-up” [ $\varphi = +0.1^\circ$ ] configuration. It also exhibits the poorest agreement between experiment and simulation. Deviation from the relationship between pitch and lift could indicate an error in the prediction of base pressure gradient. Nevertheless, a difference between simulation and measurement for drag of -5.9% is tolerable in this context — comparable to the accuracy obtained by Kremheller (2014) obtained during the development of the Nissan Qashqai SUV.

Finally, it is notable that the confidence interval associated with the lift coefficient for the lowest ground clearance is around half of that estimated for the other cases. This suggests the presence of the ground is suppressing unsteadiness normal to it; a result which is consistent with the suppression of turbulence normal to the road surface reported by Wordley and Saunders (2009).

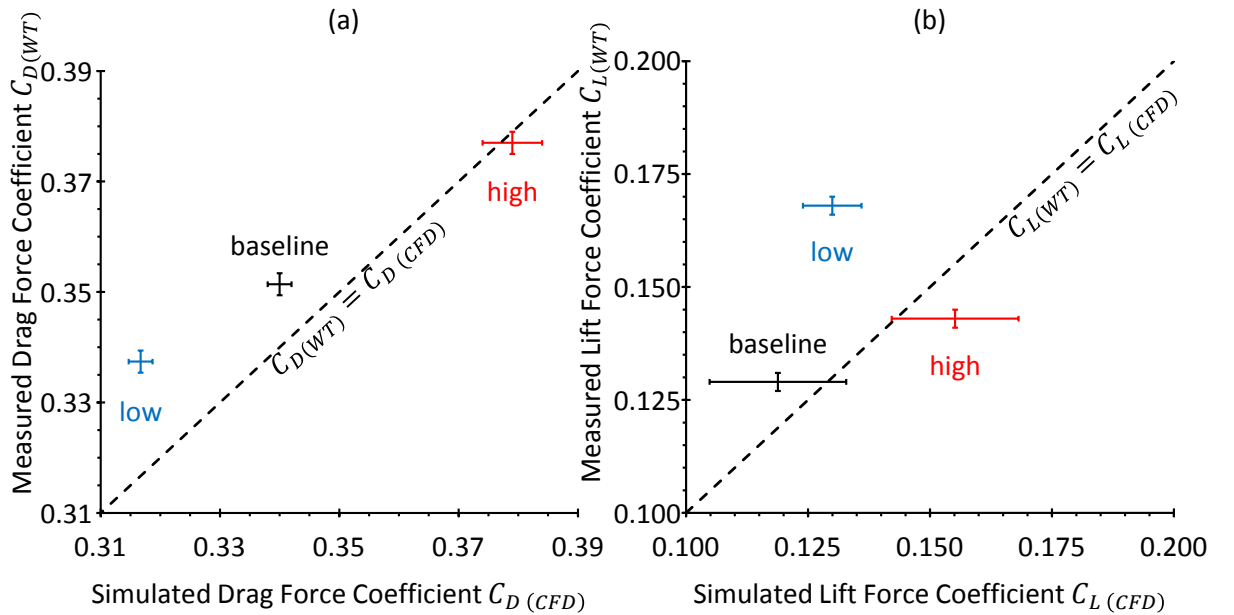


**Figure 53. Correlation between Measured and Simulated (a) Drag and (b) Lift Coefficients at Low, Baseline and High Trim Heights**



#### 4.2.2 Improved Underfloor

As previously noted in CHAPTER 1, vehicle underfloors have become smoother and more continuous as manufacturers have sought to reduce vehicle drag. BEVs provide an opportunity to take this further, as they don't include rough underbody components required for an ICE drivetrain. Although the effect of underfloor improvement on aerodynamic drag was well known (Sapnaras & Dimitriou, 2008), its implications for rear surface contamination had not been previously explored. Therefore, a large central undertray was designed for this work that could be retro-fitted to a production Range Rover whilst maintaining its ability to be used in full-scale confirmatory physical tests. This covered over a central area of the underfloor, including the transmission tunnel, a section of the exhaust run and the front of the saddle fuel tank<sup>16</sup>. Hence, it provided a smooth, largely continuous underfloor from the chin to the rear axle and would be expected to provide a reduction in aerodynamic drag (Sapnaras & Dimitriou, 2008). The drag coefficient time history for this modification is shown, along with that for the baseline in Figure 54. In addition, the effect on the time-averaged force coefficients is shown in Table 6.

**Table 6 Simulated Mean Force Coefficients for Baseline and Improved Underfloor cases.**

Configuration	Mean Force Coefficients					
	Drag, $C_D$	$\pm 95\%$	Side, $C_Y$	$\pm 95\%$	Lift, $C_L$	$\pm 95\%$
Baseline	0.340	0.002	-0.005	0.004	0.119	0.014
Improved Underfloor	0.336	0.002	-0.005	0.009	0.155	0.013
Difference (Improved Underfloor)	-0.004	0.003	0.000	0.009	0.036	0.019

As expected, the addition of the undertray reduced the drag coefficient, in this case by  $\Delta C_D = 0.004$ . The 95% confidence interval, a function of the natural unsteadiness of the flow and simulation length, spans  $-0.001 \leq \Delta C_D \leq -0.007$  providing strong evidence that this drag reduction is signal and not noise. In addition, Samples *et al.* (2010) were able to capture a drag change of the same size on an SUV, using a lattice with the same minimum voxel edge length used in this work, but half the total number of voxels. This provides some confidence that the drag reduction seen here is credible. Physically, this modest but significant reduction is attributable to reduced losses associated with underbody irregularities.

On the other hand, the increase in lift coefficient is unexpected as the reduction in separated flow associated with the inclusion of the undertray would be anticipated to reduce underbody pressures and hence lift (Sapnaras & Dimitriou, 2008). The implication is that although the undertray may reduce pressure and commensurately increase velocity locally, this more energetic flow interacts with downstream geometry to create increased pressure and lift.

<sup>16</sup> See APPENDIX C, Figure 96(c) for details

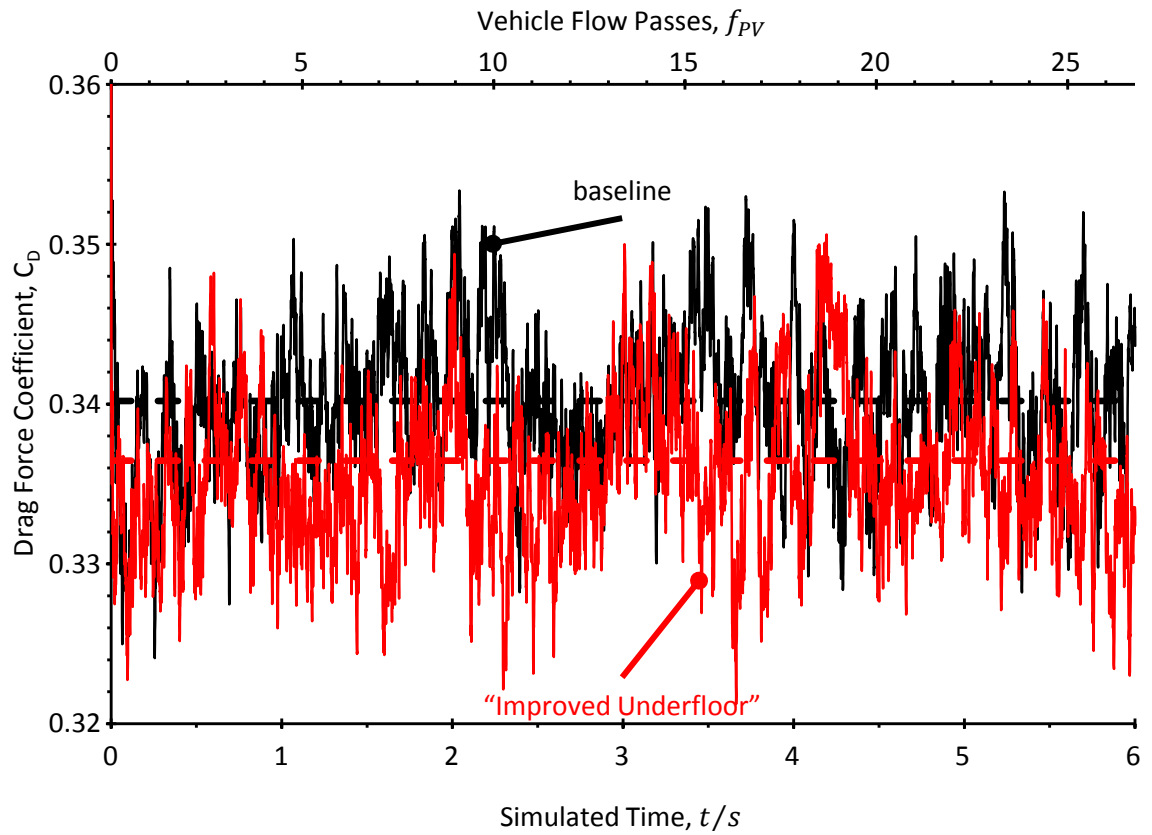


**Figure 54. Drag Force Coefficient Histories for High, Baseline and Low Trim Heights [Mean Values Shown as Broken Lines]**

The following section presents the first digital assessment of the effects of trim height and underfloor changes on rear surface contamination. This is important in its own right – given the trend towards reduced trim height and smooth underfloors, particularly apparent for BEVs. However, the main aim of this work is to provide an innovative vehicle development process. In this context, it is important to be able to reliably predict rear surface contamination changes for different vehicle configurations.

## 4.3 PREDICTING REAR SURFACE CONTAMINATION

### 4.3.1 Baseline

The following sections present the rear surface contamination results obtained for the Range Rover in its baseline condition and then explore these to demonstrate that the simulation approach captures a period of time long enough to provide data that are comparable with experiment, before presenting the first comprehensive description of the deposition mechanism.

The rear surface contamination results for the Range Rover in its baseline configuration are summarised by Figures 55 and 56. These result from seeking to match the approach typically adopted in physical experiments using the FKFS TWT, in that the spray model is applied to the rear wheels only, though all four wheels are modelled as rotating over a fixed ground. The cumulative rear surface contamination distribution [Figure 55] shows a concentration of deposits towards the centre of the rear surfaces – with little lateral deposition over the rear lamps. There are three local peaks: [1] at the centre of the rear bumper, [2] the tailgate and [3] a more diffuse region of elevated deposition over the rear screen. The general pattern on the essentially vertical tailgate is similar to that seen for the Windsor body with an underfloor flow restriction, discussed in CHAPTER 2 [Figure 33(c)]: an approximately radial distribution biased towards the top of the body. This implies a similar main deposition mechanism is at work: a tilted wake ring vortex.

The calculated deposition histories for each of the main rear surface zones are shown in Figure 56. To correct for the size differences between surface zones, these plot the cumulative *area density* of contaminant [ $\rho_A$ ] against time, rather than mass:

Eqn. 27

$$\rho_A(t) = \frac{M(t)}{A_{zone}}$$

where  $M(t)$  is the cumulative mass of contaminant deposited by time  $t$ , and  $A_{zone}$  is the area of the rear surface zone.

The plots demonstrate that as the simulation progresses, deposition quickly becomes linear with respect to time. A regression analysis returned a *minimum* coefficient of determination [ $R^2$ ] of 0.98, indicating that at most, only 2% of the variation in the time histories is not explained by a linear model (See *Portfolio Report C*: 60). This aligns with the observations made using the simple Windsor body, reported in CHAPTER 2 [Figure 32]. They also show that the highest level of contamination is found at the licence plate, followed by the tailgate and rear bumper. In comparison the rear screen has a modest level of contamination, whilst deposition on the rear lamps is very low. The latter observation suggests, at least for this vehicle, that contamination of the rear lamps is unlikely to be a significant issue.

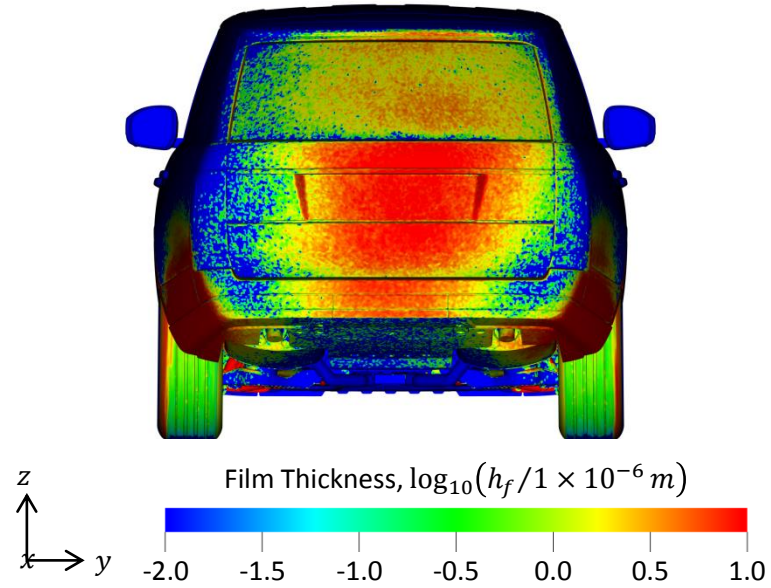


Figure 55. Predicted Cumulative Rear Surface Contamination Distribution for the Baseline 13MY Range Rover

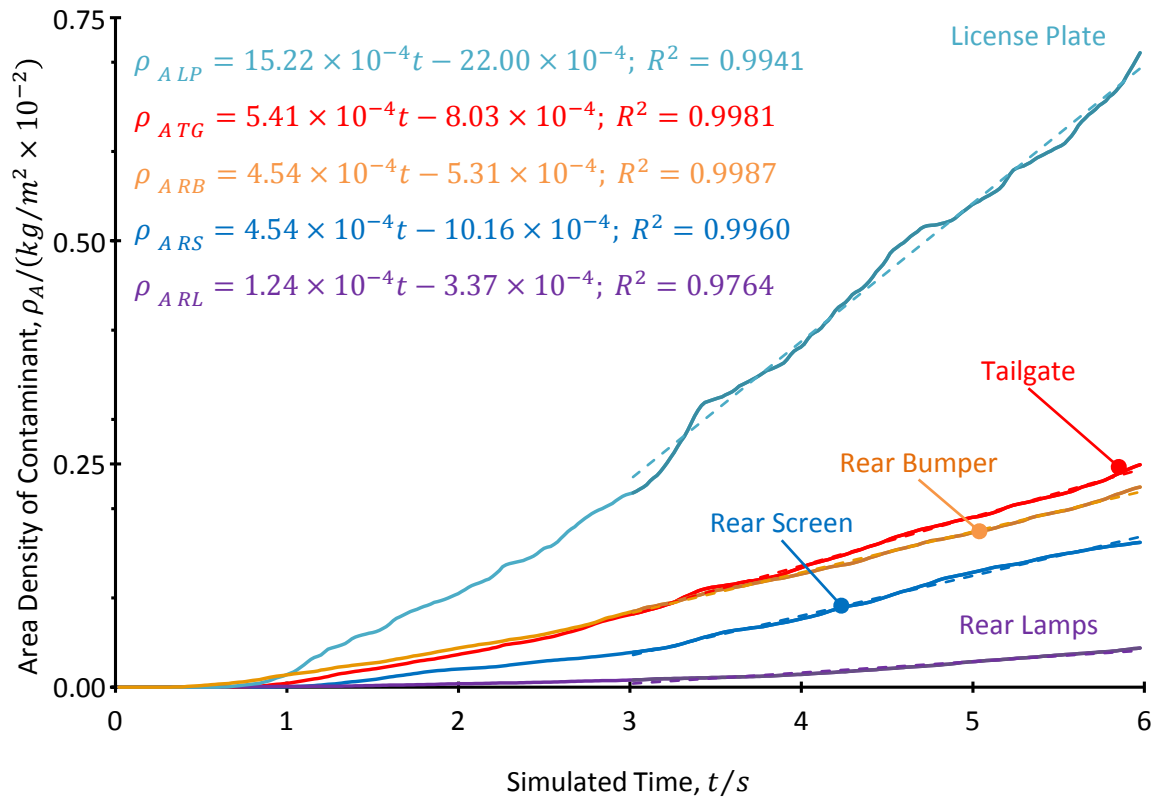


Figure 56. Simulated Deposition History for the Baseline 13MY Range Rover

### 4.3.2 Can Numerical Simulations Capture Enough Time?

As the aim of this work is to establish a simulation process that informs product development decisions, it is important to ascertain whether the numerical representation of this issue is appropriate. One of the main contrasts between numerical simulation and physical tests is that the former typically capture a few seconds of flow time, whilst the latter several hundred. Hence, it is appropriate to question whether numerical simulations can adequately describe this problem.

Here, the novel analysis approach demonstrated using the Windsor Body in CHAPTER 2 and subsequently published by the author (Gaylard *et al.*, 2017b) is extended to assess the predicted accumulation of contaminant over the rear surfaces of the Range Rover. This seeks to establish whether or not the *relative* distribution of contamination over the rear surfaces is a function of the time period simulated, by taking profiles of surface film depth at specific times through the simulation and dividing each by its own maximum. A collapse of these *relative* profiles onto a single curve would indicate that the *relative* distribution of material over the surface is time-invariant, with deposition over a longer period just adding to its depth proportionately. Figure 57 presents this original analysis; it starts with extracting surface film depth along the  $y = 0$  line (a) and a lateral line through the peak film depth (e) every half-second from  $t = 0$  s to  $t = 6$  s. In an extension to the process used for the Windsor Body, a moving [spatial] average is applied to reduce the “noise” present in the film depth caused by the increased geometric complexity of the production vehicle surfaces (b, f). Next, the relative film thickness  $\bar{h}_f / \bar{h}_{f_{max}}$  is plotted for each profile (c, g). Aside from some early time data, the profiles collapse onto a single curve; focussing on the last third of the simulation (d, h) confirms this outcome. This aligns with the behaviour of the rear surface contaminant distribution seen for the simple system based on the Windsor body [Figure 25], providing evidence that this is a general result and not specific to this vehicle.

Hence, for the first time, the relative time-invariance of the rear surface contamination distribution has been confirmed for a fully-detailed vehicle. Taking this evidence, along with the linearity with time of deposition for the main surface zones shown in Figure 56, it is warranted to consider the results of the simulations presented in this work as indicative of *relative* deposition distributions and trends that could be obtained from longer time periods typical of physical tests.

Having demonstrated that the time period simulated is long enough to provide results that do not depend on its length, the following section takes time-averaged flow fields from the simulation and uses them to provide the first comprehensive description of the aerodynamic mechanisms responsible for rear surface contamination. This exemplifies a key advantage from integrating simulation into vehicle engineering development processes: deep insight into the underlying reasons for a particular outcome.

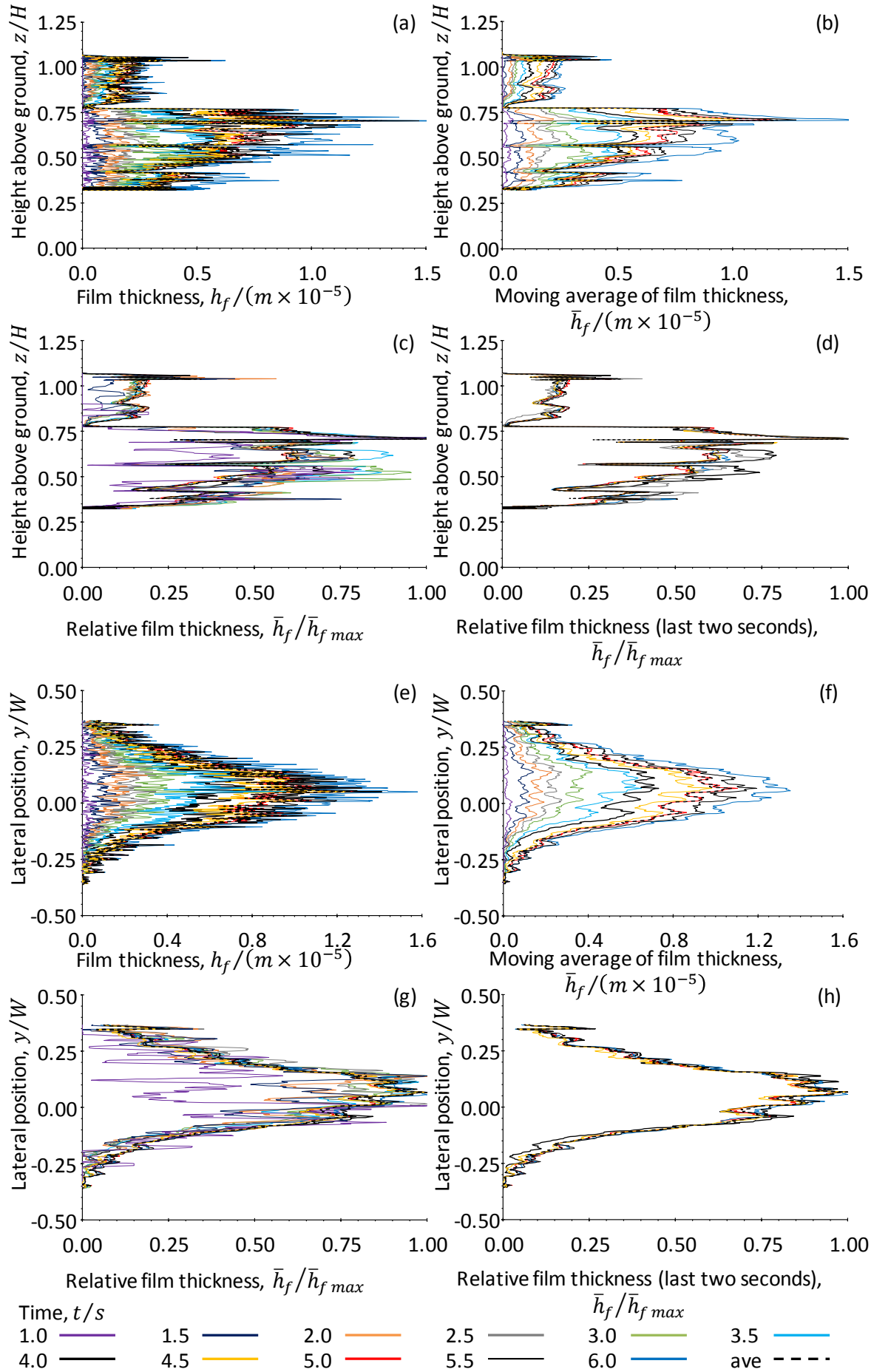


**Figure 57. Film Thickness on  $y=0$  (a) Absolute, (b) Moving Average and Relative for the (d) Complete Run and (e) Last Two Seconds; Along with Film Thickness on a Horizontal Line (e) Absolute, (f) Moving Average and Relative for the (g) Complete Run and (h) Last Two Seconds**

### 4.3.3 Rear Surface Deposition Mechanism

Previous research has identified some elements of the overall surface deposition process, but a complete three-dimensional description is not provided in the published literature. The first hint at a mechanism was provided by Maycock (1966) who remarked that, “The estate type of body tends to draw the spray-laden air into the region immediately behind it.” Other workers made broad suggestions of the importance of unsteadiness (Goetz, 1971) and the wake structure (Lajos *et al.*, 1984). In contrast, Costelli (1984) sketched droplets following two-dimensional streamlines along the  $y = 0$  centre-plane through the wake of a hatchback car. This was followed by Morelli (2000) implicating both the wheel wakes and “lower transverse vortex” in rear surface deposition. Similarly, Jilesen *et al.* (2013) deduced that contaminant was, “drawn up from the wheel wake and back towards the rear of the vehicle”.

Here, for the first time, a comprehensive description of the aerodynamics mechanisms responsible for rear surface contamination is presented. Figure 58 identifies the wake ring vortex and spray core from the rear right wheel by using isosurfaces of total pressure loss [ $C_{PTi} = 1.1$ ] and spray concentration [ $FVR = 1 \times 10^6$ ], respectively. In common with the analyses presented in CHAPTER 2 for both the Windsor body [Figure 27] and Generic SUV [Figure 45] rotation in the lower part of the wake vortex captures a fraction of the rear tyre spray and reverses its velocity, turning it back towards the rear of the vehicle (a) – shown by a change in the colour of the spray isosurface from red [ $u > 0$ ] to blue [ $u < 0$ ]. Cutting the wake isosurface on the  $y = 0$  plane (b) shows this spray fraction is caught in the return flow through the centre of the ring vortex. Overall, the aerodynamic advection mechanism can be described as: the rear wheel wakes are drawn inboard by the vehicle wake, carrying spray laterally (c) to where the lower lateral arm of the ring vortex can lift a fraction of the spray upwards (d) and back to the rear surfaces (e). Rotation in the upper lateral ring vortex arm can then draw spray upwards and over the rear screen at an oblique angle, before any remaining spray is advected away from the vehicle by the upper free shear layer. The role of the rear wheel wakes is further emphasised in Figure 59, which provides a view of their flow streamlines from the underside. This shows the outboard part of the horseshoe vortex which forms in front of the tyre contact patch remaining uninvolved with the rear wake whilst its inboard fraction and the trailing vortices formed behind the tyres are drawn into the outboard arms of the wake ring vortex (a); once entrained, this fluid can cross the  $y = 0$  centre-plane. Colouring these streamlines with spray concentration (b) shows the wheel wakes transporting contaminant into the vehicle wake, through the mechanism shown in Figure 58(c – e). Thus, the intensity and distribution of contaminant over the rear surfaces is controlled by the degree of interaction between wheel wakes and base wake along with the orientation of the ring vortex. If the latter structure is vertical, deposition will be concentrated in the centre of the rear surfaces; tilting it backwards shifts deposits towards the rear screen.



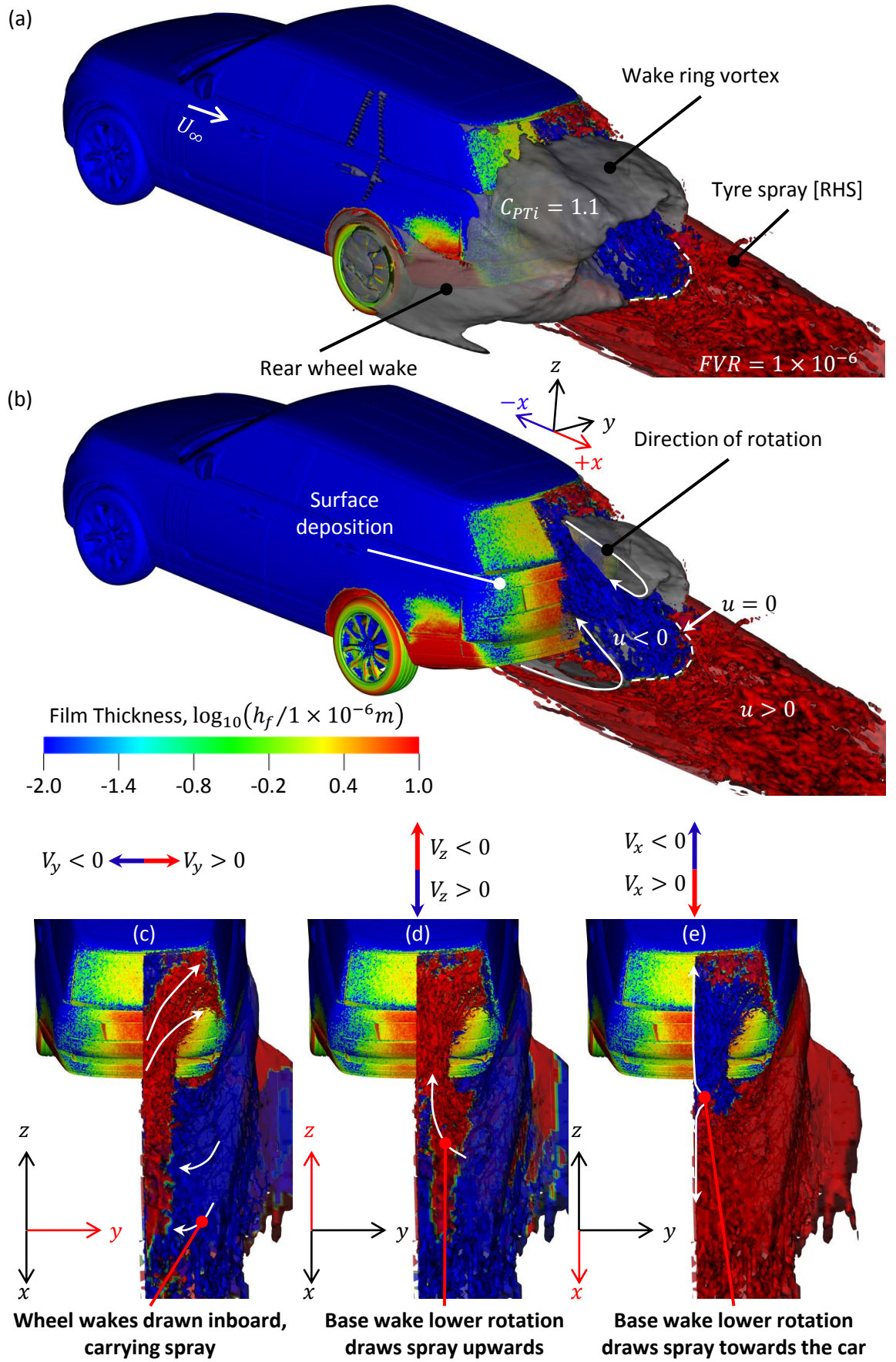
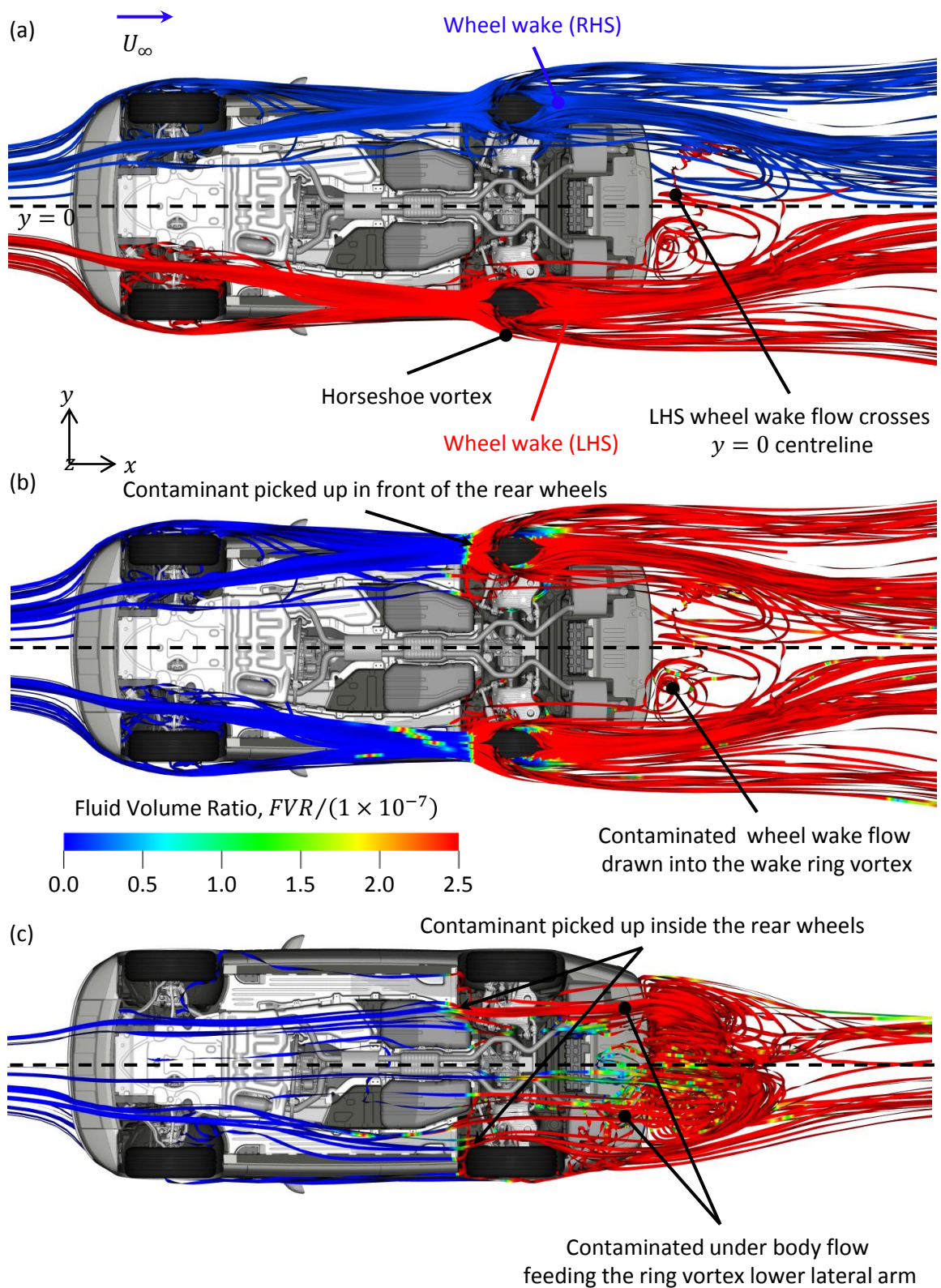


Figure 58. Rear Surface Deposition Process: (a) Wheel Wake and Ring Vortex Interaction, (b) Spray Capture by the Ring Vortex and its Effect on the Spray in the (c) Lateral, (d) Vertical, and (e) Streamwise Directions





**Figure 59. The Influence of Wheel Wakes as Shown by Flow Streamlines Tracked Upstream and Downstream from the Wheels Coloured by (a) the Release Location (b) Fluid Volume Ratio; Along with Streamlines Tracked Upstream and Downstream from the (c) Contamination Peak Coloured by Fluid Volume Ratio**

As discussed in *Portfolio Report B*, the best results for both rear surface contamination and aerodynamic drag are likely when the wake ring vortex has minimum tilt in the  $xz$  plane. Wake structures where the lower lateral ring vortex arm is placed close to the rear surface, or wraps up onto it, are likely to be associated with both high levels of drag and surface contamination.

The literature also contains some commentary on where the material deposited at the rear surface contamination peak originates. Gaylard and Duncan (2011) identified, “droplets exiting the rear underbody under the rear bumper”. This was followed by Gaylard *et al.* (2014) who observed that this material passes, “through the region close to the inboard face of the rear wheels”. In Figure 59(c) streamlines coloured by spray concentration [*FVR*] are traced *upstream* from the rear deposition peak. These can be seen to pick up contaminant inboard of the rear wheels before emerging from the underbody under the rear bumper and being entrained into the lower lateral arm of the ring vortex. This provides the first coherent explanation of these observations. It is also instructive to note that this process can be seen in the results obtained for the Generic SUV [Figure 46], suggesting that this is a general result and not a characteristic of this particular production vehicle.

#### 4.3.4 Correlation With Static Pressure

This original simulation work also provides an opportunity to explore the role of the rear surface static pressure distribution in surface contamination. This is important: as noted in CHAPTER 1 these surfaces are a major contributor to vehicle drag, hence reducing drag requires increasing the overall pressure on the rear surfaces [base pressure].

In his study of rear surface contamination on a small hatchback car Costelli (1984) asserted that deposition preferentially occurred in regions of relatively high base pressure. The author demonstrated this computationally along two cut-lines through the base of the Windsor body [See Gaylard *et al.*, 2017b and also Figure 28] discovering that not only did the surface pressure need to favour deposition but material had to be locally available. To extend these two-dimensional analyses static pressure and film thickness data was sampled from the four most contaminated surfaces in the baseline simulation and plotted against each other to uncover the degree of correlation between these two parameters. The resulting correlation plots are shown in Figure 60, along with the result of a correlation analysis based on the Pearson Product-Moment Correlation Coefficient  $r_p$  (Rodgers & Nicewander, 1988), in the form:

$$r_p(\text{degrees of freedom}, n - 2) = \text{correlation coefficient}, p > \text{significance level}, \alpha$$

**Eqn. 28**

where  $n$  is the number of points sampled on the surface and hence the number of  $(C_p, h_f)$  pairs.

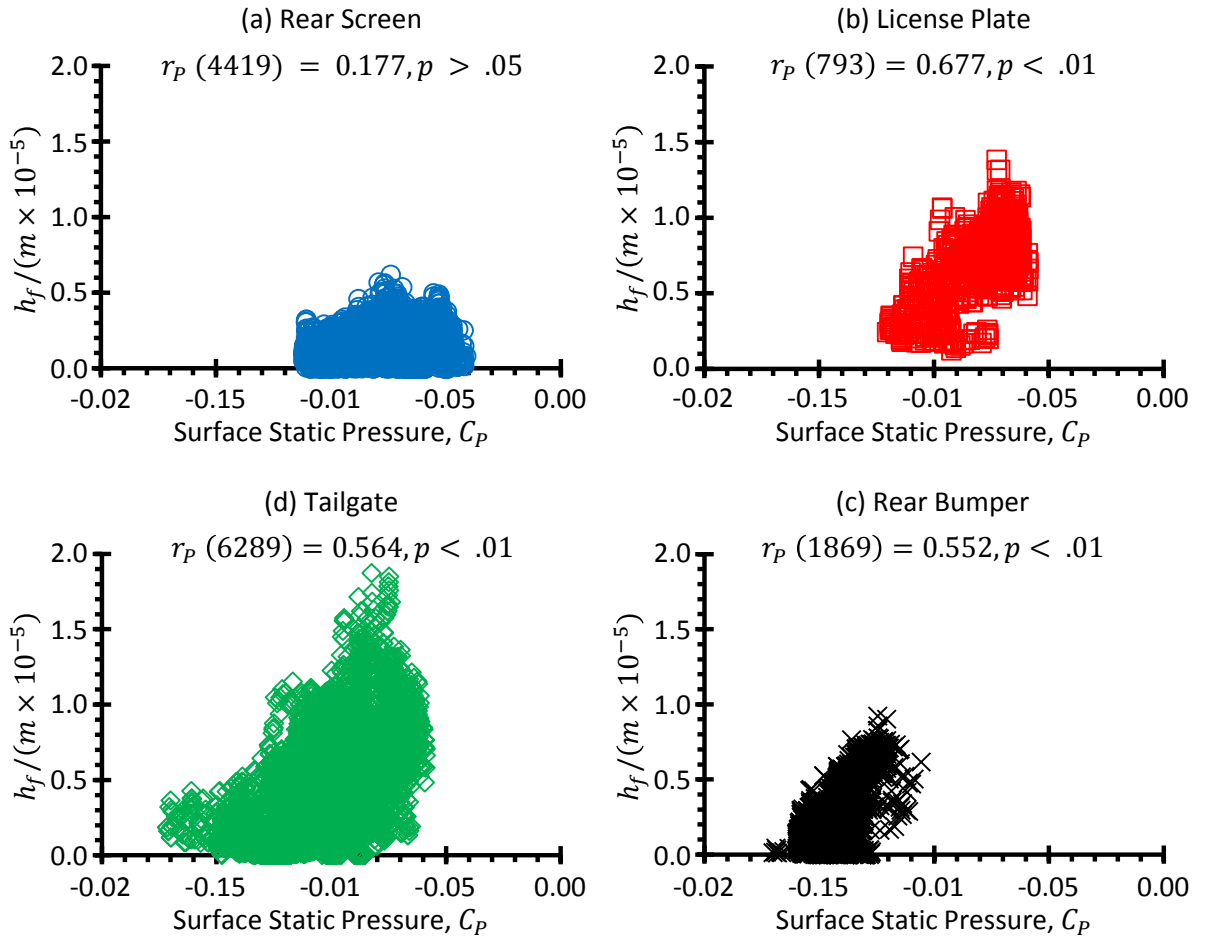


**Figure 60. Correlation Plots for Static Pressure and Film Thickness on the Rear Surfaces of a 13MY Range Rover: (a) Rear Screen, (b) Licence Plate, (c) Tailgate and (d) Rear Bumper**

All four correlation coefficients are positive, indicating a trend towards thicker surface deposits at higher base pressures. However, the correlation coefficient calculated for the rear screen does not reach significance at the 5% [ $\alpha$ ] level, hence there is insufficient evidence to reject the null hypothesis of no correlation. Conversely, in descending order of the strength of the relationship, the licence plate, tailgate and rear bumper produce correlation coefficients that are significant at the 1% level, providing strong evidence to reject the null hypothesis and assert correlation between pressure and film thickness. For the first time, this provides a three-dimensional surface zone based computational confirmation of the author's extension to Costelli's hypothesis.

The physical basis of the correlations between deposition and surface pressure is shown in Figure 58(b), the return flow path to the rear surfaces is predominantly via the centre of the wake ring vortex, which drives the bulk of the returning spray directly towards the tailgate. In contrast, the lack of correlation over the rear screen arises from only a fraction of this returning spray being advected over the screen, at an oblique angle. Some of this material is then deposited as the flow draws it past the inclined rear screen with a sub-fraction transported to the upper shear layer, where it is lost downstream.

Overall, the simulations conducted on a full-engineered SUV align well with the extension of Costelli's hypothesis derived by the author from analysis of deposition on the rear of a simple bluff body. This again supports the research strategy used in this work and also suggests that this novel observation has general validity. From a vehicle development perspective, this suggests that the key to reducing rear surface contamination without increasing drag is limiting the local availability of contaminant, rather than modifying the local pressure field. It also indicates that success may be more attainable for regions, like the rear screen, where correlation between deposition and pressure is already poor.

#### 4.3.5 The Effect of Trim Height

As discussed at the beginning of this chapter, trim height reduction is a frequently used drag-reducing technique for SUVs fitted with air suspension. Therefore, it is important that the engineering process based on the simulation approach developed here is able to capture its effect on surface contamination. In this work, vehicle pitch also changes with trim height [see Table 4] which adds an additional aerodynamic influence that the simulation approach needs to capture.

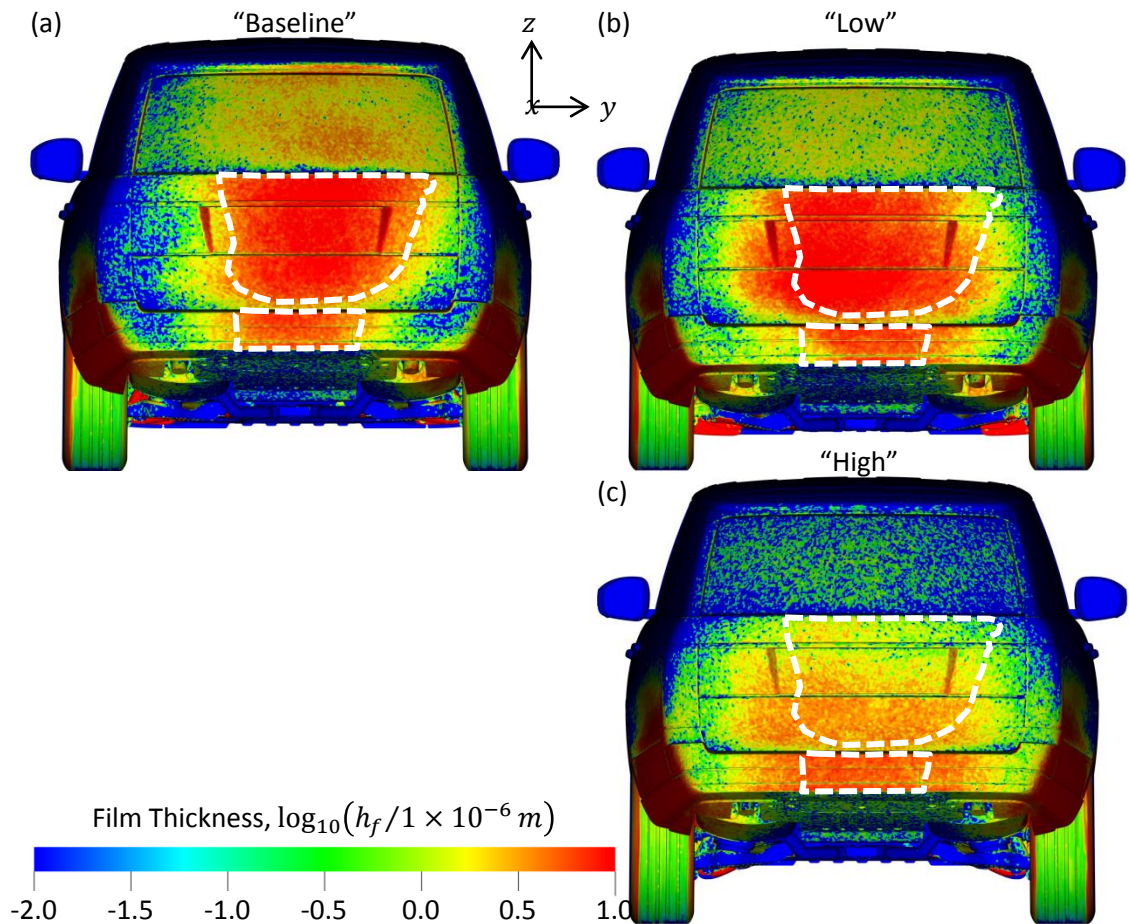


**Figure 61. Predicted Cumulative Rear Surface Contamination Distribution for the 13MY Range Rover in (a) Baseline, (b) Low and (c) Height Trim Height Configurations**

The outcome of the rear surface deposition simulations are shown in Figures 61 and 62. Cumulative deposition patterns are provided in Figure 61 for the Baseline (a) along with Low (b) and High (c) trim height configurations. The boundaries of the two most contaminated zones on the Baseline simulation, shown as broken white lines, are superimposed to aid comparison. Comparing the High trim height case (c) with the Baseline (a) reveals a shift in deposition from the rear screen and upper tailgate to the lower tailgate and bumper; along with an apparent reduction in total deposition. The former is consistent with the pitch related shift in wake-state described by Bonnavion *et al.* (2019) where the base pressure moves from increasing with height to decreasing with height, i.e. a transition from a positive to negative gradient. As previously shown numerically by the author (Gaylard *et al.*, 2017b) and inferred from experiment by Costelli (1984) surface deposition favours regions of relatively high base pressure and hence any shift towards higher pressures lower on the base would be reflected in a redistribution of contaminant favouring the lower base, as seen between Figure 61(a)—(c).

As noted earlier in this chapter, Bonnavion *et al.* (2019) suggests that the positive pitch change from the (a) Baseline [ $\varphi = -0.3^\circ$ ] to (b) Low [ $\varphi = +0.1^\circ$ ] trim height is associated with increased lift; this is borne out by the *experimental* measurement [Table 5]. There is an associated expectation that the base pressure gradient switches from positive to negative for a pitch angle *change* of this size; though this was observed over a larger range of pitch angles than seen here. In this case, a pressure—contamination correlation argument leads to the expectation that the Low trim height configuration would have deposition biased towards the lower rear surfaces and away from the rear screen. The deposition pattern shown in Figure 61(b) appears to follow that trend, with deposition reduced over the rear screen and increased on the tailgate. This suggests that along with trim height, changes in vehicle pitch are also influencing the predicted pattern of rear surface deposition. However, a degree of caution is advisable as this *simulation* result breaks the lift—pitch relationship proposed by Bonnavion and colleagues, along with exhibiting the largest difference between measured and simulated force coefficients.

The integral comparisons made in Figure 62 clarify the results of the simulation for the key rear surface zones. These are made by subtracting the Baseline surface area density history from those for the High and Low trim height configurations. This provides a view of changes in the intensity of contamination. The most consistent trend is for reduced surface contamination at the High trim height. Whereas, with the exception of the rear screen, reduced trim height leads to modest increases in deposition. The license plate experiences the largest changes, with increased contamination at the Low trim height and substantially reduced contamination at the High trim height. Finally, the rear screen is *predicted* to have reduced surface contamination with both increased and decreased trim height.



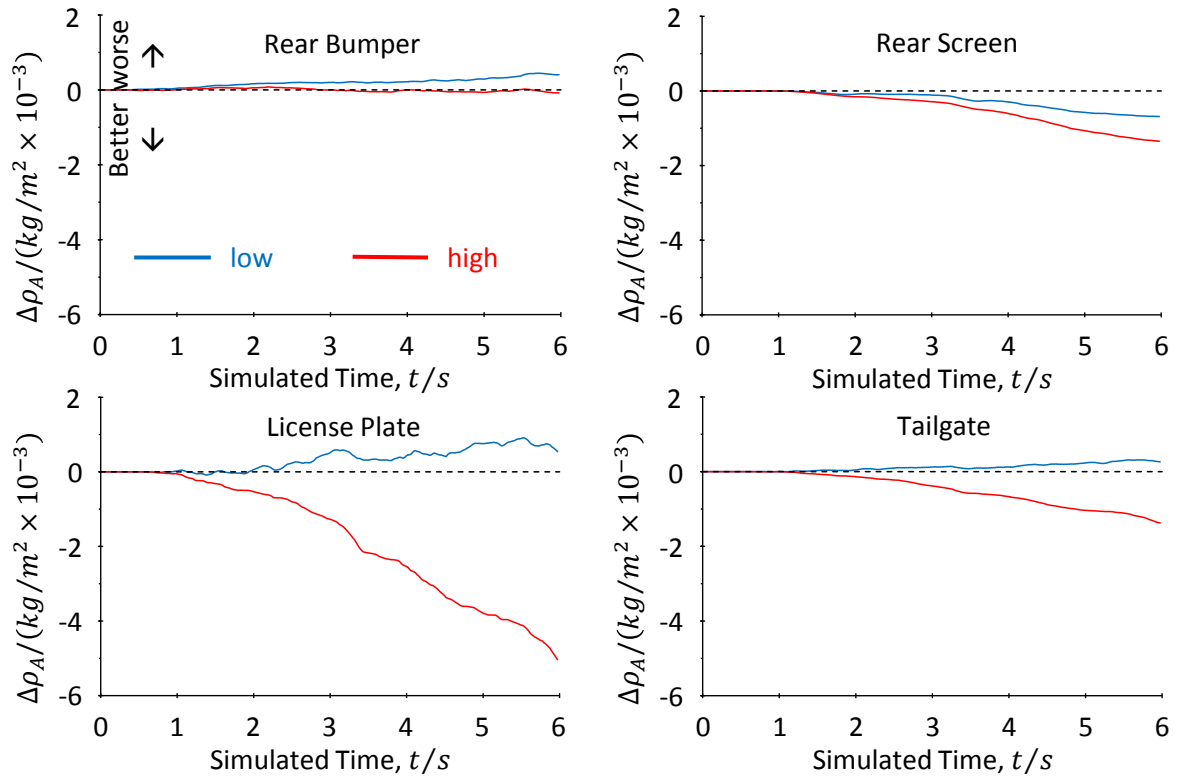


**Figure 62. Differences in Simulated Deposition History for the 13MY Range Rover Changing from the Baseline Trim Height**

The underlying flow mechanisms responsible for these trends are illustrated in Figure 63, which uses isosurfaces of zero total pressure coefficient to visualise the boundaries of the vehicle wake and wheel wakes. The side profiles (a – c) indicate that increasing trim height reduces wake length; particularly wheel wake length. They also show lower levels of contamination distributed over the wake boundaries due to the interaction between wheel and base wakes reducing as trim height increases. The underside images (d – f) provide an additional view of the wheel wake length contraction with increasing trim height. In contrast, they reveal an increased tendency for the wheel wakes to be drawn inboard as trim height reduces. The attendant surface contamination changes with trim height can be understood in terms of this wheel wake to base wake interaction: the higher the trim height the less interaction, limiting the advection of airborne spray from the wheel wakes to the base wake. As a consequence, deposition reduces over the rear surfaces. Conversely, reducing trim height brings these structures into increased proximity, where the base wake can draw the wheel wakes inboard, increasing transfer of material into the base wake and onto the rear surfaces. The increasing inwards intrusion of the rear wheel wakes as trim height is reduced also reduces underfloor flow velocity, as the “exit” from the underfloor becomes obstructed by these low-velocity flow structures. This is associated with the lower lateral ring vortex arm approaching and wrapping up over the rear surface; a wake structure identified as increasing rear surface deposition.

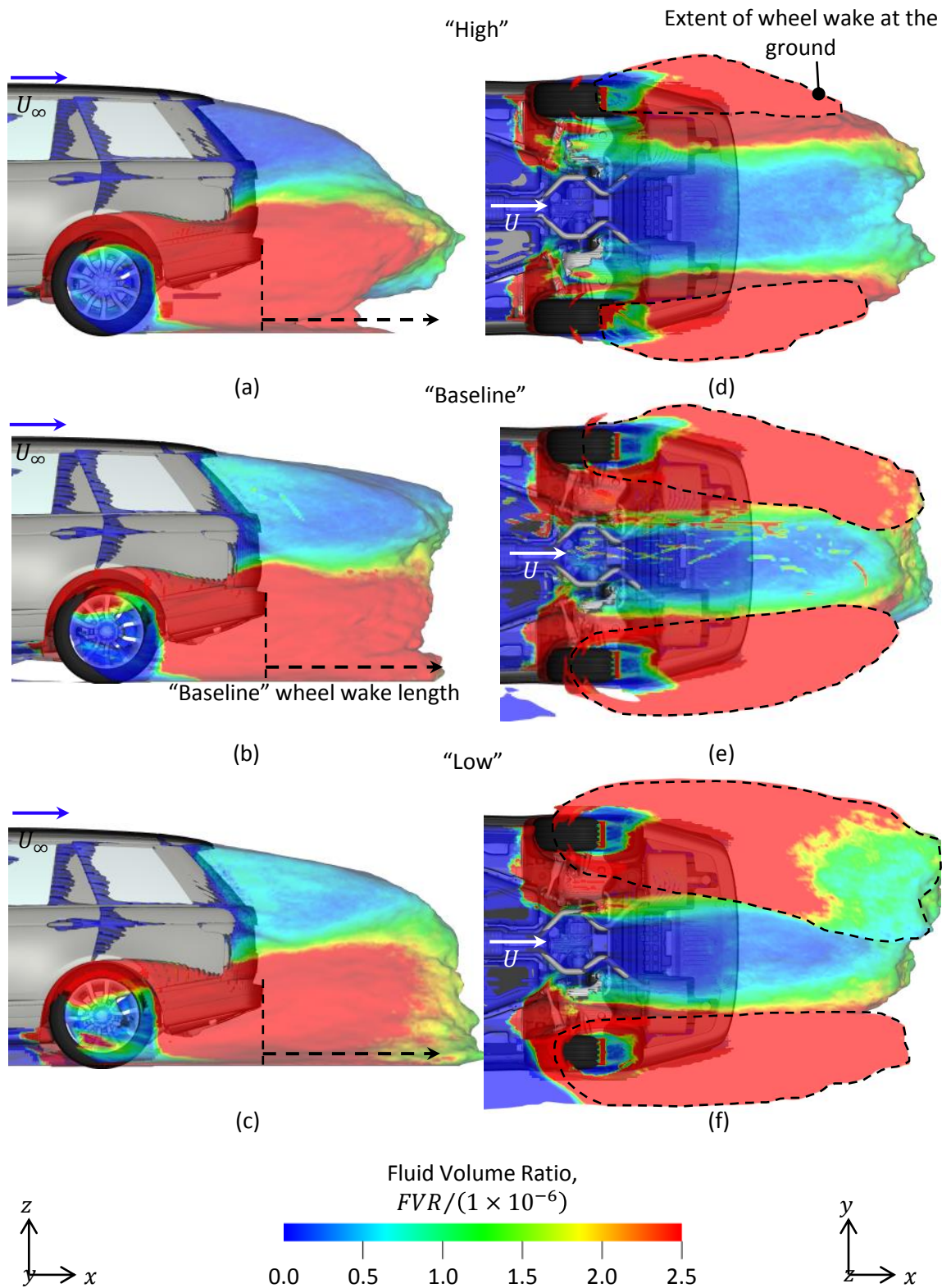


**Figure 63. The Effect of Trim Height on Wake Contamination Illustrated by Isosurfaces of Zero Total Pressure Coloured by Airborne Contaminant Concentration**

Overall, these trends match those seen in CHAPTER 3 for the simplified Generic SUV [See Figure 45(f–h)] which was based on changes to ground clearance only, with no attendant change in vehicle pitch, i.e.:  $\varphi = 0$  for all ground clearances. The alignment of trends between the fully engineered SUV and Generic SUV suggest that while the effect of vehicle pitch on rear surface contamination may be influential, ground clearance is an important factor in its own right.

Further, the agreement in overall trends obtained for a production vehicle geometry and a de-featured basic car shape lends added support to the research strategy adopted in this work: using simplified systems to aid in the development of an engineering simulation process aimed at a fully-engineered automotive product. In addition, obtaining the same flow mechanisms from both a simplified model and a production vehicle increases the likelihood that these observations are generally applicable, and are not a function of particular vehicle geometry.

#### 4.3.6 The Effect of Improved Underbody Aerodynamics

As discussed in CHAPTER 1 there is a trend towards smoother underfloors. This is seen on ICE powered vehicles, but is especially notable for BEVs. Therefore, one of the key changes explored for the Range Rover was the addition of a large central undertray<sup>17</sup> to aerodynamically improve the condition of the underfloor. Earlier in this chapter, this was confirmed to reduce the drag of the vehicle by 1.1% [ $\Delta C_D = -0.004$ ].

The effect of this type of aerodynamic intervention on rear surface contamination has not been previously assessed. However, the original simulations illustrated in Figures 64 and 65 show, for the first time, the effect of an aerodynamic underfloor improvement on rear surface contamination. The predicted distribution of material over the rear surfaces is shown in Figure 64 highlighting changes from the baseline (a) to the improved underfloor (b) condition. For reference, the border of the two highest contamination regions seen on the baseline simulation is marked by a broken line in both images. This makes it apparent that there are increases in

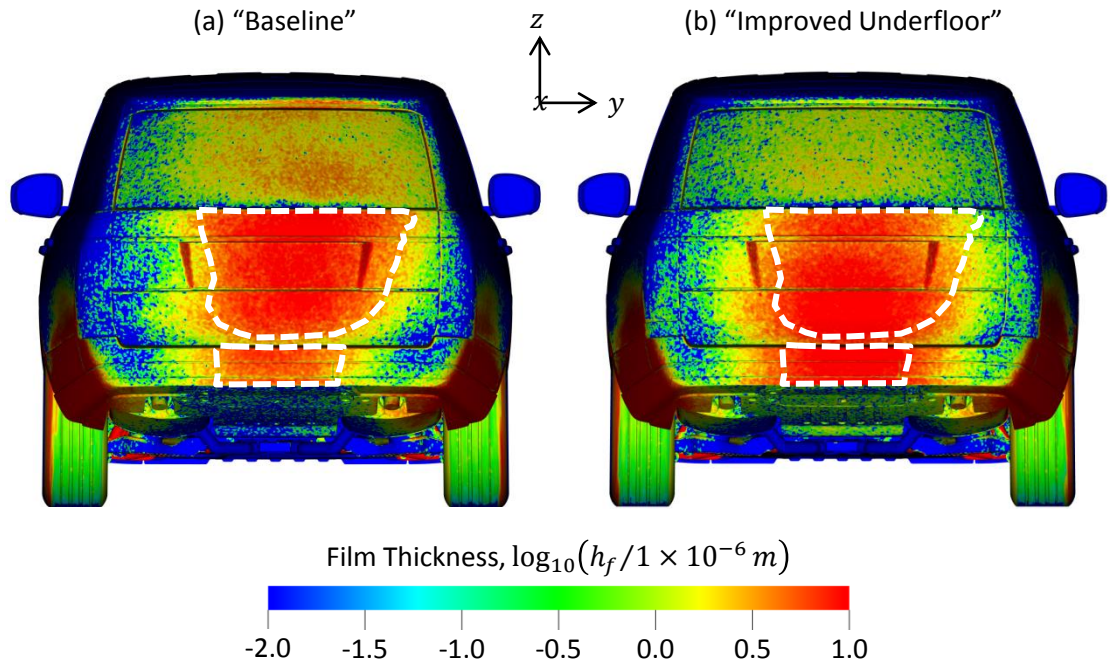


**Figure 64. Predicted Cumulative Rear Surface Contamination Distribution for the 13MY Range Rover in (a) Baseline and, (b) Improved Underfloor Configurations**

<sup>17</sup> See APPENDIX C, Figure 96(c)



surface contamination over the rear bumper and to a smaller extent, the tailgate, when the underfloor condition is improved. The largest change is a *reduction* in deposition over the rear screen. The quantitative assessment of changes provided by Figure 65 confirms these impressions, also indicating a modest reduction in contamination over the license plate.

To this point, as discussed in CHAPTER 3, a series of simplified systems have been used to develop a novel simulation process which can accurately capture aerodynamic forces and rear surface deposition for a wide range of rear wake structures, ground clearances and underbody flow conditions. In this chapter, the emerging simulation technique was applied to a production vehicle establishing that, in common with the trends seen for the simplified geometries, deposition is still linear with respect to time and the relative distribution of material over the rear surfaces does not depend on the time period simulated. This provides a degree of confidence that the deposition mechanisms identified through the full vehicle simulation, along with the trends seen for trim height change and underbody improvement are broadly indicative of real vehicle performance. The following chapters take this a step further, with CHAPTER 5 summarising full scale experiments undertaken to provide physical deposition data which are then used in CHAPTER 6 to validate the numerical representation of deposition provided by the full scale production vehicle simulations presented in this chapter.

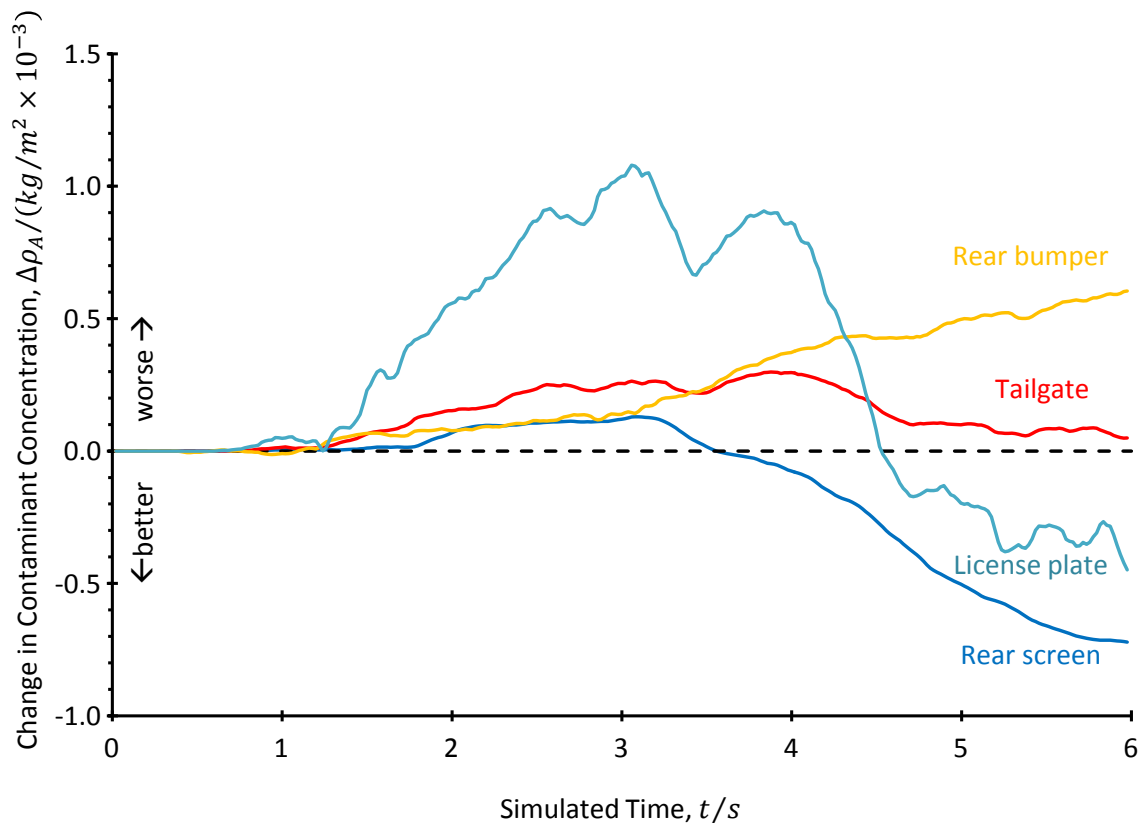


**Figure 65. Differences in Simulated Deposition History for Adding an Aerodynamically Improved Underfloor to the 13MY Range Rover**

## CHAPTER 5 FULL SCALE EXPERIMENTS

### 5.1 THE FKFS THERMAL WIND TUNNEL

To validate the computational work on rear surface contamination, the author made a series of measurements on the 13MY Range Rover using the FKFS Thermal Wind Tunnel [TWT], a schematic of which is shown in Figure 66. Its test section comprises a plenum [1], into which a jet flow is drawn through a 6 m<sup>2</sup> nozzle [2]. This flow passes over the car [3] before it is captured by a collector [4] and recirculated back around the rest of the airline [shown in blue]. As illustrated, the vehicle is installed on a twin-axle dynamometer [5] which drives its wheels to match the flow speed. This facility, although not providing flow quality comparable to an aerodynamic wind tunnel or the capability to measure aerodynamic forces, is robust to the presence of water and has therefore been widely used for the investigation of surface contamination issues (Kuthada *et al.*, 2002) including rear surface soiling (Jilesen *et al.*, 2013; Gaylard *et al.*, 2014). In this facility, tyre spray is generated by injecting water onto the rear dynamometer rollers where it is picked up by the tyres.

The following chapter summarises *Portfolio Report D*, describing the experiments undertaken using this facility to provide both a basic characterisation of the rear tyre spray and measurements of surface contamination.

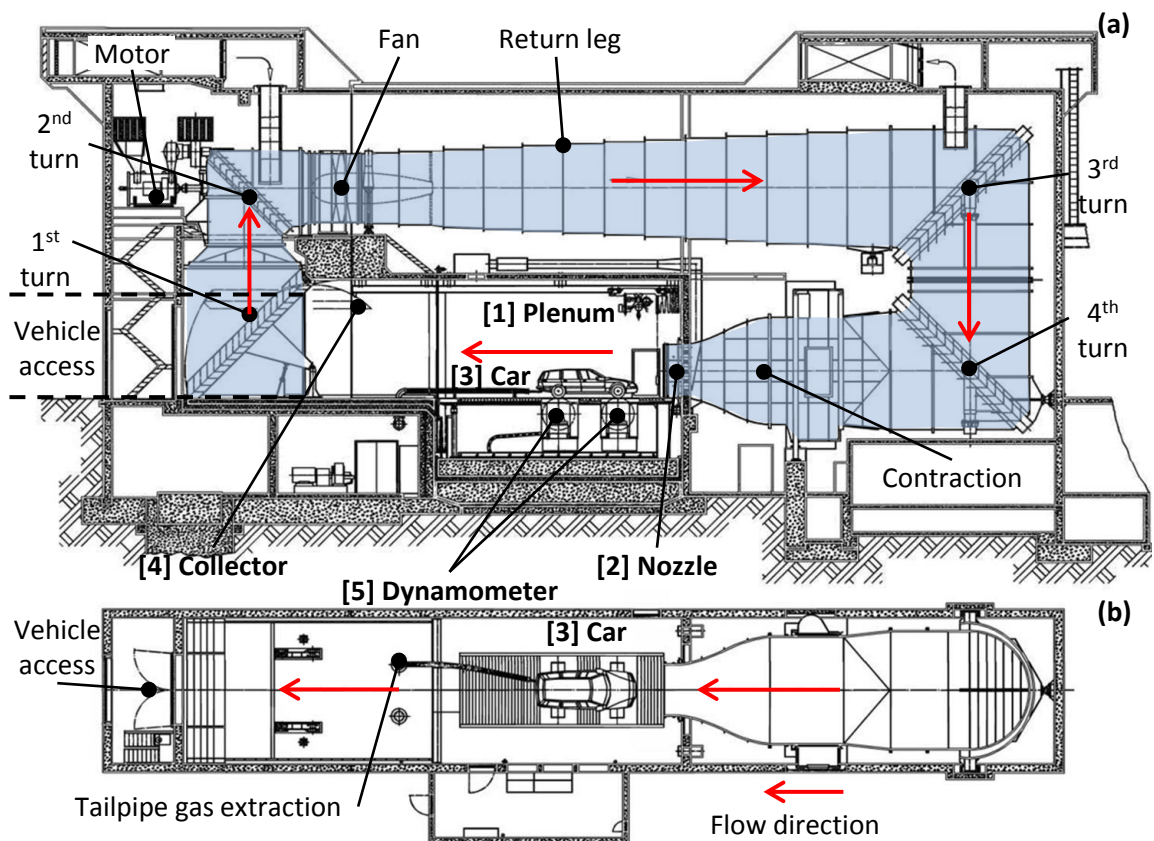


Figure 66 The FKFS Thermal Wind Tunnel (Kuthada *et al.*, 2002)

## 5.2 TYRE SPRAY CHARACTERISATION

The contamination deposited on the rear surfaces of a vehicle is initially generated by its tyres lifting material from the road surface; yet there are few published characterisations of this spray. Two studies have been reported using a laboratory rig to investigate the spray generated by a pair of simplified single-groove tyres, mounted side-by-side and rotated in contact with each other with water fed into the contact patch from above; effectively modelling ground contact via symmetry at the contact patch (Radovich & Plocher, 2009; Plocher & Browand, 2014). Light sheet illumination was used in combination with high-speed photography to examine spray formation close to the tyre surface. In contrast, the topology of tyre spray generated via contact with a surface has been explored by Kuthada and Cyr (2006) and more recently Spruss *et al.* (2011). In both of these studies, laser light sheets were used to characterise the structure of spray generated by an *isolated* rotating wheel installed in the FKFS TWT. The only previous report of similarly characterising tyre spray behind an actual car was published by Goetz and Schoch (1995). They mounted a light sheet generator on a frame attached to a car which was driven on a wetted test track. The light sheet illuminated a cross-flow plane 1 m behind a saloon car, measuring 630 mm [wide] by 1500 mm [high] and displaced laterally by 500 mm from the car's centreline to centre it behind one of the rear wheels. The intensity of light scattered by the droplets crossing the sheet was recorded by a camera mounted on an outrigger from body work in front of the rear wheels. Nine solid-state photosensitive detectors were mounted in its film-plane, each providing time-resolved integral measurements for a region of the light sheet. However, this only provided a *single* integral measurement directly behind the rear tyre. Also the camera with its frame would likely have disturbed the flow upstream of the rear wheel, providing an experimental artefact in the measurement.

Therefore, in order to obtain a basic understanding of the structure of rear tyre spray generated by an actual vehicle, and have experimental evidence against which to test the performance of the numerical simulations, novel laser light sheet visualisations were conducted of the spray generated by the rear tyres of the 13MY Range Rover installed in the FKFS TWT.

A schematic for the layout of this experiment is provided in Figure 67. The car was installed the TWT and subjected to an onset flow [ $U_{\infty}$ ] of 80 km/h; a laser was used in combination with a mirror and lens system to generate light sheets in lateral cross-flow [ $yz$ ] planes measuring approximately 2 m [wide] by 1 m [high]. This allowed the simultaneous visualisation of the spray behind both rear wheels. During the tests the light sheet was placed either 100 mm or 200 mm behind the car's rear bumper. With all four wheels rotating, plain water was injected at a rate of 1200 l/hr onto the rear dynamometer rollers in front of the tyres. The droplets generated by the rear tyres scattered the laser light as they passed through the sheet, which was recorded using a

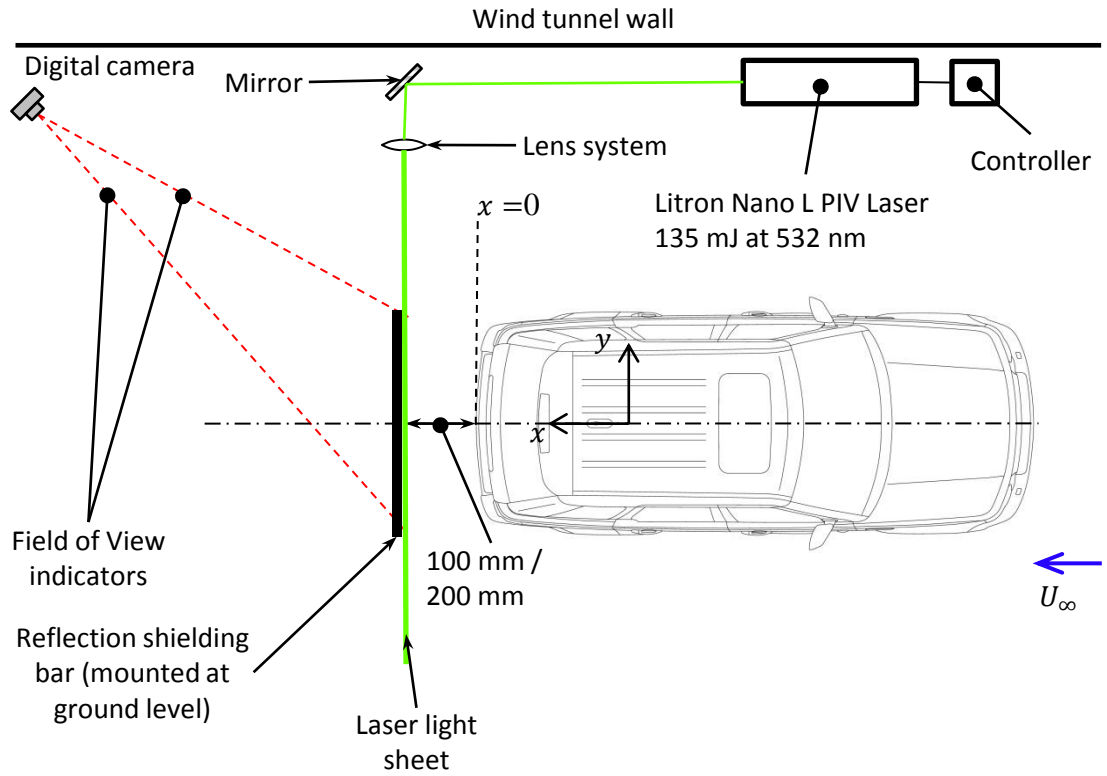


**Figure 67. Laser Light Sheet Visualisation Experiment**

digital camera. Glantschnig and Chen (1981) showed that the recorded scattering intensity  $[I_S]$  at a particular angle  $[\theta]$  is [as an approximation] proportional to the square of droplet diameter  $[r]$ , i.e.:

$$I_S(\theta, r) = K(\theta)r^2 \quad \text{Eqn. 29}$$

Although this breaks down for small droplets  $[r \lesssim 10 \mu m]$  it is applicable to droplets of the size that would be expected in the spray generated by a tyre, which have a mean diameter of around 0.2 mm (Bouchet *et al.* 2004). Hence, scattering intensities can be attributed to both droplet size and number density (Goetz & Schoch, 1995).

Digital images were acquired from the camera at a rate of 1 Hz over a 14 second period and processed to provide plots of the distribution of scattered light intensity. Digital masks were applied to remove reflections, along with thresholds to filter out the influence of out-of-plane droplets in the optical path. Finally, the images were summed to provide a representative intensity map.

The results obtained for the Range Rover in its baseline configuration are shown in Figure 68 for the crossflow planes at (a)  $x = 100$  mm and (b)  $x = 200$  mm. The shadows cast by the two rear restraint cables are visible in the images, along with some asymmetry. The latter is a commonly seen aerodynamic effect, largely attributable to asymmetric underbody layouts and cooling flow exit paths from the engine bay. Also, acquiring the images from a single laterally offset camera

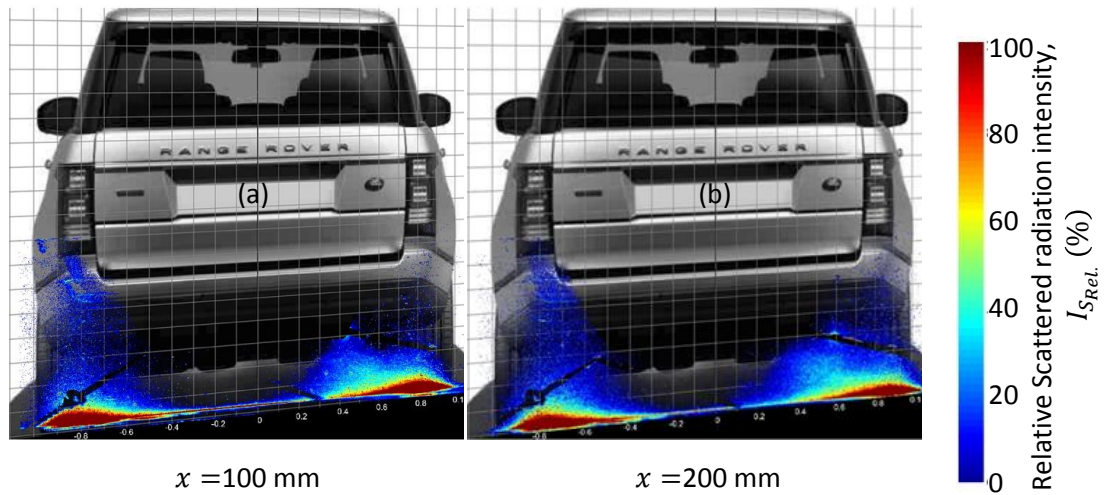


**Figure 68. Rear Tyre Spray Visualisation (a) 100 mm and (b) 200 mm behind a Range Rover**

has led to a degree of parallax in the images. However, it is clear that the rear tyre spray has two distinct zones. First, an intense spray core sits close to the ground [ $I_{S_{Rel}} \gtrsim 80\%$ ]. Moving away from this core a steep intensity gradient is evident, particularly in the vertical direction, leading to a region of more diffuse spray [ $I_{S_{Rel}} \lesssim 50\%$ ]. This observation aligns with the spray topology proposed by Weir (1980) who distinguished two spray regimes behind the tyre: [1] “tread throw” made up of larger droplets released from the tyre on ballistic trajectories close to the ground and [2] “capillary” spray, smaller droplets released further from the ground.

The spray core can be further characterised by extracting its boundary. These are plotted for both planes in Figure 69, which shows an envelope encompassing the boundaries measured during four repeat runs – effectively the summation of  $[4 \times 14 =] 56$  images. This provides an indication of both the change in the extent of the spray core as it moves downstream along with the test-to-test variability of the spray core size.

Taking these two views of the data together, it is clear that:

- a diffuse plume of spray, with its maximum height immediately behind the tyre, extends vertically to just below the height of the rear lamp clusters;
- the bulk of the tyre spray remains less than 100 mm from the wind tunnel floor, in a “spray core”;
- each spray core is highly asymmetric about the tyre centreline;
- the inboard side of the spray core is drawn towards the vehicle centreline;
- the maximum height of the spray core at  $x = 100$  mm aligns with the centre of the rear tyres [indicated by the vehicle track markers shown in Figure 69], and
- by  $x = 200$  mm the lateral location of peak height of the spray core has moved inboard.

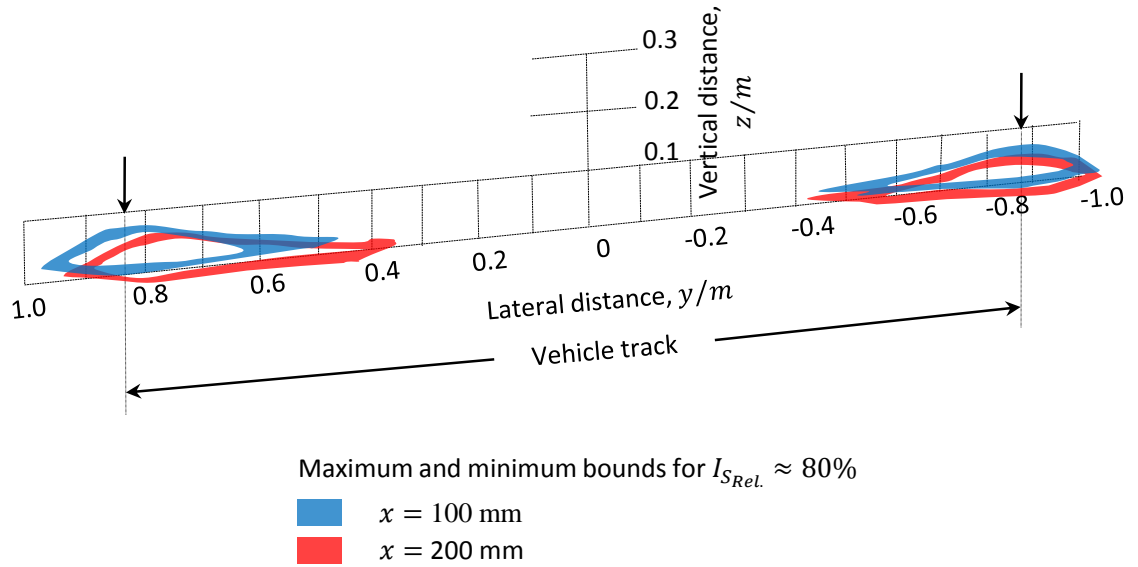


**Figure 69. Rear Tyre Spray Core Boundary Ranges**

The inboard bias of the lateral spray distribution is significant in that it places airborne droplets closer to the rear wake structures which, as discussed in CHAPTER 4, are able to transport them back to the rear surfaces; this tendency appears to increase with distance downstream. In addition, given that the spray core [“tread throw”] sits close to the ground, it is the more diffuse “capillary spray” that is likely to provide the source for rear surface contamination. This latter fraction, which the literature suggests is composed of smaller droplets and is found further from the ground, can therefore be reasonably expected to be preferentially advected into the vehicle wake and transported to its rear facing surfaces.

Clearly, more work needs to be done on this topic: as the aerodynamic structures are highly three-dimensional the spray topology will follow suit; therefore, taking data in the vertical  $[xz]$  and horizontal  $[xy]$  planes would be the next logical step. Beyond this, the use of quantitative techniques such as Particle Image Velocimetry [PIV] should also be considered. This would allow a detailed consideration of the effect of changes to the vehicle configuration on both the spray generated and, ultimately, surface deposition. Nevertheless, the work presented here provides original insights as well as useful data against which to test the numerical simulation approach.

The following section summarises the key rear surface contamination measurements made for the Range Rover, which will enable the numerical simulations of surface deposition for this vehicle to be correlated against physical data.

## 5.3 REAR SURFACE CONTAMINATION MEASUREMENTS

### 5.3.1 Experimental Setup and Data Analysis

The rear surface contamination measurements were made using the experimental design illustrated in Figure 70. In contrast to the plain water analogue for contamination used in the spray characterisation, a 0.4% solution of a UV fluorescent dye in water was injected onto the rear dynamometer rollers at a rate of 1200 l/hr. As the vehicle's rear wheels rotated at a rate that matched the 80 km/h onset flow velocity, the tyres generated spray that was advected by the wheel wakes into the base wake and back onto the rear surfaces. The rear of the vehicle was illuminated by an array of four LED UV lamps, whose radiation was absorbed by the dye deposited on the rear surfaces. This was re-emitted in the visible spectrum and the resulting intensity distribution over the surfaces was recorded by a digital camera located immediately behind the vehicle, but above the wind tunnel jet flow to maintain a clean lens. The wind tunnel's closed return path adds an additional complication: some spray is recirculated and appears in the onset flow seen by the vehicle. This provided a background artefact in the images captured by the camera, which was suppressed by setting a lower [i.e. "high-pass"] intensity threshold in the subsequent image analysis.

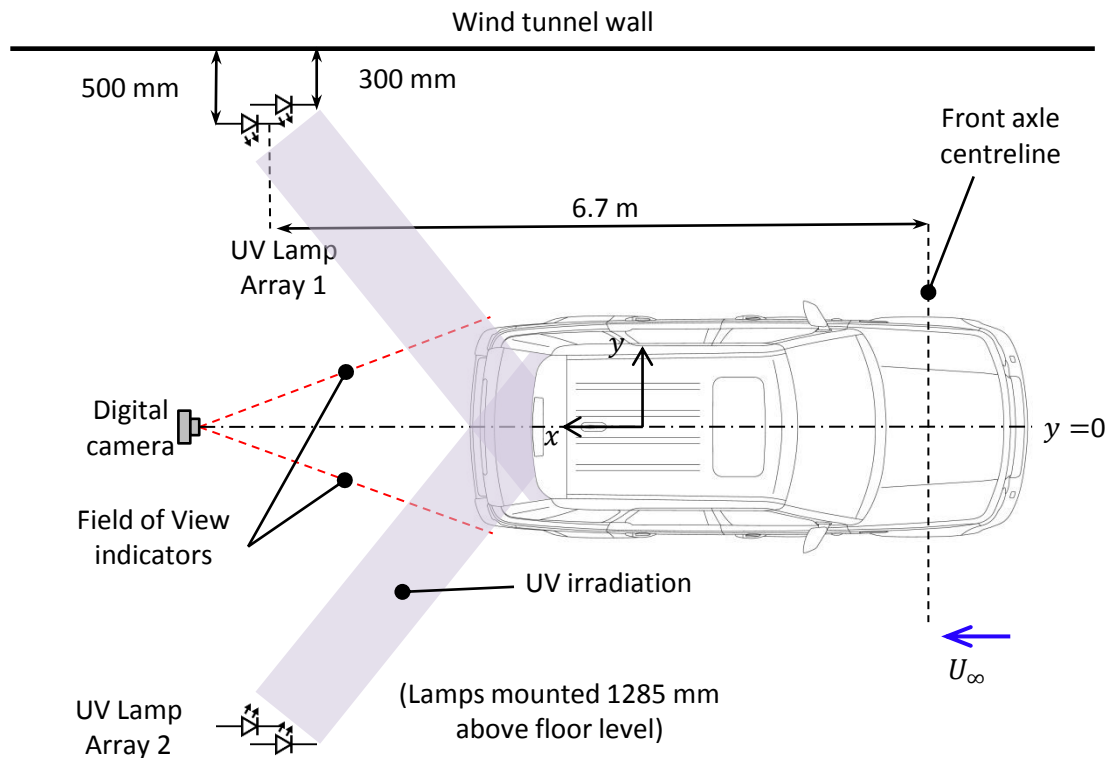
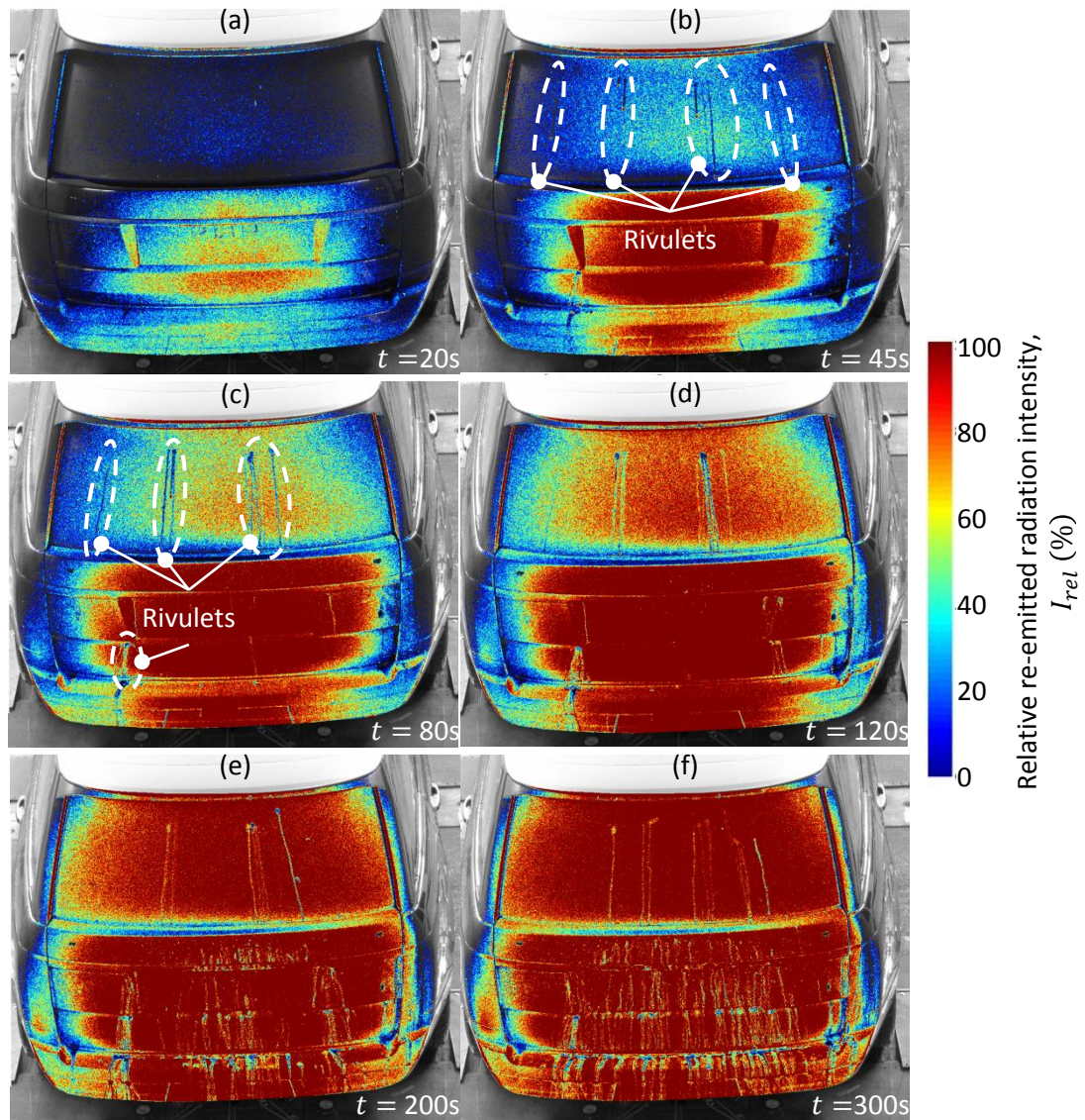


Figure 70 Rear Surface Contamination Experiment



A typical experiment is run for 300 s, during which time images are acquired every 5 s. These are subsequently processed using MATLAB code<sup>18</sup>, extracting a relative intensity distribution over the rear surfaces. In addition, semi-quantitative measurements are also obtained from the images. For predefined surface areas [e.g. rear screen, license plate, etc.] the percentage area “covered” [%A] is calculated along with an average relative radiation intensity for the zone [ $I_{av}$ ]. The latter metric can be considered as being proportional to the depth of water accumulated on the surface, generally in a film, as the relationship between measured intensity and film depth is *approximately* linear<sup>19</sup>. Therefore, the product of these two metrics  $\%A \cdot I_{av}$  is *indicative* of the volume of water deposited over a particular surface and is used in this work to measure the degree of contamination.



**Figure 71 Rear Surface Contamination Intensity Distributions for the Range Rover in its Baseline Condition from 20s to 300s**

<sup>18</sup> See *Portfolio Report D*: 31-32 for details.

<sup>19</sup> As shown by Hagemeier *et al.* (2012) the relationship between re-emitted radiation intensity and thickness for a surface film actually follows a modified version of the Beer-Lambert Law.



A sequence of post-processed images for a run with the Range Rover in its baseline configuration spanning  $20 \leq t(s) \leq 300$  are provided in Figure 71. This shows the progressive build-up of contamination, with its maximum centred on the middle of the tailgate. As time passes this intensifies and expands laterally. A secondary peak also develops in the centre of the rear bumper. Eventually the rear screen fills with contaminant, with the outboard regions – including the lamp clusters – the least soiled. By  $t = 200$  s the rear surfaces have become saturated with the image providing little indication of differences between rear surface zones. In addition to the general presence of a continuous surface film, rivulets can be seen to appear from  $t = 45$  s. Initially, they appear to be associated with a “drip line” beneath the trailing edge of the rear roof spoiler; ultimately they indicate regions where the water film can no longer be supported against gravity by surface friction and aerodynamic shear. In terms of the utility of the images, the appearance of persistent rivulets and the saturation of the rear surfaces seen for  $t \geq 120$  s limits their value, as differences between vehicle configurations will be progressively more difficult to ascertain. Hence, this work uses images taken at  $t = 80$  s to provide a visual indication of contaminant distribution.

The experiments also provide semi-quantitative data, such as the cumulative deposition histories  $[\%A \cdot I_{av} \text{ versus } t]$  presented in Figure 72. This plots the accumulation of contaminant across the rear surface zones for 4 baseline runs and shows that this goes through five distinct phases, most clearly seen in the total deposition history. Initially, there is a Start-up phase where surface

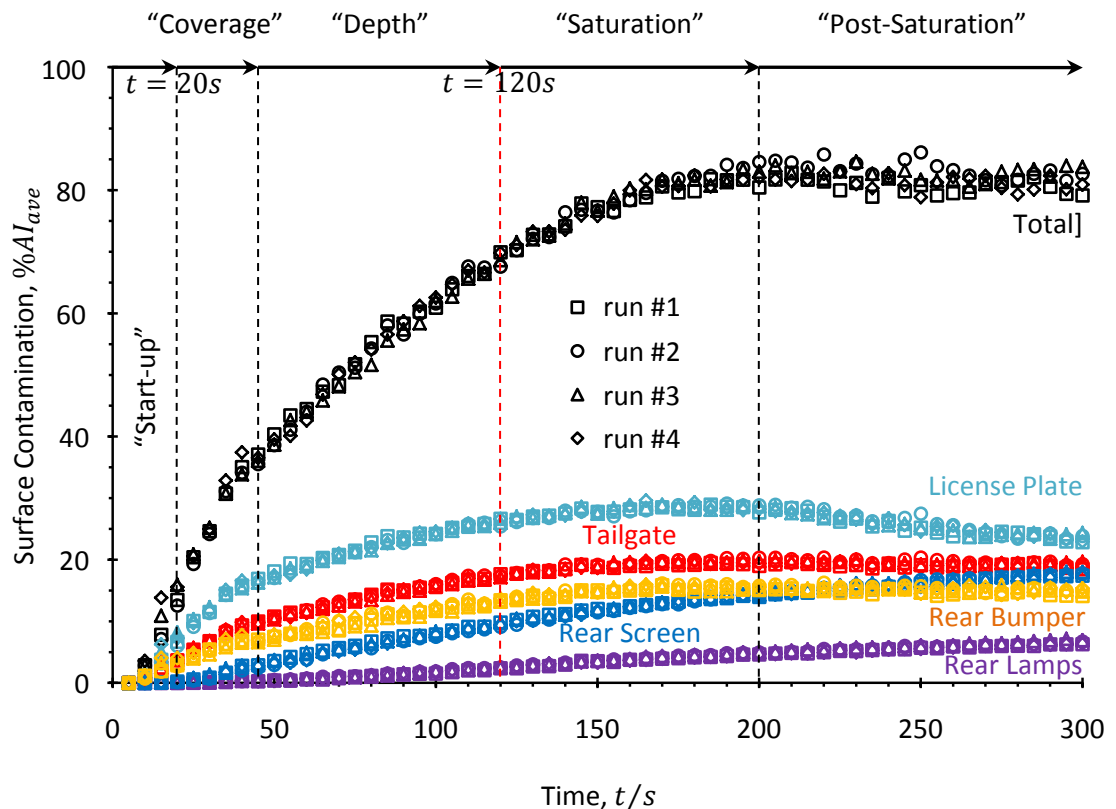


**Figure 72 Deposition Histories for the Rear Surface Zones on the Range Rover in its Baseline Condition**

deposits build up sufficiently to provide a signal that exceeds the lower detection threshold. This is followed by an approximately linear accumulation dominated by expanding coverage of the rear surfaces [%A]. By  $t = 45$  s coverage is approaching its maximum level, so from this point increasing average intensity [ $I_{av}$ ] over the surfaces provides the main increase in  $\%A \cdot I_{av}$  as the depth of the deposits increases. This Depth phase is approximately linear, but with a changed gradient, typically causing a knee-point in the plot. As surfaces become saturated the rate of accumulation slows and the linear trend breaks down. In addition, the intermittent removal of material by rivulet formation followed by the accumulation of new deposits on the surfaces increases variability in the level of contamination. These two factors identify a Saturation phase, which ends with a maximum stable level. After this, a Post-Saturation phase is entered where the influence of rivulets causes variations in the recorded deposition and, for some surfaces, a decline. This general categorisation fits best for surfaces with relatively high levels of deposition. Among those regions where accumulation is relatively low saturation may be delayed [e.g. rear screen] or not occur at all [e.g. rear lamps]. Nevertheless, this is a useful concept for assessing how to interpret the experiments. Whilst it may be tempting to examine peak levels for each surface, not all surface zones reach their peak value and those that do may see this at different times during the run. In addition run-to-run repeatability reduces from the Saturation phase onwards. Therefore the Depth phase is attractive as accumulation is linear and the less soiled zones are more contaminated than at the end of the Coverage phase. Hence, subsequent comparisons will focus on the Depth phase, which is consistent with using surface deposition images at  $t = 80$  s as this falls mid-way through the phase.

### 5.3.2 Vehicle Configuration Changes

As noted in CHAPTER 4, this work focusses on two important vehicle configuration changes: [1] trim height variation and [2] aerodynamic underfloor improvement. These were highlighted as reflecting contemporary trends in vehicle design. Reducing the height of the vehicle body above the road generally reduces aerodynamic drag. Hence, as manufacturers have come under pressure to reduce drag as part of their emissions reduction strategies, vehicles have either been built to run at a reduced ground clearance or, in the case of cars with air suspension, actively reduce ground clearance at highway speeds. The latter is attractive for large SUVs as these vehicles require large approach and departure angles for off road capability. As this type of driving is a low-speed activity, active systems for ground clearance control are a practical way of balancing these two attributes. Therefore, three trim height<sup>20</sup> configurations are considered here, previously defined in Table 4: “Baseline” — a setting indicative of typical highway trim heights; “Low” — a height used for accessing the vehicle, and “High” — aligned to an off road setting.

---

<sup>20</sup> the usual measure of ground clearance; see APPENDIX C, Figure 96(a)

The same pressures have led to a progressive improvement in the aerodynamic condition of vehicle underfloors. In times past these could be very rough, with irregularities caused by the presence of suspension and drivetrain components, along with exhaust runs and fuel tanks. Gradually, this has been improved by the addition of underbody panels. These reduce pressure losses and hence aerodynamic drag. The emergence of BEVs has allowed this to be taken further, as these vehicles do not have either exhausts or fuel tanks and their batteries can be used to form a continuous floor between the front and rear axles. For this work, which used an existing vehicle, it was not practicable to fit a completely smooth and continuous underfloor. Instead, as discussed in CHAPTER 4, a large central undertray was fitted which in combination with the existing undertrays, provided a generally smooth and continuous underfloor condition between the front and rear wheel arches<sup>21</sup>.

The following sections describe the distribution of contaminant over the rear surfaces and the time history of that build-up, as first the trim height and then the underfloor condition were varied.

### 5.3.3 The Effect of Trim Height

The rear surface deposition patterns [at  $t = 80$  s] for the trim height variants are shown in Figure 73. Some clear trends are immediately apparent:

- rear screen contamination increases as trim height reduces, and *vice versa*;
- deposition on the tailgate is reduced for the High trim height, but does not appear to change as trim height is reduced from the Baseline;
- rear bumper soiling is highest when trim height is the highest, and
- the lamps do not appear to be subject to significant deposition at any trim height.

These trends are potentially significant for future vehicle design, particularly blunt-ended BEVs. The apparent increase in deposition on the rear screen as trim height reduces means that, in the absence of countermeasures, any rear wash-wipe system would be put to more use. This has two consequences for drivers: on-board water supplies will be used more quickly and the rear wiper is likely to be in contact with elevated levels of particulates, which can increase the rate of rubber blade wear as well as abrading the rear glass (Seubert *et al.*, 2012).

---

<sup>21</sup> See APPENDIX C, Figure 96(c)

“High”  
 $h_{t,f} = (890 \pm 1) \text{ mm}$   
 $h_{t,r} = (895 \pm 1) \text{ mm}$

“Baseline”  
 $h_{t,f} = (826 \pm 4) \text{ mm}$   
 $h_{t,r} = (843 \pm 5) \text{ mm}$

“Low”  
 $h_{t,f} = (793 \pm 3) \text{ mm}$   
 $h_{t,r} = (789 \pm 4) \text{ mm}$

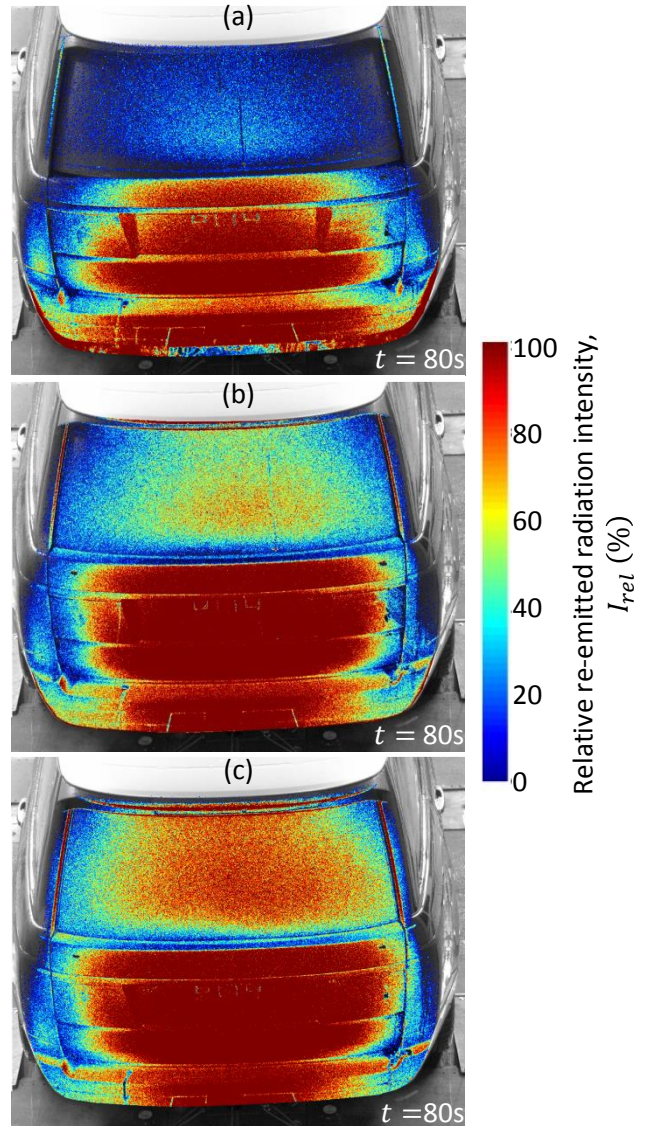


**Figure 73. Rear Surface Deposition Distribution for the Range Rover at (a) High, (b) Baseline and (c) Low Trim Heights**

Semi-quantitative deposition histories for the three trim heights are provided in Figure 74. This shows total accumulation over the linear Coverage and Depth phases, confirming the picture painted by the deposition distribution images: Low trim height is associated with increased soiling and High trim height very much reduced soiling. It is also evident that whilst the rate of accumulation over the Coverage phase for the Low and Baseline configurations is very similar, it is lower for the High trim height case – as indicated by the reduced gradient.

In Figure 75 the differences from the Baseline are explored for 4 key rear surface zones: (a) rear screen, (b) license plate, (c) tailgate and (d) rear bumper. This has been done by subtracting the Baseline history point-by-point from those for the two other trim height configurations, i.e.:

**Eqn. 30**

$$\Delta \%A \cdot I_{av} = (\%A \cdot I_{av})_{meas.} - (\%A \cdot I_{av})_{ref.}$$

where,

$\%A$  = percentage zone area contaminated;

$I_{av}$  = average relative intensity for the zone;

$meas.$  = measurement made for a vehicle trim height change, and

$ref.$  = Baseline reference measurement.

An analysis of the uncertainties indicates that differences of less than three percentage points are statistically insignificant (*Portfolio Report D: 39*); hence, there is no reliable evidence that the Low trim height configuration increases surface contamination *except* over the important rear screen zone. In contrast, moving to the High trim height reduces surface contamination significantly for the rear screen, license plate and tailgate. The apparent increase in soiling over the rear bumper is not confirmed by the integral measurement. This latter point argues for caution in the visual interpretation of deposition distribution images. Nevertheless, it is clear that rear screen cleanliness is put at risk by reduced trim height.

Finally the rear lamps have been excluded from this analysis on the basis that deposition was always very low – independent of the configuration. This finding is at odds with historical assessments made for saloon cars: Goetz (1971) observed that rear lamps required careful design to be kept free from dirt. It may be that this vehicle has by happenstance been designed in a manner which keeps the rear lamps clean, or it could be a fundamental function of its form. This would be a reassuring outcome, but requires additional investigation.

The next section summarises the use of the same techniques to examine the effect on rear surface contamination of aerodynamically improving the underfloor.

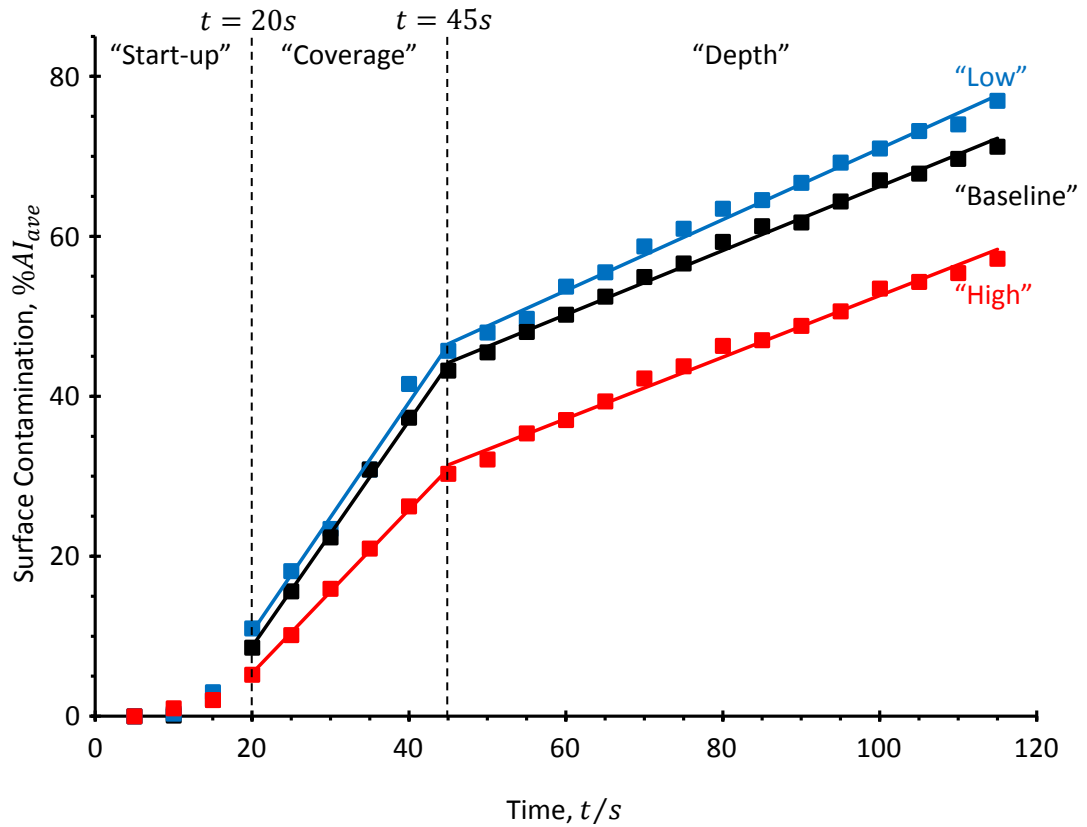


Figure 74. Deposition History for the Complete Rear Surface of the Range Rover for Low, Baseline and High Trim Heights

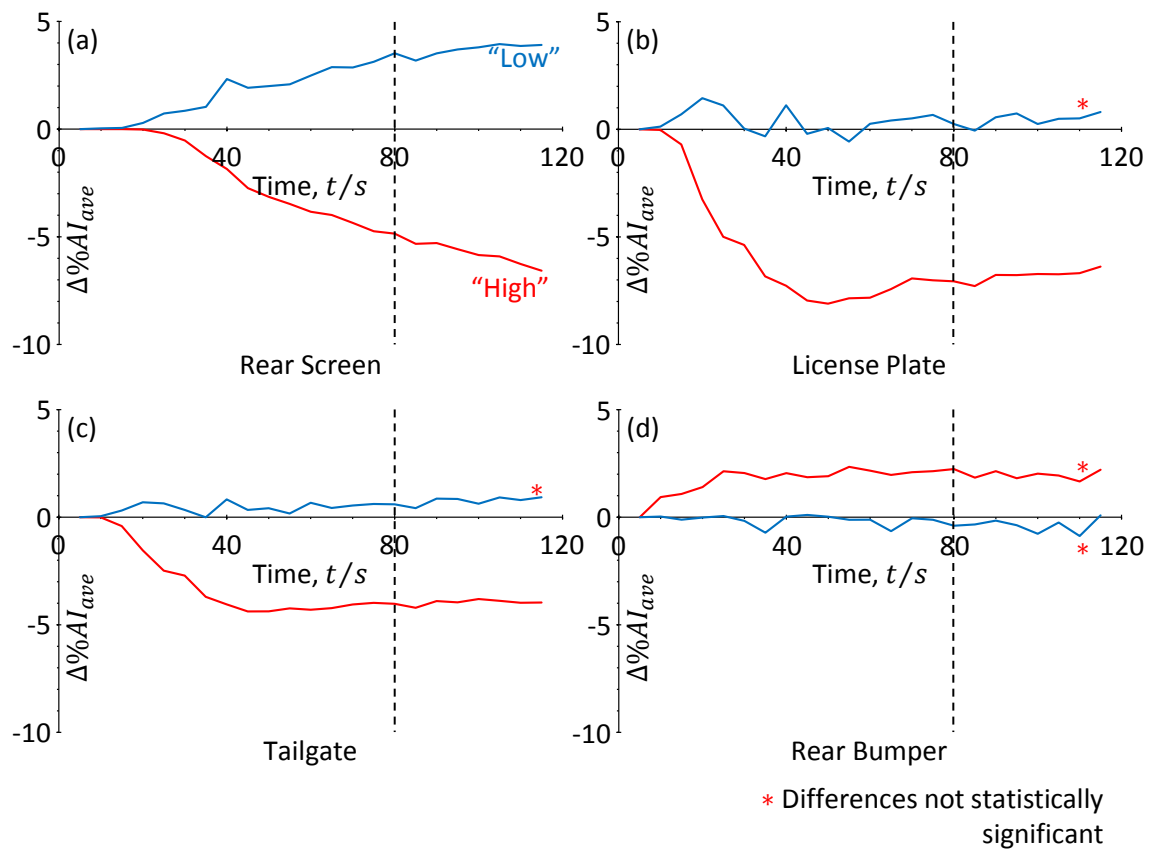


Figure 75. Differences in Rear Surface Deposition Histories from the Baseline for the Range Rover at Low and High Trim Heights for (a) Rear Screen, (b) License Plate, (c) Tailgate and (d) Rear Bumper Surface Zones [\* Statistically insignificant difference]

### 5.3.4 The Effect of Underfloor Aerodynamic Improvement

The effect on rear surface deposition of adding a large central undertray to improve the underbody flow is shown in Figures 76 to 78. Figure 76(a) compares a *local* baseline – one immediately before the addition of the undertray during the test campaign – to (b) an image obtained for the improved underfloor. The distribution of contaminant over the rear surfaces appears to indicate increases once the underfloor is improved over the rear screen, license plate and most significantly the rear bumper.

The impression that rear surface contamination has increased in total is confirmed by the deposition histories shown in Figure 77. The difference builds during the Coverage phase and remains relatively constant over the Depth phase. The constituent parts of this difference are identified in Figure 78, which shows the difference in surface contamination between the improved underfloor and baseline cases [See Eqn. 30] arising over four key surface zones. An indication is provided [red broken line] of a statistically significant difference. The clearest indication of an increase in surface contamination is over the rear bumper surface; with the license plate showing a marginal increase. The results from the tailgate and rear screen are consistent, but likely fall below the limits of reliable detection for the experiment.

The fact that any increase in rear surface contamination affects the rear bumper highlights a potential tendency of future vehicles to become soiled in a zone that users are likely to come into contact with as they access the rear load space. The marginal increase in deposition over the license plate is of potential interest as it can be taken as a proxy for rear camera and future LIDAR locations.

Having measured and characterised the spray generated by the rear tyres of a production SUV and the subsequent deposition of this material over its rear surfaces for a range of vehicle configurations, the accuracy of the numerical simulation technique can now be established.

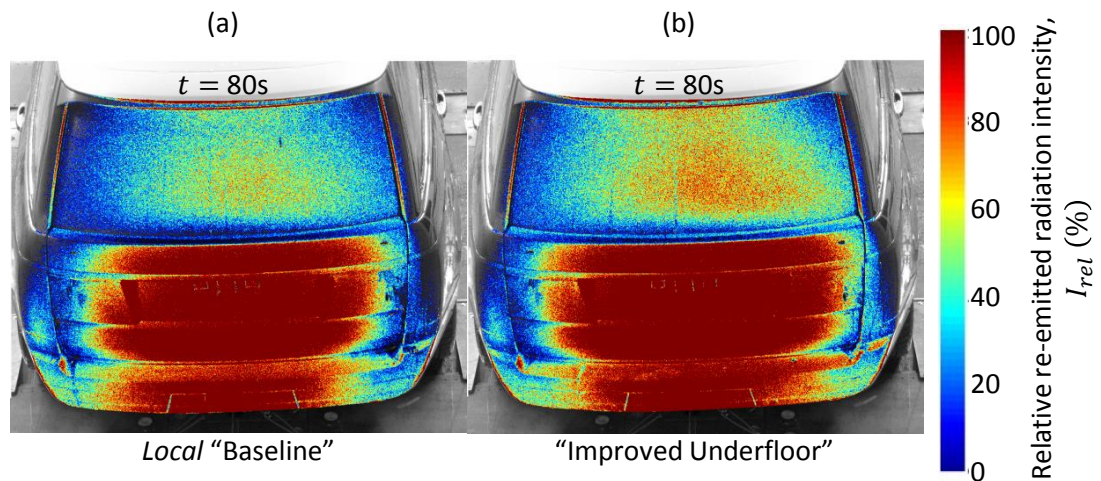


**Figure 76 Rear Surface Deposition Distribution for the Range Rover at its Baseline Trim Height for (a) Standard and (b) Improved Underfloor Condition**

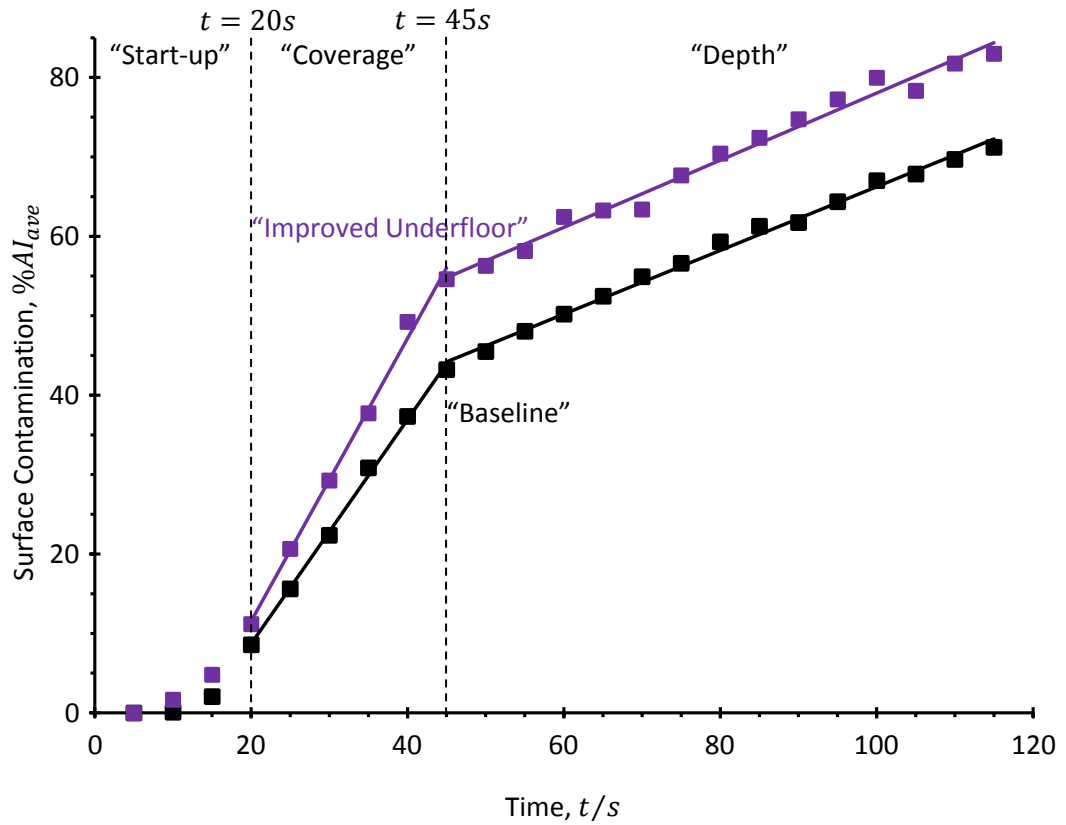


Figure 77. Deposition History for the Complete Rear Surface of the Range Rover for the Baseline and Improved Underfloor

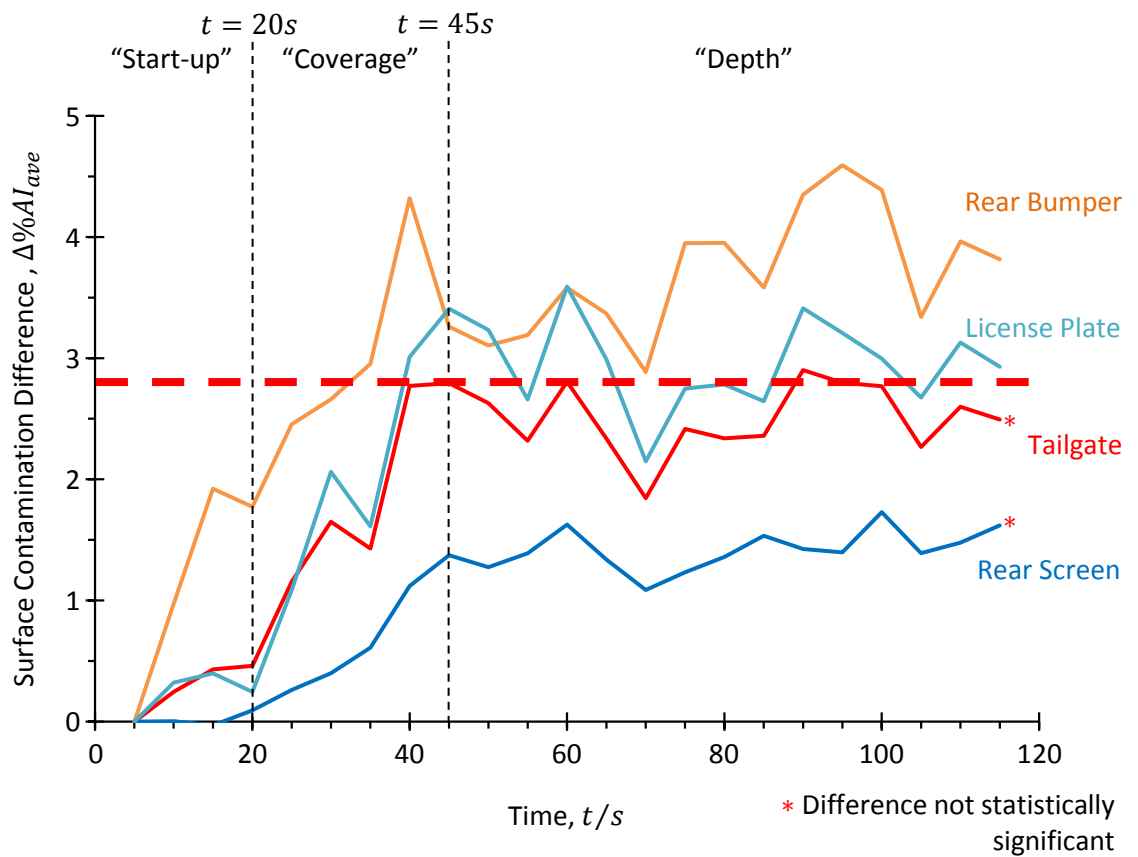


Figure 78. Differences in Rear Surface Deposition Histories from the Baseline for the Range Rover with an Improved Underfloor, over the Rear Bumper, License Plate, Tailgate and Rear Screen



## CHAPTER 6 CORRELATING AGAINST EXPERIMENT

### 6.1 SPRAY MODEL

This chapter completes the development of the novel simulation approach for rear surface contamination by using the experimental data described in CHAPTER 5 to assess its accuracy. This is approached through the use of both qualitative assessments of contaminant distribution and relative surface contamination factors. The latter providing the first quantitative assessment of accuracy for this type of numerical simulation.

The first step in this assessment was to establish the degree to which the spray model, i.e. the contaminant source, used in the numerical simulations generates a realistic spray. Figure 79 provides the first assessment of the spray model applied to a production vehicle. It makes relative comparisons between simulation (a, b) and experiment (c, d) for airborne spray at two vertical yz planes 100 mm and 200 mm behind the vehicle. This comparison relies on the commensurability of the experimental and numerical measures. The experiment records scattered laser radiation intensity, which is sensitive to both the size and number density of the airborne droplets (Goetz & Schoch, 1995). In contrast, the CFD simulation has been processed to extract the Fluid Volume Ratio [ $FVR$ ] which is the product of the particle number density and mean particle volume in each voxel. Hence, this also reflects both the number and size of particles. Therefore the parameters extracted from both the experiments and simulations are compatible and their comparability is improved by scaling them against their maximum values.

Overall, the form of the spray distribution provided by the simulation compares well with that seen in the experiment. For instance, 100 mm behind the vehicle the numerical simulation (a) recovers the high-concentration spray core which sits low to the ground [1]; as seen in the experiments (c) this is drawn inboard. However, the vertical spray plume appears over-done in the simulation, both in terms of intensity [2] and vertical extent [3]. Very little spray is seen in the experiment as high as the bottom of the lamp clusters [red broken line] whereas the simulated spray reaches above this. By the time the spray has reached the 200 mm plane then the over-prediction from the simulation has reduced somewhat.

Nevertheless, even with the limitations revealed here, this first correlation of the spray model *in situ* shows that it provides a realistic representation of the physical spray. This helps to explain why the model has previously been shown to provide the correct trends for the balance of spray arriving at the rear surface of an SUV from the front and rear wheels (Gaylard *et al.*, 2014) along with the distribution of water over the front brake disks (Schembri Puglisevich *et al.*, 2016). Next, the qualitative comparison between simulated and measured contamination distribution patterns is demonstrated.

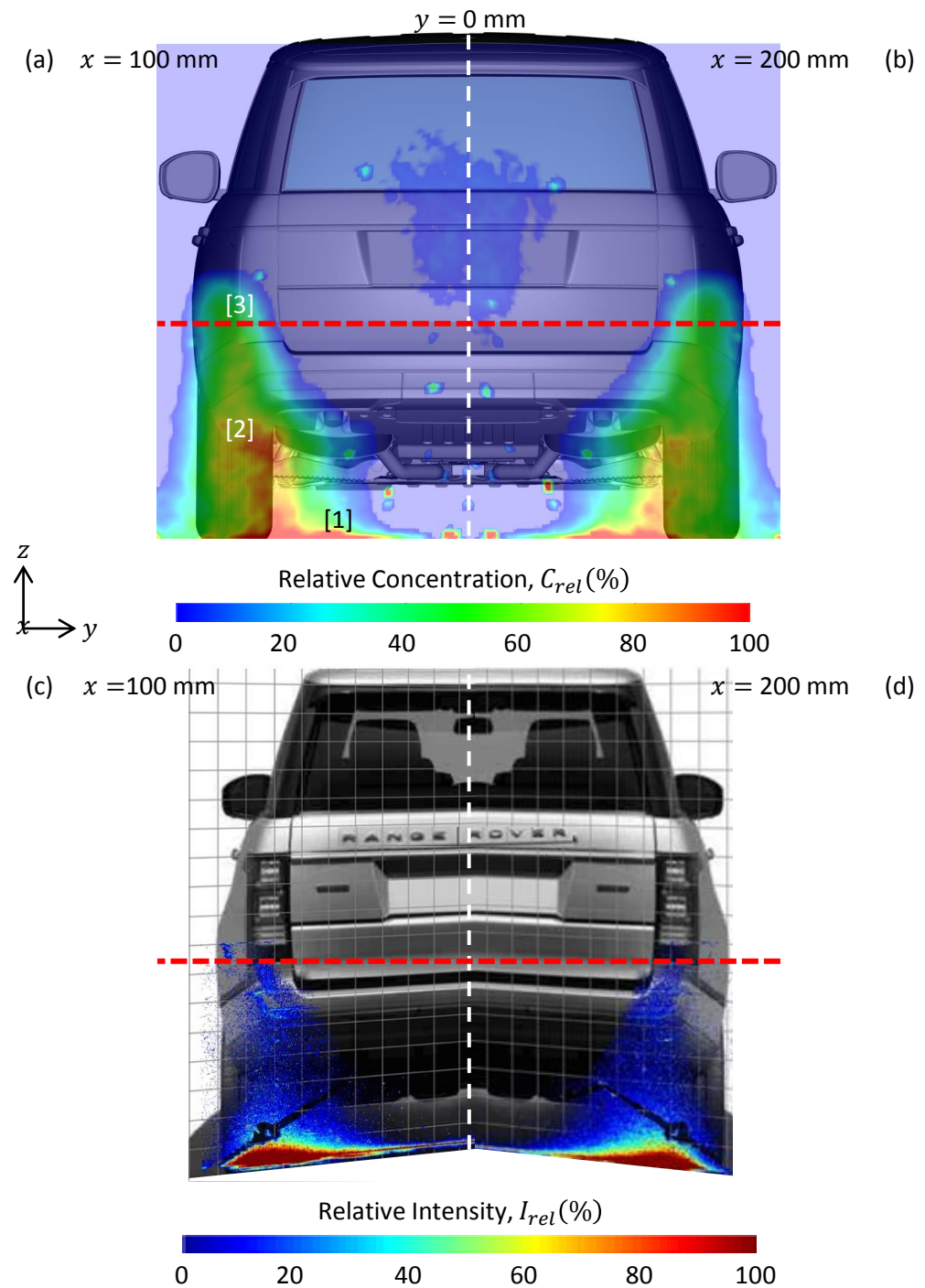


**Figure 79. Tyre Spray behind the 13MY Range Rover in Vertical Planes 100 mm and 200 mm Behind the Vehicle (a-b) Simulated (c-d) Measured**

## 6.2 DEPOSITION PATTERNS

The most straightforward approach to correlating simulation and measurement is visual inspection of the surface contamination patterns. Figures 80 and 81 provide an original qualitative assessment of simulation accuracy for the different trim height and underfloor configurations used in this work. The main difficulty with such comparisons is that the experimental and numerical data are expressed in different units of measure. As previously noted, the experiments measure the relative image intensity provided by the radiation re-emitted from the UV fluorescent dye, whilst the numerical simulations provide quantitative metrics such as film depth. The approach taken here is to scale the film depth to provide the best overall qualitative match against the rear screen distribution, as this particularly highlights any discrepancies in the main distribution over the tailgate.

The comparison between simulated and measured contaminant distributions for the trim height changes provided in Figure 80 shows that the numerical technique generally predicts the extent of the coverage of the surfaces; though on the basis of this comparison it systematically under predicts the lateral spread of the deposition peaks on the rear bumper and tailgate. The level of rear screen coverage at the High (a) and Baseline (b) trim heights appears to be reasonably well predicted. However, the simulation shows a *reduction* in rear screen contamination for the Low trim height (c) compared to the Baseline; the experiment shows the opposite (f). A similar mismatch is seen for the improved underfloor configuration, presented in Figure 81; moving from the standard underfloor simulation (a) to its improved underfloor counterpart (b) indicates a *decrease* in contamination on the rear screen. In contrast, comparing the experimental data for the Baseline pattern (c) with the improved underfloor (d) shows an *increase*. Finally, the simulation captures the increase in contamination over the rear bumper caused by aerodynamically improving the underfloor.

The poor correlation for the rear screen indicates the need for future improvements to be made to the simulation approach. The over-prediction of the vertical extent of the spray plume, noted previously, may be a contributory factor. Also, it is likely that explicitly modelling the working section of the test facility may improve the correlation over the rear screen. These should be considered as topics for future research.

Although qualitative, a comparison of these images does provide a general impression of the degree of agreement between experiment and this state-of-the-art simulation. The following section presents a novel assessment of the comparison between simulation and experiment using *relative* surface contamination factors to provide the first quantitative indication of predictive accuracy for rear surface contamination simulation.

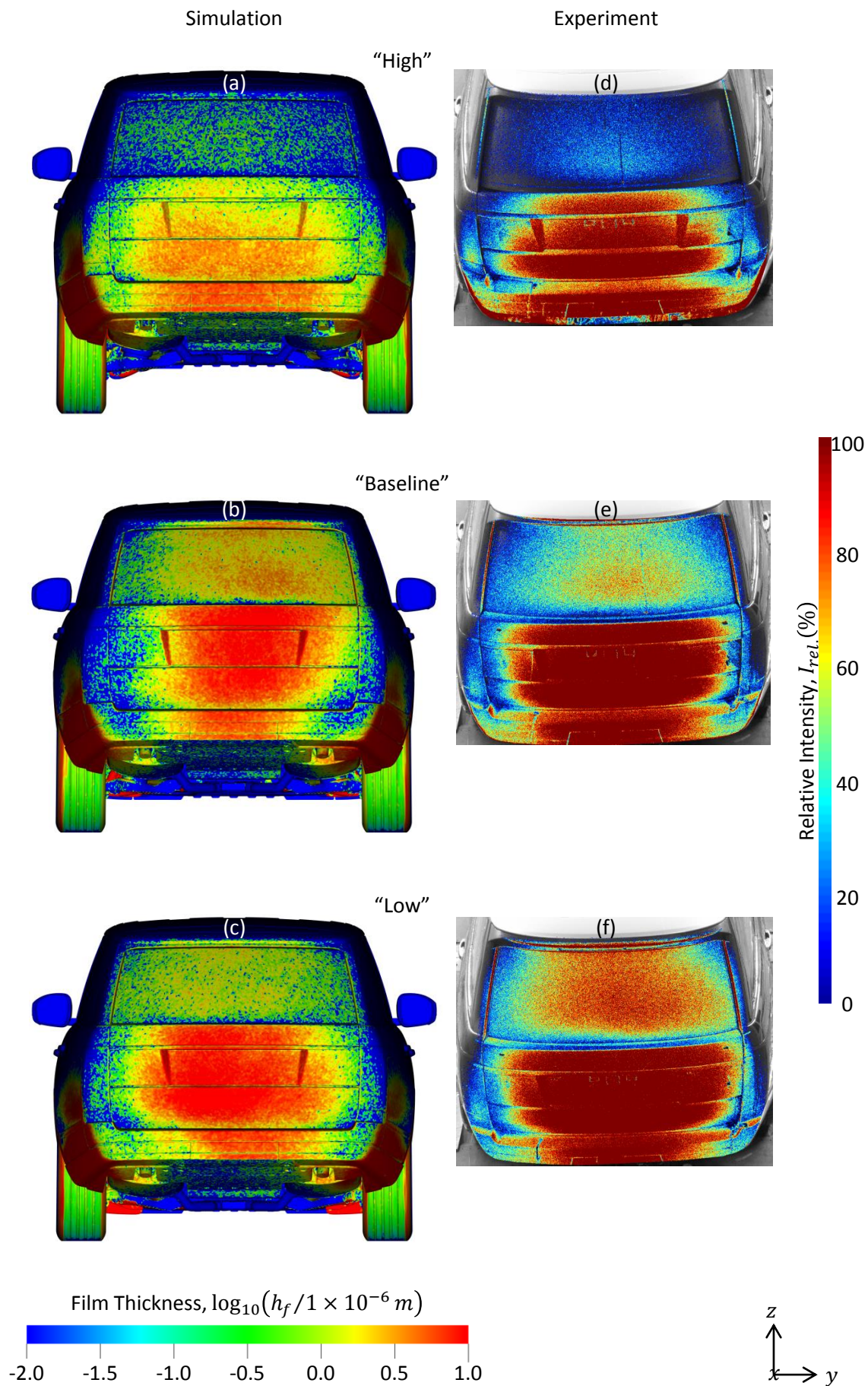


**Figure 80. Rear Surface Contamination Distribution Pattern Simulations and Measurements for the 13MY Range Rover in High, Baseline and Low Trim Height Settings**



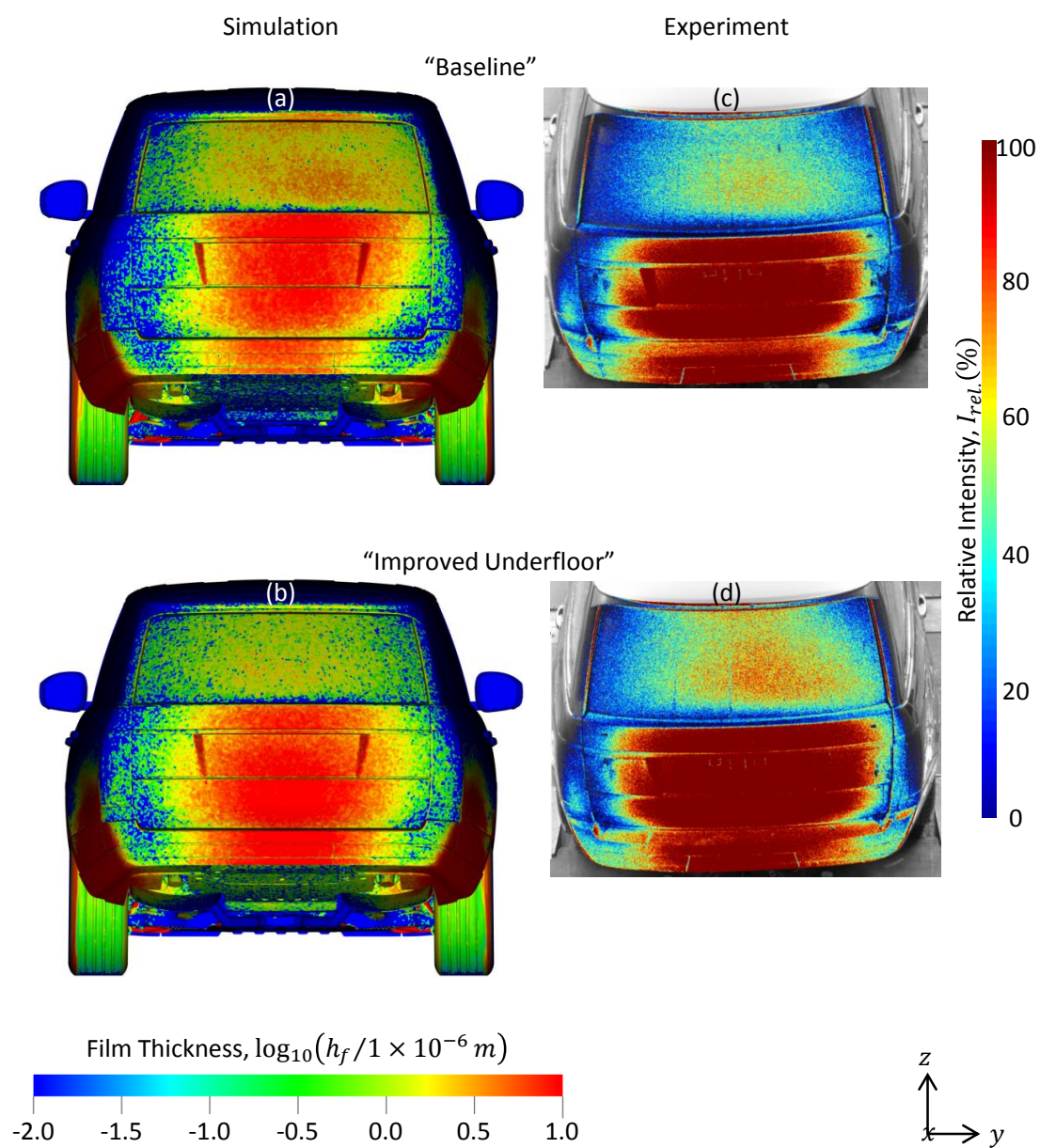


**Figure 81. Rear Surface Contamination Distribution Pattern Simulations and Measurements for the 13MY Range Rover with Baseline and an Aerodynamically Improved Underfloor**

### 6.3 RELATIVE SURFACE CONTAMINATION FACTORS

In an original analysis, two relative surface contamination factors were derived for total deposition: one from experiment and the other from simulation. These rely on dividing the cumulative deposition time history for a changed vehicle configuration  $C(t)$  by that for its baseline  $C(t)_{Baseline}$ , i.e.:

$$C_{Rel.}(t) = \frac{C(t)}{C(t)_{Baseline}} \quad \text{Eqn. 31}$$

This contamination factor is a function of time; however, if the deposition histories maintain the same proportionate relationship then this ratio will be constant. For the experimental metric  $\%AI_{ave}$  data was taken across the relatively linear Coverage phase, hence:

$$C(t)_{Rel.Expt.} = \frac{\%AI_{ave}(t)}{\%AI_{ave}(t)_{baseline}} \quad \text{Eqn. 32}$$

Further, the data can be placed on a normalised time scale representing the progress through the Coverage phase, from its start  $[t_{start}]$  at 20 s to its completion  $[t_{end}]$  at 45 s:

$$t_n = \frac{t - t_{start}}{t_{end} - t_{start}} \quad \text{Eqn. 33}$$

Hence:

$$t_{n.Expt.} = \frac{t - 20}{25} \quad \text{Eqn. 34}$$

which gives a range of  $0 \leq t_n \leq 1$  over the experimental Coverage phase.

The simulation data was treated in a similar fashion, but using the complete period of the calculation and taking cumulative deposited mass  $M(t)$  as the measure of deposition,

$$C_{Rel.CFD} = \frac{M(t)}{M(t)_{Baseline}} \quad \text{Eqn. 35}$$

These contamination factors are also plotted on a normalised timescale [as  $t_{start} = 0$ ]:

$$t_{n.CFD} = \frac{t}{6} \quad \text{Eqn. 36}$$

Temporally, the simulation period is not formally equivalent to the experimental Coverage phase perhaps capturing only a short sample of it, following the end of a Start-up phase. However, the linear trend for deposition with time justifies making a comparison with experiment by placing the normalised simulation results on a similarly transformed time scale. Finally, this treatment also neglects the Start-up phase seen in the simulations; however, as previously noted, this is *at least* twenty times smaller than that seen in the experiments and, whilst noticeable, is of little consequence to the outcome of this analysis.

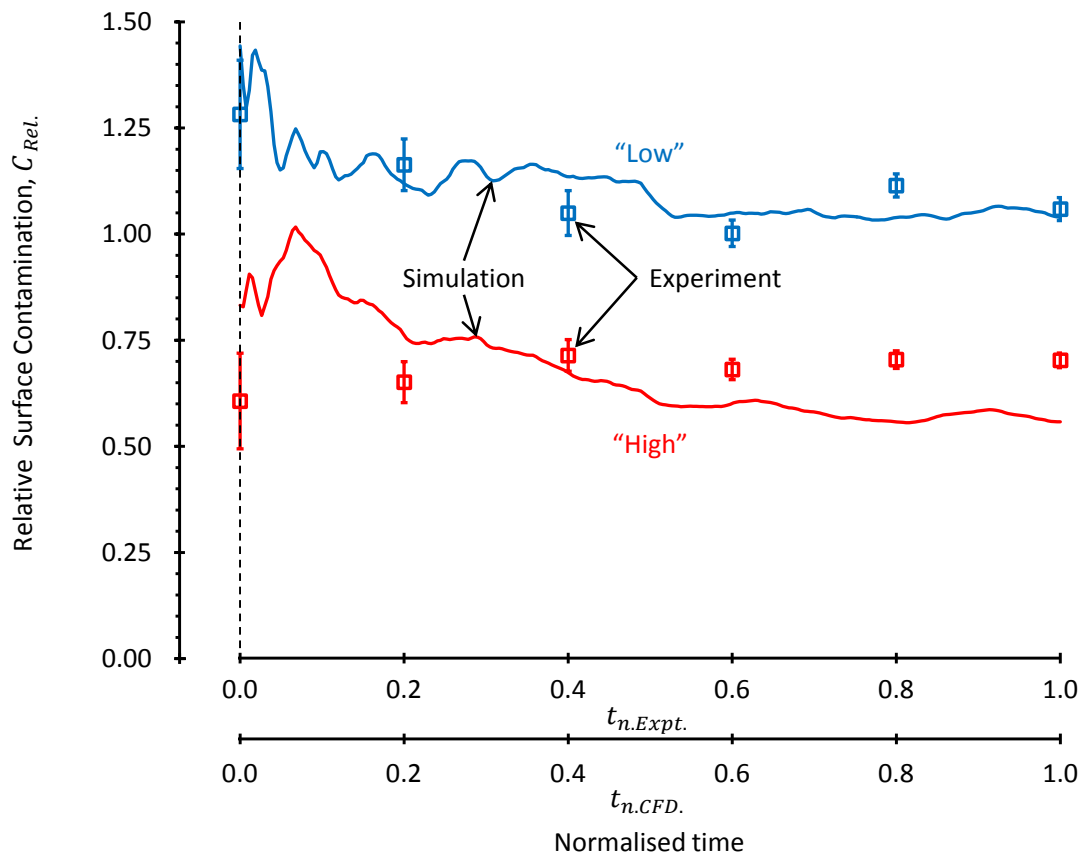


Figure 82. A Comparison of Measured and Simulated Relative Surface Contamination Factor Changes with Trim Height on the 13MY Range Rover

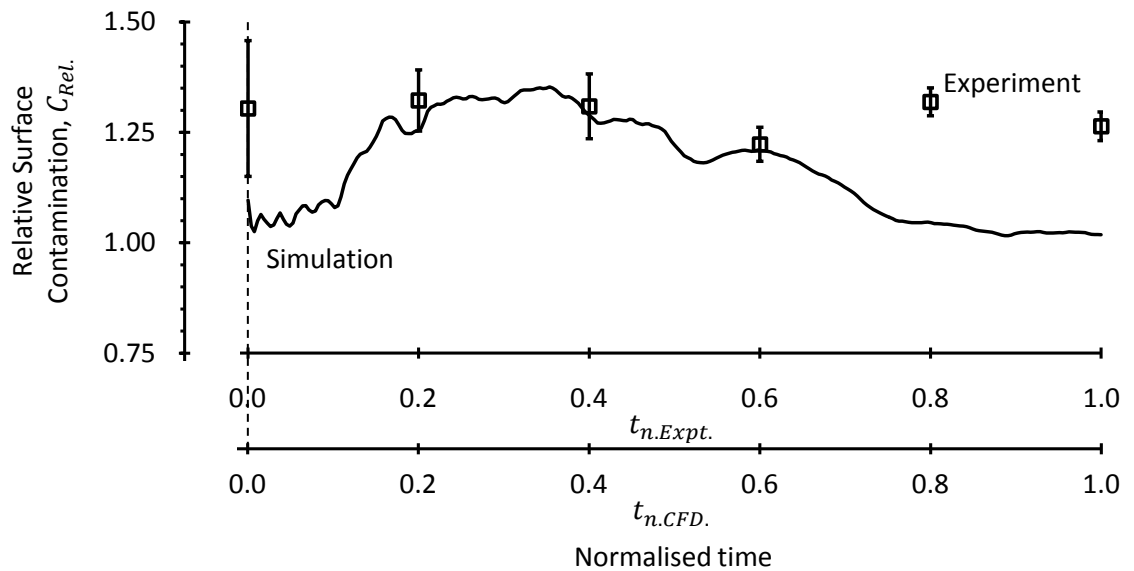


Figure 83. A Comparison of Measured and Simulated Relative Surface Contamination Factor Changes with Underfloor Improvement on the 13MY Range Rover

The relative contamination factors for the trim height and underfloor changes are presented in Figures 82 and 83. For the changes to vehicle trim height, Figure 82 shows that agreement between experiment and simulation is excellent when the trim height is reduced: over the latter half of the simulation period experiment and simulation fall within 6% of each other, differing by only 1% at the end of the comparison. When trim height is increased the agreement is poorer, with experiment and simulation differing by 21% on this measure of change in total deposition.

In making the same comparison for the aerodynamically improved underfloor Figure 83 reveals a mixed picture. Over the initial part of the simulation [ $0.2 \leq t_{nCFD} \leq 0.6$ ] there is a very close agreement with experiment, however this falls away over the remainder of the calculation and ultimately the simulation differs from experiment by 19%. This is effectively a fall in the rate of deposition and suggests a significant change in the wake dynamics. Figure 84 lends weight to this deduction by comparing the lift force histories for the improved underfloor and baseline simulations. After the first second of the simulation the baseline lift coefficient reaches a settled mean value and the two lift histories align well. After around three seconds the aerodynamic lift experienced by the improved underfloor case rises and this difference becomes substantial. This implies a transient increase of downwash in the rear wake, which could suppress the vertical advection of spray onto the rear surfaces and lead to the observed reduction in deposition. Although this perturbation appears to have passed after the five second mark, the short remaining duration of the simulation and the cumulative nature of deposition mean that the simulated result cannot recover to the relative level seen in the experiment. The appearance of vertical wake instability aligns with the wake stability model of Grandemange *et al.* (2013), as illustrated by Figure 85. This has been discussed previously in CHAPTER 3, to help explain the wake dynamics of the simplified geometries used in the early phase of this research. In contrast to the Windsor and Generic SUV models, the Range Rover sits in the “interfering region” where, “... the instability in one direction takes the advantage on the other” (Grandemange *et al.*, 2013). In this case it is plausible to suggest that the Range Rover is more likely to experience vertical, i.e. lift changing, instabilities given that it sits close to the vertical instability zone.

It is intriguing that such vertical wake instability was only seen for the case with the improved underfloor flow condition and none of the other simulations run during this work. It may be happenstance, due to the intermittent nature of the instability linked to the relatively short simulation periods used here. An alternative explanation could be that Grandemange’s wake dynamics model, derived as it is from experiments on test properties with smooth underfloors is most applicable to this particular vehicle configuration. In either case, the outcome for the improved underfloor condition illustrates that the simulation results are potentially vulnerable to this type of low-frequency or intermittent change in the unsteady wake dynamics.



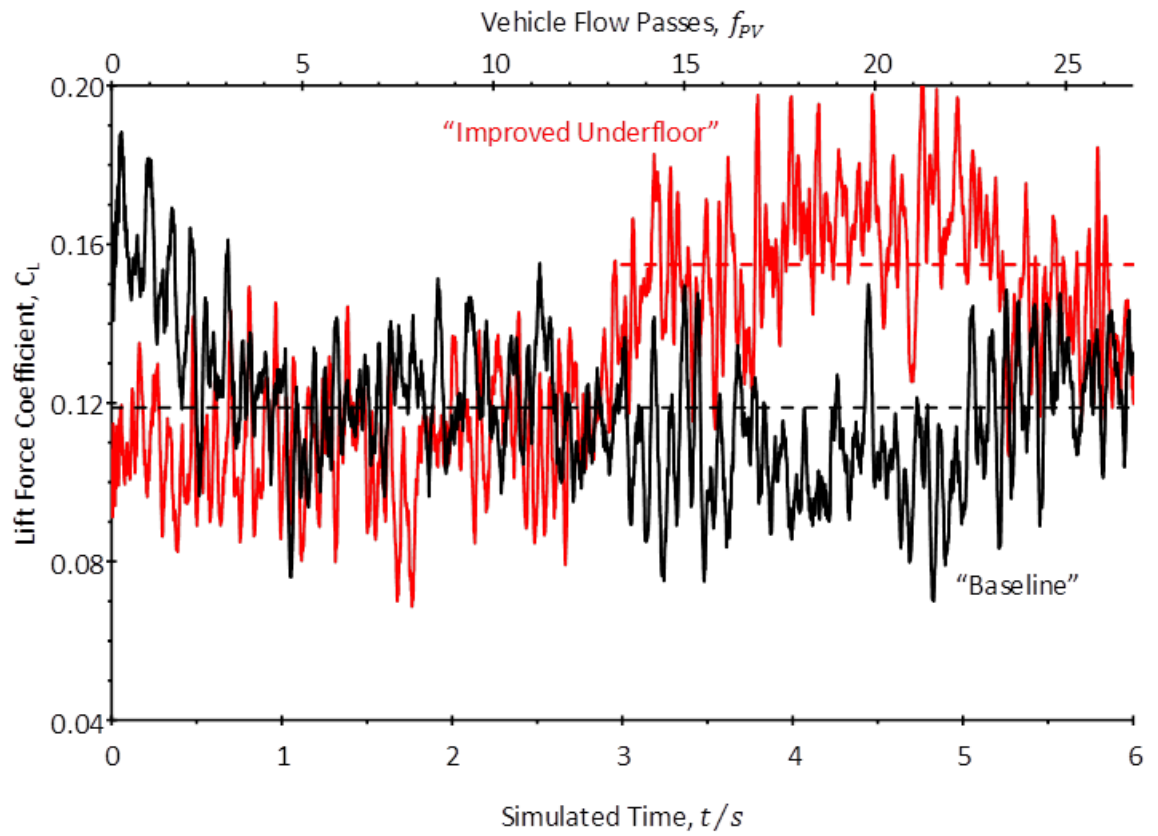


**Figure 84. A Comparison of Simulated Lift Coefficient Histories for the Baseline and Improved Underfloor Configurations on the 13MY Range Rover**

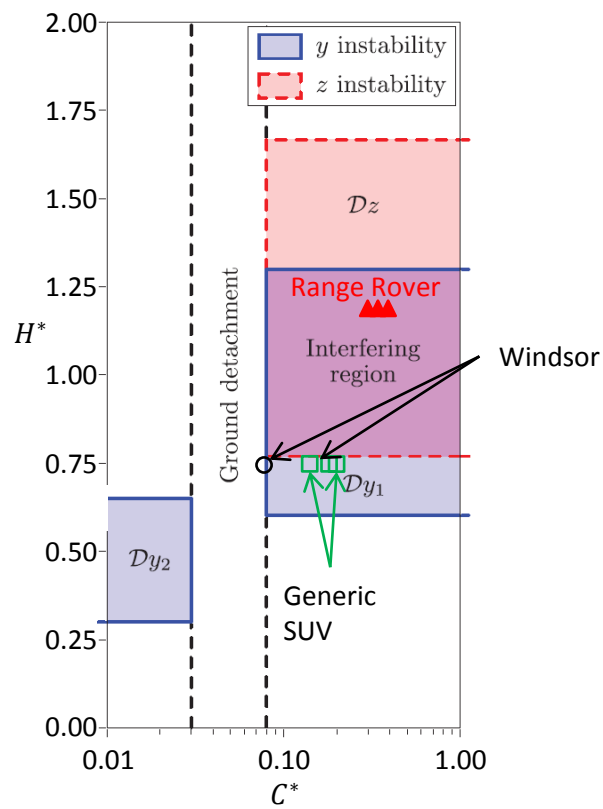


**Figure 85. The Range Rover Compared against the Wake Stability Model of Grandemange *et al.* (2013)**

## 6.4 SIMULATION ACCURACY FOR THE REAR SURFACE ZONES

The novel concept of using relative contamination factors was extended to examining not just changes to total deposition, but the changes to deposition levels for individual rear surface zones. As discussed in *Portfolio Report C*, after establishing that the simulation technique provided the correct relative ranking of rear surface zones for 80% of the available comparisons, a modified version of Eqn. 31 was used to assess how well the differences from the baseline were predicted. This approach used the final contamination levels: the contamination level at the end of each Coverage phase [% $AI_{ave\ t=45s}$ ] for the experiments; the contamination area density [ $\rho_{A\ t=6s}$ ] at the end of each simulation, i.e.

Eqn. 37

$$C_{Rel.Expt.} = \frac{\%AI_{ave\ t=45s}}{(\%AI_{ave\ t=45s})_{Baseline}}$$

Eqn. 38

$$C_{Rel.CFD} = \frac{\rho_{A\ t=6s}}{(\rho_{A\ t=6s})_{Baseline}}$$

These are compared in Figure 86 where the simulated [blue] and measured [red] relative contamination factors are provided for each rear surface zone. The overall directional trends are well matched by the simulations, with the exception of the rear bumper (b) and rear lamps (f) in the High trim height configuration. A measure of the differences between the relative contamination factors found from experiment and simulation is provided in Table 7. This quantifies these errors for the rear surfaces in total [TOTAL] along with each individual rear surface zone. Finally, it presents an average error for the latter as a mean [RMS] over all the rear surface zones  $\bar{\delta}_{RMS}$  for each vehicle configuration. This novel assessment of simulation performance shows excellent agreement between test and simulation for total deposition with the vehicle at the lowest trim height. However, it illustrates that within this, deposition for individual surface zones may not be predicted as well; for example the rear screen zone has a 65% error. For the vehicle configurations that could be taken to indicate future development trends – low trim height and improved underfloor – with the exception of the rear screen, average errors in predicting contamination on a particular rear surface zone are less than 35%.

**Table 7 Differences between Simulated and Measured Relative Contamination Factors by Rear Surface Zone**

Rear Surface Zone	$\delta = 100 \times (C_{Rel.CFD} - C_{Rel.Expt.}) / C_{Rel.Expt.}$		
	Low Trim Height	High Trim Height	Improved Floor
TOTAL	-2%	-21%	-19%
License Plate	9%	-48%	-21%
Tailgate	7%	-27%	-18%
Rear Bumper	17%	-19%	15%
Rear Screen	-65%	140%	-62%
Rear Lamps	6%	87%	34%
$\bar{\delta}_{RMS}$	31%	78%	35%

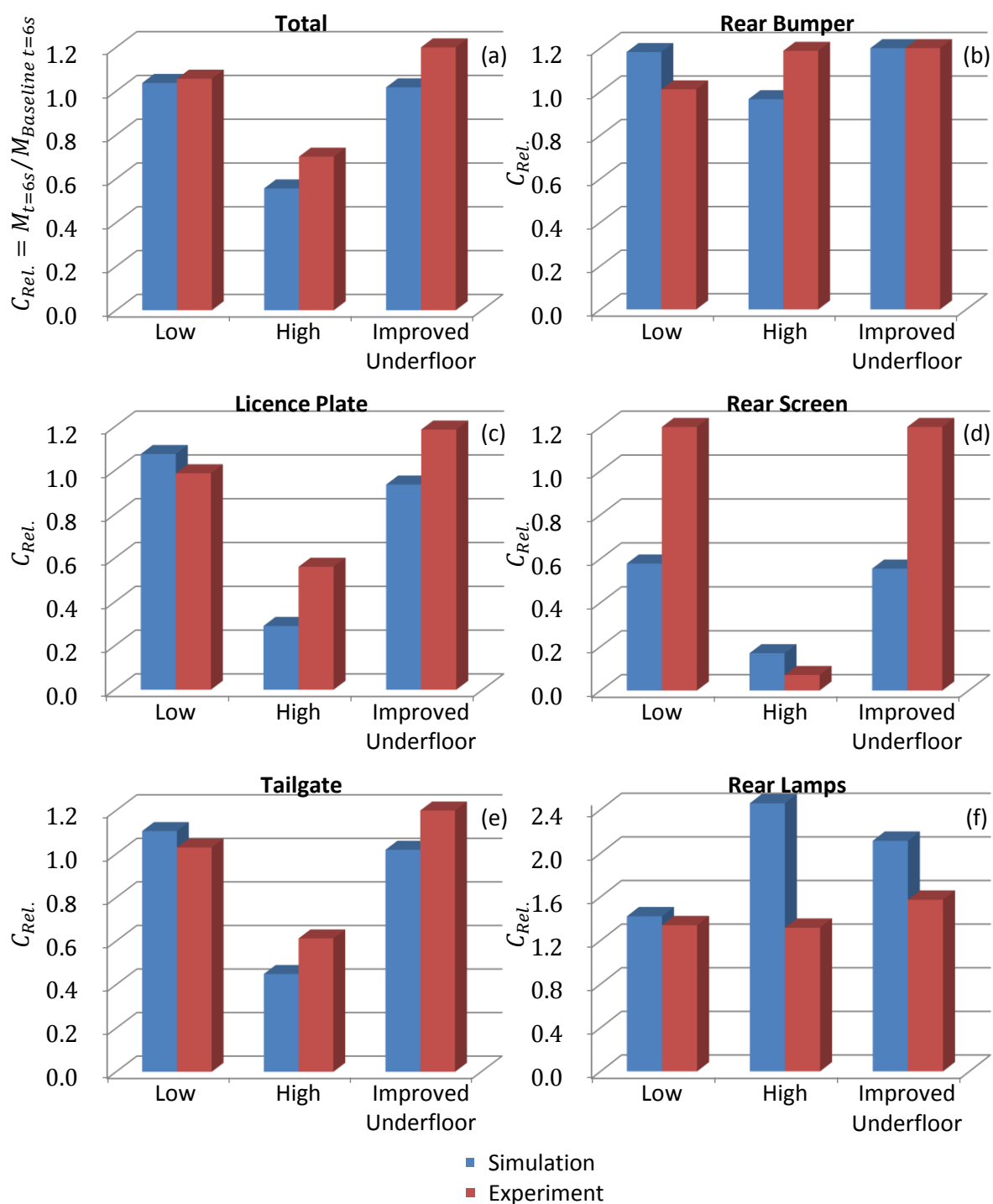


**Figure 86. Relative Contamination Factors Compared for the Rear Surface of the 13MY Range Rover**

## 6.5 SIMULATION ACCURACY FROM AN ENGINEERING DEVELOPMENT PERSPECTIVE

So far, this chapter has provided the first quantitative assessment of the accuracy attainable for rear surface contamination predictions using the state-of-the-art approach developed through this work. In doing so it sets a benchmark for future studies. However, as part of the progression towards deploying an innovative engineering simulation process, it also raises the question of whether the level of accuracy demonstrated is sufficient. This does not require the simulation approach to be flawless, as Box (1978) observed no model exactly matches the real world so, “the only question of interest is “Is the model illuminating and useful?””

Within a vehicle development process utility can be defined in a number of ways. For instance it is important not to allow failure modes in the design [i.e. ways in which the design fails to perform as intended] to pass undetected into later development stages, where rectification can be time-consuming and expensive. The question then becomes “how reliably can a simulation process prevent the propagation of failure modes?” This can be addressed through the tools provided by Failure Mode Effects Analysis [FMEA] (Stamatis, 2003: 21). One part of this approach is to score the likelihood that design controls, such as computer simulation, will detect a failure mode. This is done by matching the performance of a method to a list of standard statements aligned to a scale, generally from 1-10, with low scores indicating better performance. The resulting “detection event rating” [ $d$ ] provides a measure of an engineering simulation method’s utility.

The author, in *Portfolio Report C* describes the standard scheme for determining detection event ratings for numerical simulation methods operated by J/LR, derived from the Society of Automotive Engineers [SAE] Standard J1739 (SAE, 2009). An extract showing the most relevant ratings is provided in Table 8. With the simulation method able to correctly rank vehicle configurations and rear surface zones with 80% success a score of either  $d = 5$  or 7 is appropriate, as moving to a better score would require a 90% success rate. Both of these scores indicate that the simulation approach would fit with a test-lead process, providing some degree of simulation support. Achieving a score of  $d = 5$  requires that the method predicts both the direction and order of magnitude of the test results. However, the changes to the contamination level of the rear screen were not correctly captured, with differences between experiment and simulation in the range  $-65 \leq \delta(\%) \leq +140$  [See Table 7]. Given the importance of the rear screen for drivers’ vision and potential for degradation of the rear wiper system if soiling is excessive (Gaylard *et al.*, 2017a) a detection event rating of  $d = 5$  is not yet warranted. Nevertheless, it is clear that the method is, “Useful for predicting direction of test results and making broad A/B comparisons” hence a score of  $d = 7$  is warranted. In addition, its performance in assessing other rear surface zones and frequently generating correct rankings suggests clear potential to be developed to at least  $d = 5$ .

As Box (1978) noted, models that are incorrect in an absolute sense may still be illuminating. With the deep insight into flow structures and surface contamination mechanisms demonstrated in CHAPTER 4, the simulation process certainly has utility in this sense. Beyond that, this assessment supports its inclusion as an engineering tool into a vehicle development process on the basis of its ability to detect failure modes in the design.

The next chapter describes the integration of the simulation approach into an innovative engineering development process, along with its subsequent deployment and use at J/LR. However, to appreciate where this fits in the overall vehicle development process a general industrial approach to automotive development is outlined first.

**Table 8 Selected FMEA Detection Event Ratings**

Rating, <i>d</i>	Rating Criteria	Programme Implications
5	The method predicts direction and order of magnitude of test results with the ability to do reliable A/B comparisons	Testing driven development with analytical support In general, successful at least half the time
7	Useful for predicting direction of test results and making broad A/B comparisons	Testing driven development, with little analytical support In general, successful less than half the time

## **CHAPTER 7 A PROCESS INNOVATION**

### **7.1 AUTOMOTIVE PRODUCT DEVELOPMENT**

This work has culminated in the development of an innovative process for the numerical simulation of rear surface contamination for SUVs. Starting in CHAPTER 3 with two novel simple digital systems, one with and one without wheels, the requirements for accurately simulating vehicle and wheel wake flows, along with surface deposition processes were identified. In CHAPTER 4 these lessons were applied to a series of original simulations of rear surface deposition on a production vehicle, enabling the effect of trim height and underfloor flows to be captured numerically. A series of equivalent physical experiments were described in CHAPTER 5, enabling the accuracy of the simulations to be assessed in CHAPTER 6. Having established that this numerical approach is sufficiently accurate for product development, the following chapter summarises its integration into the J/LR aerodynamics development process, its subsequent deployment and use. However, to provide some context for this discussion a general description of automotive product development is required.

Developing cars is a complex and time-consuming activity, with premium manufacturers taking around five years to develop a vehicle, using their standard processes (Plucinsky, 2012). Vehicle development is generally conceived of as a set of sequenced, concurrent activities as shown in Figure 87. This generic model identifies three parallel work streams: (a) Development, (b) Planning and (c) Testing. Vehicle engineering development sits in the “Development” work stream, with “Planning” focussed on the preparation of production facilities and “Testing” the evolution from first prototype build to the final production vehicle.

Progress through the development is controlled via gateways [numbered in Figure 87] which mark the end of predetermined stages in the development of the vehicle. As each gateway is approached a standard set of activities will be executed, often in parallel. The stages support the product’s maturation to a point where it can be launched into the market, with successive stages reducing the scope for change. Progressing into a stage requires the relevant gateway to be passed; generally via a review where the design is assessed against a combination of performance targets and standards. This provides an opportunity to progress, delay or even terminate the project. In essence, this gated process controls risk through the progressive generation of product knowledge as the development progresses from concept definition [“Concept Book”] through its technical development [“Technical Specification”] to start of production [SOP] and the first customer car [Job #1]. This “Stage Gate” approach, derived from the work of Cooper (1990) is common across the automotive industry.

It is also important to note that under this general scheme physical prototypes are not available until after pre-development and “Styling” activities have been completed. This illustrates the necessity of numerical simulation [along with the use of bespoke test properties] to develop vehicle characteristics that are sensitive to external shape, such as aerodynamics and surface contamination.

The Development phase contains specific departmental work which is executed concurrently. Hence this single [red] bar in Figure 87 could be expanded to show the full gamut of engineering processes required to bring a vehicle to market, including its aerodynamic development. This is where the innovative rear surface contamination simulation process developed in this work fits into overall vehicle development. The following section describes the process elements and their relationship with the relevant pre-existing engineering activities in the aerodynamics and surface contamination work streams.

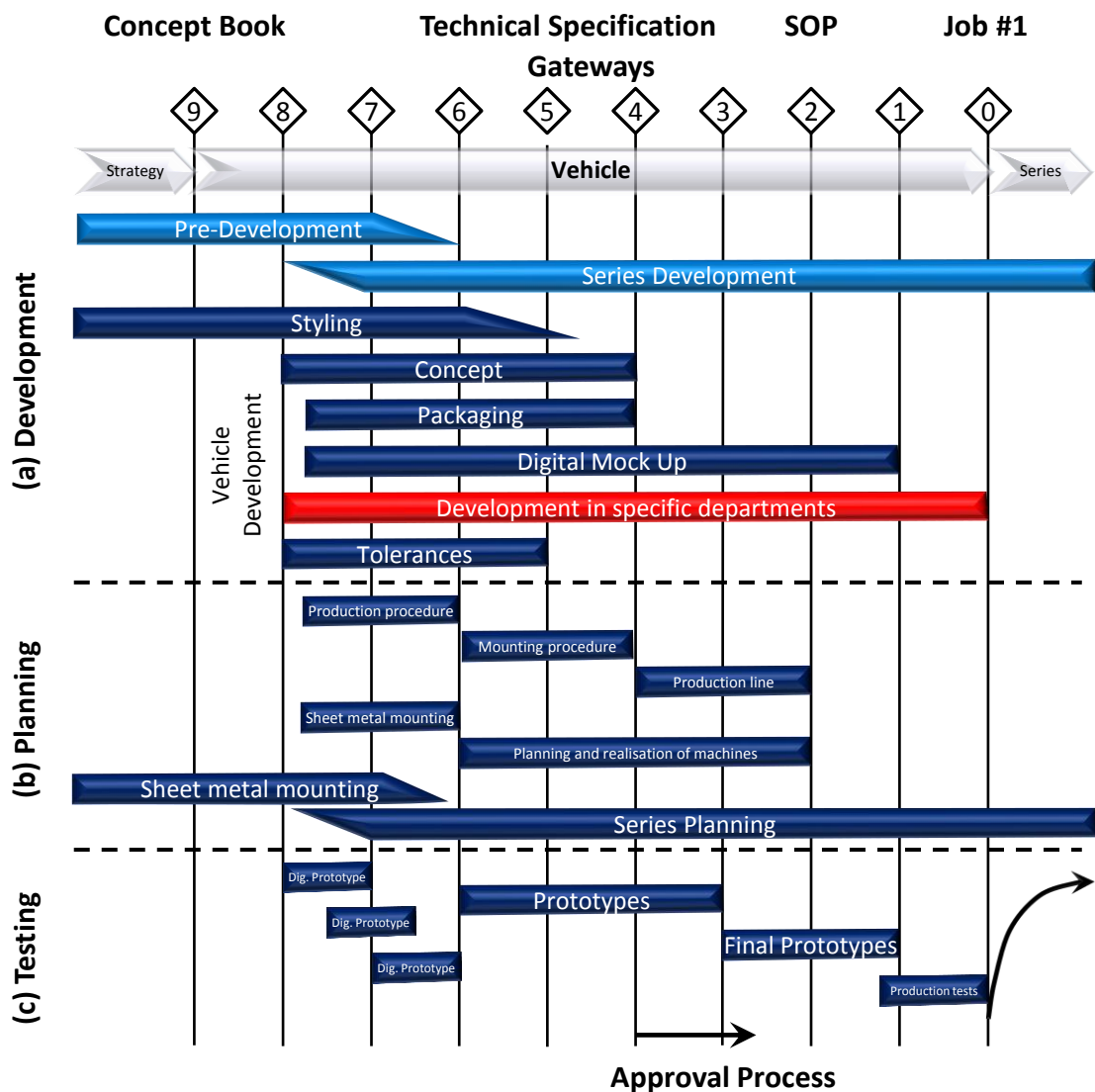


Figure 87. A Generic Automotive Development Process (Schuetz *et al.*, 2016:381)

## 7.2 AN INNOVATIVE SURFACE CONTAMINATION PROCESS

### 7.2.1 Overview

A high-level view of the innovative rear surface contamination simulation process developed through this work is set in context with aerodynamics development at Jaguar Land Rover [J/LR] in Figure 88. The timeline provided by the sequential development phases broadly aligns with the generic model shown in Figure 87, with some specific differences. For example, the J/LR process gives more prominence to the strategy phase, with “Technical Specification” conceived as a “Delivery” phase.

The main aerodynamic development tasks are placed on this programme timeline, with concurrent activities associated with surface contamination [Water & Dirt Management, W&DM]. This is appropriate as surface contamination is an integral part of the aerodynamics discipline (Gaylard *et al.*, 2017a). Importantly, Figure 88 also shows where the surface contamination simulation process is best placed: as a complement to the physical test activity; an approach that aligns with the assessment of its accuracy presented in CHAPTER 6.

In common with the aerodynamics work stream, which is largely focused on drag reduction, Figure 88 shows the W&DM process starting with providing early design guidance based on fundamental principles, distilled experience and competitor benchmarking. The innovative simulation process then provides an opportunity for design themes to be assessed [1] before any prototypes or even the bespoke aerodynamics test property [“Aerobuck”] is available. This enables the impact of aerodynamic changes to be assessed and the physical test phase [2] to be entered with a range of opportunities for improvement already identified and an understanding of the combined flow field and spray behaviour around the vehicle. The focus of the simulation process then shifts to developing countermeasures [3] to mitigate any issues, in support of the test activity. The overall objective is to have a design that meets its target performance prior to the Final Data Judgement [FDJ] gateway, as this defines the first pre-production prototypes. Subsequent design changes are more difficult past this point as both aesthetic and engineering design work is notionally complete and modifications are likely to affect other aspects of vehicle performance, or even the delivery of production tools. The process aims to develop FDJ level simulation validation models before the arrival of the physical prototypes [4] to enable the simulation methods to be assessed and improved. Once physical prototypes are available then there can be some scope for tuning of vehicle trim [e.g. wheel deflectors, underbody panels and spoilers] if the VP testing phase detects any failure modes. Both work streams conclude with a sign-off, the final tasks being correlation of the numerical simulation approaches on production geometry as a preparation for subsequent programmes.



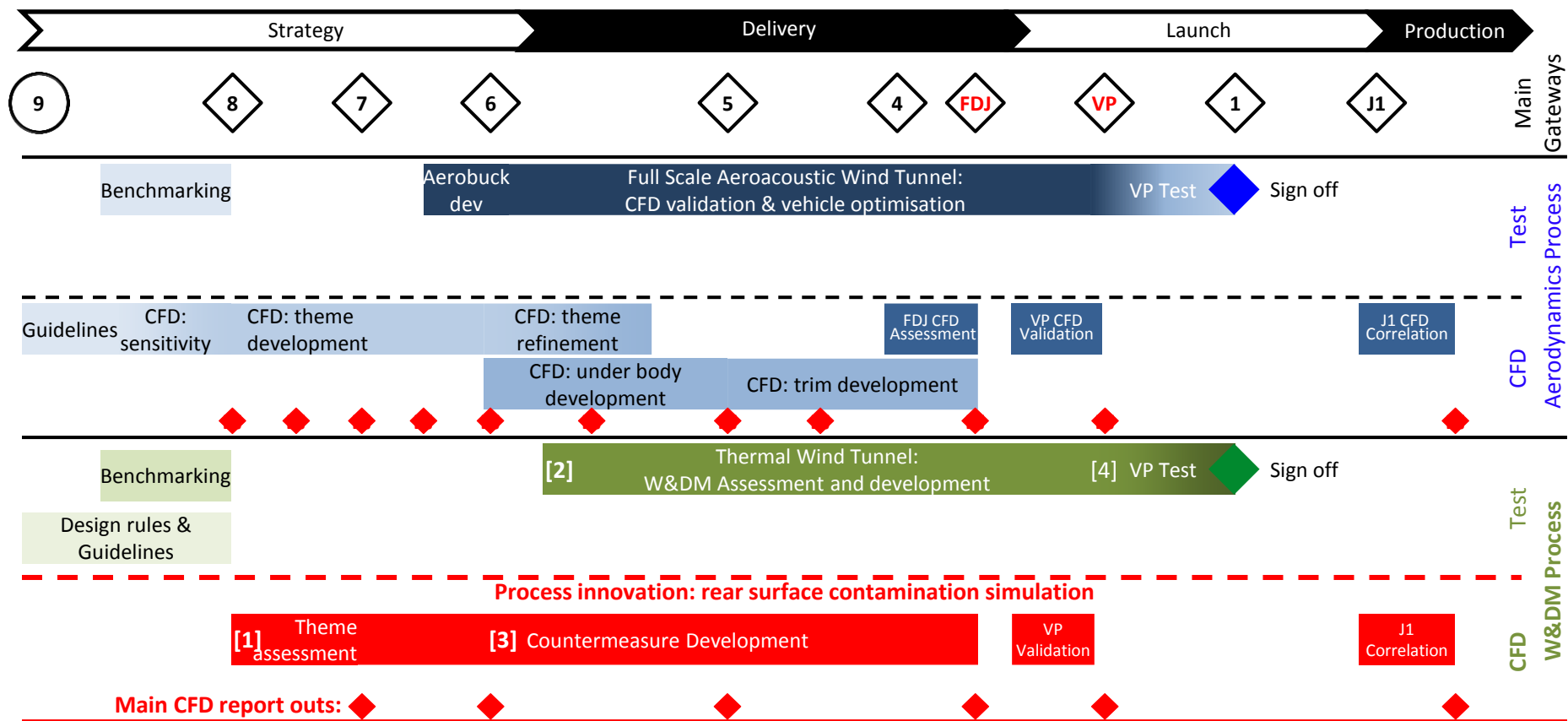
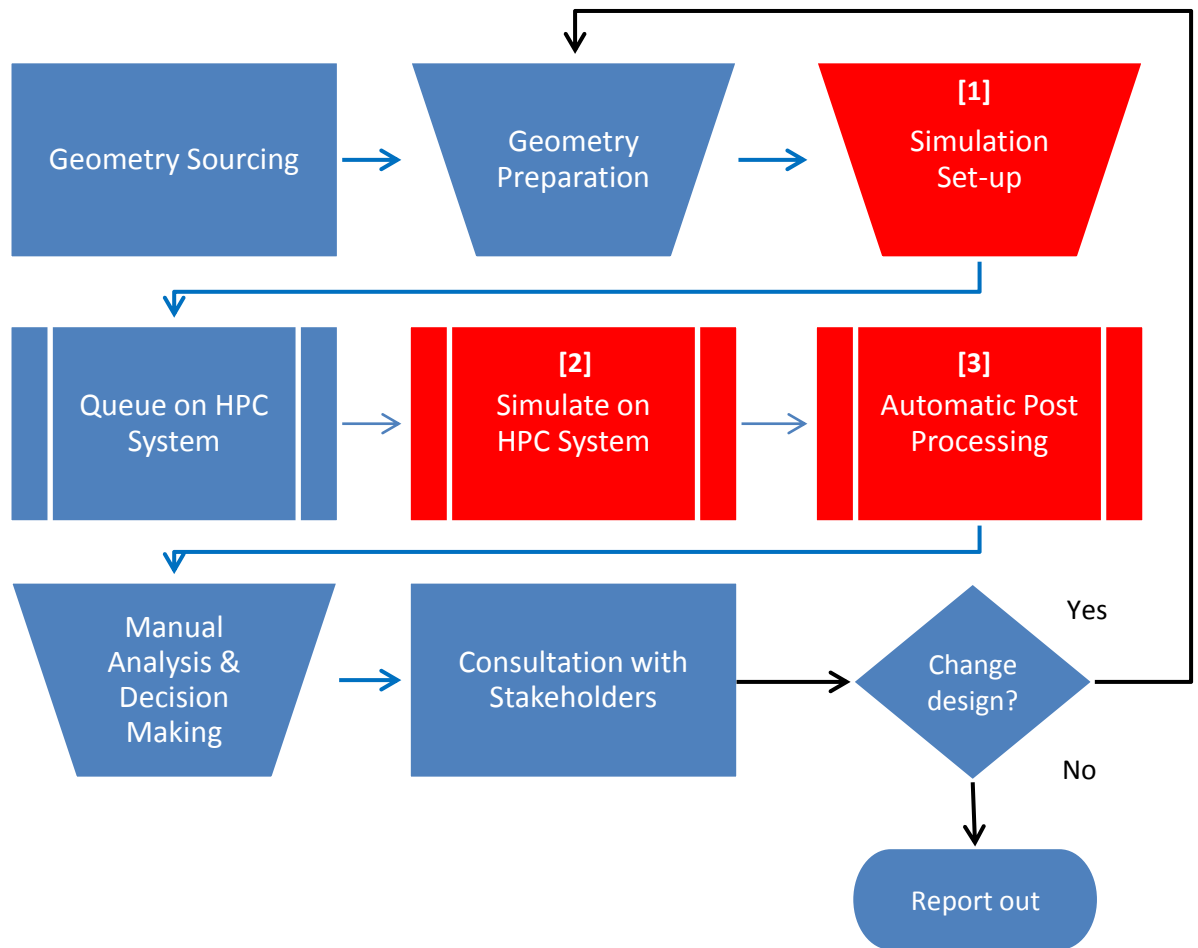


Figure 88. The New Rear Surface Contamination Simulation Process as part of Aerodynamics Development at Jaguar Land Rover



**Figure 89. Flow Chart Summarising the Aerodynamics Simulation Process with Activities Modified to Accommodate Rear Surface Contamination Simulation**

### 7.2.2 Process Elements

As discussed in *Portfolio Report C*, the surface contamination simulation approach developed in this work was integrated alongside the existing J/LR aerodynamics simulation process. The general approach was to maximise commonality between the two work streams by using existing process elements where practicable. This minimised the effort required to deploy the new simulation process, staff training requirements and the additional workload resulting from simulating both aerodynamics and surface contamination.

The main steps in the simulation processes are illustrated in Figure 89. Common elements are highlighted in blue, whilst new rear surface contamination simulation process steps are numbered and highlighted in red. The overall simulation work flow can be summarised as: digital geometry is sourced and prepared to meet the requirements of the simulation approach. Once set up, the numerical simulation is queued on a High Performance Computing [HPC] system until sufficient CPUs can be allocated to the task. Following this, the simulation runs until pre-determined criteria are met [such as stability of the mean force coefficients] and automated post-processing scripts are run to provide a basic set of data tables and images, capturing the main results. Once these are available, further manual analysis is undertaken as required and decisions are made on

how to modify the vehicle design to meet its performance targets. To effect design change that will be recognised within the development programme key stakeholders are consulted; including Designers, engineers from other relevant areas and programme management. If a formal design change is sanctioned this will generally require a confirmatory analysis, as it will typically differ from the initial proposal.

As a consequence of the author's strategic decision to use a modified version of the CFD solver currently used for aerodynamics simulations, the acquisition of digital surface geometry definitions and their preparation into a format suitable for simulation is common between both work streams. In the same vein, the existing High Performance Computing [HPC] system and queue management facility is used. Finally, the same decision-making and reporting processes within the development programme can feed back the additional data generated by the rear surface contamination simulation. In contrast, three new process steps were required for surface contamination simulation: [1] set-up, [2] execution and [3] post-processing. These are outlined in the following sections.

#### 7.2.2.1 Simulation Set-Up

As discussed in CHAPTER 2, the surface contamination simulation approach developed in this work uses a version of the CFD software used for aerodynamics simulation at J/LR, with its capabilities extended to include the simulation of airborne droplets and surface water films. This enables surface contamination simulations to be generated by converting an existing aerodynamics set-up.

The main characteristics of aerodynamics simulations are:

- use of a large low-blockage simulation domain;
- highly detailed geometric representation of the vehicle;
- simulation of wheel rotation;
- onset flow velocity set to 100 km/h;
- a moving ground-plane.

Many of these approaches can be carried over unchanged into the surface contamination simulation set-up. As seen in CHAPTER 4, the surface contamination approach developed through this work also uses a large low-blockage simulation domain. In addition, the same highly-detailed geometrical models are also used.

To maintain commonality with aerodynamics simulation practise, a moving ground plane is also included in the deployed surface contamination simulation process. This has the practical advantage of minimising the effort required to move from an exclusively aerodynamics to surface

contamination simulation; however, this does introduce a difference between surface contamination simulation and achievable full-scale tests. Thorough analysis of the effect on simulation results provided in *Portfolio Report C* showed that the ranking of rear surface zones by deposition level remains unchanged and absolute differences in deposition are typically less than 5%. The most significant exception to this was seen at the rear screen, where the moving ground plane appears to reduce predicted levels of deposition by 26%; as this is substantially over-predicted in the direct comparisons with test data there is little reason to see this as a reason not to use a moving ground plane. As with emitting spray from all four tyres, this approach provides a simulation that is more representative of the “on-road” experience of a vehicle. However, as this work is based on an SUV with typically high ground-clearance the issue should be re-visited if rear surface contamination simulation is required for lower ground clearance vehicles such as saloons, where a moving ground plane will have a larger influence on rear wake structure (Koitrant *et al.*, 2014). In addition, this outcome is surprising given observations to the contrary made by Lajos *et al.* (1984, 1986) and Jilesen *et al.* (2013) and therefore it warrants further investigation.

In contrast, it was necessary to depart from the aerodynamic simulation approach in three key aspects. First, the addition of a tyre spray model was required [See Figure 49]. The work reported in *Portfolio Report C* has confirmed that spray from the front tyres contributes little to rear surface contamination, as previously suggested by the author (Gaylard *et al.*, 2014). Therefore, spray is set to be released from all four tyres in the deployed process. This has the advantage of providing a simultaneous simulation of deposition on both body side and rear surfaces at little additional computational cost. Although body side surface contamination is outside the scope of this work, it is nevertheless a significant issue which requires assessment through the development process (See Gaylard *et al.*, 2017a). Hence, the opportunity was taken to capture this additional information in the deployed process, in anticipation of its future extension. It also has the additional advantage of making the simulation reflect “on-road” performance more closely, as a vehicle driving on a wet road will generate spray from all four tyres.

Second, the spatial [and hence temporal] resolution used in this work has been independently developed to accurately capture the time-averaged wake flow structures whilst managing the additional computational burden of simulating spray and surface water film. As a result, resolution is less than that typically used in aerodynamics simulations; for example, a similar standard aerodynamics simulation could be expected to have c.  $182 \times 10^6$  voxels, around 15% more than the baseline lattice used here. This additional resolution is focussed on regions of fine geometric detail, such as intake grilles and wheel deflectors. Third, the onset flow velocity has also been reduced from 100 km/h to 80 km/h to maintain compatibility with the tyre spray model calibrations provided by Spruss *et al.* (2011). The reduction in flow velocity makes the lower

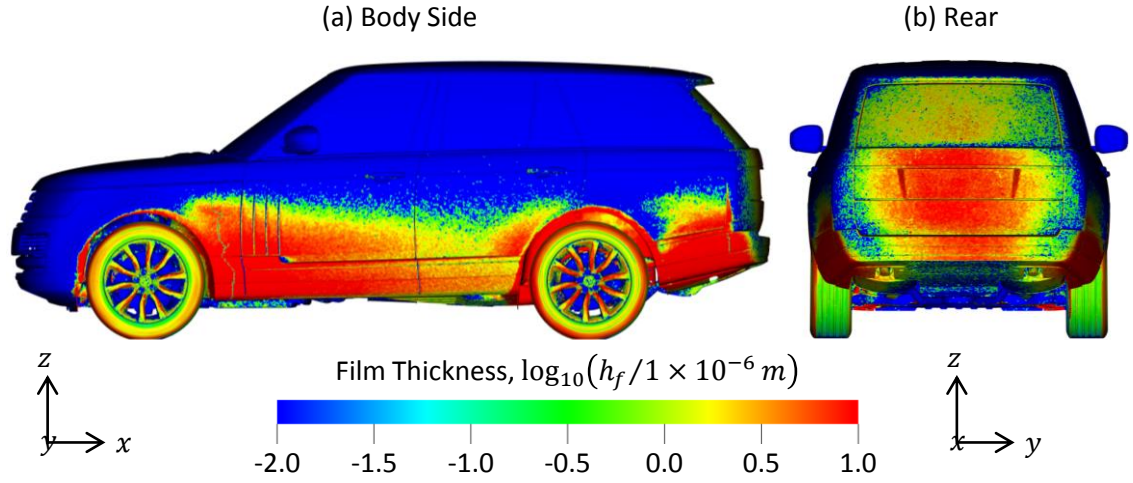


**Figure 90. Surface Contamination Distribution for the “On-Road” Configuration on (a) Body Side and (b) Rear Surfaces**

resolution lattice tolerable, as the spatial resolution required to capture attached boundary layers is reduced. In addition, the surface contamination simulation approach was shown in CHAPTER 4 to predict drag coefficients within +1% to -6% of their measured values [See Table 5]. Hence, to manage the computational effort and process throughput, the spatial resolution of the aerodynamics models is reduced to that used in this work as they are converted to surface contamination models by removing the finest [VR10] resolution zones.

In summary, the deployed process, illustrated by the simulation results presented in Figure 90, differs from the aerodynamics simulation approach only in terms of the addition of a *tyre spray* model and a *reduction in onset flow velocity*, with a commensurate *reduction in spatial resolution*.

#### 7.2.2.2 Simulation Execution

The inclusion of numerical models to represent spray and surface water films required running a modified version of the aerodynamics CFD software on the HPC system. The main difference from a user’s perspective is that surface contamination simulations are run to a fixed period of simulated time [6s] rather than stationarity of the mean force coefficients, as is the aerodynamics practise. This is generally a significantly longer period, as illustrated by the set of drag coefficient histories provided in Figure 91. In this Figure the unsteady drag coefficient history (a) is shown along with the settled mean value [blue broken line]. The derivation of this mean value is shown in Figure 91(b) where the author’s original receding averaging technique is used to identify a stationary mean value not contaminated by potentially un-physical start-up phase results (Gaylard et al., 2017b), which is provided by averaging the unsteady data from  $t = 1.5$  s onwards. Finally Figure 91(c) confirms this result by constructing a series of progressive forward averages [ $C_{Df\_ave}$ ] by incrementally extending the averaging period from  $t = 1.5$  s. The forward-averaged drag coefficient settles to within  $\pm 0.001 C_D$  of the mean value by  $t = 3$  s; half way through the

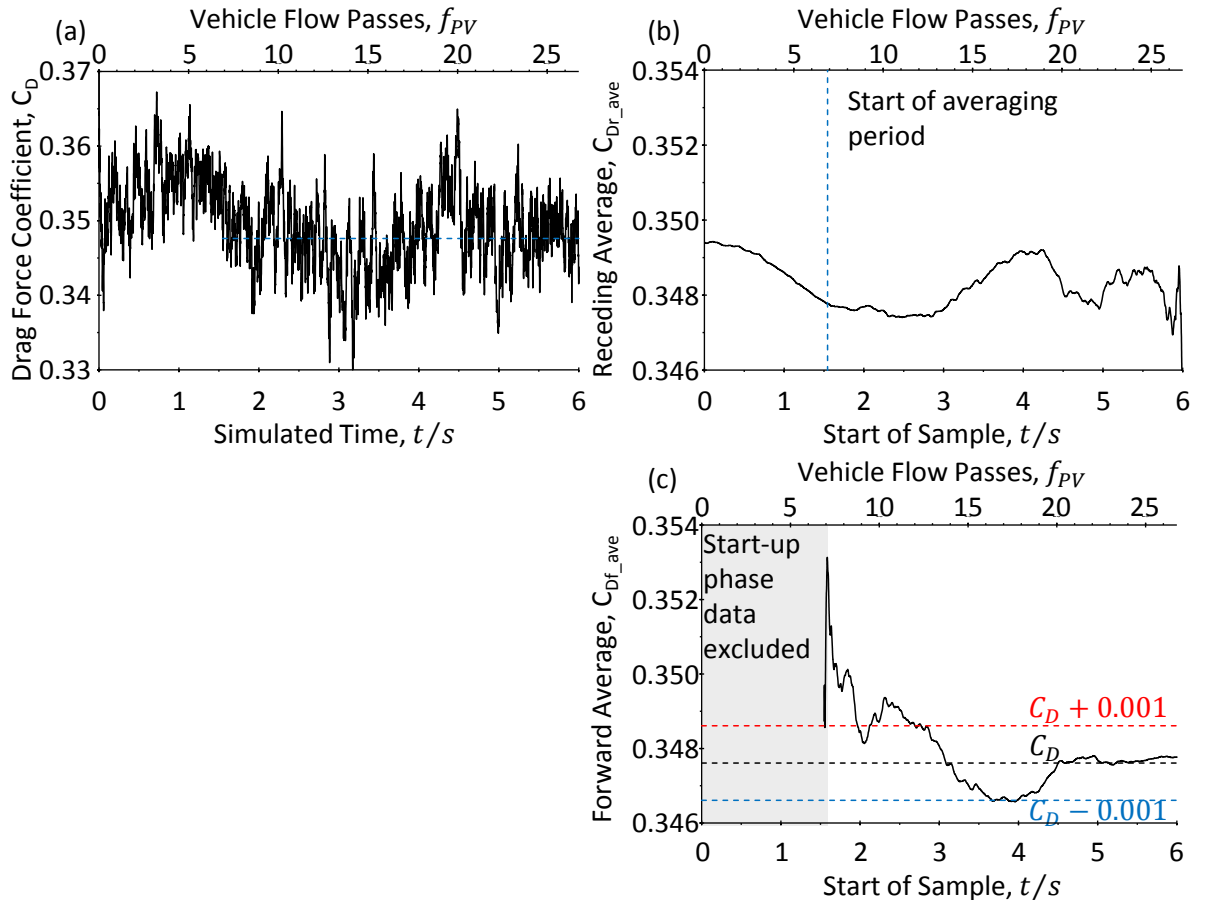


**Figure 91. Drag Coefficient Histories for the “On-Road” Configuration (a) Instantaneous, (b) Receding Average and (c) Forward Average**

simulation. This demonstrates that the surface contamination simulations are run for a substantially longer period than would be the case for a stand-alone assessment of aerodynamic drag. This additional resource requirement explains the reduced frequency of formal simulation reports out mandated by the process shown in Figure 88 for surface contamination, compared to aerodynamics.

### 7.2.2.3 Post Processing

The aerodynamics simulation process produces a set of automatically generated post-processing images, providing material for a basic assessment of the results. A similar capability has been developed for the surface contamination process. This provides visualisation of quantities and data that have been found through this work to provide insight into the distribution of contamination over vehicle surfaces and the mechanisms responsible, including:

- cumulative film thickness distribution [e.g. Figure 55];
- isosurfaces of fluid volume ratio [ $FVR$ ] [e.g. Figure 58];
- isosurfaces of total pressure coloured by  $FVR$  [e.g. Figure 63];
- surface film accumulation histories [e.g. Figure 56];
- tables of accumulated contaminant mass [at  $t = 6$  s];

This automated approach allows for the efficient generation of data that enables the effects of design changes to be understood.

This completes the development of an innovative process that uses numerical simulation to concurrently calculate rear surface contamination and aerodynamic drag for SUVs during their development. It combines eddy-resolving aerodynamic simulation with the capability to account for airborne sprays and surface water films, along with a model for the generation of tyre spray. The capability sits at the core of an efficient process that exploits a high degree of commonality with aerodynamics models, providing a new class of simulation to support vehicle development. This has been accomplished through a systematic programme of research that started by representing the problem with a simple system comprising a simple body without wheels and an idealised spray source. The approach was extended to the use of basic car shape with wheels. These novel systems have allowed the simulation approach to be developed to capture key flow features responsible for deposition of material on vehicle rear surfaces: wheel and vehicle wakes. Confidence has been established through validating these original simulations against aerodynamic force data, velocity distributions through the wake and surface deposition patterns taken from the literature; providing a solid foundation for the extension of the numerical simulation approach to a production vehicle. Full scale surface contamination experiments have enabled a sufficient level of accuracy to be demonstrated by the numerical approach to warrant its deployment in an engineering process.

The key accomplishment captured in this report is that this process innovation is being used to develop automotive products. The following section provides an example of its impact on a specific aspect of a vehicle development project: the validation of a new rear surface contamination reducing “slotted” spoiler for the 18MY Range Rover Sport. This example highlights a unique aspect of this process, when compared to traditional physical test based approaches: the ability to assess both aerodynamic drag and rear surface contamination concurrently.

### 7.3 PROCESS EXAMPLE: REAR SLOTTED SPOILER VALIDATION

As noted at the outset of this work in *Portfolio Report A*, rear surface contamination gives rise to significant levels of customer complaints for SUVs in general. Hence, when considering improvements that could be made to the 18MY Range Rover Sport it was decided to develop a rear spoiler design that diverted “clean” flow from the roof onto the rear screen as a countermeasure for this issue.

This type of spoiler is a well-known treatment for rear screen contamination experienced by blunt-ended vehicles (Goetz, 1971) though they typically increase vehicle drag (Goetz, 1983; Costelli, 1984). A design by Janson *et al.* (2000) that used a duct formed by a gap between the rear spoiler and tailgate on an estate car was found to reduce rear screen soiling by up to 65%; though obtaining this maximum benefit increased the drag of the vehicle by 4%. However, the trend they observed for different spoiler configurations indicated that a drag-neutral soiling reduction of 19% might be obtainable. A similar level of soiling reduction was also obtained from a rear spoiler developed for the new 2017 Land Rover Discovery (Chaligné *et al.*, 2018), which used three lateral slots to take air from the roof boundary layer into an internal duct and onto the rear screen, delivering a 20% reduction in rear screen soiling with a simultaneous 1% [ $0.003\Delta C_D$ ] drag reduction. This encouraging outcome set the scene for the development of the 18MY Range Rover Sport roof spoiler.

By the time the rear surface contamination simulation process had been deployed a candidate design for a “slotted” spoiler had already been developed for the Range Rover Sport using a physical test-based approach. However, a number of issues had arisen which needed to be resolved: [1] was the “slotted” spoiler simultaneously both effective and drag neutral? [2] What was the flow mechanism involved? [3] Could this approach be robustly applied across all SUV programmes?

The first question was still open as both of these aspects could not be tested physically in the same flow field: aerodynamic testing was conducted in the FKFS Aeroacoustic Wind Tunnel [AAWT] at higher speed, with a much lower solid blockage and less onset flow turbulence than available in the TWT, where surface contamination performance was tested. Given these uncertainties, the opportunity to evaluate “slotted” spoiler performance for both aerodynamics and surface contamination under the same conditions, albeit numerically, was a useful compliment to the physical test programme. Further, the deep insights provided into the flow field by simulation enabled its mechanism of action to be elucidated. In turn, this provided a clear indication of when a device of this type could be employed without adverse aerodynamic impact.



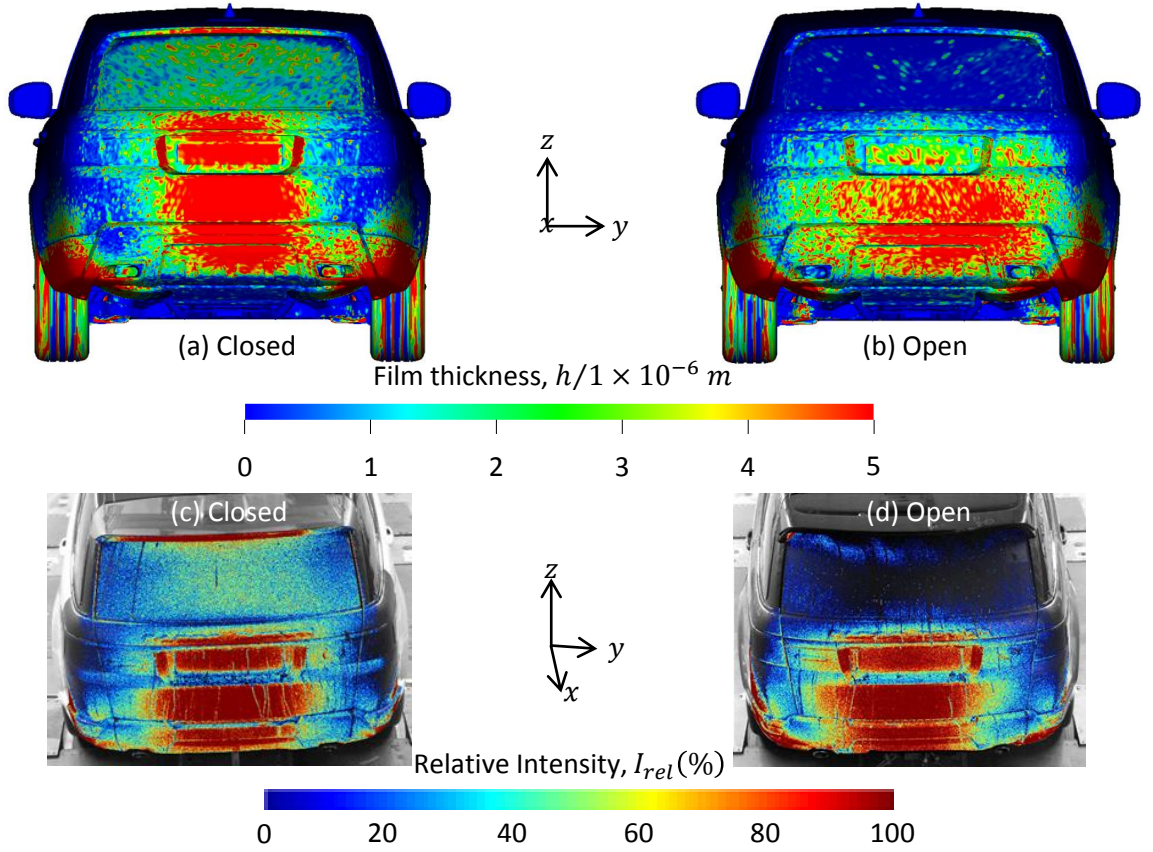


Figure 92. Rear Surface Contamination Patterns for the 18MY Range Rover Sport with the “Slotted” Spoiler Closed and Open from (a-b) Simulation and (c-d) Experiment

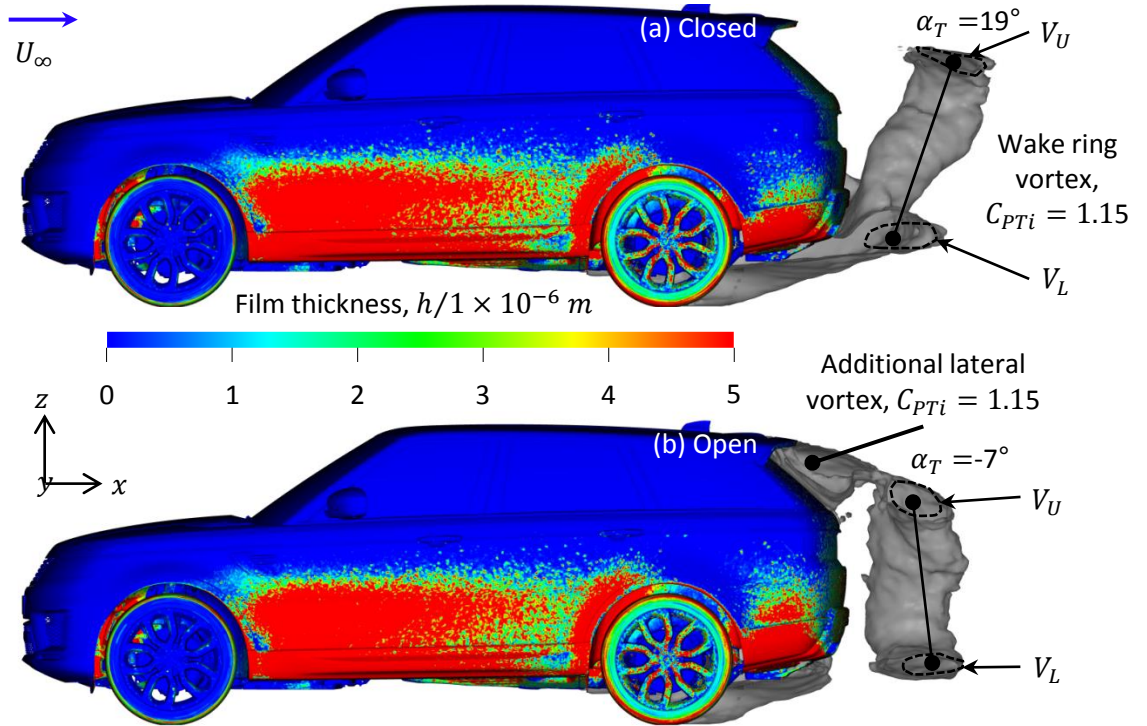


Figure 93. “Slotted” Spoiler Effect on Rear Wake Structure Shown as an Isosurface of Total Pressure Loss  $[C_{PTi}]$  Cut on the  $y=0$  Centre Plane: (a) Spoiler Slot Closed; (b) Spoiler Slot Open

The performance of the “slotted” spoiler obtained from both test and simulation is presented in Figure 92. This shows that opening the roof trailing edge spoiler slot [visible in Figure 92(d)] dramatically reduces rear screen soiling. This trend is seen both in simulation (a — b) and experiment (c — d). Assessing the data using the approach outlined in CHAPTER 6 gave contamination factors relative to the closed slot condition of  $C_{Rel.CFD} = 0.079$  and  $C_{Rel.Expt.} = 0.087$ ; reductions of 92% and 91% from simulation and experiment, respectively.

The aerodynamic impact of opening the slot is shown in Table 9, using both simulation data and measurements made in the AAWT. Both indicate that aerodynamic drag falls by  $0.002\Delta C_D$ , which is equivalent to reducing emissions by  $0.3\text{gCO}_2/\text{km}$  (Rowberry, 2017). In the context of the post-2020 EU CO<sub>2</sub> fines environment, this is a worthwhile benefit. As discussed in *Portfolio Report C*, from 2020 manufacturers face fines of 95€ for *each gram* in excess of their regulatory target, *per vehicle sold* (EC, 2017). On this basis, the author estimates that the drag saving from the slotted spoiler would reduce J/LR’s liability to fines by £705,274 *p.a.*

**Table 9 The Aerodynamic Impact of the 18MY Range Rover Sport Spoiler Slot**

Spoiler Slot "Open" – “Closed”	Changes in the Mean Force Coefficients					
	Drag,	±95%	Side,	±95%	Lift,	±95% C.I.
CFD	-0.002	0.001	0.004	0.006	0.009	0.016
Experiment	-0.002	0.001	-0.002	0.004	0.027	0.004

The mechanisms by which the spoiler simultaneously reduces rear screen soiling and vehicle drag are shown in Figure 93. The flow through the slot drives a new lateral vortex that envelops the screen in “clean” air. This restructures the wake by triggering a vertical switch between wake states similar to that reported for production minivans by Bonnavion *et al.* (2019). Thus, the tilt of the ring vortex is reduced and spray captured by the wake is re-directed to the lower rear surfaces. Hence a more balanced wake is obtained (Morelli, 2000), recovering pressure over the lower base by moving the lower lateral ring vortex arm  $V_L$  downstream. This more than compensates for the drag added by turning flow through the spoiler and the action of the new lateral vortex on the rear screen. This understanding of the flow mechanisms demonstrates that it is not a general solution to rear screen contamination: the drag reduction *relies* on the vehicle wake being sufficiently unbalanced to enable the “slotted” spoiler to save drag by re-balancing it. If this drag-saving opportunity is not present, the financial benefit from fines reduction disappears, along with the business case for fitting a more complex and hence costly part.

This use of an innovative rear surface contamination simulation process confirmed that the “slotted” spoiler design reduced both drag and rear screen soiling simultaneously and in the case of the latter, dramatically. It did so with unprecedented accuracy for soiling, concurrently with aerodynamic drag: something that is not currently possible with physical tests.

## CHAPTER 8 CONCLUSIONS

An innovative process for the concurrent simulation of rear surface contamination and aerodynamic drag has been developed and deployed. In doing so, the way SUVs are developed at Jaguar Land Rover has been changed, in that vehicle designs are now assessed for *both* requirements before physical test properties are available. Furthermore, potential surface contamination countermeasures can be developed virtually before the physical test phase is undertaken.

A novel validation approach, deriving comparable relative contamination factors from both numerical simulations and their equivalent physical tests, has shown that it is warranted to use the process to provide analytical support to vehicle development programmes; indicating directional trends and making A/B comparisons as the design is changed. In doing so, a new state of the art has been defined, setting benchmarks for accuracy.

Evidence for the utility of this innovative process is provided by the example of the validation of the 18MY Range Rover Sport "Slotted" spoiler. The surface contamination simulation approach predicted a rear screen soiling *reduction* of 91% to within 1% of experiment; with the relative rear screen contamination level predicted to within 9%. In addition, simulations matched the drag reduction measured in the wind tunnel. Such concurrent assessment of drag and soiling in the same flow field is not possible with current engineering test facilities.

The process was developed using two levels of simple system, comprising a simplified geometry and idealised spray. These generated a range of wake structures, which were validated against published experimental data; hence the simulation approach was shown to be robust to different wake flows – a vital attribute for an engineering development tool.

The similarity of the flow mechanisms that cause rear surface deposition found between the simplified and production vehicle geometries, along with trends associated with ride height change, underbody flow and wheel wake interactions, strongly suggests that these processes are general and not particular to the production SUV that has been the focus in this work.

This work has provided the first comprehensive description of the mechanisms causing rear surface contamination for blunt-ended vehicles. This can be understood in terms of the interaction between key time-averaged flow structures which emerge from the unsteady flow field: the rear wheel wakes are drawn inwards by the wake ring vortex enabling them to advect airborne spray from the rear tyres into this wake structure, where rotation in its lower lateral arm draws spray upwards and back towards the rear of the vehicle. The bulk of this captured spray is advected via the return flow through the centre of vortex and is deposited around the centre of

the tailgate. Rotation in the upper lateral arm of ring vortex also draws spray upwards over the rear screen with the vertical arms drawing some spray towards the outer regions of the vehicle rear.

A previously partial understanding of the relationship between surface static pressure and rear surface contamination has been extended: deposition is correlated with surface static pressure, *providing spray is locally available*. Hence correlation is strong around the rear stagnation zone where the spray-laden return flow is driven largely normally against the rear surface. This leads to high deposition over the centre of the vehicle tailgate, bumper and license plate [including the rear camera]. Consequently, the correlation between pressure and deposition is at its highest in these regions. In contrast, flow over the rear screen tends to be oblique and advects a spray fraction parallel to the surface; hence the correlation is low at this location due to low local availability of contaminant. Hence, reducing soiling for the rear surfaces should be considered in terms of reducing contaminant availability, by limiting the interaction between wheels wakes and the base wake, or feeding “clean” air into the vehicle wake from the roof or body side.

For the first time it has been shown that the resulting deposition process passes through two linear phases: a Coverage phase where the contaminated area expands and a Depth phase where the contaminated area remains largely stable, but contaminant concentration increases. The relative ranking of rear surface regions by contamination level is generally consistent between these two deposition phases. The numerical simulations also predict the same essentially linear trends for a wide range of wake structures and demonstrate that the relative spatial distribution of contaminant becomes time-invariant. Hence, short-time simulations can be considered to provide relative rankings and deposition distributions that are indicative of longer physical tests.

A series of original experiments and simulations have shown that reduced vehicle ride heights can lead to increased rear surface contamination as these tend to reduce underbody flow, along with moving the vehicle wake closer to the highly contaminated wheel wakes. This poses a challenge for vehicle developers as lower ride heights are also associated with reduced aerodynamic drag; an increasingly important target for both ICE and BEV products to support CO<sub>2</sub> emissions reduction and enhanced range, respectively.

Finally, the first evidence has been presented to suggest that aerodynamically improved underfloors can lead to increased rear surface contamination, or at least redistribution towards regions which sit lower on the rear surface, such as the bumper. This raises a risk for future BEVs that combine aerodynamically advantageous smooth underfloors with vulnerable ADAS features such as rear bumper mounted LIDAR.

## CHAPTER 9 RECENT DEVELOPMENTS AND FUTURE WORK

### 9.1 RECENT DEVELOPMENTS IN THE FIELD

This report has summarised the progressive development of an innovative process for the concurrent numerical simulation of rear surface contamination and aerodynamic drag for SUVs. As noted in CHAPTER 1, these two topics are of considerable interest to manufacturers as they seek to reduce CO<sub>2</sub> emissions from ICE vehicles, increase the range of BEVs and ensure that ADAS sensor installations are robust to on-road conditions. Therefore, it is not surprising that since the completion of the main elements of the research programme, progress has been reported in the understanding of vehicle wakes, the role of unsteadiness in rear surface soiling and the representation of contaminants in simulations. These are briefly reviewed in this final chapter, before recommending a programme of work for the future.

The research strategy adopted here was to progressively build understanding of the requirements for effective simulation of this issue and the physical processes involved, by starting with very simple representations of vehicle geometry. As discussed in CHAPTER 3, this progression started with the wheel-less Windsor Body (Windsor, 1991) before moving the more representative Generic SUV (Wood *et al.*, 2015). During an examination of the spatial resolution required to capture rear surface deposition it became evident that lateral wake instabilities could be a significant influence on the results obtained. Whilst low-frequency general wake motions can be resolved through additional simulation time, there is no guarantee that a plausibly extended simulation would capture an intermittent bi-stability. This could reduce the level of confidence achievable when comparing experiments and simulations. Pavia and Passmore (2018) have examined this issue in more depth and found that adding a short slant to the bottom trailing edge of the Windsor body and including wheels removed this intermittent instability. In essence they found that such wake flow intermittency disappears as the geometry comes to more closely resemble an actual car. If this finding is general, it implies rear soiling simulations are unlikely to be at risk from wake bi-stability.

An additional relevant aspect of Pavia and Passmore's study is their assessment of the effect of wheel rotation on rear surface pressure and wake structure. This work moved directly from the simplified Generic SUV geometry with fixed wheels, to production geometry with rotating wheels. CHAPTER 3 also sought to draw general lessons about the effect of underbody flows and wheel wakes from this simplified fixed-wheel system. In this light it is reassuring to note that Pavia and Passmore (2018) found, "no significant differences ... in either the wake topology or the wake dynamics between having the wheels stationary or rotating". This confirms the validity of the

research strategy adopted here and helps explain why the general trends obtained for the Generic SUV carried over to the production geometry, as noted in CHAPTER 4.

The type of eddy-resolving flow simulation approach used in this work is becoming increasingly popular in the automotive industry for both vehicle development and research. This has increased the need for systematic approaches for deciding when to judge simulations as complete. In CHAPTER 3 the author introduced the “receding average” technique; subsequently published in *Journal Paper B.1* (Gaylard *et al.*, 2017b). This has since been used by other workers to judge convergence of aerodynamic forces obtained from eddy-resolving simulations (Aljure *et al.*, 2018).

Studies by Kabanovs *et al.* (2017a & b) have continued to emphasise the importance of flow unsteadiness in rear surface deposition for SUVs, supporting the approach used in this work. Using cases based on the Generic SUV, these predominantly numerical studies have shown that failing to include the effect of large scale, spatially correlated, wake flow structures on airborne spray leads to under-predicting deposition by a factor of at least two. In addition, an analysis of the unsteady wake dynamics supports a strong association between the modes driven by these structures and contaminant deposition. This could open up a new approach to rear soiling reduction: active flow control of specific wake modes; however, further research is required to understand if this carries over onto real car geometries.

Finally, as explained in *Portfolio Report A*, this work has focussed on a single surrogate model for contamination: water. The original numerical simulations undertaken by the author assign its properties to both airborne particles and any surface deposits. Similarly, the experiments reported in CHAPTER 5 used water with a low concentration of a UV fluorescent dye added. Whilst a reasonable model for a “wet road” scenario, other contaminants are of industrial interest; for example, there is evidence that Volvo are developing a capability to simulate snow adhesion to cars. A report from Chalmers University of Technology (Enmark, 2017) described field and Climatic Wind Tunnel tests of snow build-up on the rear of a saloon car, along with options for numerical simulation. This has been followed up with an in-field study of snow properties, to allow them to be parametrised and included in numerical models (Abrahamsson *et al.*, 2018). Both of these studies were directly supported by Volvo. This shows a broadening of the field beyond the historic boundaries, noted by the author in the comprehensive review published as *Journal Paper A.1* (Gaylard *et al.*, 2017a) and reflects a growing focus on safety and the interaction between ADAS sensors and the on-road environment.

## 9.2 FUTURE WORK

This research programme has led to the successful deployment of an innovative engineering process; however, further work is needed to improve its accuracy. This is particularly evident in the poor predictions made for rear screen contamination. Work should focus on [1] better representation of the experimental boundary conditions; [2] improved spray modelling and [3] increased spatial resolution. The first two approaches will require additional experiments. The latter is important to meet the need for predictions of contamination at the locations of specific ADAS sensors.

This work has focussed on large SUVs; other vehicle types are similarly vulnerable to this issue, such as estate cars and cross-overs. Hence, the approach demonstrated here would benefit from being correlated against these vehicle types.

As it is important to establish the performance of numerical simulations against test data there has been a focus in this work on matching results obtained under the idealised flow conditions provided by wind tunnels capable of assessing rear surface contamination. A consequence of this is that flow effects that vehicles experience in operation, such as yawed [steady and unsteady] and turbulent onset flows have been neglected. Similarly, the effect of a moving ground plane has only received brief attention. Therefore, systematic work needs to be undertaken to explore the relevance of these “real world” boundary conditions and include them in the simulation approach, as appropriate.

The physics embodied in the simulation technique are relevant to other automotive engineering challenges. This provides opportunities for the development of new applications within the fields of aerodynamics, thermal management and vehicle durability. As a first step, extending the process formally to assess body side soiling is logical; given that the deployed process already captures data for this region of the car. Also, as door mirrors are essentially small bluff bodies with the mirror glass providing the rear face, the technique developed here should be adapted to assess mirror glass contamination. In this work the surface film model has only been used to “record” the contamination distribution; however, it can capture surface water film dynamics. Therefore, adapting this approach to simulate a-post overflow and side glass water management should be considered. Moving to the thermal domain, it is known that brake performance is affected by wetting. As the technique developed in this work models a major contributor to this issue – tyre spray – it could be extended by the addition of spray in the onset flow to provide a tool for assessing this issue during the development of the brake cooling strategy. Finally, because the method also captures tyre spray interaction with the underside of the vehicle, it is warranted to consider this approach may provide indications of underbody corrosion risk.

## REFERENCES

- Abrahamsson, P., Eng, M. & Rasmuson, A. (2018). An infield study of road snow properties related to snow-car adhesion and snow smoke. *Cold Reg. Sci. Technol.*, **145**:32-39.
- Ahmed, S. R., Ramm, G., & Faitin, G. (1984). Some salient features of the time-averaged ground vehicle wake. SAE Technical Paper 840300. In: *SAE 1984 World Congress & Exhibition*, Detroit, February 1, 1984. Warrendale: SAE International.
- Al-Garni, A., Bernal, L., & Khalighi, B., (2004). Experimental Investigation of the Flow Around a Generic SUV. SAE Technical Paper 2004-01-0228. In: *SAE 2004 World Congress & Exhibition*, March 8-11, 2004. Detroit. Warrendale: SAE International.
- ADL. (2014). *The Automotive CO<sub>2</sub> Emissions Challenge - 2020 Regulatory Scenario for Passenger Cars*. Arthur D. Little.
- Aljure, D. E., Calafell, J., Baez, A. & Oliva, A. (2018). Flow over a realistic car model: Wall modeled large eddy simulations assessment and unsteady effects. *J. Wind Eng. Ind. Aerodyn.*, **174**: 225-240.
- Amodeo, J. (2004). The Development of CFD as a Primary Design Tool at Jaguar Cars. In: *5<sup>th</sup> MIRA International Conference on Vehicle Aerodynamics*, October 13-14, 2004, Gaydon, UK. Nuneaton: MIRA Ltd.
- Ask, J. & Davidson, L. (2006). The Sub-Critical Flow Past a Generic Side Mirror and its Impact on Sound Generation and Propagation, AIAA-2006-2558. In: *12<sup>th</sup> AIAA/CEAS Aeroacoustics Conference (27<sup>th</sup> AIAA Aeroacoustics Conference)*, May 8-10, 2006, Cambridge, Massachusetts. Reston, Virginia: American Institute of Aeronautics and Astronautics.
- Arai, M., Tone, K., Taniguchi, K., Murakami, M. *et al.* (2015). Development of the Aerodynamics of the New Nissan Murano. SAE Technical Paper 2015-01-1542. In: *SAE 2015 World Congress and Exhibition*, April 21-23, 2015, Detroit. Warrendale: SAE International.
- Bai, C. & Gosman, A. (1995). Development of Methodology for Spray Impingement Simulation. SAE Technical Paper 950283. In: *International Congress and Exposition*, February 27-March 2, 1995, Detroit. Warrendale: SAE International.
- Bhatnagar, P. L., Gross, E. P. & Krook, M. (1954). A Model for Collision Processes in Gases. I. Small Amplitude Processes in Charged and Neutral One-Component Systems. *Phys. Rev.*, **94**(3):511-525.
- Blumrich, R., Grün, N. & Schuetz, T. C. (2016) Numerical Methods. In: Schuetz, T. C. (Ed.) *Aerodynamics of Road Vehicles*, 5<sup>th</sup> Edition. Warrendale: SAE International.



- Bonnaivon, G., Cadot, O., Herbert, V., Parpais, S. *et al.* (2019). Asymmetry and global instability of real minivans' wake. *J. Wind Eng. Ind. Aerodyn.* **184**: 77-89.
- Borman, G. and Johnson, J. (1962). Unsteady Vaporization Histories and Trajectories of Fuel Drops Injected into Swirling Air. SAE Technical Paper 620271. In: *National Powerplant Meeting*, Philadelphia, Pa., and October 29— November 2, 1962. New York: Society of Automotive Engineers, Inc.
- Bouchet, J. P., Delpech, P. & Palier, P. (2004). Wind tunnel simulation of road vehicle in driving rain of variable intensity. In: *5th MIRA International Conference on Vehicle Aerodynamics*, October 13 – 14, 2004, Gaydon, UK. Nuneaton: MIRA Ltd.
- Box, G. E. P. (1978). Robustness in the Strategy of Scientific Model Building. In: *Army Research Office Workshop on Robustness in Statistics*, April 11—12, 1978, Research Triangle Park, North Carolina.
- Borg, A. & Vevang, R. (2006). On The Prediction of Exterior Contamination with Numerical Simulations (Simple Lagrangian Particle Tracking methods with and without Wall Film Model). In: *6<sup>th</sup> MIRA International Conference on Vehicle Aerodynamics*, October 25-26, 2006, Gaydon, UK. Nuneaton: MIRA Ltd, pp. 380-388.
- Carr, G. & Stapleford, W. (1986). Blockage Effects in Automotive Wind-Tunnel Testing. SAE Technical Paper 860093. In: *SAE International Congress and Exposition*, February 24-28, 1986, Detroit. Warrendale: Society of Automotive Engineers Inc.
- Chaligné, S., Turner, R. & Gaylard, A. (2018). The Aerodynamics Development of the New Land Rover Discovery 5. In: Wiedemann, J. (Ed.) *Progress in Vehicle Aerodynamics and Thermal Management. FKFS 2017*. Springer, Cham.
- Chen, H., Chen, S., & Matthaeus, W. H. (1992). Recovery of the Navier-Stokes equations using a lattice-gas Boltzmann method. *Phys. Rev. A*, **45**(8): R5339-R5342.
- Chen, H., Teixeira, C., & Molvig, K. (1997). Digital physics approach to computational fluid dynamics: some basic theoretical features. *Int. J. Mod. Phys. C*, **8**(4): 675-684.
- Chen, H., Kandasamy, S., Orszag, S., Shock, R., *et al.* (2003). Extended Boltzmann kinetic equation for turbulent flows. *Science*, **301**(5633): 633-636.
- Chen, S., Chen, H., Martinez, D. *et al.* (1991). Lattice Boltzmann Model for Simulation of Magnetohydrodynamics. *Phys. Rev. Lett.* **67**(27): 3776 - 3779.

- Chen, Q., Wu, H., Zhou, J., & Liu, J. (2013) A Combined Digital and Experimental Process for the Aerodynamic Optimization of the New Lavidia. SAE Technical Paper 2013-01-0204. In: *SAE 2013 World Congress and Exhibition*, April 16-18, 2013, Detroit. Warrendale: SAE International.
- Cho, M., Oh, C., Kim, H.G. & Ih, K-D. (2014). Benchmark Test of CFD Software Packages for Sunroof Buffeting in Hyundai Simplified Model. *Trans. Korean Soc. Noise Vib. Eng.* **24**(3):171-179.
- Clift, R. & Gauvin, W. H. (1970). The motion of particles in turbulent gas streams. *Proc Chemeca*, **1**(1):14-28.
- Cooper, R. G. (1990). Stage-gate systems: A new tool for managing new products. *Business Horizons*, **33**(3): 44–54.
- Costelli, A. F. (1984). Aerodynamic Characteristics of the Fiat UNO Car. SAE Technical Paper 840297. In: *SAE 1984 International Congress & Exposition*, February 27-March 2, 1984, Detroit. Warrendale: SAE International.
- Cyr, S., Ih, K-D., & Park, S-H. (2011). Accurate Reproduction of Wind-Tunnel Results with CFD. SAE Technical Paper 2011-01-0158. In: *SAE 2011 World Congress & Exhibition*, Detroit, April 12–14, 2011. Warrendale: SAE International.
- Dávila, A., del Pozo, E., Aramburu, E., & Freixas, A. (2013). Environmental Benefits of Vehicle Platooning. SAE Technical Paper 2013-26-0142. In: *Symposium on International Automotive Technology (SIAT'13)*, January 9-11, 2013, Pune. India: The Automotive Research Association of India.
- Duell, E. G., & George, A. R. (1999). Experimental Study of a Ground Vehicle Body Unsteady Near Wake. SAE Technical Paper 1999-01-0812. In: *International Congress & Exposition*, March 1-4, 1999, Detroit. Warrendale: SAE International.
- Dukowicz, J. K. (1980). A particle-fluid numerical model for liquid sprays. *J. Comput. Phys.*, **35**(2):229-53.
- Duncan, B. D., Fischer, A. & Kandasamy, S. (2010). Validation of Lattice-Boltzmann Aerodynamics Simulation for Vehicle Lift Prediction. In: *ASME 2010 3rd Joint US-European Fluids Engineering Summer Meeting*, August 1-5, 2010, Montreal, Canada: **1**(A-C):2705-2716.
- EC. (2017, November 27). *Reducing CO<sub>2</sub> emissions from passenger cars. Climate Action – European Commission*. [Online]. (URL [https://ec.europa.eu/clima/policies/transport/vehicles/cars\\_en](https://ec.europa.eu/clima/policies/transport/vehicles/cars_en)) Brussels: European Commission (Accessed 27 November 2017).

- Elghobashi, S. (1991). Particle-laden turbulent flows: direct simulation and closure models. *Appl. Sci. Res.*, **48**:301–14.
- Elghobashi, S. (1994). On Predicting Particle-Laden Turbulent Flows. *Appl. Sci. Res.*, **52**(4): 309-329.
- Enmark, M. (2017, February). *CFD Modelling of Snow Contamination on Cars. Implementation of a Snow Adhesion Regime Map by User Defined Functions*. [Online]. (URL <http://publications.lib.chalmers.se/records/fulltext/248293/248293.pdf>) Gothenburg: Chalmers University of Technology (Accessed 05 March 2018).
- Fares, E. (2006). Unsteady flow simulation of the Ahmed reference body using a lattice Boltzmann approach. *Comput. Fluids*, **35**(8–9):40–95.
- Fischer, O., Kuthada, T., Wiedemann, J. *et al.* (2008). CFD Validation Study for a Sedan Scale Model in an Open Jet Wind Tunnel. SAE Technical Paper 2008-01-0325. In: *SAE 2010 World Congress*, April 14-17, 2008, Detroit. Warrendale: SAE International.
- Fischer, O., Kuthada, T., Mercker, E. *et al.*, (2010). CFD Approach to Evaluate Wind-Tunnel and Model Setup Effects on Aerodynamic Drag and Lift for Detailed Vehicles. SAE Technical Paper 2010-01-0760. In: *SAE 2010 World Congress*, April 13-15, 2010, Detroit. Warrendale: SAE International.
- Forbes, D. C., Page, G. J., Passmore, M. A. *et al.* (2014). Computational study of wake structure and base pressure on a generic SUV model. In: *The International Vehicle Aerodynamics Conference*, October 14 – 15, Loughborough, UK. Cambridge: Woodhead Publishing. pp. 67-79.
- Forbes, D., Page, G., Passmore, M. *et al.* (2017). A study of computational methods for wake structure and base pressure prediction of a generic SUV model with fixed and rotating wheels. *Proc. Inst. Mech. Eng., Part D*, **231**(9): 1222 – 1238.
- Frisch, U., Hasslacher, B. & Pomeau, Y. (1986). Lattice-Gas Automata for the Navier-Stokes Equation. *Phys. Rev. Lett.* **56**(14): 1505 – 1508.
- Froling, T. & Juechter, T. (2005). 2006 Chevrolet Corvette C6 Z06 Aerodynamic Development. SAE Technical Paper 2005-01-1943. In: *2005 SAE World Congress*, April 11-14, 2005, Detroit. Warrendale: SAE International.
- Gaylard, A. P. (2008). Aerodynamic Development of the New Jaguar XF. In: *7<sup>th</sup> MIRA International Conference on Vehicle Aerodynamics*, October 22-23, 2008, Coventry. Nuneaton: MIRA Ltd.

- Gaylard, A. (2009). The Appropriate Use of CFD in the Automotive Design Process. SAE Technical Paper 2009-01-1162. In: *SAE 2009 World Congress*, April 20-23, 2009, Detroit. Warrendale: SAE International.
- Gaylard, A. P., & Duncan, B. (2011). Simulation of Rear Glass and Body Side Vehicle Soiling by Road Sprays. *SAE Int. J. Passeng. Cars – Mech. Syst.*, **4**(47):184-196.
- Gaylard, A., Pitman, J., Jilesen, J. *et al.* (2014). Insights into Rear Surface Contamination Using Simulation of Road Spray and Aerodynamics. *SAE Int. J. Passeng. Cars - Mech. Syst.* **7**(2):673-681.
- Gaylard, A. P., Kirwan, K. & Lockerby, D. A. (2017a). Surface contamination of cars: a review. *Proc. Inst. Mech. Eng., Part D*, **231**(9): 1160-1176.
- Gaylard, A. P., Kabanovs, A., Jilesen, J. *et al.* (2017b). Simulation of rear surface contamination for a simple bluff body. *J. Wind Eng. Ind. Aerodyn.*, **165**: 13-22.
- Glantschnig, W. J. & Chen, S.-H. (1981). Light scattering from water droplets in the geometrical optics approximation. *Appl. Opt.*, **20** (14): 2499-2509.
- Goetz, H. (1971). The Influence of Wind Tunnel Tests on Body Design, Ventilation, and Surface Deposits of Sedans and Sport Cars. SAE Technical Paper 710212. In: Gleason, M., Romberg, G. F. & Scharpf, G., (Eds.) *Automotive Aerodynamics (Selected SAE Papers through 1977.)* SAE/PT-78/16. Warrendale: Society of Automotive Engineers, Inc., pp.109 – 127.
- Goetz, H. (1983). Bus design features and their aerodynamic effects. In: Dorgham, M. A. & Businaro, U. L. eds., *Impact of Aerodynamics on Vehicle Design: Proceedings of an International Conference*, June 16-18, 1982, Café Royal, London. St. Helier, Jersey: Interscience Enterprises, pp. 229-255.
- Goetz, H. & Schoch, R. (1995). Reducing Splash and Spray of Trucks and Passenger Cars. SAE Technical Paper 950631. In: *SAE International Congress & Exposition*, February 27 – March 2, 1995, Detroit. Warrendale: SAE International.
- Grandemange, M., Gohlke, M. & Cadot, O. (2013). Bi-stability in the turbulent wake past parallelepiped bodies with various aspect ratios and wall effects. *Phys. Fluids*, **25**(9): 095103-1 - 095103-9.
- Hagemeier, T., Hartmann, M. & Thevenin, D. (2011). Practice of vehicle soiling investigations: A review. *Int. J. Multiphase Flow*, **37**(8): 860-875.

- Hägemeier T., Hartmann M., Kühle M., Thévenin D., *et al.* (2012). Experimental characterization of thin films, droplets and rivulets using LED fluorescence. *Exp. Fluids*, **52**(2): 361-374.
- Hahn, S. A., Kruse, N. & Werner, F. (2007). Virtual Aerodynamic Engineering at GM Europe Development of the 2006 OPEL Corsa. SAE Technical Paper 2007-01-0102. In: *2007 World Congress*, April 16-19, 2007, Detroit, Warrendale: SAE International.
- Harada, N., Kitamura, K., Okutsu, Y., Hamamoto, N. *et al.* (2015). Preliminary, one-way coupled, rain-droplets/airflow simulations over automobile. *Int. J. Automot. Eng.*, **6**(4), 105-112.
- Hoffman, J. & Johnson, C. (2006). A new approach to computational turbulence modelling. *Comput. Methods Appl. Mech. Engrg.*, **195**(23-24): 2865-2880.
- Höld, R., Brenneis, A., Eberle, A., Schwarz, V. *et al.* (1999). Numerical simulation of aeroacoustic sound generated by generic bodies placed on a plate. I - Prediction of aeroacoustic sources, AIAA-1999-1896. In: *5<sup>th</sup> AIAA/CEAS Aeroacoustics Conference and Exhibit*, May 10 - 12, 1999, Bellevue, USA. Reston, Virginia: American Institute of Aeronautics and Astronautics.
- Howell, J., Sherwin, C., Passmore, M., & Le Good, G. (2002). Aerodynamic Drag of a Compact SUV as Measured On-Road and in the Wind Tunnel. SAE Technical Paper 2002-01-0529. In: *SAE 2002 World Congress & Exhibition*, March 4-7, 2002, Detroit. Warrendale: SAE International.
- Hunt, J. C. R, Wray, A. A. & Moin, P. (1988). Eddies, streams, and convergence zones in turbulent flows, In: *Studying Turbulence Using Numerical Simulation Databases, Proceedings of the 1988 Summer Program*, Report No. 89N-24555. USA: NASA. pp. 193-208.
- Hutchinson, J. (2016, December 21). CLEAN YOUR CAR! Bastian Schweinsteiger turns up in his muddy £80,000 motor for Manchester United training... but leaves 15 minutes later. *The Sun*. [Online]. (URL <https://www.thesun.co.uk/sport/2451126/bastian-schweinsteiger-turns-up-in-his-muddy-motor-for-manchester-united-training-but-leaves-15-minutes-later>) London, UK: News UK & Ireland Limited (Accessed 14 May 2017).
- IHS Automotive (2014, July 16). SUVs and Crossovers Overtake Sedans to Become Most Popular Vehicle Body Style in the U.S., IHS Automotive Finds. [Online]. (URL <http://press.ihs.com/press-release/automotive/suvs-and-crossovers-overtake-sedans-become-most-popular-vehicle-body-style->). Colorado, USA: IHS Automotive (Accessed 8 February 2016).
- Irving Brown, Y., Windsor, S., & Gaylard, A. P., (2010). The Effect of Base Bleed and Rear Cavities on the Drag of an SUV. SAE Technical Paper 2010-01-0512. In: *SAE 2010 World Congress & Exhibition*, April 13-15, 2010, Detroit. Warrendale: SAE International.

Janson, J., Darrieutort, L., Bannister, M. & Seremak, P. (2000). New Development and Working Methods used in the Aerodynamic Development of the New Large Estate. JSAE Paper Number: 20005352. In: *JSAE Spring Convention*, May 2000, Yokohama. Tokyo: Society of Automotive Engineers of Japan, Inc, pp. 5-8. (No. 13-00).

JATO Dynamics (2016, February 2). SUV takes over as the Best-Selling Segment in Europe for the first time. [Online]. (URL <http://www.jato.com/suv-takes-over-as-the-best-selling-segment-in-europe-for-the-first-time/>). London, UK: JATO Dynamics Ltd. (Accessed 8 February 2016).

Jilesen, J., Gaylard, A., Duncan, B., Konstantinov, A., *et al.* (2013). Simulation of Rear and Body Side Vehicle Soiling by Road Sprays Using Transient Particle Tracking. *SAE Int. J. Passeng. Cars - Mech. Syst.*, **6**(1): 424-435.

Jilesen, J., Alajbegovic, A., & Duncan, B. (2015). Soiling and Rain Simulation for Ground Transportation. In: *7th European-Japanese Two-Phase Flow Group Meeting (7TH-EUJPTPFGM 2015)*, October 11-15, 2015, Zermatt, Switzerland.

Johl, G., Passmore, M., & Render, P. (2004). Design Methodology and Performance of an indraft wind tunnel. *The Aeronautical Journal*, **108**(1087): 465-473.

Kabanovs, A., Varney, M., Garmory, A., Passmore, M. *et al.* (2016a) Experimental and Computational Study of Vehicle Surface Contamination on a Generic Bluff Body. SAE Technical Paper 2016-01-1604. In: *SAE 2016 World Congress and Exhibition*, April 12-14, 2016, Detroit. Warrendale: SAE International.

Kabanovs, A., Hodgson, G., Garmory, A., Passmore, M. A. *et al.* (2016b). Experimental and Computational Study of Vehicle Soiling on a Generic SUV. In: *AEROVEHICLES 2, Second International Conference in Numerical and Experimental Aerodynamics of Road Vehicles and Trains*, June 21-23, 2016, Göteborg, Sweden. Göteborg: Chalmers University of Technology.

Kabanovs, A., Hodgson, G., Garmory, A., *et al.* (2017a). A Parametric Study of Automotive Rear End Geometries on Rear Soiling. *SAE Int. J. Passeng. Cars - Mech. Syst.* **10**(2).

Kabanovs, A., Garmory, A., Passmore, M. & Gaylard, A. (2017b). Computational simulations of unsteady flow field and spray impingement on a simplified automotive geometry. *J. Wind Eng. Ind. Aerodyn.*, **171**:178-195.

Kandasamy, S., Duncan, B., Gau, H., Maroy, F. *et al.* (2012). Aerodynamic Performance Assessment of BMW Validation Models using Computational Fluid Dynamics. SAE Technical Paper 2012-01-0297. In: *SAE 2012 World Congress & Exhibition*, April 24-26, 2012, Detroit. Warrendale: SAE International.

- Keating, A., Shock, R., & Chen, H. (2008). Lattice Boltzmann Simulations of the Unsteady Flow Behind the Ahmed Body. SAE Technical Paper 2008-01-0740. *SAE 2008 World Congress*, April 14-17, 2008, Detroit. Warrendale: SAE International.
- Koitrand, S., Lofdahl, L., Rehnberg, S., & Gaylard, A., (2014). A Computational Investigation of Ground Simulation for a Saloon Car. *SAE Int. J. Commer. Veh.*, **7**(1):111-123.
- Kotapati, R., Keating, A., Kandasamy, S. *et al.* (2009). The Lattice-Boltzmann-VLES Method for Automotive Fluid Dynamics Simulation, a Review. SAE Technical Paper 2009-26-0057. In: *SAE 2009 World Congress*, Detroit, April 20-23, 2009. Warrendale: SAE International.
- Krajnović S., & Davidson L. (2003). Numerical Study of the Flow Around a Bus-Shaped Body. *ASME. J. Fluids Eng.*, **125**(3):500-509.
- Krastev, V. & Bella, G. (2011). On the Steady and Unsteady Turbulence Modeling in Ground Vehicle Aerodynamic Design and Optimization. SAE Technical Paper 2011-24-0163. In: *ICE2011 - 10th International Conference on Engines & Vehicles*, September 11-15, 2011, Capri, Italy. Warrendale: SAE International.
- Kremheller, A. (2014). The Aerodynamics Development of the New Nissan Qashqai. SAE Technical Paper 2014-01-0572. In: *SAE 2014 World Congress & Exhibition*, April 8-10, 2014, Detroit. Warrendale: SAE International.
- Kuthada, K., Widdecke, N. & Wiedemann, J. (2002). Advanced Investigation Methods on Vehicle Soiling. In: *4<sup>th</sup> MIRA International Vehicle Aerodynamics Conference*, October 16-17, 2002, Warwick, UK. Nuneaton: MIRA Ltd.
- Kuthada, T. & Cyr, S. (2006). Approaches to Vehicle Soiling. In: Wiedermann, J. & Hucho, W-H. (Eds.) *Progress in Vehicle Aerodynamics, IV, Numerical Methods*. Renningen: Expert-Verlag, pp. 111-123.
- Lajos T., Preszler L. & Finta L. (1984). Wind tunnel investigation of mud deposits on the body of a bus. *Int. J. Veh. Des.*, **5**( 6): 693-703.
- Lajos, T., Preszler, L. & Finta, L. (1986). Effect of moving ground simulation on the flow past bus models. *Wind Eng. Ind. Aerodyn.*, **22**(2-3): 271-277.
- Le Good, G. & Garry, K. (2004). On the Use of Reference Models in Automotive Aerodynamics. SAE Technical Paper 2004-01-1308. In: *SAE 2004 World Congress & Exhibition*, March 8-11, 2004, Detroit. Warrendale: SAE International.

- Lienhart, H. & Becker, S. (2003). Flow and Turbulence Structure in the Wake of a Simplified Car Model. SAE Technical Paper 2003-01-0656. In: *2003 SAE World Congress*, March 3-6, 2003, Detroit. Warrendale: SAE International.
- Li, Y., Shock, R., Zhang, R. *et al.* (2004). Numerical study of flow past an impulsively started cylinder by the lattice-Boltzmann method. *J. Fluid Mech.*, **519**: 273-300.
- Li, Y., Zhang, R., Shock, R. *et al.* (2009). Prediction of vortex shedding from a circular cylinder using a volumetric Lattice-Boltzmann boundary approach. *Eur. Phys. J. Spec. Top.*, **171**(1): 91-97.
- Lietz, R., Pien, W., & Remondi, S. (2000). A CFD Validation Study for Automotive Aerodynamics. SAE Technical Paper 2000-01-0129. In: *SAE 2000 World Congress*, Detroit, March 6-9, 2000. Warrendale: SAE International.
- Lietz, R., Mallick, S. & Kandasamy, S. (2002). Exterior Airflow Simulations Using a Lattice Boltzmann Approach. SAE Technical Paper 2002-01-0596. In: *SAE 2002 World Congress*, March 4-7, 2002, Detroit. Warrendale: SAE International.
- Lockard, D. P. (2010). In search of grid converged solutions. *Procedia Eng.* **6**: 224-233.
- Machida, K., Kaneko, M., & Ogawa, A. (2015) Aerodynamic Development of the New Honda FIT/JAZZ. SAE Technical Paper 2015-01-1535. In: *SAE 2015 World Congress*, April 21-23, 2015, Detroit. Warrendale: SAE International.
- Maycock, G. (1966). *The problem of water thrown up by vehicles on wet roads*. Harmondsworth: Road Research Laboratory. (LR004).
- Mayer, W. & Wickern, G. (2011). The New Audi A6/A7 Family – Aerodynamic Development of Different Body Types on One Platform. *SAE Int. J. Passeng. Cars - Mech. Syst.* **4**(1): 197 – 206.
- Meredith, K. V., Heather, A., De Vries, J., *et al.* (2011). A numerical model for partially-wetted flow of thin liquid films. In: Mammoli, A. A. and Brebbia, C. A. (eds) *Computational Methods in Multiphase Flow VI*. Southampton: WIT Press, pp.239-250.
- Morelli, A. (2000). A New Aerodynamic Approach to Advanced Automobile Basic Shapes. SAE Technical Paper 2000-01-0491. In: *SAE 2000 World Congress*, March 6-9, 2000, Detroit. Warrendale: SAE International.
- Mundo, C., Sommerfeld, M. & Tropea C. (1995). Droplet-wall collisions: Experimental studies of the deformation and breakup process. *Int. J. Multiphase Flow*, **21**(2): 151-173.



O'Rourke, P. & Amsden, A. (1987). The TAB Method for Numerical Calculation of Spray Droplet Breakup. SAE Technical Paper 872089. In: *International Fuels and Lubricants Meeting and Exposition*, November 2-5, 1987, Toronto. Warrendale: Society of Automotive Engineers.

O'Rourke, P. & Amsden A. (1996). A Particle Numerical Model for Wall Film Dynamics in Port-Injected Engines. SAE Technical Paper 961961. In: *International Fall Fuels & Lubricants Meeting & Exposition*, October 14-17, 1996, San Antonio. Warrendale: SAE International.

O'Rourke, P. & Amsden A. (2000). A Spray/Wall Interaction Submodel for the KIVA-3 Wall Film Model. SAE Technical Paper 2000-01-0271. In: *SAE 2000 World Congress*, March 6–9, 2000, Detroit. Warrendale: SAE International.

Oettle, N., Meskine, M., Senthoooran, S., Bissell, A. *et al.* (2015). A Computational Approach to Assess Buffeting and Broadband Noise Generated by a Vehicle Sunroof. *SAE Int. J. Passeng. Cars - Mech. Syst.*, **8**(1):196-204.

Paschkewitz, J. S. (2006). Simulation of spray dispersion in a simplified heavy vehicle wake. United States: Lawrence Livermore National Laboratory. (UCRL-TR-218207)

PA Consulting. (2017). *THE CO<sub>2</sub> EMISSIONS CHALLENGE: Some carmakers are running late in the race to 2021*. London: PA Knowledge Limited.

Palin, R., Johnston, V., Johnson, S., D'Hooge, A. *et al.* (2012). The Aerodynamic Development of the Tesla Model S - Part 1: Overview. SAE Technical Paper 2012-01-0177. In: *SAE 2012 World Congress & Exhibition*, April 24-26, 2012, Detroit. Warrendale: SAE International.

Paul, A., Chauhan, R., Srivastava, R., & Baruah, M. (2016). Advanced Driver Assistance Systems. SAE Technical Paper 2016-28-0223. In: *9<sup>th</sup> SAEIndia International Mobility Conference*, February 8-10, 2016, New Delhi. Warrendale PA: SAE International.

Pavia, G., Passmore, M., & Gaylard, A. (2016). Influence of Short Rear End Tapers on the Unsteady Base Pressure of a Simplified Ground Vehicle. SAE Technical Paper 2016-01-1590. In: *SAE 2016 World Congress and Exhibition*, April 12-14, 2016, Detroit. Warrendale: SAE International.

Pavia, G. & Passmore, M. (2018). Characterisation of Wake Bi-stability for a Square-Back Geometry with Rotating Wheels. In: Wiedemann, J. (Ed.) *Progress in Vehicle Aerodynamics and Thermal Management*. FKFS 2017. Springer, Cham.

Perry, A. & Passmore, M. (2013). The Impact of Underbody Roughness on Rear Wake Structure of a Squareback Vehicle. SAE Technical Paper 2013-01-0463. In: *SAE 2013 World Congress & Exhibition*, April 16-18, 2013, Detroit. Warrendale: SAE International.

- Perry, A., Passmore, M., & Finney, A., (2015). Influence of Short Rear End tapers on the Base Pressure of a Simplified Vehicle, *SAE Int. J. Passeng. Cars - Mech. Syst.* **8**(1):317-327.
- Perry, A-K., Pavia, G. & Passmore, M. (2016). Influence of short rear end tapers on the wake of a simplified square-back vehicle: wake topology and rear drag. *Exp Fluids*, **57**: 169.
- Perry, A-K. (2016). *An investigation into the base pressure of simplified automotive squareback geometries* (PhD thesis). Loughborough University, UK.
- Phan, V., Tanaka, H., Nagatani, T., Wakamatsu, M. *et al.* (2017). A CFD Analysis Method for Prediction of Vehicle Exterior Wind Noise. *SAE Int. J. Passeng. Cars - Mech. Syst.* **10**(1):286-298.
- Plocher, D. A., & Browand, F. K., (2014). Comparing Spray from Tires Rolling on a Wet Surface. *Tire Science and Technology*, **42**(3): 145–165.
- Plucinsky, T. (2012, January). *Vision meets fascination. The design process at the BMW Group*. [Online]. (URL [https://www.press.bmwgroup.com/usa/article/detail/T0125226EN\\_US](https://www.press.bmwgroup.com/usa/article/detail/T0125226EN_US)) Germany: BMW Group (Accessed 12 October 2017).
- Radovich, C. & Plocher, D. (2009). Experiments on Spray from a Rolling Tire. In: Browand, F., McCallen, R. & Ross, J. (Eds.) *The Aerodynamics of Heavy Vehicles II: Trucks, Buses, and Trains*. Springer Berlin Heidelberg: 403-417.
- Rodgers, J. L. & W. Nicewander, A. (1988). Thirteen Ways to Look at the Correlation Coefficient. *Am Stat.*, **42**(1):59-66.
- Rouméas, M., Gilliéron, P., & Kourta, A. (2009). Analysis and control of the near-wake flow over a square-back geometry. *Comput. Fluids*, **38**(1): 60-70.
- Rowberry, C. (2017). Aerodynamic Development of the new Bentley Continental GT. In: *International Forum – Advanced Automotive Aerodynamics 2017*, Manchester, November 31 – December 1, 2017. Stockport: interNéct Ltd.
- Samples, M., Gaylard, A. P. & Windsor, S. (2010). The Aerodynamics Development of the Range Rover Evoque. In: *8th MIRA International Conference on Vehicle Aerodynamics*, October 13-14, 2010, Grove, UK. Nuneaton: MIRA Ltd.
- SAE. (2009). *Potential Failure Mode and Effects Analysis in Design (Design FMEA)*. (SAE J1739).
- Sapnaras, D. & Dimitriou, I. (2008). Experimental Analysis of the Underbody Pressure Distribution of a Series Vehicle on the Road and in the Wind Tunnel. SAE Technical Paper 2008-01-0802. In: *2008 World Congress*, April 14-17, 2008, Detroit. Warrendale: SAE International.

Schembri Puglisevich, L., Gaylard, A., Osborne, M., Jilesen, J. *et al.* (2016). Application of CFD to Predict Brake Disc Contamination in Wet Conditions. *SAE Int. J. Passeng. Cars - Mech. Syst.*, **9**(2):800-807.

Schnepf, B., Schütz, T., & Indinger, T. (2015). Further Investigations on the Flow Around a Rotating, Isolated Wheel with Detailed Tread Pattern. *SAE Int. J. Passeng. Cars - Mech. Syst.*, **8**(1):261-274.

Schuetz, T., Krüger, L. and Lentzen, M. (2016). Aerodynamic Forces and Their Influence on Passenger Vehicles. In: Schuetz, T., (Ed.) *Aerodynamics of Road Vehicles*, 5th Ed., Warrendale: SAE International.

Sims-Williams, D., Dominy, R., & Howell, J. (2001). An Investigation into Large Scale Unsteady Structures in the Wake of Real and Idealized Hatchback Car Models. SAE Technical Paper 2001-01-1041. In: *SAE 2001 World Congress*, March 5-8, 2001, Detroit. Warrendale: SAE International.

Sims-Williams, D. & Duncan, B. (2003). The Ahmed Model Unsteady Wake: Experimental and Computational Analyses. SAE Technical Paper 2003-01-1315. In: *SAE 2003 World Congress & Exhibition*, March 3-6, 2003, Detroit. Warrendale: SAE International.

Spalart, P. R. (2000). Strategies for turbulence modelling and simulations. *Int. J. Heat Fluid Flow*, **21**(3):252-263.

Spruss, I., Kuthada, T., Wiedemann, J., Cyr, S. *et al.* (2011). Spray Pattern of a Free Rotating Wheel: CFD Simulation and Validation. In: *Progress in Vehicle Aerodynamics and Thermal Management*. Stuttgart: Expert-Verlag, pp.64-80.

Stamatis, D. H. (2003). *Failure Mode and Effect Analysis: FMEA from Theory to Execution*. 2nd Ed. Milwaukee: ASQ Quality Press.

Sterken, L., Sebben, S. & Löfdahl, L. (2016). Numerical Implementation of Detached-Eddy Simulation on a Passenger Vehicle and Some Experimental Correlation. *J. Fluids Eng.*, **138**(9):091105-1 - 091105-14.

Stern, F., Wilson, R. V., Coleman H. W., & Paterson E. G. (2001). Comprehensive Approach to Verification and Validation of CFD Simulations—Part 1: Methodology and Procedures. *J. Fluids Eng.*, **123**(4):793-802.

Storms, B., Satran, D., Heineck, J., & Walker, S. (2004). A Study of Reynolds Number Effects and Drag-Reduction Concepts on a Generic Tractor-Trailer. In: *34<sup>th</sup> AIAA Fluid Dynamics Conference*

- and Exhibit, June 28 –July 1, 2004, Portland, Oregon. Reston, Virginia: American Institute of Aeronautics and Astronautics.
- Seubert, C., Nietering, K., Nichols, M., Wykoff, R. *et al.* (2012). An Overview of the Scratch Resistance of Automotive Coatings: Exterior Clearcoats and Polycarbonate Hardcoats. *Coatings*, **2**(4): 221-234.
- Subramaniam, S. (2013). Lagrangian–Eulerian methods for multiphase flows. *Prog Energy Combust. Sci.*, **39**(2–3): 215-245.
- Tivert, T. & Davidson, L. (2010). Experimental study of water transport on a generic mirror. In: *7<sup>th</sup> International Conference on Multiphase Flow, ICMF 2010*, May 30 – June 4, 2010, Tampa. Gainesville: University of Florida.
- Tutuianu, M., Marotta, A., Steven, H., Ericsson, E., *et al.* (2013). *Development of a World-wide Worldwide harmonized Light duty driving Test Cycle (WLTC)*. Draft Technical Report, DHC subgroup, GRPE-67-03. Geneva: United Nations.
- Uchida, K. & Okumura, K., (1999). Aerodynamic Noise Simulation based on Lattice Boltzmann Method (Surface Pressure Fluctuations around A-pillar). SAE Technical Paper 1999-01-1127. In: *SAE International Congress and Exposition*, March 1-4, 1999, Detroit. Warrendale: SAE International.
- UNECE (2017). *Addendum 15: Global technical regulation No. 15: Global technical regulation on Worldwide harmonized Light vehicles Test Procedure*, Amendment 2, ECE/TRANS/180/Add.15. Geneva: United Nations.
- Wang, F., Yin, Z., Yan, S., Zhan, J. *et al.* (2017). Validation of Aerodynamic Simulation and Wind Tunnel Test of the New Buick Excelle GT. *SAE Int. J. Passeng. Cars - Mech. Syst.*, **10**(1):195-202.
- Windsor, S. C. (1991). The Effect of Rear End Shape on Road Vehicle Aerodynamic Drag. Paper C427/6/031. In: *IMEchE Autotech*, Birmingham, UK: Institution of Mechanical Engineers.
- Weinman, K. A., van der Ven, H., Mockett, C. R., Knopp, T. A., *et al.* (2006). Study of Grid Convergence Issues for the Simulation of the Massively Separated Flow around a Stalled Airfoil Using DES and Related Methods. In: Wesseling, P., Onate, E. & Périaux, J. (Eds.) *European Conference on Computational Fluid Dynamics ECCOMAS CFD 2006*. The Netherlands: TU Delft.
- Weir, D. H. (1980). Truck Splash and Spray - Full Scale Tests and Alleviation Devices. In: *18<sup>th</sup> Aerospace Sciences Meeting*. Pasadena: American Institute of Aeronautics and Astronautics.

- Wood, A., Passmore, M., Forbes, D., Wood, D. *et al.* (2015). Base Pressure and Flow-Field Measurements on a Generic SUV Model. *SAE Int. J. Passeng. Cars - Mech. Syst.*, **8**(1): 233-241.
- Wordley, S. & Saunders, J. (2009). On-road Turbulence: Part 2. *SAE Int. J. Passeng. Cars – Mech. Syst.*, **2**(1):111-137.
- Wu, H., Zhou, J., Chen, Q., Liu, G. *et al.* (2016). Validation and Application of Digital Simulation for Improving Rear Side Window Buffeting of a Sedan. *SAE Int. J. Passeng. Cars - Mech. Syst.* **9**(2):638-644.
- Yakhot, V. & Orszag, S. A. (1986). Renormalization Group Analysis of Turbulence. I. Basic Theory. *J. Sci. Comput.*, **1**(1): 3-51.

## APPENDIX A: THE WINDSOR BODY

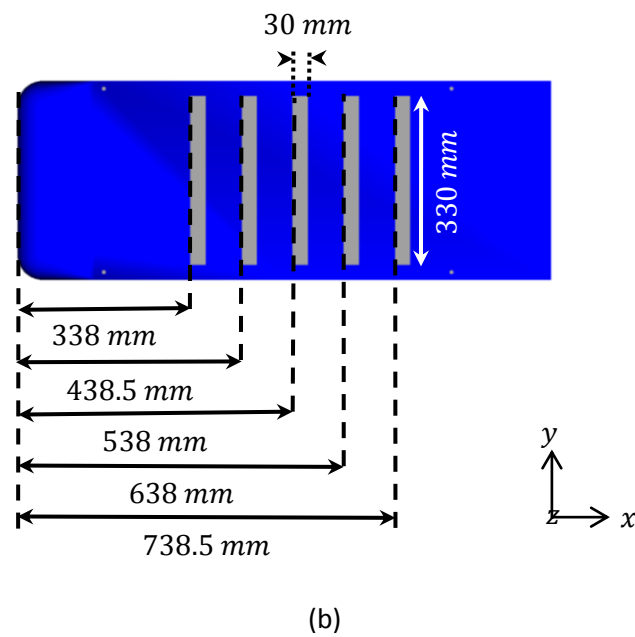
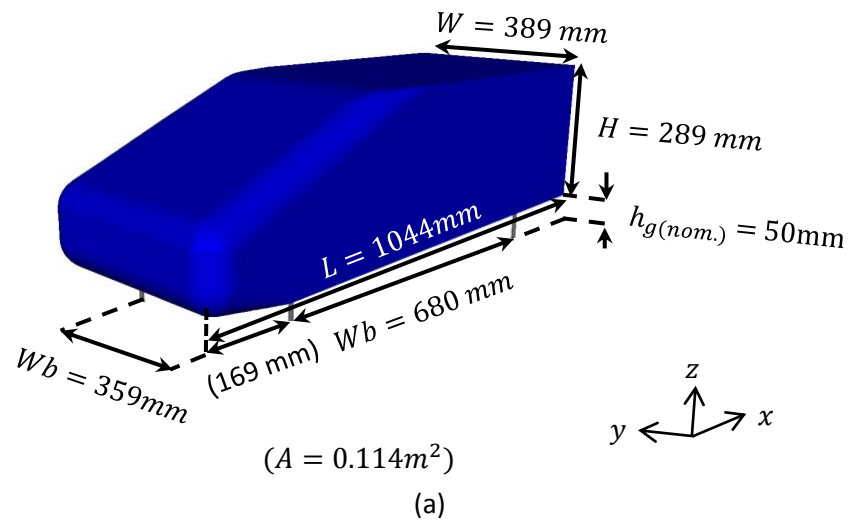


Figure 94. The Windsor Body with (a) Principal Dimensions Shown and (b) a Scheme for Representing Underbody Roughness (Perry and Passmore, 2013)

## APPENDIX B: THE GENERIC SUV

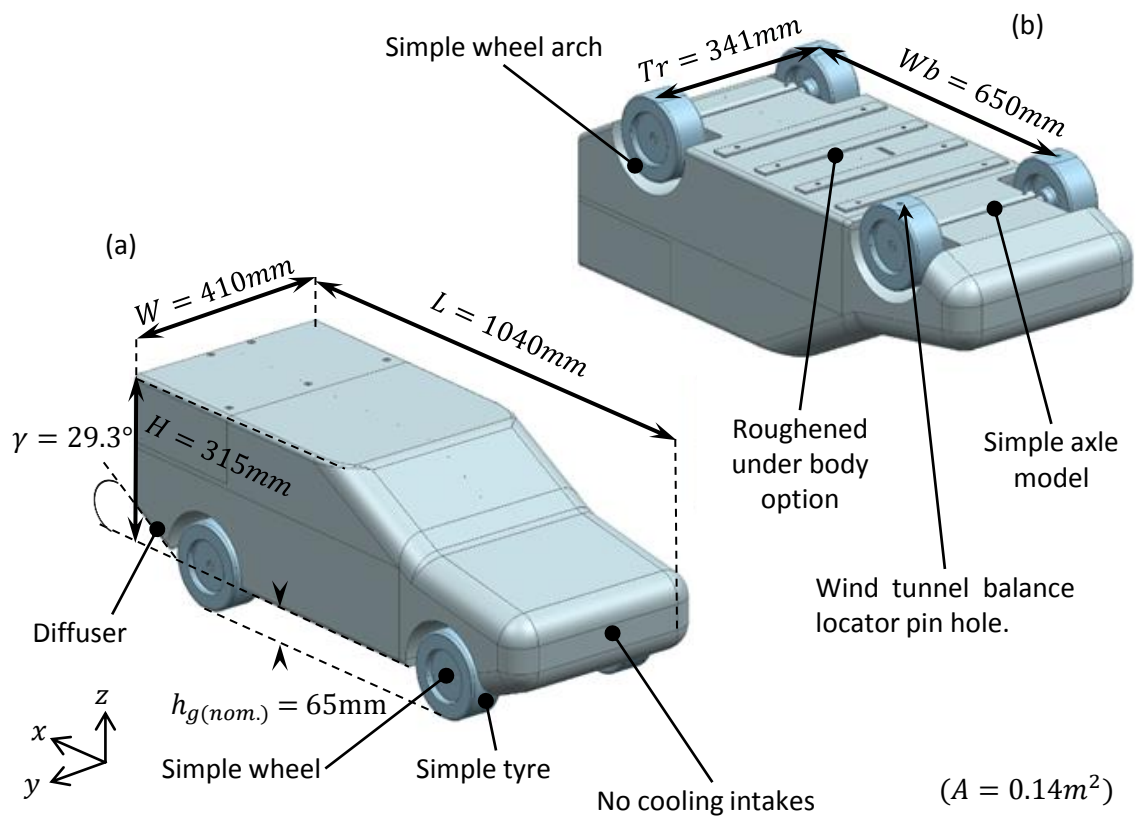


Figure 95. The Generic SUV Shown with its (a) Principal Dimensions and (b) Mounting Details and an Optional Scheme for Underbody Roughness (Wood *et al.*, 2015)

## APPENDIX C: THE 13MY RANGE ROVER

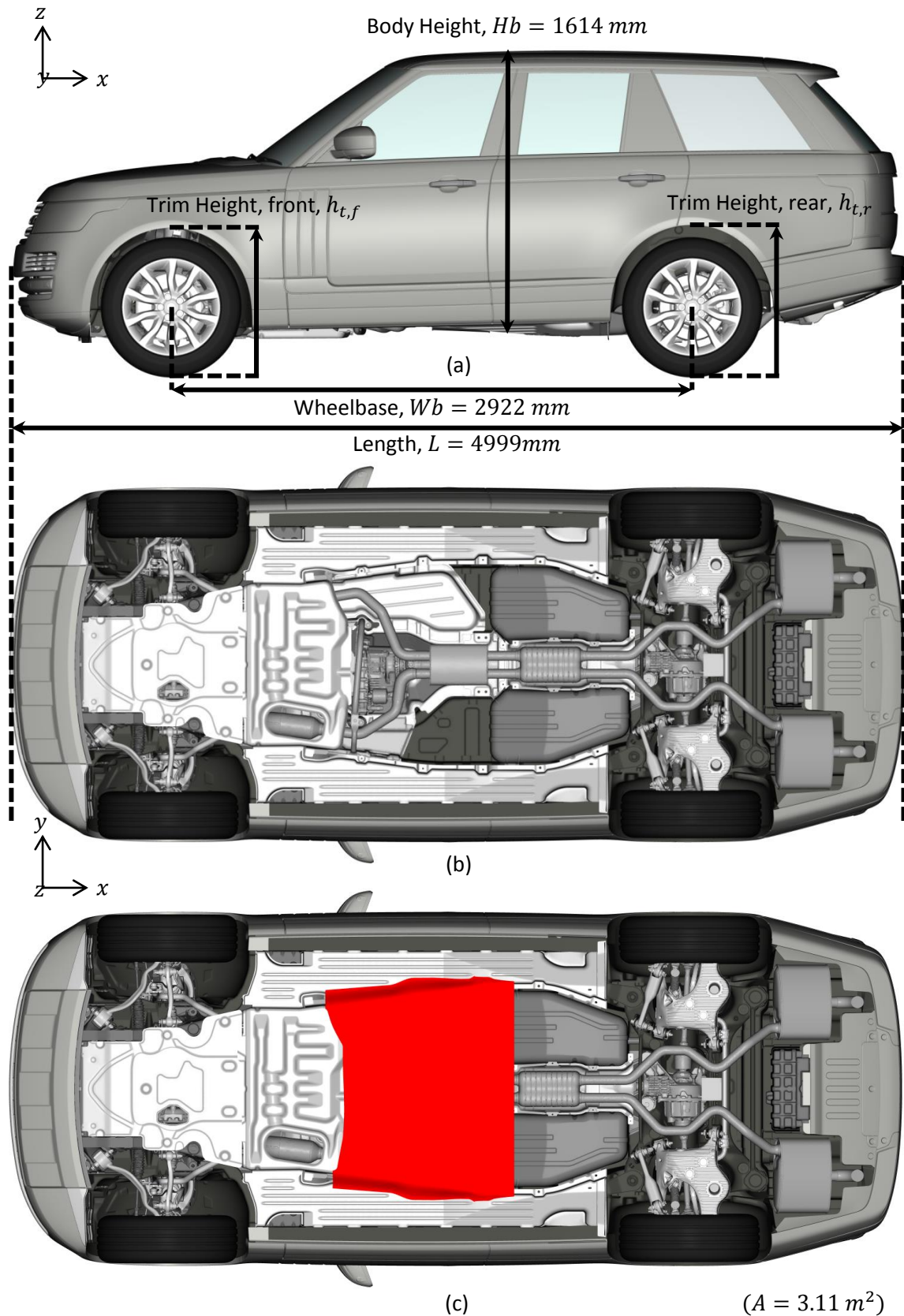


Figure 96. The 13MY Range Rover Principal Dimensions (a) in Side Elevation (b) from the Underside and (c) with an Aerodynamically Improved Underfloor